THE BEHAVIOUR OF GRANULAR MATERIAL IN PURE SHEAR, DIRECT SHEAR AND SIMPLE SHEAR

LING ZHANG, BSc, MSc

Doctor of Philosophy

ASTON UNIVERSITY

September 2003

THESIS CONTAINS CD/DVD

Aston University

THE BEHAVIOUR OF GRANULAR MATERIAL IN PURE SHEAR, DIRECT SHEAR AND SIMPLE SHEAR

Ling Zhang, BSc, MSc
Doctor of Philosophy
2003

SUMMARY

This thesis reports the results of DEM (Discrete Element Method) simulations of the mechanical behaviour of granular material subjected to pure shear, direct shear and simple shear deformation. In all cases, the state of stress has been evaluated in terms of (a) the volume average of the contact force distribution within the specimen and (b) the distribution of forces transmitted to the wall boundaries.

In biaxial compression tests, the stress calculations based on boundary information underestimate the principal stresses leading to a significant overestimation of the shear strength. In direct shear tests, the shear strain becomes highly concentrated in the mid-plane of the sample during the test. Although the stress distribution within the specimen is heterogeneous, the evolution of the stress ratio inside the shear band is similar to that inferred from the boundary force calculations. It is also demonstrated that the dilatancy in the shear band significantly exceeds that implied from the boundary displacements. In simple shear tests, the stresses acting on the wall boundaries do not reflect the internal state of stress but merely provide information about the average mobilised wall friction. It is demonstrated that the results are sensitive to the initial stress state defined by $K_0 = \sigma_h/\sigma_v$. For all cases, non-coaxiality of the principal stress and strain-rate directions is examined and the corresponding flow rule is identified.

Periodic cell simulations have been used to examine biaxial compression for a wide range of initial packing densities. Both constant volume and constant mean stress tests have been simulated. The characteristic behaviour at both the macroscopic and microscopic scales is determined by whether or not the system percolates (enduring connectivity is established in all directions). The transition from non-percolating to percolating systems is characterised by transitional behaviour of internal variables and corresponds to an elastic percolation threshold, which correlates well with the establishment of a mechanical coordination number of ca. 3.0. Strong correlations are found between macroscopic and internal variables at the critical state.

Finally, an attempt has been made to investigate strain localization. It is shown that, associated with the formation of a shear band, there are a number of distinct characteristics: discontinuities in the displacement and fluctuating velocity fields across the shear band, large particle rotations and expansion within the shear band, buckling of the strong force transmission pathways as they cross the shear band and sliding contacts concentrated along the shear zone. The shear band inclination is found to depend on (a) wall friction and (b) in periodic cell simulations the shear band inclination changes as the sample dimensions change.

KEY WORDS: Discrete Element Method; Shear strength; Percolation; Critical State; Strain localization.

ACKNOWLEDGEMENTS

An historian said that a man's greatness could be measured by whether he started others to think along fresh lines. I believe that Dr. Colin Thornton is a great supervisor. He is the person who introduced the fascinating area of granular materials to me and the constant and penetrating discussions with him have always inspired me to seek insight and knowledge in this area of research. Therefore, I would like to express my highest and heartfelt gratitude to him.

I wish to extend my gratitude to my friends and colleagues who in many ways have contributed to this work. In particularly I would like to acknowledge Dr. David Kafui for his invaluable assistance in helping me to understand and modify the original TRUBAL code for this study. I also thank Dr. L. Y. Li., who taught me how to cope with the difficulties I met as a foreigner living abroad. Over the years, I have grown to appreciate and love the UK and its people and will fondly remember my years at Aston for many years to come. I am also grateful for the assistance helps from Prof. R. J. Kettle during the course of my PhD study.

It has been an honour and privilege to receive the Overseas Research Studentship award (ORS) provided by the Committee of Vice-Chancellors and Principals (CVCP) of the UK universities, to whom I am very grateful for the financial support for this study. I also would like to acknowledge Aston University for awarding me the James Watt Fellowship, and IChemE for providing me the Travel Grant, which provided me the opportunities to attend the International Conference Powders & Grain 2001 in Japan and the World Congress on Particle Technology 2002 in Australia, respectively.

Finally, I would like to thank my parents for their unwavering and unstinting support and encouragement. Great acknowledgement is given to my husband Dr. Charley C. Y. Wu, who read the first draft of my thesis and gave me a lot of good ideas on organizing this thesis; Also for his patience, understanding and encouragement. Without the constant help and love from him and my family this thesis would not have been completed so smoothly.

Contents

List of Figures

List of Tables

Notation

φ_c	Coulomb friction angle
φ_m	Mohr friction angle or angle of shearing resistance
ψ	angle of dilation
i	angle of non-coaxiality
σ_1, σ_2	principal stress
ε_1, ε_2	principal strain
ϕ_1, ϕ_2	principal fabric
ε_v	volumetric strain, $\varepsilon_1 + \varepsilon_2$
γ	shear strain
K_0	initial stress ratio, σ_h/σ_v
e	void ratio
n	porosity
sf	solid fraction
υ	Possion's ratio
E	Young's modulus
Z_m	mechanical coordination number

CHAPTER 1: INTRODUCTION

1.1 General background

Granular materials such as soil, powders and grains are very common in nature and in the processing industries. Recently there has been a rapid expansion in research activities of both scientists and engineers investigating the behaviour of granular media due to their fascination with the complex behaviour and the technological importance of such materials. Granular materials consist of individual particles in contact and the surrounding voids, so that they are generally multiphase media of solid, liquid and gas, and sometimes appear to behave as fluids or solids. However, the behaviour of granular materials is more complicated than that of a fluid or a solid due to the fact that the solid phase is composed of discrete solid particles, so they cannot be simply characterised as either liquid or solid.

The mechanical behaviour of granular materials has been widely investigated using the principles of continuum mechanics. According to continuum mechanics, the function of external loads is expressed by the continuous mechanical state variable 'stress' and the relation between loads and stresses is given by equilibrium equations; deformations are reflected by another continuous mechanical state variable 'strain' and the link between displacements and the strain field is given by compatibility equations. Stress and strain are related to each other through constitutive equations, which are expected to contain all the necessary information about the mechanical characteristics of the material. However, at the microscopic scale, granular materials are neither continuous nor homogenous in nature. Thus, the generalized continuum mechanics is not sufficient to adequately predict the mechanical behaviour of granular materials. Any improvements to constitutive equations based on continuum mechanics require information about the evolution of the microstructure and the micromechanical behaviour occurring at the particle scale. It is hence of fundamental interest in both engineering and scientific fields to link macro-level state variables with micro-variables, such as contact forces, particle displacements and local geometrical characteristics. Some studies have been conducted to establish the discrete mechanics of granular materials and to establish the relationship with continuum mechanics (Satake and Jenkins, 1988). Attempts were also made to understand the

mechanical behaviour of granular materials at the microscopic scale. For instance, Bagi (1996a) and Satake (1985) investigated the geometrical aspects of grains and associated voids mathematically to specify the spatial distribution and orientation of grains and their contact conditions.

Laboratory experiments are traditionally used to directly observe the behaviour of granular materials. Various experimental techniques have been developed for this purpose. The Casagrande direct shear box is one of the earliest devices developed to measure the mechanical properties of granular materials. However, using this device has the disadvantage that the shear plane is predetermined at the intersection between the two halves of the box that constitute the apparatus. In order to overcome this limitation, various types of so-called simple shear apparatuses have been developed, which can impose a uniform deformation on the sample. There were several versions of the simple shear apparatus. Among others, the simple shear tester developed by the Swedish Geotechnical Institute (SGI) in the early 1950s (Kjellman, 1951), Cambridge Simple Shear Apparatus (Roscoe, 1953; Stroud, 1971) and the apparatus developed by the Norwegian Geotechnical Institute (NGI) (Bjerrum and Landva, 1966) that can test a cylindrical sample. However, it has been argued (Budhu, 1984) that the state of stress or strain in either the Cambridge version or the NGI version of the simple shear apparatus is far from homogeneous. Many other types of testing devices for determining the shearing characteristics of granular materials have also been developed and gradually increased in complexity. These include: the 'true triaxial cell' in which the three principal stresses can be varied independently (Ko and Scott, 1967; Pearce, 1971; Lade, 1978; Lanier and Zitouni, 1987); the hollow cylinder apparatus (Saada, 1988; Ishihara and Towatha, 1983); the directional shear cell (DSC) (Arthur *et al.*, 1977); and, more recently, the true biaxial shear tester (Harder and Schwedes, 1985); the Matsuoka apparatus (Matsuoka *et al.*, 1986); and the 1γ2ε apparatus (Joer *at el.*, 1992). Experiments conducted with these various types of apparatus can provide the necessary information for developing constitutive models. However, the boundary effects and the operator effects are inevitable in such experiments, which always result in the data obtained from real experiments being questionable. Also, the reproducibility of real experiments is generally very low. In addition, the experiments do not give sufficient information about what happens inside the specimen.

With the rapid development in computer technology, numerical simulation has become a powerful tool to study the behaviour of granular materials. Cundall (1971) developed a computer program to model the progressive failure of systems of discrete rectangular blocks. From this study the concept of the Discrete Element Method (DEM) originated. Further developments of the program for simulating the quasi-static shear deformation of the large assemblies of discs were reported in detail by Cundall (1978), Cundall and Strack (1979a) and the principles of the method were described by Cundall and Strack (1979b). The simulations were qualitatively validated by comparisons with laboratory tests on photo-elastic disc assemblies reported by de Josselin de Jong and Verruijt (1969) and Oda and Konishi (1974). Cundall (1988) developed a three dimensional version of the program, named TRUBAL. In this program, a periodic cell was employed as a parallelepiped with numerical connection between opposite faces and the system was treated as a continuum. The force-displacement relationship was adapted so that either the linear spring-dashpot system or Hertz-Mindlin theory could be used. The DEM has also proved to be very effective for studying various dynamic problems of granular materials as illustrated by Thornton (2001). Therefore, DEM simulations open up pathways to new knowledge of particulate media because it is now possible to observe and quantify phenomena in minute detail at the microscopic level. In contrast, laboratory experiments resist attempts to glean micro-structural information because of the difficulty in viewing and/or measuring phenomena that are interior to the specimen.

From numerical simulations with DEM, information about what happens inside assemblies of particles can be obtained. The motions of all the constituent particles are continuously tracked and the interactions between particles are modelled directly. Consequently, the statistical distributions and temporal evolution of all internal variables can be determined and ensemble averages of the stress-strain behaviour can be obtained. Cundall's program was first adapted at Aston University by Blackburn (1983), who only considered regular arrays of discs. Barnes (1985) extended the Aston version of the program to simulate the quasi-static shear deformation of random assemblies of different sized discs. Thornton and Barnes (1986) presented simulation results for both a constant mean stress test and a constant volume test performed on the sample with same initial configuration. It was shown that, for these two tests, the evolution of the angle of internal shearing resistance and the evolution of the induced structural anisotropy were essentially identical. General three-dimensional numerical simulations of quasi-static shear

deformations have been performed over the complete range of deviatoric radial loading paths for both dense and loose polydisperse systems by Thornton and Sun (1993, 1994). The reported macroscopic behaviour was in good qualitative agreement with results obtained from real experiments on sand. Further examinations of shear deformation of three-dimensional disperse systems of elastic spheres subjected to different complex loading histories have been reported by Thornton and Antony (1998) and Thornton (2000a). These works demonstrated that DEM simulated experimentation is a versatile and convenient technique that can be used to examine the sophisticated behaviour of granular materials under complex loading histories.

The study reported in this thesis deals with numerical simulations of the quasi-static mechanical behaviour of granular materials under various stress and strain paths, in which inertia effects are negligible. Some modifications of the Aston version of TRUBAL have been made in order to model different types of shear test and the corresponding results are reported.

1.2 Research objectives

Traditionally, theories are validated by experiments or new experimental information leads to new theoretical developments. However, laboratory tests used to determine the compressibility and strength of granular materials rely very much on boundary measurements and cannot give sufficient information regarding the internal deformation processes. It is not clear how reliable the information, obtained at the boundaries of a specimen, can represent the ensemble state of stress and strain inside the specimen, which is supposed to represent the constitutive behaviour of the material at a point in a continuum, i.e. the data required for constitutive modelling. Numerical simulations can, in principle, provide the necessary link between what happens at the grain scale and the continuum interpretation and also assess how well laboratory experiments can reliably measure the true material behaviour. Therefore, the work presented in this thesis is focussing on the following two main topics:

1. To examine the advantages and disadvantages of three shear testers commonly used in the laboratory and to investigate the boundary effect on the behaviour of granular materials in these testers. The traditional interpretations of the mechanical

behaviour of granular materials based on these laboratory tests are also examined.

2. To study the quasi-static shear characteristics of granular media at both the macro- and micro- scales by conducting DEM simulations. To examine in detail the spatial distribution and temporal evolution of contact force transmission, interparticle sliding and structural anisotropy; aiming at obtaining a better understanding of how the physics observed at the micro-scale is related to the macro-scale mechanics of granular media.

Within this context, the main objectives of this study are:

(i) To conduct biaxial compression tests with both periodic (**BCP**) and wall (**BCW**) boundaries under both constant volume and constant mean stress conditions. The boundary effect is examined by comparing the results obtained from these tests.

(ii) To simulate a series of direct shear tests (**DST**) under different boundary conditions and to compare the apparent stress-strain data obtained from boundary information with the corresponding ensemble stress-strain behaviour in the shear band.

(iii) To develop an algorithm to model the simple shear test (**SST**) and examine the performance of such a test and to explore the non-coaxiality of stress and strain rate direction.

(iv) To conduct periodic cell simulations of biaxial compression for a wide range of packing densities so that the macroscopic and microscopic behaviour for both non-percolating collisional systems and compacted percolating systems with enduring contacts can be examined.

(v) To explore strain localization and the micromechanics of shear band formation.

1.3 Typical tests considered

Three types of shear tests commonly performed in the laboratory are considered to investigate the micro- and macro- mechanical behaviour of granular materials. The effects of stress path, boundary condition and principal stress direction on the behaviour of granular material are examined. Among the tests considered, two of them, which involve the rotation of principal stress directions during shear, are sketched in Fig. 1.1. The most common test to measure the shear strength is the direct shear test (Fig. 1.1a). In particle

technology this is performed in a Jenike shear cell, which is circular in cross section, whereas in soil mechanics the Casagrande shear box (with square cross-section) is generally used. The simple shear test (Fig. 1.1b) seems to be, in theory, a simple test for measuring the shear modulus and the shear strength directly.

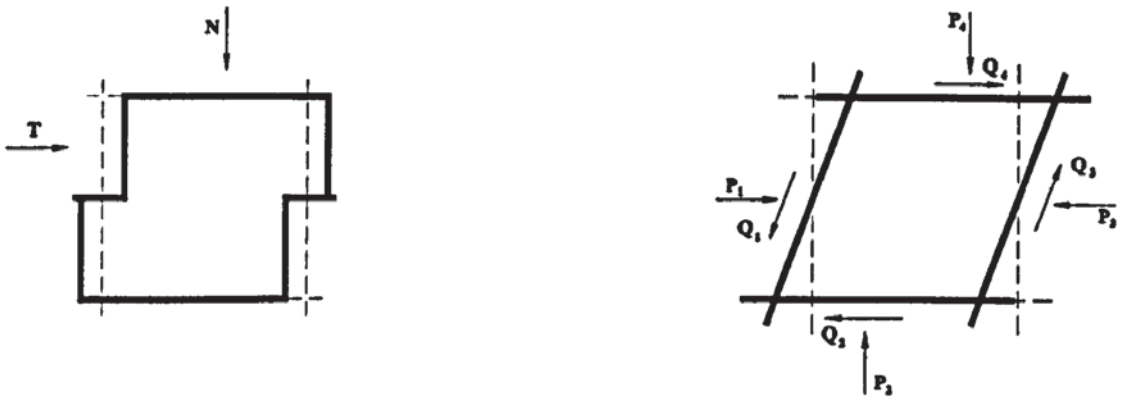

(a) direct shear test (b) simple shear test

Fig. 1.1 Shear tests with principal stress rotation

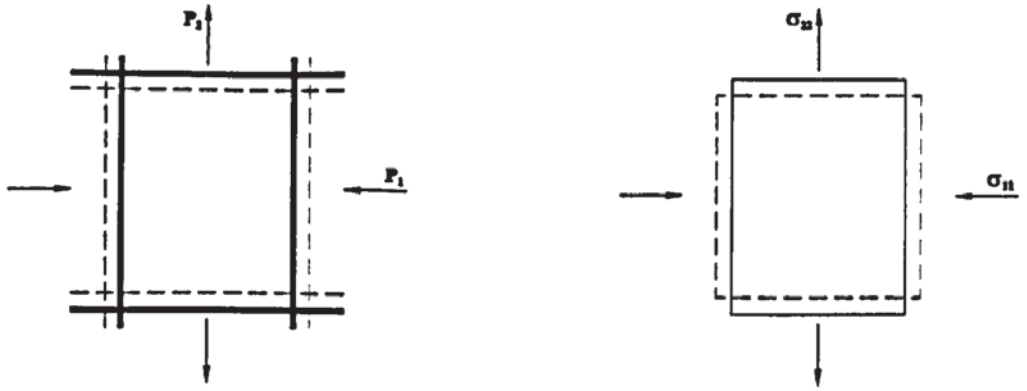

(a) with wall boundaries (b) with periodic boundaries

Fig. 1.2 Biaxial compression test

The biaxial compression test is a plane strain test that provides principal stresses on the face of the sample. It is strain-controlled. Nearly all tests that are simple monotonic or involve 90° changes in principal stress directions are performed in this test. Two different boundaries are chosen for this type of tests. One is with real wall boundaries (Fig.1.2a) and the other is with periodic boundaries (Fig. 1.2b).

All the tests are simulated in two-dimensional space. Although this two-dimensional analogue material cannot reproduce all the features of the three-dimensional behaviour of real materials, the great simplicity with this analogue is, in particular, the ability to

visualize the behaviour in detail. The reported simulation results are believed to be qualitatively representative of the plane strain behaviour of real granular media.

1.4 Order of the thesis

The main text described in this thesis can be classified into two general catalogues. The methodology and computational techniques are described in Chapter 2 and Appendix A. The details of numerically simulated experiments and results are presented in Chapters 3-7. The presentation of the thesis is organized as follows:

In Chapter 2, basic principles of the mechanics and the microscopic characterization of granular materials are discussed.

Two series of biaxial compression tests on an assembly of 5000 polydisperse spheres with periodic boundaries and wall boundaries are reported in Chapter 3. Preliminary testing and initial considerations are explained, including the choice of particle size distribution, assembly generation, choice of physical and control parameters, preparation method and also several servo-control techniques used. Comparisons between the results obtained from these two sets of tests are provided and the effect of wall friction on the behaviour of the specimen is discussed.

Two shear tests involving principal stress rotation during shearing are presented in Chapters 4 and 5. In Chapter 4, the effects of the aspect ratio of the shear box and boundary friction are first examined by a set of constant volume tests. The influence of different stress levels on the mechanical behaviour of the sample is then investigated by carrying out constant normal stress tests. The behaviour of the material within the central shear zone is examined in detail.

In Chapter 5, the results of simple shear tests are presented. In addition to the examination of the effect of boundary friction and different stress levels, the simple shear tests are carried out on three samples with different initial stress ratio K_0. Based on the calculations of the stress tensor, the non-coaxiality of principal stress and strain rate directions are identified and the effects of K_0 on the behaviour of the material are discussed. The deformation patterns in the simple shear test are examined from the area

variation of local void cells and particles rotations. Comparisons between the results of the simple and pure shear test results based on volume-averaged data are also made.

The macroscopic and microscopic behaviour of both non-percolating collisional systems and compact percolating systems with enduring contacts is examined in Chapter 6. The details of the spatial distribution and temporal evolution of contact force transmission are presented and better understanding on the correlation of the physics observed at the micro-scale with the macro-scale mechanics of granular media are hence achieved. The localisation phenomenon and shear band formation are discussed in Chapter 7. The particle kinematics, such as displacement field and velocity field together with the distribution of sliding contacts and particle rotations are analysed. The measured shear band inclination angles and shear band thickness are reported.

In Chapter 8, a summary of the main conclusions and achievements of this study are given. Recommendations for future study are also suggested.

In addition, there are four appendices attached:
In Appendix A, the principles of the Discrete Element Method are described. In this appendix, not only the force-displacement law used at inter-particles contacts is prescribed, but also numerical stability and the suppression of natural assembly oscillations by viscous damping are discussed. Moreover, this appendix also gives the details of the logic framework within the computer program TRUBAL that allows efficient control of the numerical apparatus.

In Appendix B, new input commands that are required to run the numerical tests with wall boundaries implemented into the TRUBAL code during the course of this study and some examples of input command files are provided.

In Appendix C, video clips illustrating the grain scale behaviour of granular material are discussed and the locations of these videos on the website are provided.

Finally, in Appendix D, the difference between two implementation schemes for the simple shear test is discussed. In addition, the effects of each implementation on both the micro- and macroscopic behaviour of granular materials are presented.

CHAPTER 2: MECHANICS AND MICRO-MECHANICS OF GRANULAR MATERIALS

2.1 Introduction

A bulk solid may be defined as an assembly of discrete solid particles dispersed in a volume. Bulk solids may comprise of only a solid phase or a two-phase disperse system of solid and fluid, solid and gas or even a three-phase system made up of solid-fluid-gas. The bulk behaviour is governed primarily by interparticle forces, friction, and collisions. In general, such materials are so complex that understanding their overall behaviour requires the knowledge of several scientific areas, such as traditional fluid mechanics, plasticity theory, soil mechanics, rheology and kinetic gas theory. In this study only one phase systems made up of cohesionless granular media is considered. These types of material are often handled in many processing industries, geotechnical and other technical applications. Knowing the mechanical behaviour of these media is essential for understanding and solving a wide range of technological and scientific problems concerning granular materials and therefore, it is necessary to develop relevant constitutive theories for such materials in order to analyse their mechanical behaviour.

The mechanical behaviour of granular materials is often studied at two scales: the macro scale and the micro scale. The macro scale study corresponds to the discretization of boundary value problems to be solved using a global constitutive equation. The micro scale study corresponds to a smaller level at which a microstructure exists and which essentially governs the global behaviour. Generally, there are two approaches to formulating the mechanical behaviour of granular materials: a macro approach which is generally based on continuum mechanics (Goodman and Cowin, 1971, 1972; Savage, 1979, Massoudi and Mehrabadi, 2001) and a micromechanical approach, in which granular materials are considered as a complete discrete structure and are generally modelled as an assembly of particles interacting at contacts (Cundall *et al.* 1982; Bathurst and Rothenburg, 1988; Rothenburg and Bathurst, 1989). However, a complete, well accepted theory for granular materials has not yet been proposed. Since granular materials consist of grains in contact and surrounding voids, the micromechanical behaviour is

therefore inherently discontinuous and heterogeneous. The macroscopic (overall or averaged) behaviour of granular materials is determined not only by the spatial arrangement of the discrete grains, but also by the type of interaction operating between them. In order to understand the mechanical behaviour of granular materials from a microscopic point of view, the spatial distribution and orientation of grains and their contact conditions should be specified. Many pioneering works are devoted to this topic, dealing mathematically with the geometrical aspects of grains and associated voids (Satake, 1978, 1993a; Bagi, 1996a, b). The macroscopic properties of these materials are obviously related to the basic structure and properties of their constituents and their interactions. It is therefore a goal in the study of the mechanics of granular materials to correlate their macro- (overall) behaviour in terms of micro- (local) quantities.

In this chapter, previous work on the mechanics of granular materials is reviewed. This commences with an introduction to the frictional behaviour of granular materials; followed by a review of statistical and numerical micromechanical approaches to the mechanics of granular materials. Finally some microscopic characteristics of granular materials are described.

2.2 Frictional behaviour of granular materials

Granular materials are an assembly of discrete particles, in which interparticle forces are transmitted through the system via the points of contact. If no friction is present at the contacts, the material cannot sustain any shear forces and behaves like a pseudo-fluid. Interparticle friction therefore plays a significant role in the macro-deformation and strength behaviour of granular materials. In the next section, the continuum approach for bulk solids with respect to the definition of state of stress will be presented.

2.2.1 The state of stress in a solid

Assume that the stresses acting on a continuum element ***abcd*** are as shown in Fig. 2.1a. The stresses on a plane inclined at an angle θ to the direction of the plane on which σ_y acts can be calculated by:

$$\sigma_\theta = \sigma_y \cos^2\theta + \sigma_x \sin^2\theta + \tau_{yx} \sin 2\theta \qquad (2.1)$$

$$\tau_\theta = \frac{1}{2}(\sigma_x - \sigma_y)\sin 2\theta + \tau_{yx}\cos 2\theta \qquad (2.2)$$

Here, it is appropriate to consider the conventions of stress representation usually adopted in soil mechanics. Referring to Fig. 2.1a, we have

a. Shear stress τ_{yx} acts tangentially along the face normal to the direction y and in the direction x.
b. Compressive normal stresses are positive and tensile normal stresses are negative.
c. Counter-clockwise shear stresses are positive and clockwise shear stresses are negative.

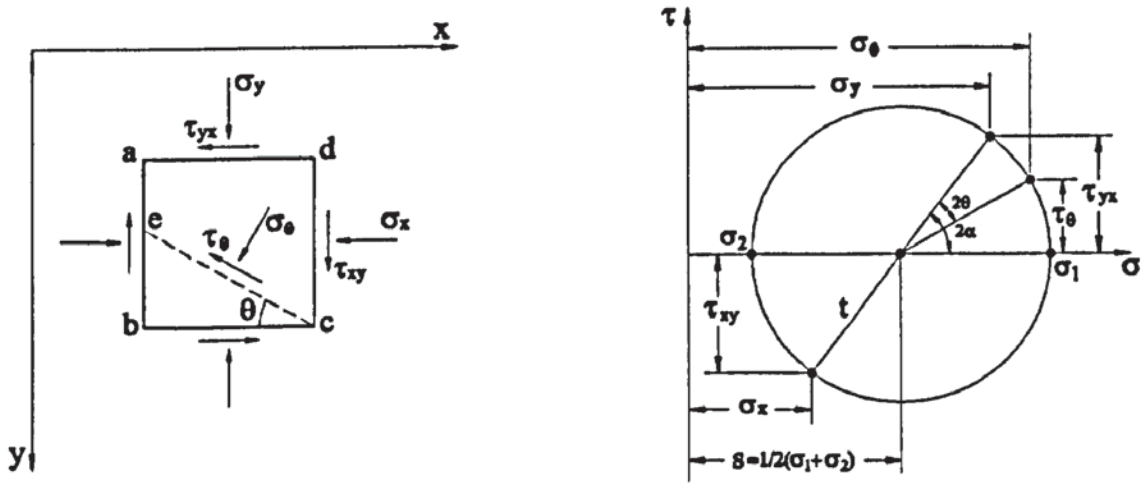

(a) (b)

Fig. 2.1 Stresses and Mohr circle: (a) stresses on element ***abcd*** ; (b) Mohr stress circle

If (2.1) and (2.2) are squared and added, we obtain:

$$(\sigma_\theta - s)^2 + \tau_\theta^2 = r^2 \qquad (2.3)$$

where

$$s = \frac{1}{2}(\sigma_x + \sigma_y)$$

$$r^2 = \left[\frac{1}{2}(\sigma_y - \sigma_x)\right]^2 + \tau_{yx}^2 = \left(\frac{\sigma_1 - \sigma_2}{2}\right)^2$$

It is clear that (2.3) is the equation of a circle with radius r, and with the centre at the point $(s, 0)$.

A graphical means of representing the foregoing stress relationships was developed by Mohr, after whom the graphical method is now named. The Mohr circle can represent completely the two-dimensional stresses acting within the element ***abcd*** and the major and minor principal stresses σ_1, σ_2 respectively (Fig. 2.1b). This is a very useful graphical description of stress for, in the case that the principal stresses are known, the stresses on any other plane can be calculated. The stresses σ_θ, τ_θ acting on a plane at an angle θ clockwise to the plane on which σ_y acts, as shown in Fig. 2.1a, can be found by travelling clockwise around the circle from stress point σ_y, τ_{yx} a distance subtending an angle 2θ at the centre of the circle. The major principal stress σ_1 acts on a plane inclined at an angle α to the plane on which σ_y acts, which can also be determined from the geometry of the Mohr circle of stress (Fig. 2.1b),

$$\tan 2\alpha = \frac{2\tau_{yx}}{\sigma_y - \sigma_x} \tag{2.4}$$

2.2.2 Shear strength of granular materials

The shear strength of granular materials can be adopted from soil mechanics, which has been developed for a long time. In soils, failure occurs as a result of mobilising the maximum shear stress that the soil can sustain, therefore an understanding of shear strength is fundamental to the behaviour of a soil mass. Shear strength is a material property, which enables soil to maintain equilibrium on an inclined surface, such as a natural hillside, the sloping sides of an embankment or earth dam. This strength materially influences the bearing capacity of a foundation soil and the stability of a retaining wall. The shear strength of soil will determine the maximum or ultimate (failure) load that can be applied on a foundation resting on soil or the probability of the occurrence of failure of a soil mass forming a slope. In the field of geotechnical engineering, all stability problems require a knowledge of the shear strength parameters of the soil.

Typical stress-strain curves are shown in Fig 2.2. There are several points marked on the curve in Fig. 2.2 that need to be defined, which are widely used in soil and geotechnical engineering:

a) Peak shear strength τ_p

This is the maximum shear stress, which the soil can sustain. It may be dangerous to rely on this value for some brittle soils due to the rapid loss of strength that occurs when the soil is strained beyond this point.

b) Ultimate strength τ_u

For loose sands and soft clays, work hardening may continue to increase the shear stress even at very large strains so a maximum stress is not achieved. A maximum strain limit must then be imposed at about 10 to 20% strain, see point *U* in Fig. 2.2.

c) Critical state strength τ_{cv}

After a considerable amount of shear strain a soil will reach a constant volume state and it will continue to deform without further change in volume or stress ratio. It is also referred to as the constant volume strength.

d) Residual strength τ_r

After a considerable amount of strain on a single slip zone or surface (point *R* in Fig. 2.2) the material on each side of this surface will rearrange to produce a more parallel orientation and this will produce the lowest possible or residual strength.

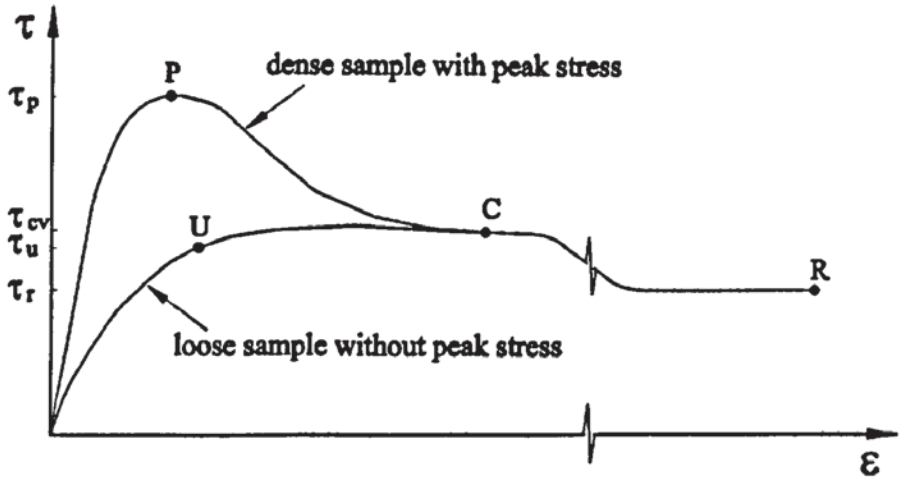

Fig. 2.2 Two typical stress-strain curves

2.2.3 Failure criterion of granular materials

The failure surface, which would develop during the shear test, will be at an angle to the principal stress planes. The failure plane is the particular plane where some critical

combination of normal and shear stress is first reached. The Mohr-Coulomb theory states that this critical combination is given by the following expression,

$$\tau = c + \sigma \tan \varphi_c \tag{2.5}$$

The parameter c is called cohesion and the parameter φ_c is often called the internal friction angle. In this thesis φ_c is particularly referred to as Coulomb friction angle since it is based on Coulomb's friction law. For cohesionless soils, c is equal to zero, and (2.5) becomes,

$$\tau = \sigma \tan \varphi_c \tag{2.6}$$

A sample, whose strength relies solely on interparticle friction, would be expected to obey the failure criterion given in the above equation, which is referred to as a Mohr-Coulomb failure criterion. In fact, the Coulomb friction angle φ_c is not a physical constant, but is strongly dependent on the void ratio, fabric, stress states and other details. This suggests that a granular assembly should be more than simply a frictional material.

Equation (2.6) can be rewritten in terms of the major and minor principal stresses, σ_1 and σ_2, by assuming that the general shear plane accords with the maximum obliquity plane on which the stress ratio, τ/σ, is a maximum. Thus, the angle of shearing resistance on the plane of maximum stress obliquity is given by:

$$\sin \varphi_m = \frac{t}{s} \tag{2.7}$$

where t is the radius of the Mohr circle (Fig. 2.1b) and equals half of the deviator stress,

$$t = \frac{\sigma_1 - \sigma_2}{2} \tag{2.8}$$

and s is the mean stress and is also the distance between the origin and the centre of Mohr circle (Fig. 2.1b).

$$s = \frac{\sigma_1 + \sigma_2}{2} \tag{2.9}$$

Thus, (2.7) can be rewritten as

$$\sin\varphi_m = \frac{\sigma_1 - \sigma_2}{\sigma_1 + \sigma_2} \tag{2.10}$$

In this thesis, φ_m is also referred to Mohr friction angle in comparison with the Coulomb friction angle φ_c.

2.2.4 Dilatancy of granular materials

A unique property of granular materials is dilatancy. The concept of dilatancy is generally taken to be the increase of voidage that occurs in a tightly packed granular assembly when it is subjected to a shear deformation. The angle of dilation ψ is defined as the ratio of volumetric strain increment to deviator strain increment:

$$\sin\psi = -\frac{d\varepsilon_v}{d\gamma} \tag{2.11}$$

where, in two dimensions,

$d\varepsilon_v = d\varepsilon_1 + d\varepsilon_2$

$d\gamma = d\varepsilon_1 - d\varepsilon_2$

and $d\varepsilon_1$ and $d\varepsilon_2$ are the major and minor principal strain increments, respectively.

It is generally considered that a dense granular soil dilates during shear. On the other hand, a loose soil sample contracts. It is also well known that a dense soil exhibits a higher shear resistance than a loose one. Casagrande (1940) noted the importance of the associated dilatancy in dealing, in general, with the friction angle of granular soils. This parameter is often considered as a function of the stress ratio (Taylor 1948; Rowe 1962; Wood 1990). The experimental and numerical studies strongly suggest that dilatancy is a significant factor in the deformation of shear bands (Roscoe, 1970; Arthur *et al.*, 1977; Vardoulakis, 1980).

2.3 Fundamental mechanics of granular materials

Granular materials can be viewed at three levels: assembly level, microelement level and interparticle level. A granular assembly contains a sufficient number of particles to

provide representative behaviour of the bulk material. These particles can form a small particle group, termed a microelement. A microelement is an elementary unit at the microscopic level. Each particle in the assembly is in contact with several neighbouring particles. A contact between a pair of particles is regarded as the basic level of granular materials. A schematic representation of these three levels of granular material is shown in Fig. 2.3.

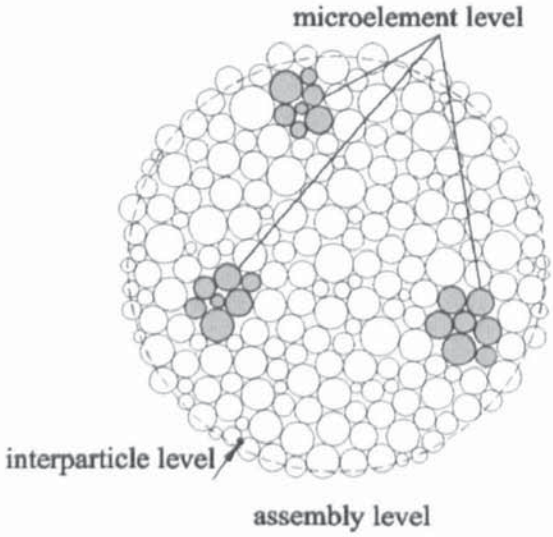

Fig. 2.3 A particle assembly system

In micromechanics, the constitutive behaviour is defined according to these three levels.

1. From a microscopic point of view, interparticle forces are very complicated and depend on material properties. They can also include van der Waals forces, liquid bridge forces or electrostatic forces. When two particles are in contact, the contact force is related to the relative movement between the two particles. At this interparticle level, the continuum concept has not yet been introduced. Details about how to calculate various interparticle forces are well documented by Johnson (1985).

2. At the microelement level, the constitutive law gives the stress and strain relations for the microelement. The continuum concepts of stress and strain are now introduced. People seek to derive the stress-strain relationship for a microelement based on the contact behaviour. To accomplish this objective, it is necessary to establish: (a) the relationship between stress and contact forces; and (b) the relationship between particle movement and strain.

3. At the assembly level, the constitutive law relates the overall stress and overall strain. The behaviour of the representative unit is obtained by averaging the

behaviour of microelements utilizing the principle of volume averaging. Therefore, the macro-behaviour of an assembly can eventually be derived from the micro-behaviour of a contact.

In the mechanics of granular materials, some continuum mechanical concepts such as stress and strain tensor are necessary to formulate some problems in a consistent manner, since the degrees of freedom of contact forces and movements at the grain level become tremendously large. In principle, if the microscopic mechanical properties of the single contacts making up a particle assembly are known, it should be possible to calculate the macroscopic properties of the assembly. The following is a brief review of the approaches adopted to convert the microscopic information to macroscopic properties of the assembly.

2.3.1 Micromechanical stress and strain tensors (Kruyt and Rothenburg, 1996)

Using constitutive relations that are developed from the continuum-mechanical viewpoint does not recognize the discrete nature of granular materials. As an alternative, the interpretation of the continuum-mechanical stress tensor for granular assemblies is not new. Hill (1967) showed that, for heterogeneous materials, the overall stress and strain could be expressed as volume averages of their corresponding quantities at the local level. Thus, the overall stress and strain are regarded as volume averages of the local stresses and local strains at the microelement level. The strain and stress, for a microelement, are defined in connection with the relative movement of the particles and the resulting contact forces, respectively. The stress-strain relationship is then derived based on contact behaviour. Several definitions of the micromechanical stress tensor have been suggested and these different approaches lead to the same results. The first definition suggested by Drescher and de Josselin de Jong (1972) is rather close to the continuum-mechanical approach. A micro-structural definition based on the principle of virtual work was given by Christoffersen *et al.* (1981), in which the volume average stress of an assembly of grains with arbitrary shape is expressed in terms of the individual contact forces inside the assembly. A similar definition was suggested by Rothenburg and Selvadurai (1981), based on different theoretical considerations. Kanatani (1981) also proposed a definition for the stress tensor with the help of the virtual work principle. His results were in agreement with previous ones. Since the virtual work principle expresses the equilibrium condition of the system, it is no wonder that these three definitions are equivalent to each other. During a

small strain increment, the kinematics of two particles in contact includes the translation and rotation movement. The details of how to calculate the contact force and deformation of the contact between them are described in Appendix A.

2.3.1.1 Micromechanical stress tensor

The derivation of the expression for the average stress tensor proceeds in two steps. In the first step the average stress tensor is related to quantities involving forces exerted on the particles by the boundary that encloses the assembly of particles. The second step equates these quantities involving external forces to quantities involving internal forces. The result is the micromechanical expression for the average stress tensor.

1) Average stress tensor in terms involving external forces

The expression for the average stress tensor is derived under conditions of stress equilibrium and in the absence of body forces. The (continuum) equilibrium conditions are

$$\frac{\partial \sigma_{ij}}{\partial x_j} = 0 \tag{2.12}$$

The two-dimensional average stress tensor in area S with boundary B (see Fig. 2.4) is defined by

$$\bar{\sigma}_{ij} = \frac{1}{S} \int_S \sigma_{ij} dS \tag{2.13}$$

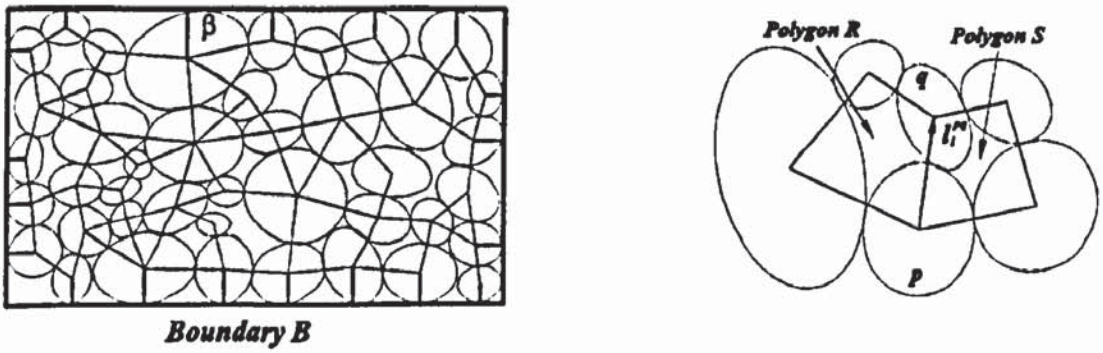

Fig. 2.4 Polygons and branch vectors

From (2.12) and Gauss' theorem it follows

$$\bar{\sigma}_{ij} = \frac{1}{S}\int_B n_k \sigma_{ik} x_j dS \tag{2.14}$$

where n_i is the vector normal to the boundary; the vector tangential to the boundary is denoted by t_i. Considering the loads to be point loads on the boundary $\boldsymbol{B}$, it follows:

$$\bar{\sigma}_{ij} = \frac{1}{S}\sum_{\beta \in B} f_i^{\beta} x_j^{\beta} \tag{2.15}$$

where f_i^{β} is the boundary force exerted on boundary particle β. This is the expression for the average stress tensor in terms involving external forces.

2) Average stress tensor in terms involving internal forces

The equilibrium conditions for particle p in the absence of a body force read

$$\sum_q f_i^{pq} = 0 \tag{2.16}$$

where the summation is over the particle q that is in contact with particle p and f_i^{pq} is the force exerted by particle q on particle p.

Multiplication of (2.16) by the position vector x_j^p of the centre of mass of particle p and addition of all equations gives

$$\sum_p \sum_q f_i^{pq} x_j^p = 0 \tag{2.17}$$

This double sum contains one term for each boundary contact β with particle p $f_i^{\beta} x_j^p$, which can be rewritten as $f_i^{\beta}\left(x_j^{\beta} - l_j^{p\beta}\right)$, where $l_j^{p\beta}$ is the so-called contact vector connecting the centre of mass of particle p to the boundary contact point β.

Each internal contact between particles p and q contributes a term $(f_i^{pq} x_j^p + f_i^{qp} x_j^q)$. Since $f_i^{pq} = -f_i^{qp}$, terms corresponding to internal contacts can be written as $-f_i^{pq}(x_j^q - x_j^p)$ or $-f_i^{pq} l_j^{pq}$, where l_j^{pq} is the so-called branch vector connecting the centres of the particles p and q. Combinations $f_i^{pq} l_j^{pq}$ can be rewritten as $f_i^c l_j^c$, since $f_i^{pq} = -f_i^{qp}$ and $l_i^{pq} = -l_i^{qp}$. As a result it follows that

$$\sum_{\beta \in B} f_i^{\beta} x_j^{\beta} = \sum_{c \in S} f_i^c l_j^c \tag{2.18}$$

Hence it follows from (2.15),

$$\bar{\sigma}_{ij} = \frac{1}{S} \sum_{c \in S} f_i^c l_j^c \tag{2.19}$$

This is the expression for the average stress tensor in terms involving internal forces, i.e., the micromechanical expression for the average stress tensor.

2.3.1.2 Micromechanical strain tensor

Analogous to the expression for the average stress tensor, an expression for the average displacement gradient can be derived. The strain tensor is obtained by taking the symmetric part of the displacement gradient tensor.

The derivation of the expression for the average displacement gradient tensor also proceeds in two steps. In the first step the average displacement gradient tensor is related to quantities involving relative displacements of the boundary particles. The second step equates these quantities to internal relative displacements. The result is the micromechanical expression for the average displacement gradient tensor, and hence for the average strain tensor.

1) Average displacement gradient tensor in terms involving external relative displacements

The average displacement gradient tensor is defined by

$$\bar{\theta}_{ij} = \frac{1}{S} \int_S \frac{\partial u_i}{\partial x_j} \tag{2.20}$$

where u_i is the displacement vector. Using Gauss' theorem it follows that

$$\bar{\theta}_{ij} = \frac{1}{S} \int_B u_i u_j ds \tag{2.21}$$

A relation based on (2.21) has been proposed by Strack and Cundall (1978). Constitutive relations at the contact will involve relative displacements between particles. Therefore it

is desirable to transform (2.21) to a form containing derivatives of the displacements. This is done using the following identity:

$$\int_B u_i t_k ds = \int_B u_i \frac{dx_k}{ds} ds = -\int_B \frac{du_i}{ds} x_k ds \tag{2.22}$$

Combining (2.21) and (2.22) gives

$$\bar{\theta}_{ij} = -\frac{1}{S} e_{jk} \int_B \frac{du_i}{dx} x_k ds \tag{2.23}$$

where e_{ij} is the two-dimensional permutation tensor. The discrete formulation of (2.23) in terms of relative displacements at the boundary is

$$\bar{\theta}_{ij} = -\frac{1}{S} e_{jk} \sum_{\alpha \in B} \Delta l_i^{\alpha} x_k^{\alpha} \tag{2.24}$$

This expression for the average displacement gradient tensor is analogous to Eqn. (2.15) for the average stress tensor. It gives the average displacement gradient in terms involving external relative displacements.

2) Average displacement gradient tensor in terms involving internal relative displacements

The derivation of the stress tensor employed the equilibrium conditions for the particles. The equivalents for the displacement gradient tensor are the compatibility conditions for polygons. These polygons arise as a way of dividing the plane network of particle centres of mass and contacts into polygons, as depicted in Fig. 2.4. Various properties associated with such a subdivision of the assembly into polygons were studied by Satake (1992).

Since the polygons form closed loops, the compatibility condition for polygon r is

$$\sum_s \Delta l_i^{rs} = 0 \tag{2.25}$$

where the summation is over the sides of polygon r and Δl_i^{rs} is the relative displacement between particles comprising side s of polygon r. Multiplication of (2.25) by the position vector V_i^r of the centre of gravity of polygon r and addition of all equations gives

$$\sum_r \sum_s \Delta l_i^{rs} V_j^r = 0 \tag{2.26}$$

This double sum contains one term for each external side α of polygon r, $\Delta l_i^{r\alpha} V_j^r$, which can be rewritten as $\Delta l_i^{\alpha}(x_j^{\alpha} - g_j^{r\alpha})$, where $g_j^{r\alpha}$ is the vector connecting the centre of gravity of polygon r to boundary point α.

Each internal side contributes a term $(\Delta l_i^{rs} V_j^r + \Delta l_i^{sr} V_j^s)$. Since $\Delta l_i^{rs} = -\Delta l_i^{sr}$, the term corresponding to internal contacts can be rewritten as $-\Delta l_i^{rs}(V_j^s - V_j^r)$ or $-\Delta l_i^{rs} g_j^{rs}$, where g_j^{rs} is the vector connecting the centres of gravity of polygons r and s. Combinations $\Delta l_i^{rs} g_j^{rs}$ can be written as $\Delta l_i^c g_j^c$, since $\Delta l_i^{rs} = -\Delta l_i^{sr}$, and $g_j^{rs} = -g_j^{sr}$. The resulting expression for (2.26) becomes

$$\sum_{\alpha \in B} \Delta l_i^{\alpha} x_j^{\alpha} = \sum_{c \in S} \Delta l_i^c g_j^c \tag{2.27}$$

Hence it follows from (2.24)

$$\bar{\theta}_{ij} = \frac{1}{S} \sum_{c \in S} \Delta l_i^c h_j^c \tag{2.28}$$

where the so-called polygon vector h_j^c is defined by

$$h_j^c = -e_{jk} g_k^c \tag{2.29}$$

Equation (2.28) is the expression for the average displacement gradient tensor in terms involving the internal relative displacement gradient tensor is analogous to the micromechanical expression for the average stress tensor (2.19). Equation (2.28) was first reported by Rothenburg (1980).

The expression for the average strain tensor then becomes

$$\bar{\varepsilon}_{ij} = \frac{1}{S} \sum_{c \in S} \frac{1}{2} \left(\Delta l_i^c h_j^c + \Delta l_j^c h_i^c \right) \tag{2.30}$$

2.3.2 Stress partitions (Thornton and Barnes, 1986)

The average stress tensor for the volume V^p occupied by a single particle may be written as

$$\sigma_{ij}^{p} = \frac{1}{V^{p}} \int \sigma_{ij} dV^{p} = \frac{1}{V^{p}} \int t_j x_i dS \tag{2.31}$$

If we consider the tractions t_j to consist solely of discrete forces F_j acting at point contacts defined by the coordinates x_i then the integral in (2.31) may be replaced by a summation over the n contacts for the particle p. Thus

$$\sigma_{ij}^{p} = \frac{1}{V^{p}} \sum_{1}^{n} F_j x_i \tag{2.32}$$

since the tractions acting on the surface of a particle are discrete forces acting at the points of contact with adjacent spheres.

For a large assembly of particles occupying a volume V the average stress tensor for the assembly may be obtained from

$$\bar{\sigma}_{ij} = \frac{1}{V} \int \sigma_{ij} dV = \frac{1}{V} \sum_{1}^{m} V^{p} \sigma_{ij}^{p} \tag{2.33}$$

where the assembly consists of m number of particles.

Therefore, combining (2.32) and (2.33) the macroscopic stress tensor can be defined as:

$$\bar{\sigma}_{ij} = \frac{1}{V} \sum_{1}^{m} \sum_{1}^{n} F_j x_i = \frac{2}{V} \sum_{1}^{C} F_j x_i \tag{2.34}$$

where there are C contacts.

The observed stress tensor can be decomposed into several 'partitions', each of which is associated with a different aspect of behaviour. The total force F_j at a contact can be divided into its normal force component (N_j) and tangential force component (T_j). The basic definition of the stress tensor can be rewritten as

$$\bar{\sigma}_{ij} = \frac{2}{V} \sum_{1}^{C} N_j x_i + \frac{2}{V} \sum_{1}^{C} T_j x_i \tag{2.35}$$

Restricting attention to disc assemblies

$$N_j = N n_j, \; T_j = T t_j, \; x_i = R n_i \tag{2.36}$$

where n_i define the contact normal, t_i is the unit vector orthogonal to n_i and R is the

particle radius. Substituting (2.36) into (2.35) the ensemble average stress tensor is calculated from

$$\bar{\sigma}_{ij} = \frac{2}{V}\sum_{l}^{c} RNn_i n_j + \frac{2}{V}\sum_{l}^{c} RTn_i t_j \text{ , where } n_i t_i = 0 \tag{2.37}$$

Rn_i defines the radius vector to the contact, Nn_i and Tt_i are the normal and tangential contact forces. Equation (2.35) may be rewritten, using $\langle\cdot\rangle$ to represent statistical average, as

$$\bar{\sigma}_{ij} = \sigma_{kk}\left[\frac{\langle RNn_i n_j\rangle}{\langle RN\rangle} + \frac{\langle RTn_i t_j\rangle}{\langle RN\rangle}\right] = \sigma_{ij}^{N} + \sigma_{ij}^{T} \tag{2.38}$$

where σ_{ij}^{N} and σ_{ij}^{T} are the normal and tangential contact force contributions to the stress tensor and

$$\sigma_{kk} = \frac{2C}{V}\langle RN\rangle \tag{2.39}$$

The tangential forces contribute only to the deviatoric components of the stress tensor and the isotropic part derives solely from normal forces at contacts. This is because $n_i t_i = 0$ in (2.38), i.e. the vectors R and T are orthogonal.

2.4 Microscopic characteristics of granular materials

The overall macroscopic behaviour of granular materials requires a micromechanical formulation of stress and deformation measurements. It should be noted that the stress-force relationship explained above links the discrete mechanics of granular materials and the continuum mechanics. The correlation seems sufficient, but generalized continuum mechanics may not be sufficient to adequately express the overall mechanical properties of granular materials. Therefore, more quantities, such as a fabric tensor and some other quantities, may be needed to be taken into consideration in the formulation of the mechanics of granular materials. Both the number of contacts and their orientations are essential for defining the physical model and should be monitored to measure their evolution during deformation. This can be done by determining some characteristic parameters described in the following sections.

2.4.1 Coordination number

An important statistical measurement of the physical model is the average coordination number. This number is an alternative parameter to the contact density. The assembly average coordination number is the average number of contacts per particle. The average coordination number is defined as:

$$Z_a = \frac{2C}{N} \tag{2.40}$$

where C is the number of contacts and N is the number of particles. However, numerical simulations have revealed that, at any time during shear, there are some particles with no contacts and some particles with only one contact. None of these particles contributes to the stable state of stress. Hence, a mechanical coordination number is defined:

$$Z_m = \frac{2C - N_1}{(N - N_1 - N_0)}, \quad Z_m \geq 2 \tag{2.41}$$

where N_1 and N_0 are the number of particles with one or no contacts respectively (see Fig. 2.5).

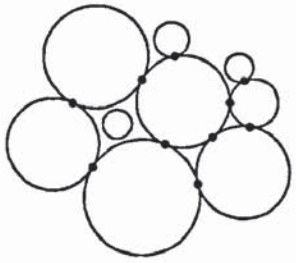

$C = 10$
$N = 9$
$N_0 = 1$
$N_1 = 2$
$Z_a = 2.22$
$Z_m = 3.0$

Fig. 2.5 Coordination number

The coordination number is widely used in the evaluation of structural properties related to the connectivity between particles, such as the force transmission and tensile strength (Cundall and Strack, 1979a). Results from numerous investigations showed that the assembly average coordination number is strongly correlated to common measurements of particle packing such as the assembly density or void ratio (Oda, 1977).

2.4.2 Isotropy

A particle assembly behaves isotropically with respect to a certain property if the values of that property are identical in all directions. When a property has different values in

different directions, the material is anisotropic with respect to that property. For instance, the bulk material can behave isotropically with respect to the strain tensor. In the case that a bulk material is isotropically loaded, it will isotropically deform if the stresses are increased isotropically. Feda (1982) made a distinction between inherent and induced anisotropy. A bulk material can be inherently anisotropic because of the fact that the particles are elliptical in shape. Anisotropy can be induced by different proportions of deformation being applied to an isotropic sample. The sample then has deformation induced anisotropy as defined by Feda (1982). Various types of anisotropy, whether inherent or induced, include deformation, strength, structural and fabric anisotropy.

2.4.3 Fabric tensor

To quantify the fabric of a granular mass, various measures have been used. One of such measures is the void ratio, which is closely related to the coordination number. However, experiments show that the void ratio is not sufficient to completely describe the microstructure of a granular assembly, since two samples of the same granular material of the same void ratio may have very different mechanical responses (Oda 1972, Oda *et al.* 1980). Thus, other measures of fabric have been introduced and used in the constitutive characterization of granular materials. A fabric tensor was introduced by Satake (1978) as a measurement of changes in the fabric of granular materials. This parameter emerges naturally as a measure of stress in an assembly of particles characterized by an induced anisotropy in contact normal orientations only.

The structural anisotropy is defined by the distribution of contact normal vectors. If the distribution is random and can be approximated by a uniform distribution, the structure is in effect isotropic. Anisotropy is indicated by a non-uniform distribution. Satake (1982) suggested that, for disc or sphere assemblies, the structural anisotropy defined by the distribution of the contact normals n_i could be characterised by a fabric tensor ϕ_{ij} where

$$\phi_{ij} = \langle n_i n_j \rangle = \frac{1}{2C} \sum_{l}^{2C} n_i n_j \tag{2.42}$$

For a complete characterisation of the microstructure, a second order tensor, also termed a fabric tensor, was proposed by Oda *et al.* (1982),

$$F_{ij} = F_{kk}\phi_{ij} \tag{2.43}$$

where

$$F_{kk} = \frac{2C\overline{R}}{V}$$

and $\overline{R}$ is the mean particle radius. This definition of fabric incorporates both the packing density and the structural anisotropy and appears to be a satisfactory method to characterize the microstructure of granular materials.

2.4.4 Contact normal orientations

The load-induced anisotropy in contact normal orientations is not confined to the maximum and minimum load-directions but affects all directions. A convenient means of illustrating a possible bias in the contact normal orientation distribution is by plotting a histogram of the proportion of contact normals falling within a series of adjacent orientation classes that partition the full orientation space. The unit circle is partitioned into a finite number of group orientations to accommodate the finite number of contacts in the assembly. A polar histogram is used to show the distributions of contact orientations. In order to construct this diagram each contact is interrogated to find out which of the eighteen 10° bands between 0° and 180° (contact normal direction) its inclination belongs to. If a contact falls into band *i*, the total contact number for this band is increased by one. After all contacts have been scanned, the total contact number of each band is divided by *C*, the total number of contacts of whole assembly, to obtain the radial coordinate of each band as follows:

$$r_i = \frac{nc_i}{C} \tag{2.48}$$

where nc_i is the total number of contacts mapping into band *i*. The part of the histogram between 180° and 360° is skew-symmetrical to that between 0° and 180°.

Using the same method, the distribution of contact normals weighted to the magnitude of the contact normal force can be obtained by normalizing the total normal force accumulated for each band by the total normal force of the whole assembly. Hence, the radial coordinates p_i for bands between 0° and 180° is given as:

$$p_i = \frac{\sum_{j}^{nc_i} F_n^i}{\sum_{j} F_n} \tag{2.49}$$

where F_n^i is the contact normal force of a contact mapping into band i. This plot can also be interpreted as the distribution of contact normal forces.

Figure 2.6 illustrates three typical shapes of the contact normal orientation distribution. If the distribution is isotropic its shape is close to a circle. With increasing anisotropy, the shape mutates to a peanut shape. Isotropic distributions are usually encountered in assemblies under isotropic load conditions. Anisotropic distributions characterize either a state of initially anisotropic assemblies, for instance due to some depositional history (inherent anisotropy), or initially isotropic materials that become anisotropic in order to accommodate an applied anisotropic load (induced anisotropy).

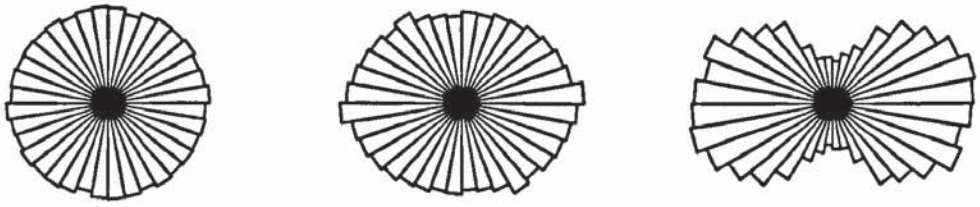

(a) Isotropic distribution (b) Weak anisotropy (c) Strong anisotropy

Fig. 2.6 Typical shapes of the contact normal orientation distribution

2.5 Summary

In this chapter, some basic concepts for cohesionless granular materials are described. The general approaches used to describe the mechanical behaviour of granular materials are then reviewed. Finally, several other parameters related to the microscopic characteristics of granular materials are introduced. In general, there are two main methods to predict the mechanical behaviour of granular material: the continuum approach and the microscopic approach. Many experiments and numerical analyses have been carried out to verify these approaches. However, there are still many aspects of the behaviour of such materials that have not been fully understood, such as strain localization. Although real experiments can reveal the phenomenon to a certain extent, the accuracy and reproducibility of the

experiments rely heavily on the equipment design and other conditions. Fortunately, with the development of numerical methods, such as DEM, and the high speed computer, it is now possible to investigate the mechanical behaviour of granular materials inside the specimen in great detail so as to better understand it. It has been demonstrated that the simulations using DEM can provide detailed new information about the mechanical behaviour of granular materials (Cundall and Strack, 1979a; Thornton and Barnes, 1986; Thornton and Sun, 1993; Thornton, 2000a). Therefore, the macro- and micro- mechanical behaviour of granular material will be investigated by using DEM in this study.

CHAPTER 3: BIAXIAL COMPRESSION TESTS

3.1 Introduction

Traditionally, theoretical models of material behaviour are validated by physical experiments. However, for granular materials, laboratory studies are inherently difficult due to the inability to prepare exact replicas of the physical system and the fact that attempts to measure what goes on inside the system invariably intrude upon the material response. Although some non-intrusive measuring techniques have been developed, quantitative information about the forces acting at the contacts between constituent particles cannot be determined and, consequently, interpretation of the state of stress relies primarily on boundary measurements. It is not clear if information obtained at the boundaries of a specimen can reliably represent the ensemble state of stress and strain inside the specimen; which is normally supposed to represent the constitutive behaviour of the material at a point in a continuum and, thereby, provide the data required for continuum modelling.

This study of quasi-static behaviour of granular materials starts with an investigation of the biaxial compression test by conducting DEM simulations using the Aston TRUBAL code. The objective is to examine the shear behaviour of particulate systems and to show evidence that the numerical simulations can provide reliable data that are normally obtained from physical experiments. The simulation results reported in this chapter were first reported in Zhang and Thornton (2001).

In order to examine the effect of boundary conditions on the mechanical behaviour, two sets of tests on a polydisperse system of spheres have been conducted: one is biaxial compression using periodic boundaries (named **BCP**); the other test is biaxial compression with kinematically controlled wall boundaries (named **BCW**). For each set of tests, simulations under both constant volume and constant mean stress conditions have been carried out. For the **BCP** tests, the stress state is determined as a volume average of the distribution of interparticle contact forces over all the contacts inside the assembly. For the **BCW** tests, two approaches are employed to calculate the stress state: one is the same as

that used in **BCP** tests; the other is from the wall forces at the boundaries, which is similar to that used in laboratory experiments.

In this chapter, numerical simulation techniques and the methods used to prepare the specimen for different boundaries are described. The observed macroscopic and microscopic behaviour are provided. Finally, results obtained using different values of wall friction are presented.

3.2 Brief literature review

The principle of a true biaxial test was first proposed by Hambly (1969). In the test, the sample is constrained in the lateral and axial directions by four interlocking platens and remains as a rectangular prism during compression so that the strain throughout the sample is homogeneous. Since there are no shear stresses on the boundary surfaces the stresses on the boundaries are principal stresses. Hence, both principal stresses can be measured directly in the biaxial test, and the Mohr stress circles can be determined for each state of stress.

Biaxial compression tests have been performed on assemblies of oval cross-sectional rods, to evaluate the effects of interparticle friction, particle shape, and initial fabric on the overall strength of granular materials (Oda *et al*, 1983; Konishi *et al*, 1983). The variation in the spatial arrangement of the particles (fabric) and particle rolling and sliding are monitored by taking photoelastic pictures at various stages during the course of deformation. It was found that particle rolling appears to be a major microscopic deformation mechanism, especially when interparticle friction is large, which is in contradiction to the common assumption that particle sliding is the major microscopic deformation mode. Based on the experimental observations, the major principal axis of fabric tends to rotate toward the major principal axis of stress during the course of deformation. Biaxial experiments were performed with rod assemblies also by Misra and Jiang (1997), who studied the micro-mechanical deformation behaviour of granular materials. These experiments were focused upon the micromechanical behaviour under mixed boundary conditions, with stress-controlled lateral boundaries and displacement-controlled axial boundaries. Particle motions, such as displacements and rotations, were measured during the test. Deformation patterns in a number of rod assemblies with

random packing structures were also analysed.

A true biaxial shear tester was developed by Harder and Schwedes (1985), in which stresses or strains in the x- and y- directions can be applied independently of each other to investigate the influence of the stress history on the yield limit. Results from shear tests with limestone showed a significant influence of the different ways of consolidation on the yield limit, *i.e.* the flow properties of a bulk solid would depend on the stress history. The flow function, however, which is essential for silo design, proved to be independent of stress history. A flexible wall biaxial tester was designed to produce a determined state of stress or strain by Kraan (1996) and used to measure powder flow properties. The flexible membranes allowed the tester to be operated in both a stress and a strain controlled mode. It was shown that the flow function measured with this tester was higher than the flow function as measured with the Jenike shear tester.

Han and Vardoulakis (1991) presented some experimental results focussing on the pre-failure and post-failure behaviour of water-saturated fine-grained sand in the biaxial compression test. The experiments were performed in a plane strain apparatus, which allows a detailed study of bifurcation and post-bifurcation phenomena to be carried out. The failure modes of each test were illustrated with x-ray radiographs. Failure in the form of shear band formation was found to take place only when the specimen was dense enough to behave in a dilatant fashion.

In contrast to conventional experimental approaches, numerical investigations allow the observation of the changes of structure in an idealized material for any loading and unloading paths. Numerical simulation also provides detailed information on micromechanical statistics, particle motions and interparticle forces. Cundall and Strack (1979a) proposed a computational algorithm for assemblies of circular particles, originally named as the distinct element method (DEM). In this model, the interaction of the particles is considered as a transient problem with a state of equilibrium developed whenever internal forces balance and later extended to 3D by Cundall (1988).

The results of numerical simulations of planar assemblies of elliptical particles subjected to biaxial compression were presented by Rothenburg and Bathurst (1992). The influence of particle eccentricity on peak friction angle and peak dilation rate was explored.

Qualitative features of these systems were similar to real sand behaviour and the mechanical behaviour of elliptical assemblies is not significantly different from that of assemblies of discs. The results were also used to verify the accuracy of the proposed stress-force-fabric relationship based on the assemblies of discs and of spherical particles (Rothenburg and Bathurst 1989). The influence of particle shape on the strength and deformation behaviours of two-dimensional assemblies of ellipse-shaped particles were investigated using DEM by Ting *et al.* (1995). Assemblies with varying individual particle aspect ratios were formed with a preferred bedding plane, then isotropically compressed to different confining stresses before subjected to biaxial compression. For systems composed of flatter particles, particle rotations were greatly inhibited, while observed strength increased dramatically. This strongly suggested that using disc and sphere-based DEM codes to analyse micromechanical aspects of soil behaviour would result in overestimating individual particle rotations.

Williams and Rege (1997a) examined the formation of microstructures within a granular material undergoing biaxial compression. They simulated ensembles of particles with different geometrical shapes and size. It was shown that the motion of the particles deviated significantly from that predicted by continuum theory. Lanier and Jean (2000) presented numerical simulations of quasi-static biaxial compression of a 2D disc assembly, based on "contact dynamics". The comparison with a real experiment showed that many features such as maximum shear strength, plastic flow with dilatancy, evolution of contact orientations can all be well described by numerical simulations.

All the above numerical studies were performed using either wall boundaries or periodic boundaries. As far as it is known, no comparison has been made for the same test carried out with these two different boundary conditions. This will be addressed in the following sections.

3.3 Sample preparation

3.3.1 Periodic boundaries

Initially, a system with 5000 particles is generated randomly in a periodic cell as a 'granular gas' with all particle centres located in the same plane. During the simulation the

motion of all the particles is restricted to this plane. Thus the test is essentially a two dimensional problem. The packing density of the sample is decided by the solid fraction (sf) or porosity (n),

$$sf = \frac{\sum_{i=1}^{N} V_i}{V} \tag{3.1}$$

$$n = 1 - sf = \frac{V - \sum_{i=1}^{N} V_i}{V} \tag{3.2}$$

where V_i is the volume of particle i ($i = 1, N$), N and V are the total particle number and total volume of the sample, respectively. When calculating the volume, the dimension in the third direction is taken to be the average particle diameter.

When initially generated the system has a solid fraction ca. 0.375 and there are no interparticle contacts. In order to obtain compact, random and isotropic samples, the initial system is isotropically compressed to obtain ten different values of solid fraction in the range between 0.563 and 0.648. To achieve this, a numerical servo control is used so that the applied strain rate is continuously adjusted according to the difference between the desired solid fraction (sf_d) and the current solid fraction (sf_c). At each time step, the strain rates are set to,

$$\dot{\varepsilon}_{11} = \dot{\varepsilon}_{22} = 0.5g(sf_d - sf_c), \quad \dot{\varepsilon}_{12} = \dot{\varepsilon}_{21} = 0 \tag{3.3}$$

The parameter g is the gain of the servo mechanism. A gain parameter g of 0.03 was used. This value was set after a detailed trial and error process. After isotropic compression, all the samples are initially square in shape and surrounded by two pairs of periodic boundaries. By using this technique, particles near the boundaries of the volume interact with images of particles found near the opposite boundary. Particles that exit through one boundary re-enter the domain through the opposite one. Therefore, the number of particles remains constant and boundary effects are eliminated. In this way, "perfect" experiments are performed free from boundary effects.

3.3.2 Wall boundaries

The actual particle packing arrangement is expected to have a significant influence on the shear behaviour of granular material and so the sample preparation process should be

modelled carefully. There are several procedures for numerically generating an initial state of a granular assembly when using wall boundaries in the simulation. One method is to drop the particles, like raindrops, into a container. The particles can be dropped either one by one or all together. The heterogeneity and statistics of the resulting packing depend on the technique chosen.

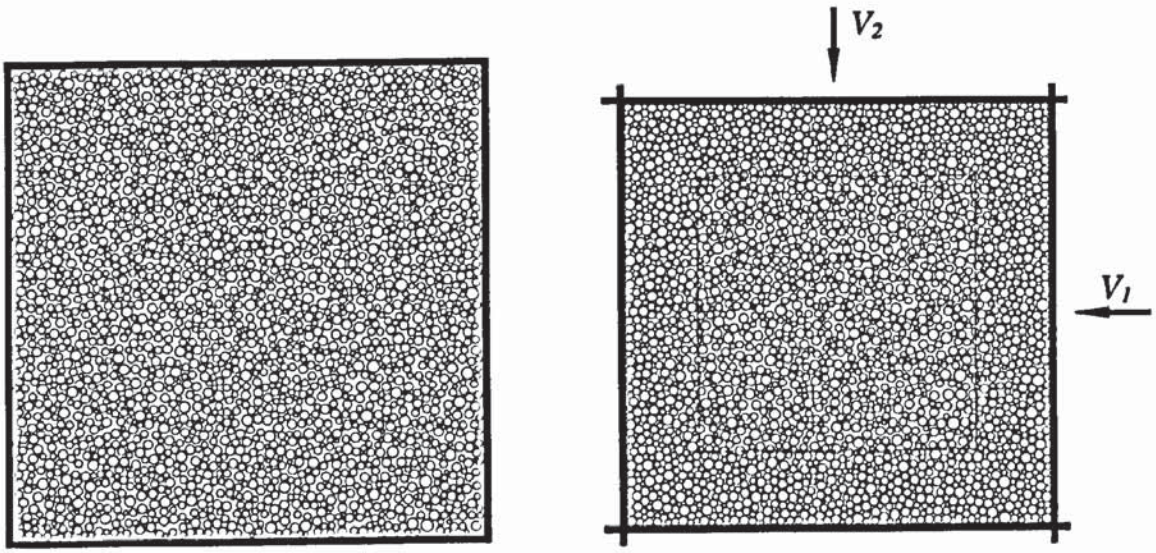

(a) sample generation (b) isotropic compression

(c) force connection diagram

Fig. 3.1 Sample preparation by driving walls

The second method used to prepare a sample is to generate the particles randomly as a 'granular gas' in the space with very low solid fraction ca. 0.385 (Fig. 3.1a). Then the particles are driven together to obtain a dense system by moving the four boundary walls inwards at equal speeds until the desired solid fraction is obtained (Fig. 3.1b). The

shortcoming of this method is that the walls interact with the particles near the boundaries first and the disturbance progressively propagates to the inner particles through particle-particle interactions. This leads to the density near the boundaries being denser than the central area as can be seen from Fig. 3.1b. Consequently, by the end of isotropic compression large forces always concentrate near the boundaries and the sample generated by this method is far from homogeneous (Fig. 3.1c).

Alternatively, the particles can be generated in such a way that they float freely in space and then provide a mechanism for bringing them into close proximity. One mechanism is to switch on gravity. Another is to switch on a central force field which attracts the particles to a common point. Again, the packing structure throughout the sample can vary depending on the technique chosen. All the samples in the simulations with wall boundaries were generated by the following method.

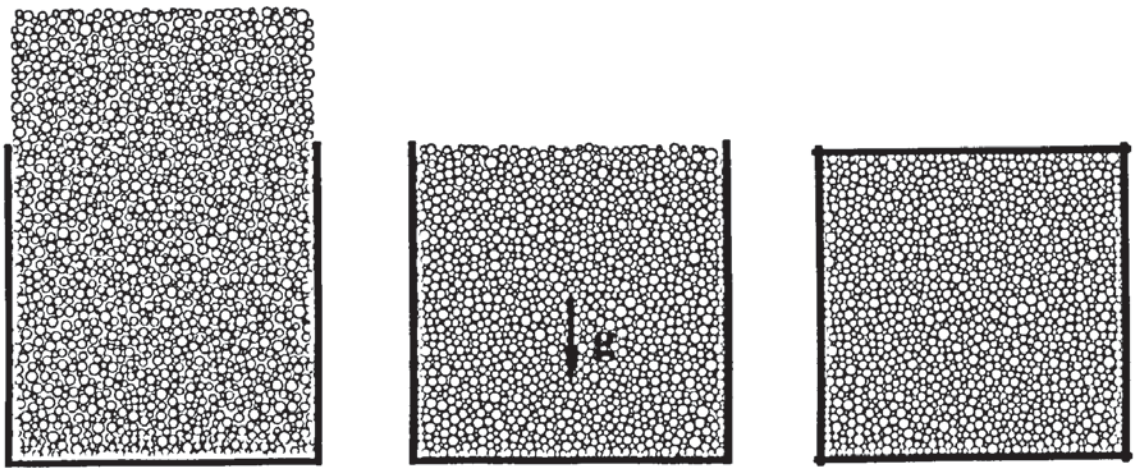

(a) generation (b) deposition (c) isotropic compression

Fig. 3.2 Three stages of sample preparation

At the first stage of sample preparation, the particles are generated randomly floating in a container with the top wall omitted. There are no contacts between particles at this stage and the solid fraction is about 0.385 (Fig. 3.2a). Then gravity is introduced to create a bed of particles above the bottom wall (Fig. 3.2b), which is called the deposition stage. On completion of the sample deposition the solid fraction is 0.584. The top wall is then positioned above all the particles and moved downwards a bit to bed the sample. In the last stage, the four boundary walls are moved inwards at the same speed to isotropically compress the sample until a desired high packing density is obtained, say 0.620 (Fig. 3.2c), whereupon the velocities of the four walls are set to zero and the sample is allowed

to relax. Eventually the system reaches equilibrium with all particles velocities being essentially zero. The sample is then saved and used as the initial configuration for the shear tests.

3.3.3 Simulation parameters

In the simulations, the collection of particles consists of seven different sizes varying from 30μm to 90μm with an average diameter D_{50} of 60μm. The mechanical properties of all the particles are given in Table 3.1 and the particle size distribution is shown in Fig. 3.3. These parameters, unless indicated otherwise, will be used for all the shear tests in the following chapters.

Table 3.1 Mechanical properties used in the simulation

DEM parameters and material properties	Selected value
Number of particles	5000
Diameter of particles (μm)	30, 40, 50, 60, 70, 80, 90
Friction coefficient between particles, μ_p	0.5
Friction coefficient between particles and walls, μ_w	0.1, 0.5
Cohesion c	0.0
Young's modulus, E (GPa)	8.34
Poisson's ratio, ν	0.35

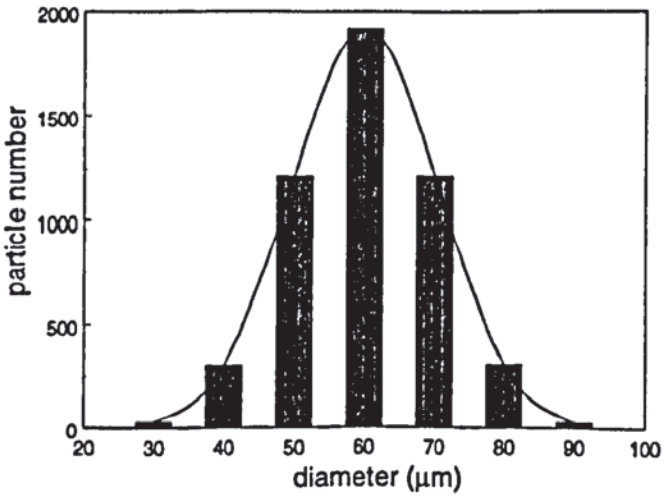

Fig. 3.3 Particle size distribution

3.4 Constant volume tests

3.4.1 Test set-up of BCP

Biaxial compression simulations with periodic boundaries have been performed using a representative volume element subjected to a uniform strain field. By considering the particle assembly in the working space as a continuum element of a unit cell, a strain-rate tensor $\dot{\varepsilon}_{ij}$ is superimposed on the assembly so that the incremental displacement of each constituent sphere Δx_i^S is given as,

$$\Delta x_i^S = \dot{\varepsilon}_{ij} x_j \Delta t \tag{3.4}$$

where x_i are the coordinates of the sphere centre and Δt is the small time step used to advance the evolution of the system. Superimposing the incremental displacements due to the prescribed strain rate field on the updated incremental displacement due to the out-of-balance force leads to the total incremental displacement of each sphere as,

$$\Delta x_i = \Delta x_i^F + \Delta x_i^S \tag{3.5}$$

where Δx_i^F represents the updated incremental displacements of each sphere due to the out-of-balance force, see Appendix A.

During the biaxial compression stage, strains are computed directly from the length along the sides of the periodic cell. From these measurements, strains in the lateral and axial directions are computed from

$$\varepsilon_i = \frac{l_i^n - l_i^o}{l_i^n} \tag{3.6}$$

where l_i^n, l_i^o are current and previous dimensions of the specimen in the i $(i=1, 2)$ direction respectively. Volumetric strains and deviator strains are calculated from the two dimensionally invariant strain measurements as follows

$$\varepsilon_v = \varepsilon_1 + \varepsilon_2 \tag{3.7}$$

$$\gamma = \varepsilon_1 - \varepsilon_2 \tag{3.8}$$

In the constant volume **BCP** test, each sample is strain controlled. The sample is compressed horizontally and expanded vertically at an equal but opposite constant strain

rate to maintain the volume (area) constant. The DEM, however, explicitly integrates Newton's second law for every particle. Hence, an idealized sample in a quasi-static experiment must be loaded at such a low rate that inertial effects can be negligible. The strain rates should be small enough to avoid collisions in the simulation. In the simulations reported here, they are set as $\dot{\varepsilon}_{11} = -1 \times 10^{-5} s^{-1}$, $\dot{\varepsilon}_{22} = +1 \times 10^{-5} s^{-1}$ and $\dot{\varepsilon}_{12} = \dot{\varepsilon}_{21} = 0$ to ensure deformation at constant volume. The simulations for all samples is continued until $\varepsilon_{11} = -0.15$, $\varepsilon_{22} = 0.15$, i.e. 15% axial strain. The results for the sample of solid fraction 0.620 are reported in this chapter. Results of **BCP** simulations on other samples with different initial solid fractions are reported in Chapter 6. The particle pattern at the beginning of shearing is shown in Fig. 3.4a and the pattern after 30% deviator strain is shown in Fig. 3.4b. In Fig. 3.4, all 5000 particles are colour banded. It's can be seen that the particle pattern by the end of test is totally different from that at the initial state in that there is a distinct shear band inclined at about 35° to the vertical direction. Further discussion of shear band formation will be presented in Chapter 7.

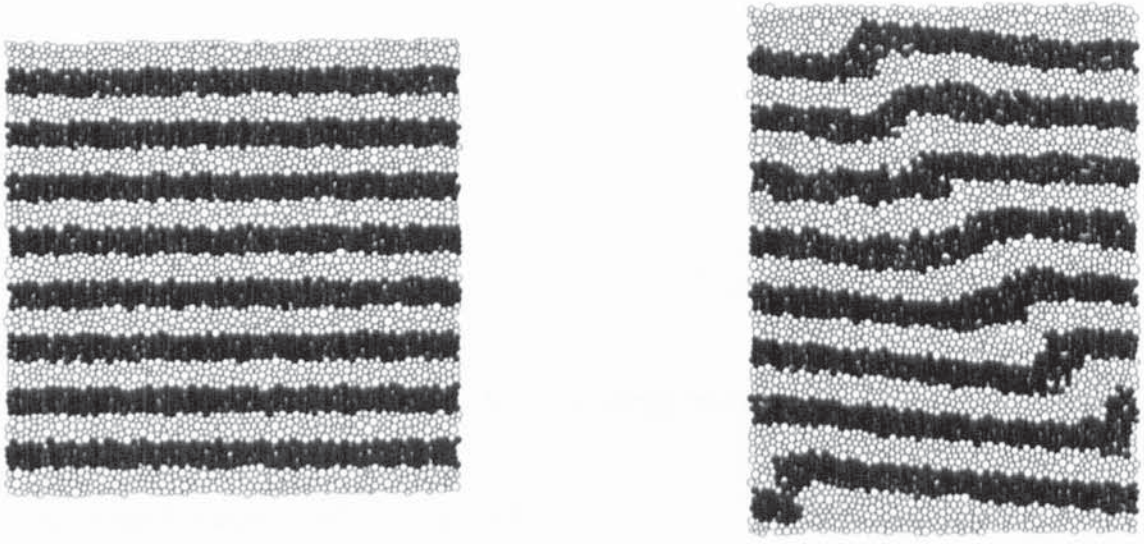

(a) (b)

Fig. 3.4 Snapshots of **BCP** test at: (a) Prior to shearing; (b) 30% deviator strain

3.4.2 Test set-up of BCW

Once a sample with a solid fraction of 0.620 had been prepared, as described in section 3.3.2, the system was then ready to undergo biaxial compression by moving the four boundary walls at a specified strain rate. The strain rates were set to be the same as in the **BCP** constant volume test. The wall friction was set to 0.1. For the **BCW** constant volume

test, the left and right-hand walls were moved towards each other, while the top and bottom walls were moved apart.

In order to achieve constant volume conditions, kinematically controlled wall boundaries were employed. The velocity of each wall was updated at every time step by:

$$v_i = \dot{\varepsilon}_{ij} * l_j \tag{3.9}$$

where v_i are the velocities of the walls, $\dot{\varepsilon}_{ij}$ is the desired strain rate tensor and l_j are the current dimensions of the sample (Fig. 3.5). The velocity of the walls can be derived from,

$$\begin{bmatrix} v_1 \\ v_2 \end{bmatrix} = \begin{bmatrix} \dot{\varepsilon}_{11} & 0 \\ 0 & \dot{\varepsilon}_{22} \end{bmatrix} \begin{bmatrix} l_1 \\ l_2 \end{bmatrix} \tag{3.10}$$

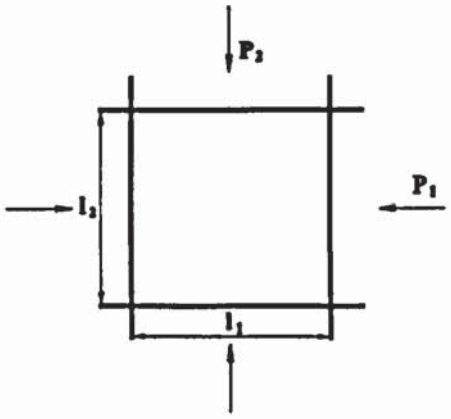

Fig. 3.5 Definition of stress in wall boundaries simulation

As mentioned in section 3.1, for the tests using wall boundaries, the stress states are calculated in two different ways:

(i) from the forces at the boundary wall:

$$\sigma_{ij} = \frac{P_i l_j}{V} \tag{3.11}$$

where P_i are the forces acting on the walls and the principal stresses can be derived as,

$$\sigma_{11} = \frac{P_1 l_1}{V} = \frac{P_1 l_1}{l_1 l_2 \langle d_p \rangle} = \frac{P_1}{l_2 D_{50}} \tag{3.11a}$$

$$\sigma_{22} = \frac{P_2}{l_1 D_{50}} \tag{3.11b}$$

where d_p is the diameter of each particle.

(ii) as a volume average of the contact forces over all the contacts in the assembly (as in periodic cell calculations):

$$\sigma_{ij} = \frac{2}{V}\sum_{I}^{C} P_I x_J \qquad (3.12)$$

and the summations are over all the contacts in the volume V.

3.4.3 A comparison between BCP and BCW tests

Figure 3.6 shows the stress-strain curves obtained for the **BCP** and **BCW** tests. It can be seen that, when the system is deformed by kinematically controlled wall boundaries, the calculations based on boundary information (p-w) give slightly smaller values of both the major and minor principal stresses when compared to the volume-averaged calculations (p-p). It is also noted that the difference is greater when the walls move outwards, as in the case of the minor principal stress. As a result, the boundary measurements overestimate the deviator stress and underestimate the mean stress, as shown in Figs. 3.7 and 3.8, respectively. It can be seen from Fig. 3.7 that the deviator stress increases rapidly at a decreasing rate until 10% shear strain after which some strain softening occurs. The mean stress increases gradually throughout the test as shown in Fig. 3.8. Interestingly, as can clearly be seen in Fig. 3.9, the boundary measurements indicate an initial decrease in mean

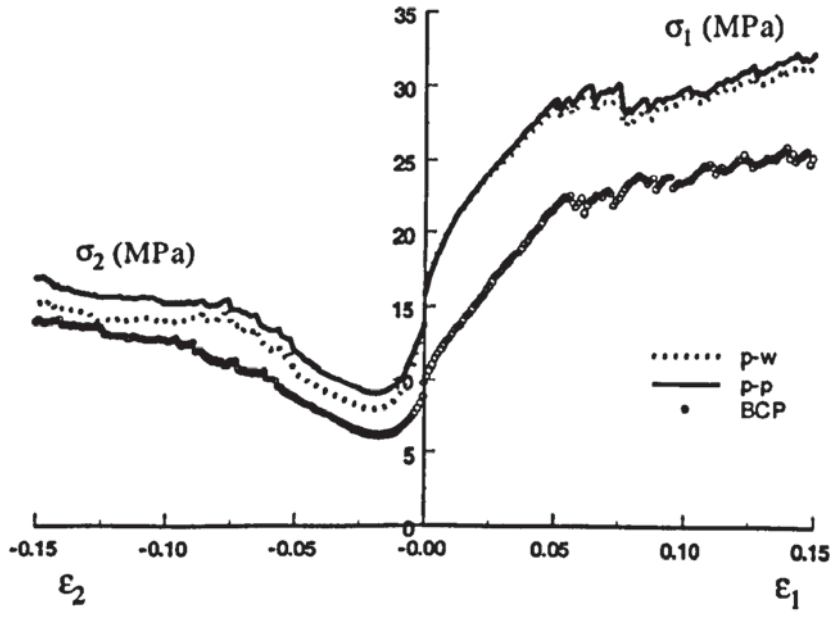

Fig. 3.6 Stress-strain relationships

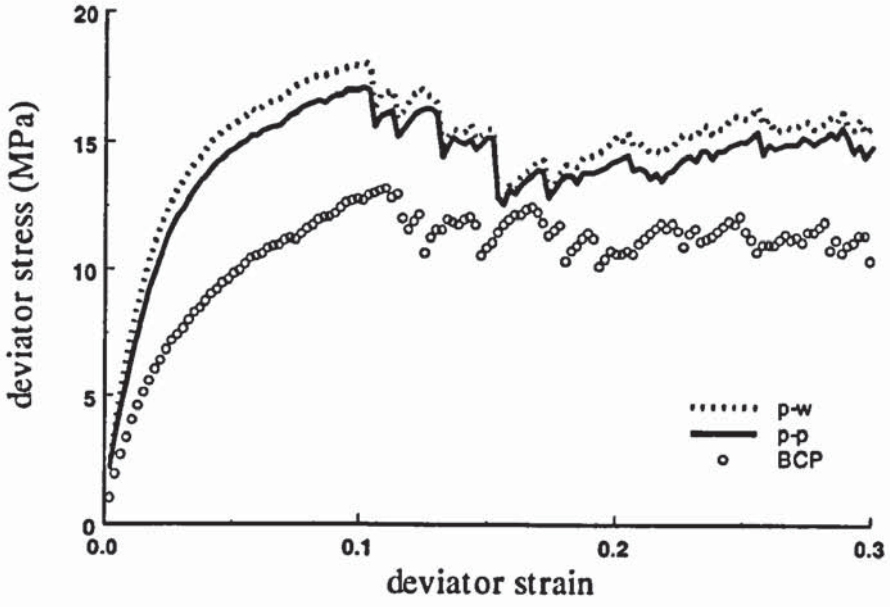

Fig. 3.7 Evolution of deviator stress

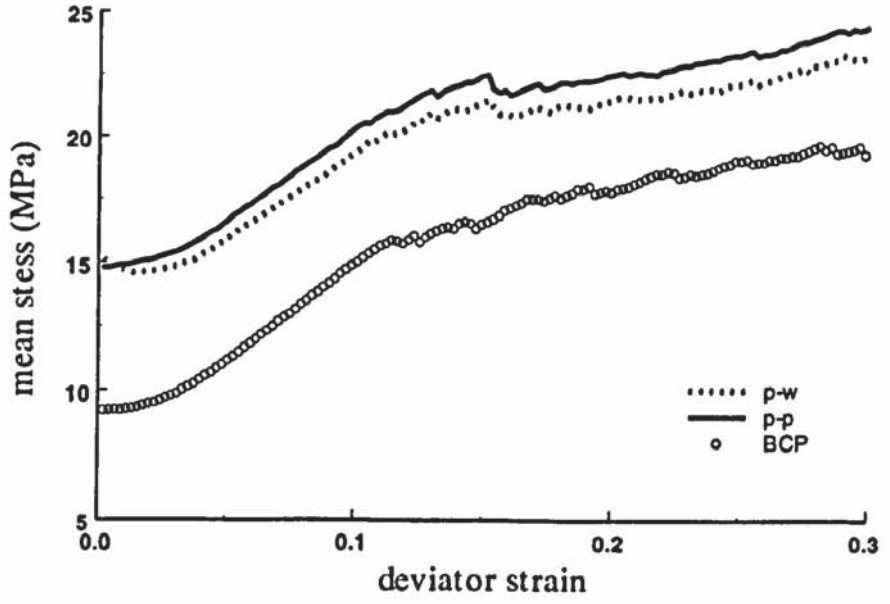

Fig. 3.8 Evolution of mean stress

stress, which is not observed when volume-averaged measurements are used. This is also apparent in the stress path evolution shown in Fig. 3.10.

In order to obtain the same solid fraction at the start of the shear stage, it was necessary to increase the isotropic stress in the wall-bounded system to a higher stress level than that of the periodic cell. It can be seen from Fig. 3.8 that the initial mean stress of the sample in the **BCW** test is about 6MPa higher than that in the **BCP** test. Consequently, only

qualitative comparisons are possible when considering the individual stress components in the two test simulations. The change in mean stress during biaxial compression is defined as the mean stress (s) minus the initial mean stress (s_0) and, as can be seen in Fig. 3.9 when the volume-averaged data is considered, the change in mean stress during shearing is almost identical, until the deviator strain is 15%, whereupon the deviator stress during post-peak deformation of the wall-bounded system starts to increase (see Fig. 3.7).

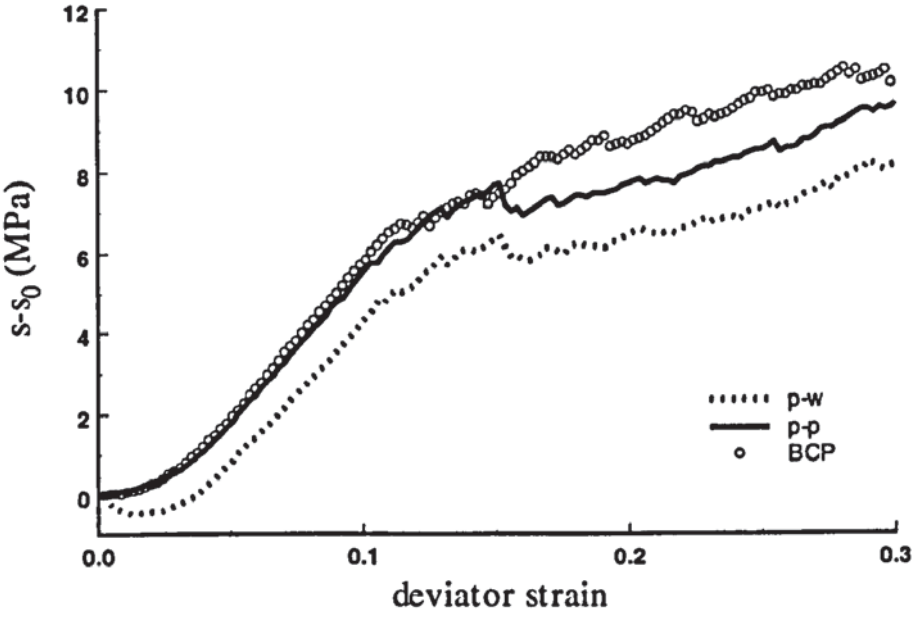

Fig. 3.9 Changes in mean stress during constant volume deformation

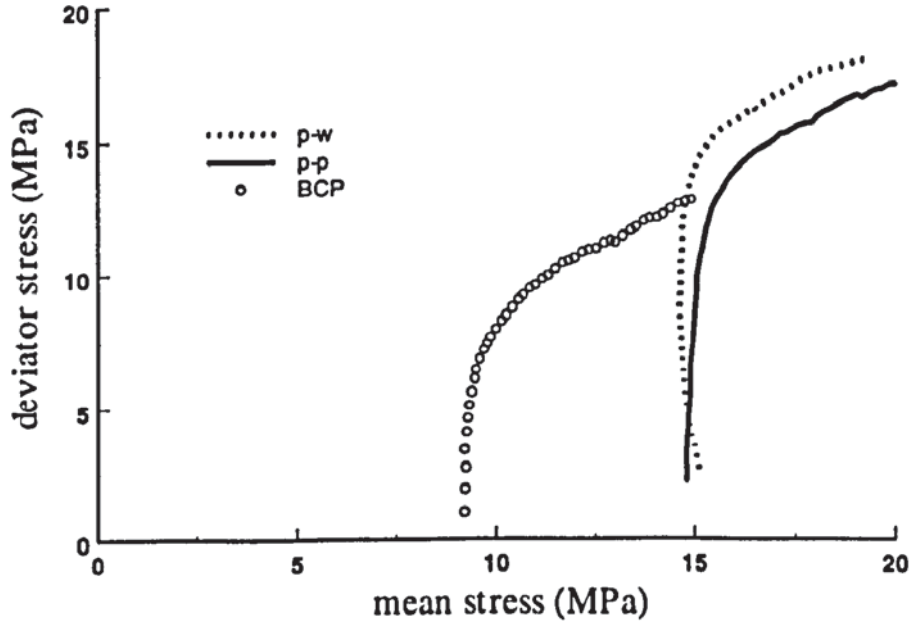

Fig. 3.10 Stress paths

The mobilised shear strength defined in terms of the angle of internal shearing resistance φ_m is shown in Fig. 3.11. The maximum value of φ_m obtained from the boundary calculations is 30° compared to a value of 26° obtained from the volume-averaged stress calculations. However, remarkable agreement is obtained between the two test results when the evolution of $sin\varphi_m$ is examined in terms of volume-averaged calculations. It is also noted that, in the wall boundary controlled test, the stress fluctuations exhibited by the volume-averaged data is reflected in the boundary calculations.

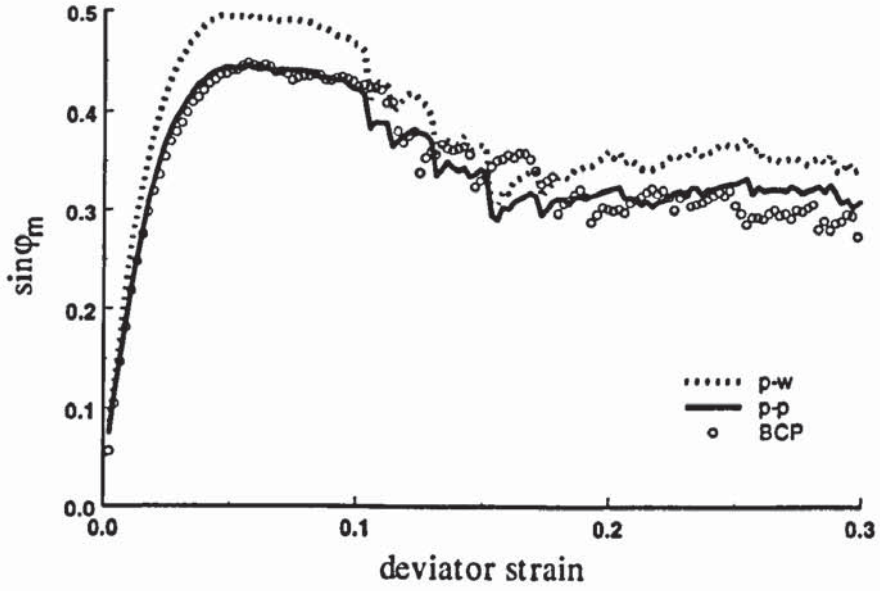

Fig. 3.11 Evolution of $sin\varphi_m$

The evolutions of internal variables during the two simulations are shown in Figs. 3.12 - 3.14. Figure 3.12 shows the evolution of the mechanical coordination number, Z_m. It is clear that Z_m is similar in both tests. Figure 3.13 shows the evolution of deviator fabric. It can be seen that although the degree of induced structural anisotropy is slightly higher in the periodic cell test, the trends in the evolution of structural anisotropy in the two tests are very similar. However, the values of deviator fabric developed are rather low compared to the theoretical prediction that the maximum possible value is 0.5 in 2D. This is due to the increase in mean stress, which suppresses the induced structural anisotropy (Thornton and Zhang, 1999). In addition, it is not necessary for the system to develop a strong structural anisotropy because the deviator stress depends only on the sub-network of larger than average contact forces, which selects the most favourably oriented pathways within the overall anisotropic structure (Thornton, 2000b).

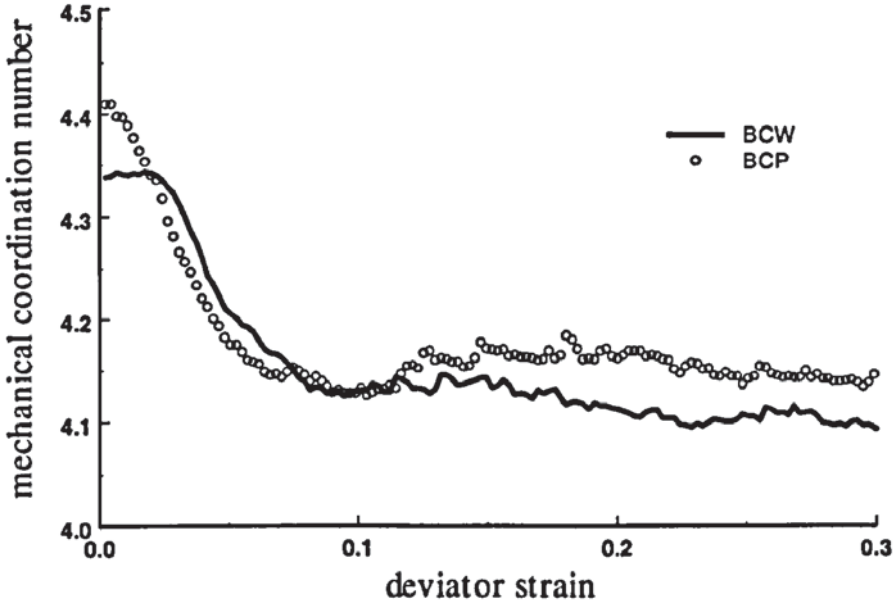

Fig. 3.12 Evolution of mechanical coordination number

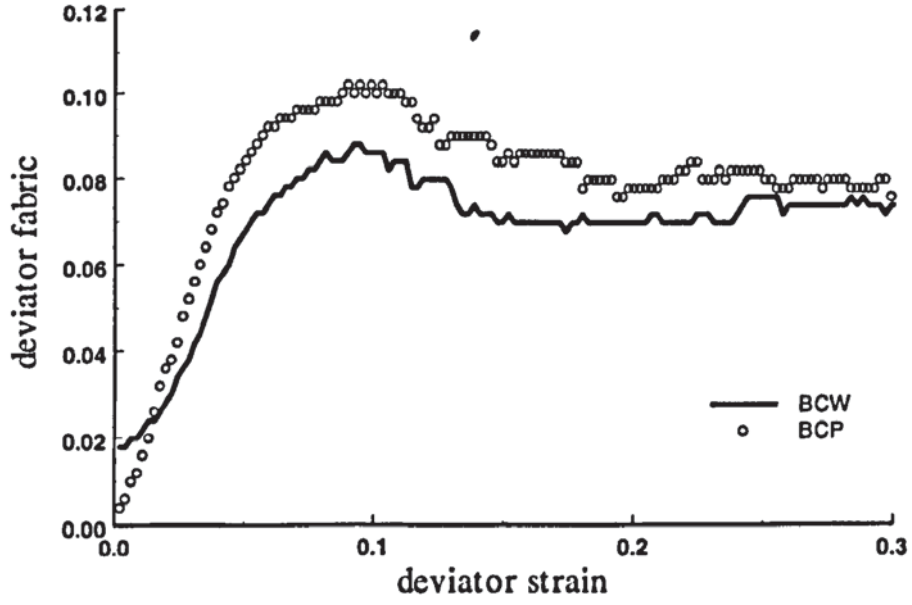

Fig. 3.13 Evolution of induced structure anisotropy

The evolution of the percentage of sliding contacts is also similar in both tests, as shown in Fig. 3.14, although there are more sliding contacts recorded in the simulation using wall boundaries. The reduction in the percentage of sliding contacts at high deviator strains is due to the high mean stress developed as a consequence of maintaining the sample volume constant.

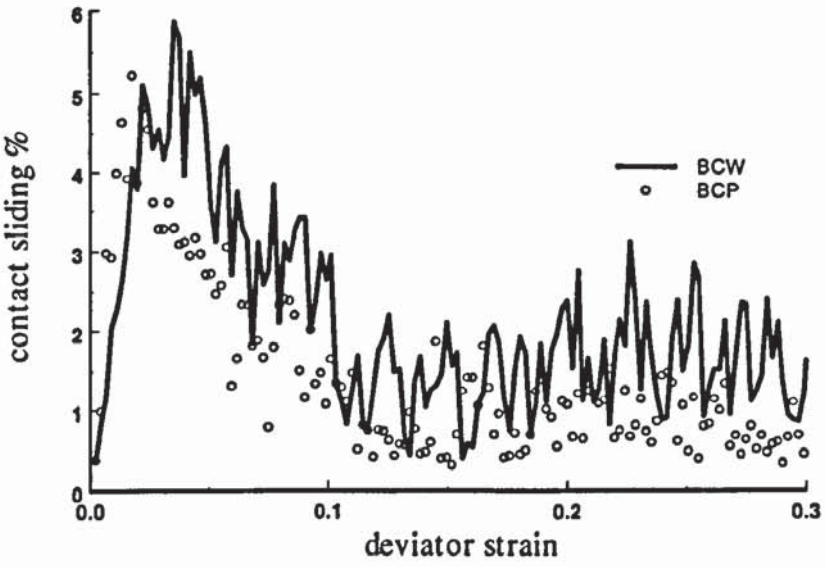

Fig. 3.14 Evolution of percentage of sliding contacts

3.5 Constant mean stress tests

3.5.1 Test set-up

In the constant mean stress test, the strain rates are initially specified as those used in constant volume test to the sample. However, in order to keep the mean stress constant, the strain rate tensor is continually adjusted using a numerical servo control,

$$\dot{\varepsilon}_{ii}^{s} = \dot{\varepsilon}_{ii} + sign(\, g(\sigma_d - \sigma_c\,), \dot{\varepsilon}_{ii}\,), \; \dot{\varepsilon}_{12} = \dot{\varepsilon}_{21} = 0 \tag{3.13}$$

where σ_d is the desired mean stress to be achieved and σ_c is the current actual mean stress of the assembly. In the **BCW** test, the velocity of each wall is modified according to the current adjusted strain rate by using (3.9). The wall friction is again set to 0.1.

3.5.2 A comparison of BCP and BCW tests

Except that the magnitudes and the trends of the curves are different from those of the constant volume tests, the same observations can be made for this set of results, shown in Figs. 3.15-17, when making the comparison between **BCP** and **BCW** tests. Since this is constant mean stress test, the magnitudes of both the principal stresses (Fig. 3.15) and the deviator stress (Fig. 3.16) are much lower than in the constant volume tests. However, the

evolution of $sin\varphi_m$ is similar to the results for the constant volume tests. These results further demonstrate that periodic boundaries can provide qualitative results of macroscopic behaviour of the sample, while the measurements from the wall boundaries are far from the true material behaviour.

The microscopic behaviour of the specimen in the constant mean stress tests are compared in Figs. 3.18 - 3.20. Once again the results from the **BCP** test are comparable to the results from **BCW** tests based on the volume averaged calculation. More results of **BCP** constant mean stress tests will be discussed in Chapter 6.

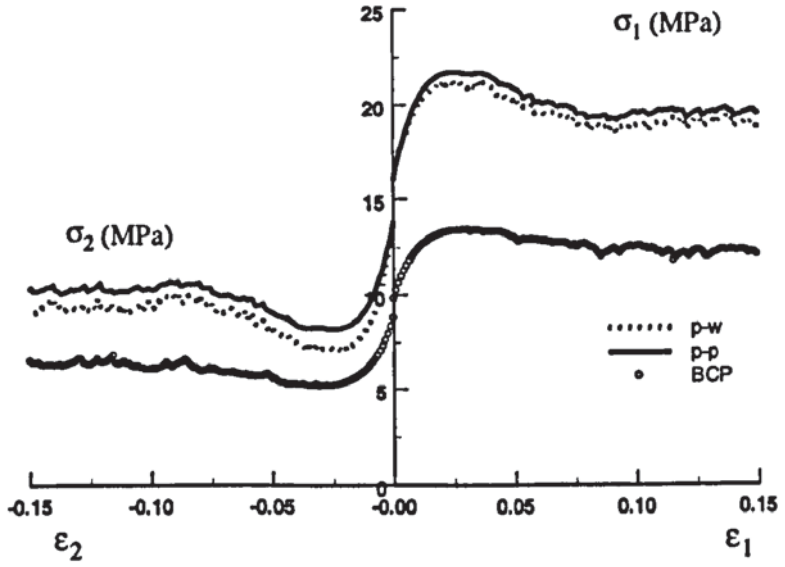

Fig. 3.15 Stress-strain relationships

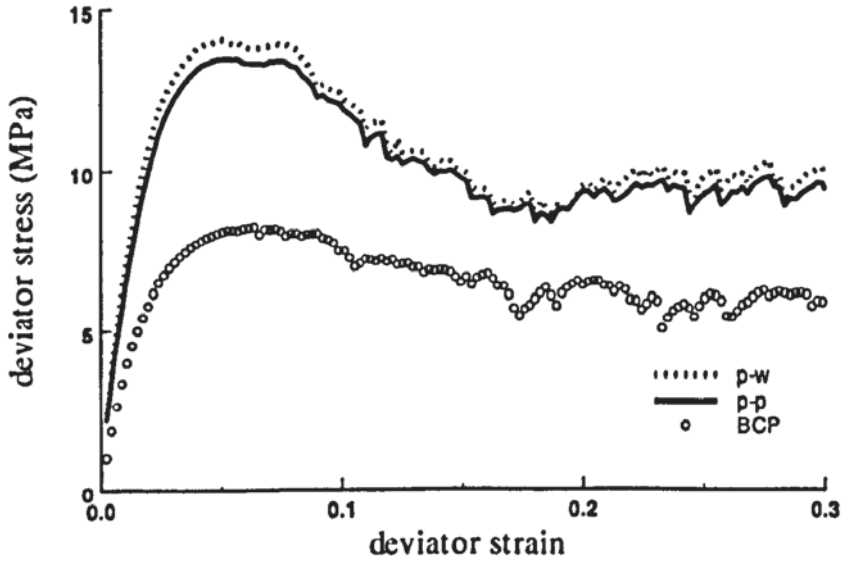

Fig. 3.16 Evolution of deviator stress

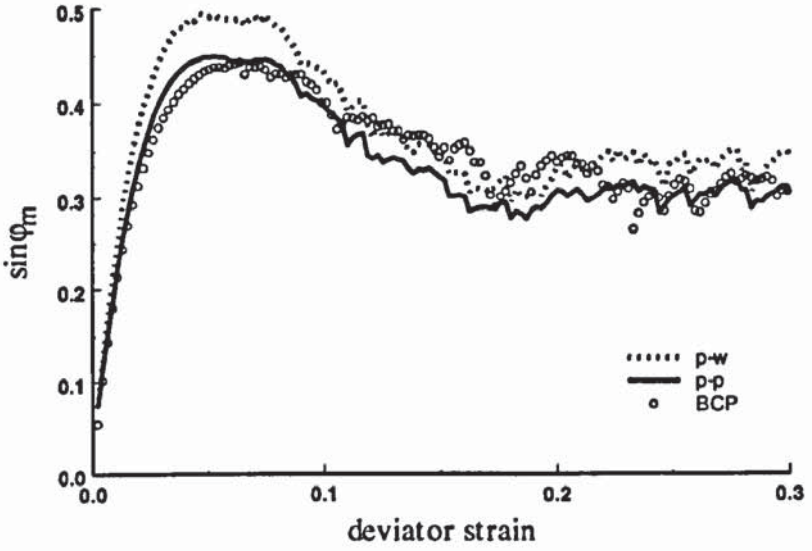

Fig. 3.17 Evolution of $sin\,\varphi_m$

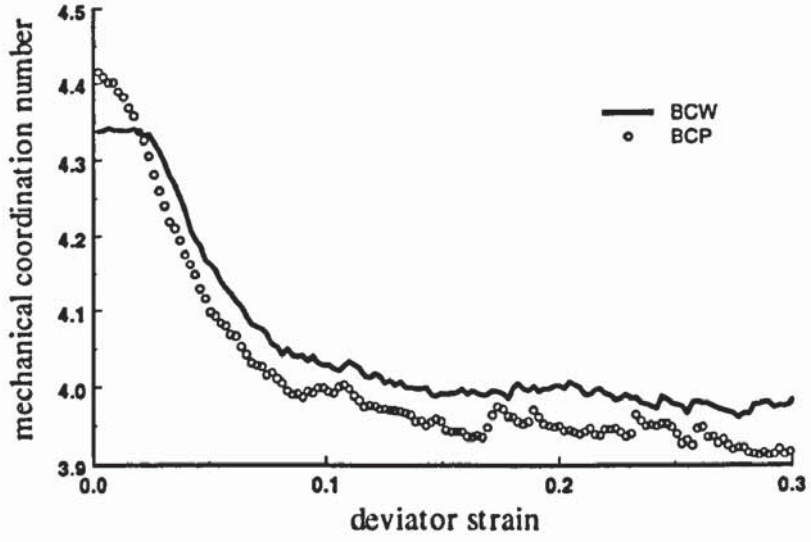

Fig. 3.18 Evolution of the mechanical coordination number

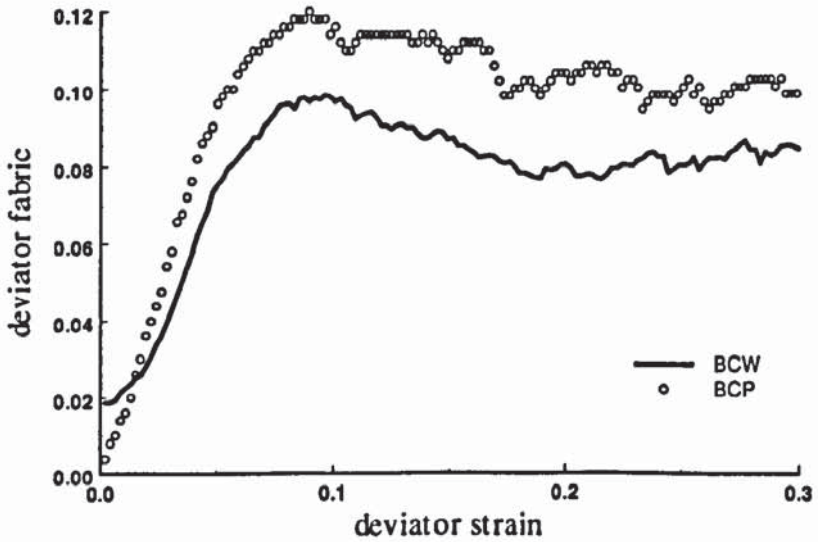

Fig. 3.19 Evolution of induced structural anisotropy

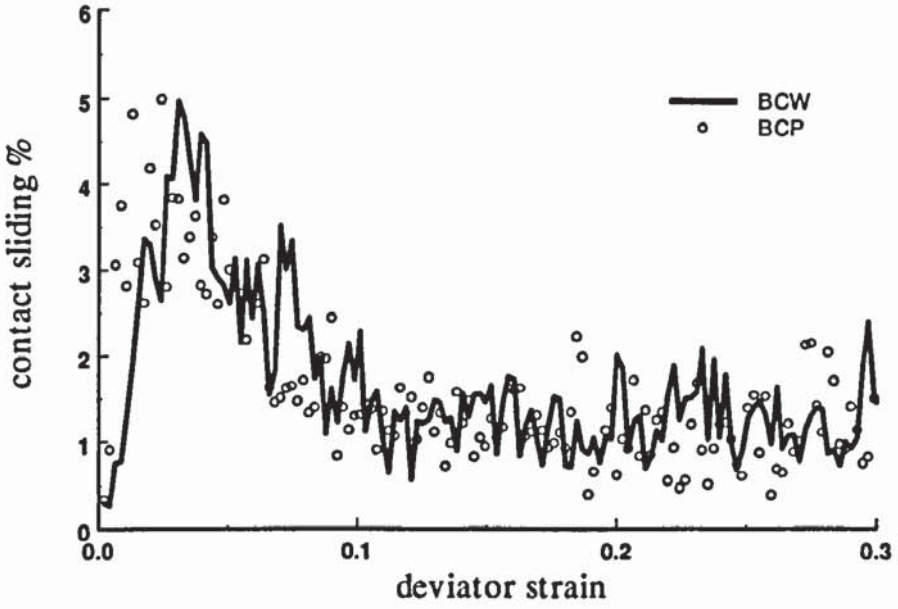

Fig. 3.20 Evolution of percentage of sliding contacts

3.5.3 The effect of wall friction on the results of BCW tests

In order to investigate the effects of different boundary conditions, a series of tests were performed in which the friction between walls and particles μ_w was set as 0.0, 0.1 and 0.5. It is noted that the arrangement of individual particles prior to biaxial compression is not exactly the same in the **BCP** and **BCW** tests, compare Fig. 3.4a with Fig. 3.21a. It is interesting to see that the particle pattern at 30% shear strain in the **BCW** tests is different from that in the **BCP** test and the deformation pattern of the **BCW** test depends on the wall friction specified. When the wall friction is zero there is only one shear band that is inclined at about 46° to the vertical direction (Fig. 3.21b). Two approximately conjugate intersecting shear bands form when the wall friction is set to a high value of $\mu_w = 0.5$ as shown Fig. 3.21c. Further discussion of shear bands is provided in Chapter 7.

It has been shown that the measurements from wall boundaries underestimate the principal stresses and result in a significant overestimation of the angle of internal shearing resistance. Therefore, in the following section the state of stress is calculated by volume averaging over all the contacts inside the sample. Based on these results the following observations can be made.

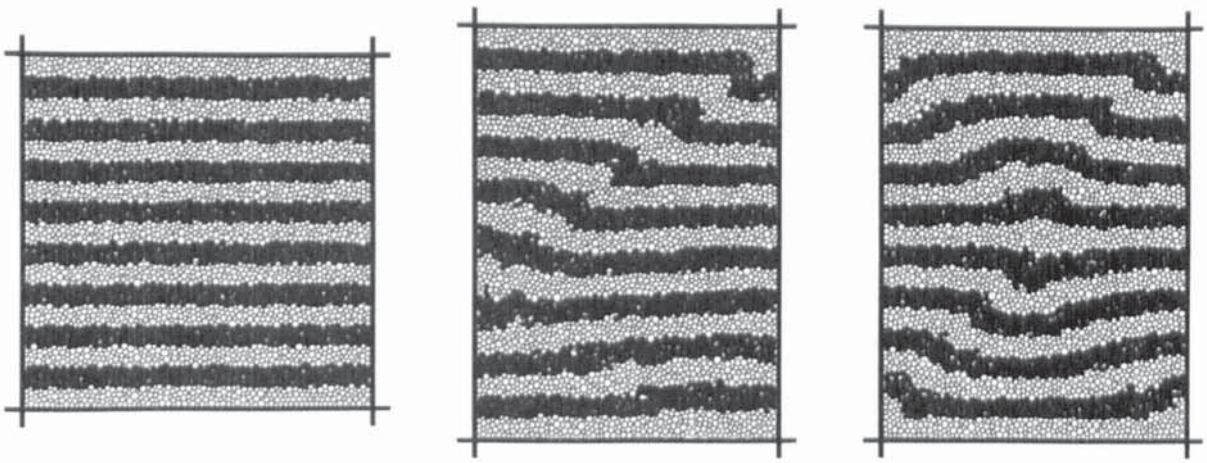

(a) (b) (c)

Fig. 3.21 Snapshot of **BCW** test at (a) Prior to shearing;
(b) 30% deviator strain ($\mu_w = 0.0$); (c) 30% deviator strain ($\mu_w = 0.5$)

3.5.3.1 The macroscopic behaviour

The macroscopic measures for the **BCW** constant mean stress test are given in Figs. 3.22 - 3.24. Figure 3.22 shows the deviator stress plotted against deviator strain and Fig. 3.23 presents the volumetric strain versus deviator strain for the test using different wall friction. It can be seen that the deviator stress for the three tests reaches a peak at about the same strain, and then decreases as the deviator strain increases. Eventually the deviator stress remains nearly constant around 8MPa at large strain in all three cases. It is found that before the deviator strain reaches 10%, the results for the simulations with the two lower wall friction values are quite close. In addition, the peak deviator stresses for these two tests are higher than that obtained with a high wall friction (Fig. 3.22). This is also true for the evolution of $\sin\varphi_m$ as shown in Fig. 3.24. The maximum value of the angle of internal shearing resistance φ_m for the test with highest wall friction is about 2 degrees lower than that in the other two tests. In all cases, the volumetric strain increases with increasing deviator strain, i.e. dilates during shearing (Fig. 3.23). The sample with the highest wall friction exhibits the least amount of expansion by the end of the test. From comparisons of the **BCP** and **BCW** constant mean stress test presented in the last section, it was found that the shear strength obtained from the two tests were essentially the same. However, the sample used for comparison had a wall friction of 0.1. This means that the shear test that was carried out on the highest wall friction sample underestimated the shear

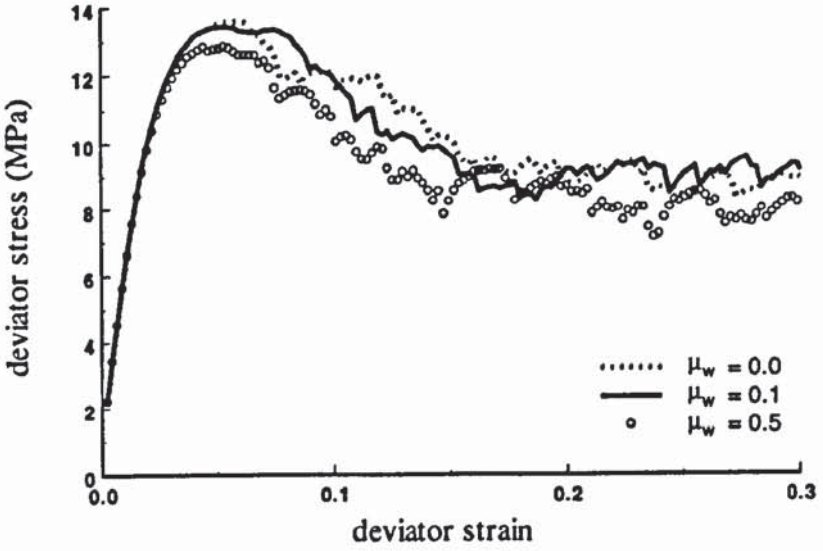

Fig. 3.22 Evolution of deviator stress

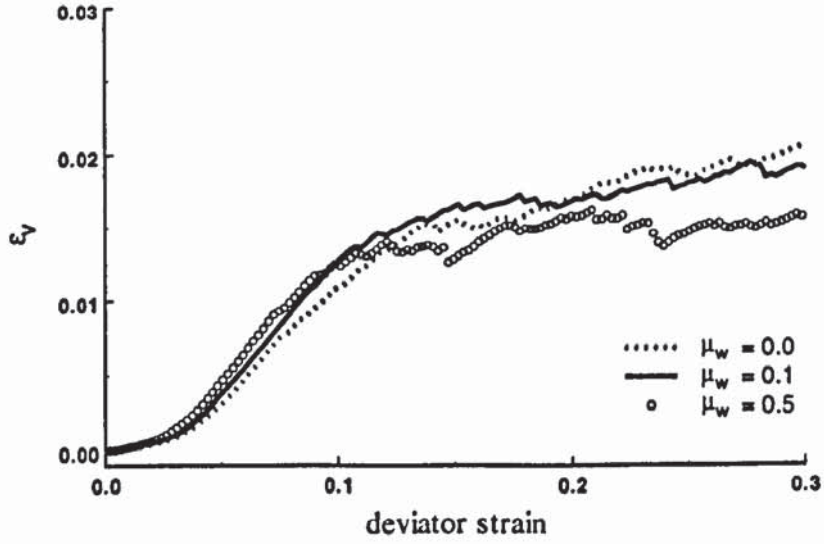

Fig. 3.23 Evolution of volumetric strain

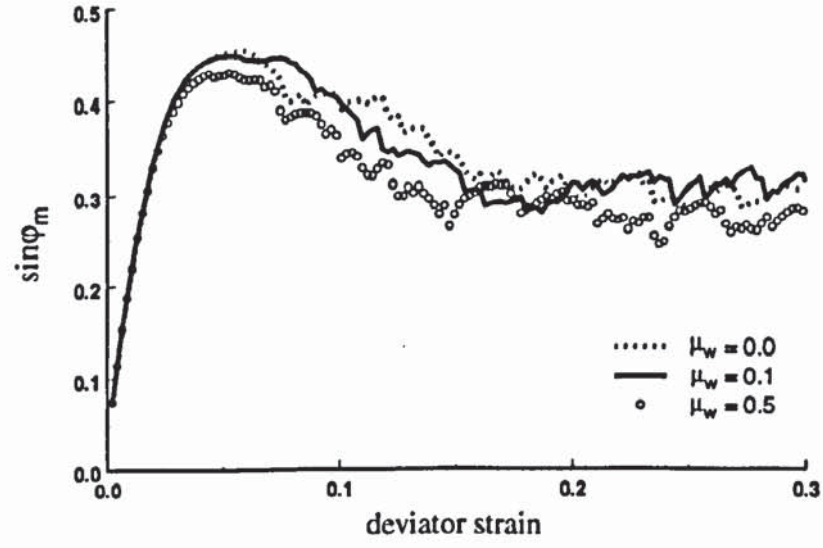

Fig. 3.24 Evolution of $sin\varphi_m$

strength of the material. This suggests that in a real experiment smooth boundaries rather than rough ones should be chosen for the biaxial compression test to overcome the boundary effect on the measurement of shear strength.

3.5.3.2 The microscopic behaviour

The effects of wall friction on the microscopic behaviour are shown in Figs. 3.25 - 3.28. Figure 3.25 shows the evolution of the mechanical coordination number with deviator strain. It can be seen that the evolution of the mechanical coordination number in all three tests is identical until 8% deviator strain. With further shearing there is a slight divergence among the three test results and by then the highest wall friction sample gives the greatest coordination number. The variation of the deviator fabric with deviator strain is shown in Fig. 3.26. It can be seen that, at very low strains (say ≤4%) the deviator fabric is the same for all three tests. However, at high deviator strain, the sample with the highest wall friction generally exhibits the lowest degree of induced structural anisotropy. The evolutions of the principal fabrics of the two samples are presented in Fig. 3.27. It is clear that, when the strain is less than 6%, the results obtained from two tests are identical. At high strain (≥6%), the major principal fabric of the sample with higher wall friction becomes less than that for the sample with zero wall friction. On the contrary, the minor principal fabric of the high wall friction sample becomes greater than the other.

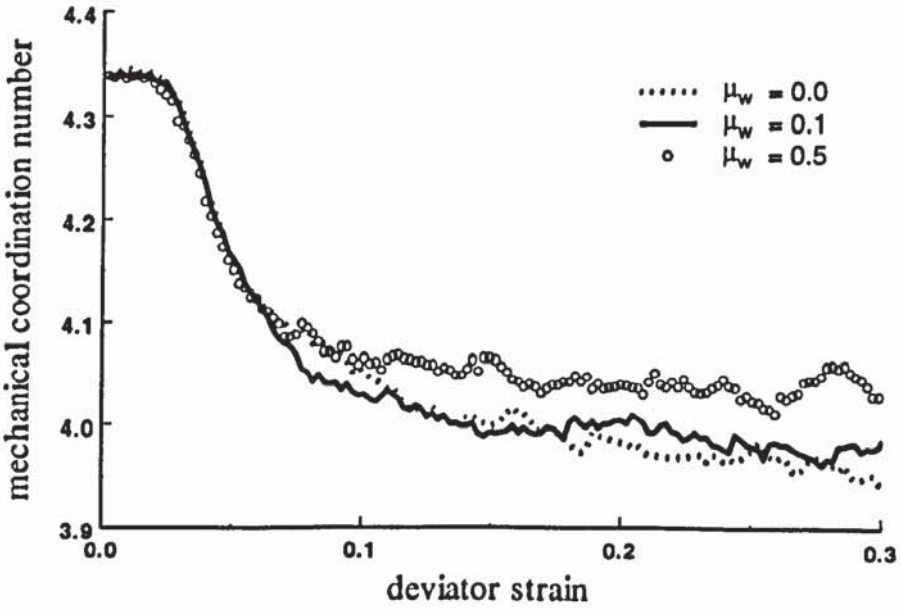

Fig. 3.25 Evolution of coordination number

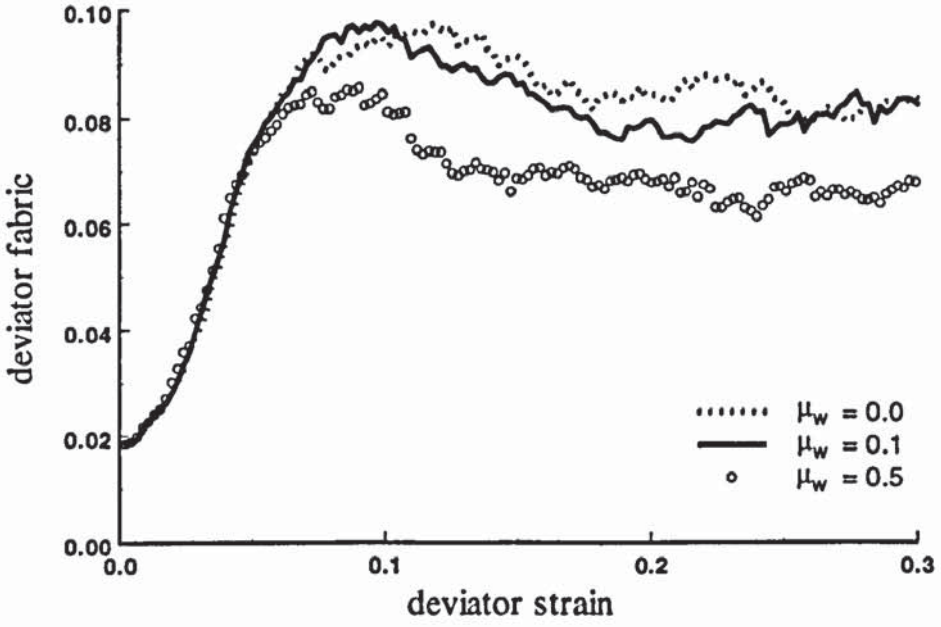

Fig. 3.26 Evolution of induced structure anisotropy

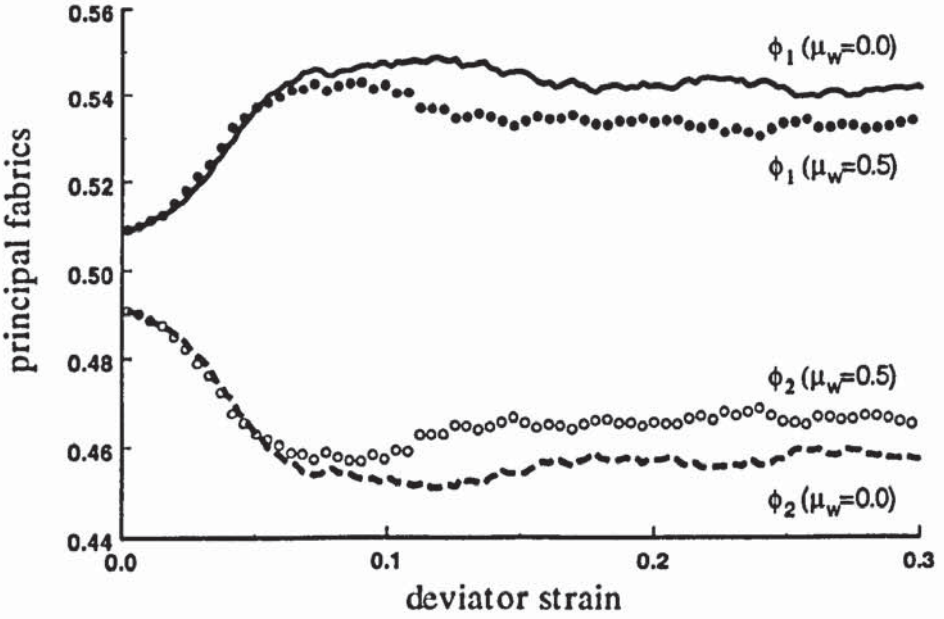

Fig. 3.27 Evolution of principal fabrics

It can be seen from the Figs. 3.25-3.27 that before the peak strength (see Fig. 3.24) the two samples show the essentially the same results and the divergence only occur during the post-peak stage, which implies that the effect of wall friction becomes significant after peak strength. As illustrated in Figs. 3.21b and c the appearance of shear bands in these two cases are different, hence the amount of strain localization inside the sample are not the same. Since the strain localization always starts at about the peak strength stage and

will cause non-uniform deformation inside the sample, the significance of this effect on the overall calculation of the mechanical coordination number and the deviator fabric is not clear. Although there is a notable difference between the deviator fabric of the two samples, the difference is actually very small in value. Further examination of the correlation between the strain localization and these microscopic behaviours are worthwhile carrying out.

Figure 3.28 shows the percentage of sliding contacts plotted against deviator strain. It is clear that the sample with zero wall friction has more contacts sliding. This is attributed to the fact that particles which are in contact with the walls are all sliding and cause other particles which are in contact with them to be more mobile. Consequently, more contact slidings are induced.

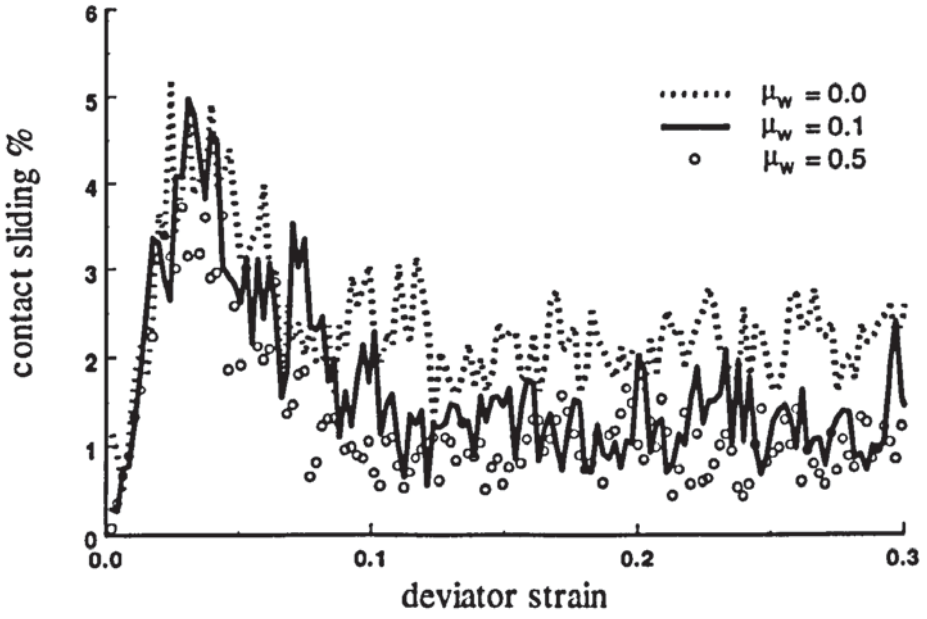

Fig. 3.28 Evolution of percentage of sliding contacts

3.6 Summary

Biaxial compression tests of 2D systems of elastic spheres have been simulated using both a periodic cell and wall boundaries. In all the tests simulated, the systems are deformed either at constant volume or under constant mean stress conditions. Aspects of both the macroscopic and microscopic responses have been presented. It has been shown that wall measurements underestimate the principal stresses leading to a significant overestimation

of $sin\varphi_m$, although qualitative comparisons showed good agreement. Nevertheless, the results obtained from volume-averaged data are in good agreement for both types of simulations.

The problem in physical experiments is the assumption that boundary measurements can provide reliable estimates of the state of stress in the specimen. However, the forces transmitted to the walls are not typical of the contact forces between the constituent particles. The forces transmitted to a wall depend on the contact curvature and, therefore, are increased if the wall is planar but decreased if the wall is rough due to asperities. The magnitude of the wall forces also depend on the elastic properties of the wall. The comparison between tests with different wall frictions demonstrates that the sample generates a higher deviator stress and angle of internal shearing resistance when the wall friction is set to a lower value. There are also fewer contacts with a wall than the contacts between particles in any cross-section within the particle assembly. Therefore, there is no reason why any boundary measurements should necessarily reflect the true material behaviour of the specimen.

Failure and post-failure analyses are very important in soil mechanics and geotechnical engineering. Failure of material is often characterized by the formation and propagation of localized shear zones. It is interesting to find that shear bands form in both **BCP** and **BCW** tests though the deformation patterns are different when the boundary conditions are changed. This makes it very difficult to examine localization phenomenon in detail in biaxial compression test simulations. The direct shear test is another conventional experiment, which intentionally generates a shear band in the central plane of the sample. Hence, it is instructive to perform direct shear simulations in order to examine behaviour of granular materials within shear bands and this will be discussed in the next chapter.

CHAPTER 4: DIRECT SHEAR TESTS

4.1 Introduction

In the direct shear test, the top half of the specimen is translated relative to the bottom half of the specimen in order to create a shear band/plane across the mid-height of the specimen. This test is widely used to measure the flow properties (in particle technology) or the shear strength (in geotechnical engineering) of granular materials. In particle technology the test is performed in a Jenike shear cell, which is circular in cross section, whereas the Casagrande shear box (square cross-section) is used in geotechnical engineering. In both cases, the applied vertical and horizontal forces are measured and the ratio of horizontal to vertical load is assumed to provide an estimation of the average ratio of shear to normal stress acting in the shear band, and thereby provide a direct measure of the internal friction angle. It is, however, unclear how reliable this traditional interpretation is since the exact state of stress within the shear band is unknown.

The above problem can easily be examined by using DEM simulations, in which not only the boundary information can be obtained, but also detailed information inside the sample. The numerical model of the apparatus and the procedure of the simulations are reported in this chapter. The main goals are to investigate the advantages and disadvantages of this tester; to explore how the applied loads are distributed within the sample; to investigate the shear behaviour of granular materials and the effect of boundary conditions in this test. Some of the simulation results reported in this chapter were first reported by Zhang and Thornton (2002).

Two types of direct shear tests have been conducted: one is a constant volume test (CV test) and the other is a constant normal stress test (CN test). In the CV tests, three samples with different aspect ratio are employed and two different boundary frictions are considered. The corresponding results are presented to show how the average stress ratio acting in the shear band compares with the force data at the boundaries. The effects of the aspect ratio of the shear box and the boundary friction are also investigated. In the CN tests the above three samples are subjected to different constant normal stresses in order to

examine the effect of stress level. Based on the calculations of the stress tensor inside the shear band, the corresponding Mohr's circles are obtained and the principal stress directions are identified. According to the state of stress and strain in the shear band, the interpretation of direct shear test data is discussed in the context of traditional experimental measurements.

4.2 Brief literature review

Although strength tests on engineering materials such as wood, metal and glass apparently began in the early seventeenth century, the available literature on soil testing only dates back to the early eighteenth century. The works of the early engineers were concentrated on military fortifications or were limited to speculation on the angle of the shear surface behind a retaining wall. Even Coulomb (1776), tested materials such as mortar rather than soils. Today there are basically four principle methods employed in soil strength testing: direct shear, triaxial compression, torsional, and vane tests. Skempton and Bishop (1950) presented the measurement of the shear strength parameters c and φ on some principal soil types by the above methods practiced in Great Britain in detail. Here we only focus on the shear box test and a brief review of the experimental and numerical investigations of the direct shear test is presented in this section.

It appears that Collin (1846) was the first to propose a real soil shear test, in which a long clay specimen was loaded transversely at its centre until it failed. This arrangement was used to apply double direct shear to the specimen. Leygue (1885) described a single direct shear test for cohesionless soils in a shear box, which was tilted until the top half slid across the bottom half and was similar to the modern device except for the loading technique. The advantage of the test is that it is very easy to set up and the results can be obtained within a very short period of time. However, experimentalists and researchers are sceptical of its reliability as a shear strength test. A serious drawback in the direct shear test is the non-uniformities of stress and strain distribution within the shear apparatus, which means that the interpretation of direct shear test results is not straightforward and may be misleading when based on external measurements.

There are many variations in the loading conditions in contemporary direct shear test devices. Modified loadings have been employed attempting to develop more uniform

strain conditions within the specimen. An annular direct shear apparatus was proposed for soil by Lambe (1951). Such a test was used to determine the shear strength of soft rock, but apparently it was not employed otherwise. A shear box developed by Peltier (1957) in the Central Laboratory of Bridges and Roads of France has movable sides by which a controlled force can be applied to the intermediate principal plane. Although the intermediate principal stress was probably not uniformly distributed over the sides of the box its average value can be computed. Later on, very large shear boxes have been designed to permit testing of soils containing gravel-size and large soils that cannot be tested in the ordinary laboratory apparatus (Sowers, 1961). Such a box, permitted burying the shear box in an embankment and rolling the broken rock to be tested in the manner as it would be compacted in the structure. It was claimed that the test results made it possible to check the design with greater assurance and to plan the construction more fully.

Bishop *et al* (1971) described a ring shear apparatus and commented on both the design and principles of operation, and its application to the measurement of the residual strength of undisturbed and remoulded samples. The results of tests on five soils were presented and discussed in relation to other published residual strength data from tests on these materials. The factors controlling the brittleness of soils tested under drained conditions were also examined. As the test results differed significantly from those obtained in multiple reversal direct shear box tests, a critical examination was made of all possible sources of error in both measurement and interpretation.

Matsuoka *et al* (2001) developed an in-situ direct shear apparatus, which can be used in both small (60 cm square by 8.5cm high) and large sizes (120cm square by 17cm high) to perform direct shear tests on several kinds of coarse-grained granular materials at different construction sites. In contrast with the traditional direct shear test, the lower shear box is not used in the test. This test was performed simply by pulling horizontally a latticed shearing frame, embedded in the ground, with a flexible rope or chain under the application of a constant vertical load on the sample. It was argued that the extreme simplicity and high accuracy of this newly developed test were demonstrated and emphasized by performing a number of direct shear tests in-situ. In addition, the dimensions of the shearing frame did not significantly affect the shear strength when the frame was greater than four times the maximum grain size of the sample.

However, as a research tool, it is hard to clearly interpret the results in terms of the shear mechanism due to the indeterminacy of the stresses, the rotation of the direction of principal stresses, and the nonuniformity of strains distribution. The most serious disadvantage is the preselection of the shear surface. If the soil is not perfectly homogeneous, the plane determined by the position of the specimen in the shear box is not likely to be the weakest or representative of the mass as a whole. Consequently, it has been suggested that the test results, therefore, are likely to present an optimistic picture of the over-all strength (Sowers, 1963).

A series of direct shear tests that illustrate the influence of the orientation of soil reinforcement on the response of a cohesionless soil were reported by Dyer and Milligan (1984). Crushed glass was used to represent soil in the tests. This enabled a photo-elastic technique to be used to display the directions of maximum compressive stress in the specimen. When the granular assembly was stressed in a plane strain condition an almost orthogonal network of light stripes were observed. One family of stripes was found more pronounced than the other. These stripes were produced by the discrete distribution of load through a granular material by highly loaded columns of particles. The average effect produced by a highly loaded column of glass particles is a continuous light stripe, although irregular, that on average coincides with the principal stress trajectories. The picture of principal stress trajectories from such tests is shown in Fig. 4.18d later in this Chapter. Opaque markers were incorporated into the transparent particle assembly to allow simultaneous measurement of displacements and hence could be used to determine the direction and magnitude of strains.

Shear box tests on both sands and clays were reported by Airey (1987), in which problems with apparatus and test procedure were examined in detail. An analysis of the shear box test using finite elements method was also conducted. The results demonstrated that the design of the shear box could have a significant effect on the observed soil behaviour. It was suggested that future shear boxes should have shear couplings that permit vertical movement of the top half of the shear box and the shear load should be applied level with the split between the two halves of the box. It appeared that problems with the apparatus were responsible for the disagreement of the interpretation of the results from direct shear test with other shear tests.

Direct shear tests on sand were reported by Jewell (1989), in which the influence of the boundary conditions on the test measurements was presented. A new analysis method for the direct shear test was introduced on the basis of the relationship between the shearing resistance and dilatancy. The analysis provides an independent check on the conventional analyses and on the consistency of the data from direct shear tests. Comparisons between the tests with the conventional test arrangement (free top platen) and a modified symmetrical test arrangement (fixed top platen) were examined. The results showed that the symmetrical direct shear test is an effective method for the measurement of the plane strain and direct shear angles of friction and the angle of dilation for sand. The deformation was more uniform in the symmetrical test so that the boundary measurements better reflect the behaviour of the soil. Finally, a simple modification for the standard laboratory direct shear apparatus and suggestions for the analysis of standard test data were recommended. The influence of non-uniform deformation and non-coaxiality between the principal axes of stress and incremental strain on the interpretation for the direct shear test results were also discussed.

Shibuya *et al* (1997) developed a new direct shear box apparatus to examine the deformation of sand as quasi-simple shear. Boundary effects, such as the wall friction, the size of the opening between the two halves of the shear box and the constraint imposed by the loading platen, were each independently examined and their influences on the measurements of strength and angle of dilatancy were investigated. The results showed that the conventional measurement of vertical load involves a considerable error in estimating the average normal stress on the horizontal shear plane, owing to the interface friction developed at the vertical face of the specimen. It has also been shown that the loading platen should be prevented from rotating throughout testing, to reduce the occurrence of progressive failure. It was also recommended that the size of opening between the two halves of the box should be maintained at a fixed value of approximately 10-20 times the mean particle diameter of the test material. Below this limit, the measured peak strength increases as the size of the opening between the two halves of the box decreases.

The shear region that forms in a simple direct shear tester has been investigated with the Neutron Depolarisation (ND) technique by Janssen (2001). This technique has proven to be a very powerful tool for the microscopic investigation of a shear region because aspects

like the shape and width of the region can be visualized as well as the rotations of the particles and the local bulk density. The ND experiments showed that the rotation of particles in a shear region is proportional to the applied shear deformation. The ND technique indicated that the shear region is lens shaped and the width increases with the applied normal load. The shear region in a direct shear tester was also simulated by using DEM and the simulation results agreed qualitatively with those from the ND experiments. However, it remained unclear whether the shear region consists of individual shear zones with stagnant regions in between or whether the particles in the region all contribute to the rotation.

Recently, numerical methods have been used to examine details of stress and strain development within a shear box. Potts *et al* (1987) employed finite element methods with a continuum constitutive model for the sand to investigate the direct shear test. The effects of non-uniformities of stress introduced by the rigid ends of the shear box were examined. The soil was modelled using an elasto-plastic constitutive law, and the influences of volume change, initial stress and strain softening were also examined. It was found that the stress-strain behaviour depended on the volume change characteristics and the initial stress. A continuum approach, such as the finite element method, requires a material constitutive model a *priori*. However the behaviour observed in a continuum approach may strongly depend upon the model used. In contrast, in the discrete element method, the required inputs are more fundamental in nature: for example, only the particle-particle contact stiffness and friction coefficient need to be specified.

The effects of the micro-properties of granular material on its shear strength and shear stress-strain behaviour have been investigated using DEM simulations of a standard laboratory direct shear test (Ni *et al*, 2000). Different particle shapes and sizes were used and sample was sheared under a number of different vertical loads. The results of the numerical analysis were then compared with a laboratory test using Leighton Buzzard sand with a similar relative particle size distribution. It was found that the bulk friction angle and dilation of a sample increase as the interparticle friction angle increases. It was also shown that particle rotation plays an important role in the micro-mechanism of deformation in the shear zone. The DEM simulations of direct shear test were reported by Zhang and Thornton (2002). The detailed information about the state of stress and strain within the shear band was obtained from their simulations and the comparisons between

these results with the results traditionally obtained from boundary measurements were made.

Normally the direct shear test employs a cylindrical or rectangular specimen, which is encased in a split box, as shown in Fig. 4.1a. In the test, a normal force, N, acts on the top box in the vertical direction, while a shear force, T, is applied to the top box in the horizontal direction so that the top box moves across the bottom box during the test. The applied forces cause the soil specimen to shear along a thin plane between the top and bottom box. In addition, the normal loads are usually applied via a rigid plate that is free to move vertically as the specimen deforms.

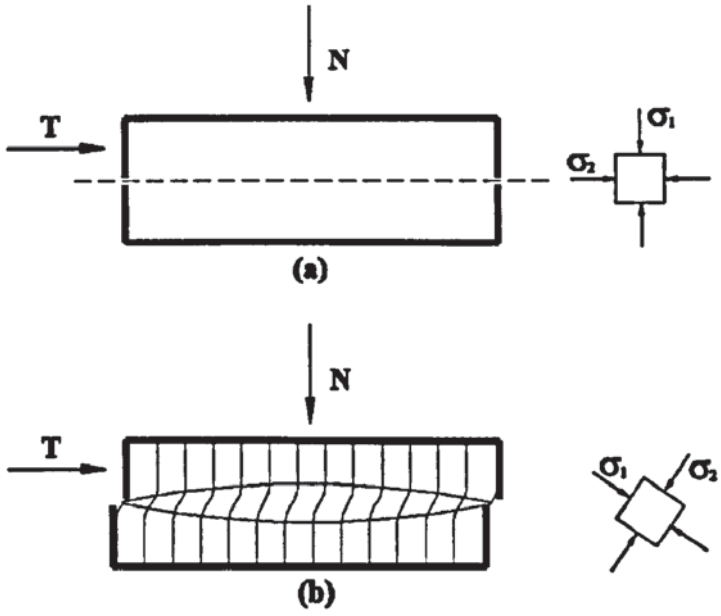

Fig. 4.1 Illustration of the direct shear test: (a) initial state; (b) after shearing

Before any shear load is applied, the state of principal stresses are as shown in Fig. 4.1a. The major principal stress is applied to the top and bottom of the specimen before shearing. Although the distribution of this stress is not uniform, because of the rigidity of the top and bottom of the boxes, it is assumed to be equal to the normal load divided by the area. The minor principal stresses act on the sides of the box, and these are probably not uniformly distributed as well. When the shear load is applied, the major and minor principal stresses rotate, as shown in Fig. 4.1b. Although vanes, pins, and similar irregular materials are introduced at the top and bottom surfaces of the box in an attempt to distribute the shear force uniformly, the actual distribution remains unknown. In a 'conventional' analysis the principal stresses cannot be computed. The deformation in the

direction of the normal or confining load during shear is either uniform outside the shear zone or tilting inside shear zone (see Fig. 4.1b) and can be observed by experimental or numerical approaches. However, the distribution of shearing strains within the soil is extremely nonuniform and highly indeterminate. At the ends of the box the shear strains are concentrated at the shear surface and are the greatest because of the movement of the end walls; in the centre of the box they are more uniformly distributed and are the smallest, as indicated in Fig. 4.1b.

It is assumed that failure is accompanied by the development of a shear band or bands having a certain thickness. Figure 4.2 illustrates the failure mode of specimens subjected to a direct shear test. Because the complementary shear stresses cannot fully develop on the rigid vertical boundaries, stress and strain are not uniformly distributed in the direct shear specimen. In addition, at large strains, a single shear band attempts to form along the horizontal plane at the mid-height of the specimen. These features are often considered as the intrinsic drawbacks, which make the proper interpretation of the direct shear test more difficult.

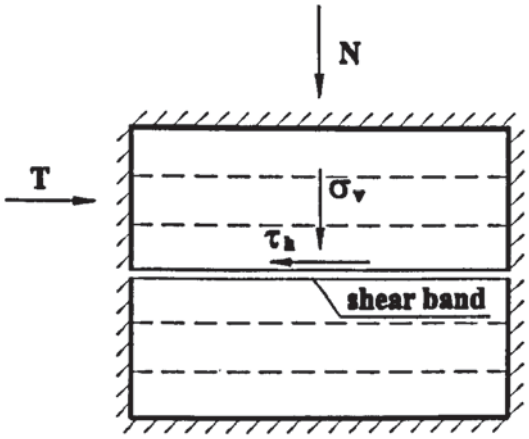

Fig. 4.2 Illustration of a shear band in the direct shear test

In the analysis of a shear box test, it is conventionally assumed that the stress state is uniform throughout the sample, and the ratio of the average shear to normal stress (τ_h/σ_v) is the greatest on the horizontal plane. The plane of maximum stress ratio is called the plane of maximum stress obliquity. Figure 4.3 shows the Mohr stress circle corresponding to the failure plane of Fig. 4.2, in which it is assumed that the plane associated with the major principal strain increment is the same as the plane on which the major principal stress acts, i.e. coaxiality of stress and strain rate direction.

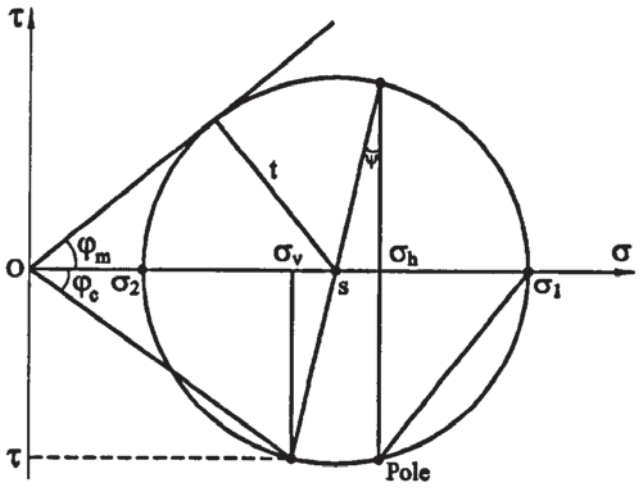

Fig. 4.3 Mohr circle of stress for the direct shear test

From the geometry of the Mohr circle, we have

$$\sin\varphi_m = \frac{t}{s} = \frac{\sigma_1 - \sigma_2}{\sigma_1 + \sigma_2} \tag{4.1}$$

From Fig. 4.3,

$$\tan\varphi_c = \frac{\tau}{\sigma_v} = \frac{t\sin(90° - \psi)}{s - t\cos(90° - \psi)} \tag{4.2}$$

where ψ is the angle of dilation and was defined by (2.11).

Combining (4.1) and (4.2), and noting that $\sin(90° - \psi) = \cos\psi$, $\cos(90° - \psi) = \sin\psi$, the relationship between φ_c and φ_m can be given by the following equation (Davis, 1968),

$$\tan\varphi_c = \frac{s\sin\varphi_m\cos\psi}{s - s\sin\varphi_m\sin\psi} = \frac{\sin\varphi_m\cos\psi}{1 - \sin\varphi_m\sin\psi} \tag{4.3a}$$

or

$$\sin\varphi_m = \frac{\tan\varphi_c}{[\cos\psi(1 + \tan\varphi_c\tan\psi)]} \tag{4.3b}$$

At the critical state, the angle of dilation $\psi = 0$, giving

$$\tan\varphi_c = \sin\varphi_m \tag{4.4}$$

If $\psi = \varphi_m$ then $tan\varphi_c = tan\varphi_m$. For values of ψ between 0 and φ_m, $tan\varphi_c$, which represents the Coulomb definition of shear strength, varies from $sin\varphi_m$ to $tan\varphi_m$.

4.3 Simulation details

The direct shear test model used in the simulation is shown in Fig. 4.4. The shear box consists of two separate halves, a top and a bottom box. The top box *ABCD* consists of walls *AB*, *CD*, *AD* and *BI*. The bottom box *EFGH* consists of walls *EF*, *GH*, *FG* and *CJ*. It is obvious that a reliable result is only obtained when a well-defined boundary condition exists. However, for the conventional shear box test, this is not the case because the upper box often tilts and moves in the vertical direction and causes the sample to be subjected to an equal and opposite couple (Jewell, 1989). This results in a non-uniform distribution of stress on the central plane and difficulty to interpret the result. To avoid the tilting of the top box, the top platen *AD* is firmly connected to the top frame so that the upper box *ABCD* moves as a whole during shear in the simulations. In Fig. 4.4, the dashed lines represent the initial position of the specimen. Both top and bottom boxes can only translate and are not permitted to rotate. The direct shear tests considered here are displacement-controlled tests. The top and bottom box move relative to each other by specifying a constant horizontal velocity in opposite directions to shear the sample across the central plane.

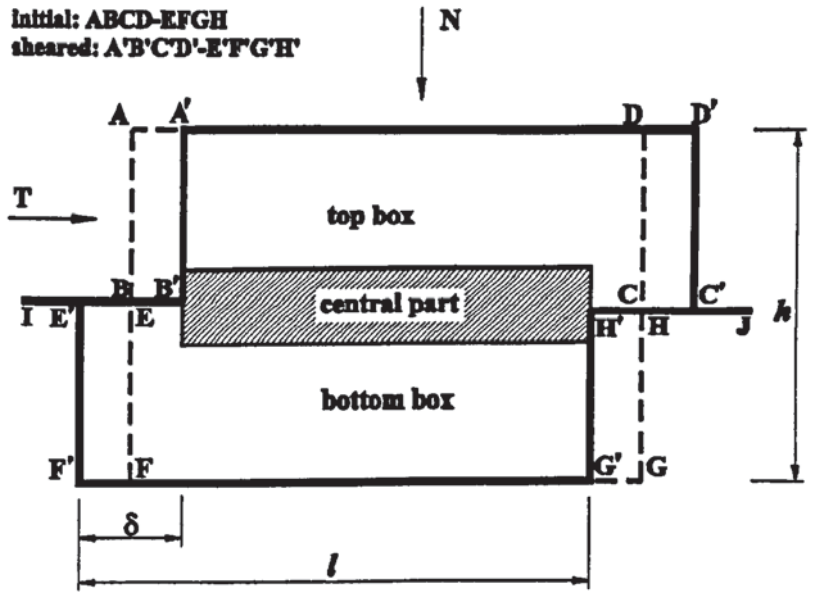

Fig. 4.4 Schematic diagram of the direct shear test

During shearing the walls *BI* and *CJ* are used to prevent particle flow out of the boxes. Because the shear deformation only occurs over a very thin layer at mid-height, a so-called central part where the shear band will deform is defined to investigate the behaviour of granular material (shaded part in Fig. 4.4). It is worth noting that in the simulations the walls do not interact with other walls, only with adjacent particles. The mechanical properties of the walls are assumed to be the same as those of the particles.

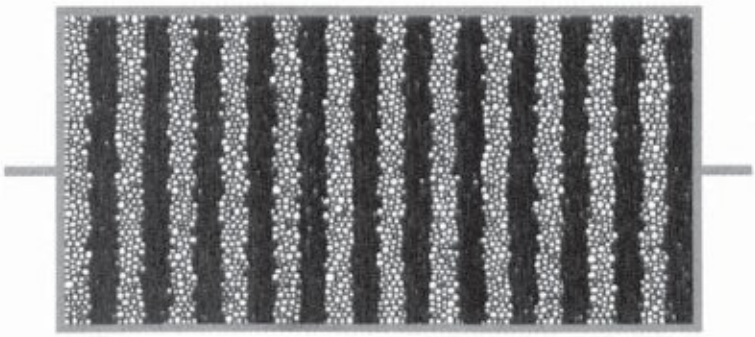

(a) before shearing

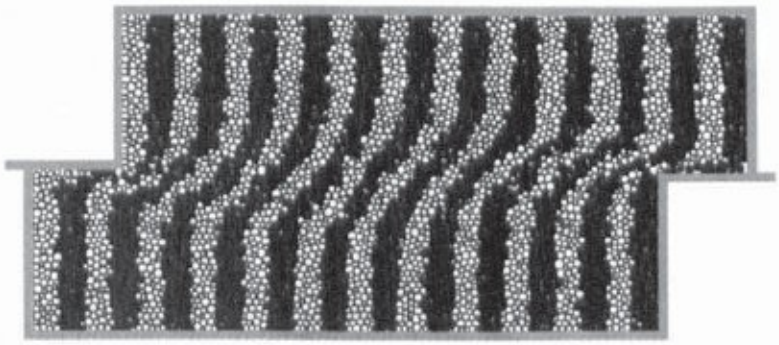

(b) end of shearing

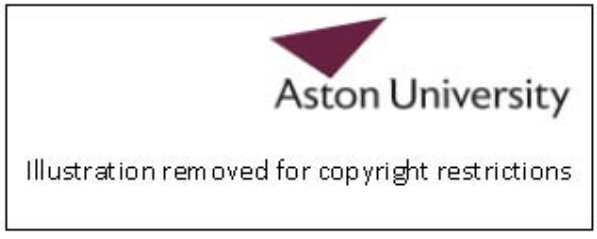

(c) in experiment (By Mr E. Dawson, Vardoulakis and Sulem 1995)

Fig. 4.5 Deformation pattern of specimen in the direct shear test

The particle deformation patterns are shown in Fig. 4.5, in which Fig. 4.5a shows the particle configuration before the test, Fig. 4.5b shows the particle configuration at the end of shearing together with a real experimental result shown in Fig. 4.5c. The particles inside the specimen are coloured-banded before the test (Fig. 4.5a). It can be seen from Fig. 4.5b that, by the end of the test, deformation is localized in a narrow shear zone located at the mid-height of the specimen. The actual shape of the shear zone is lenticular and not like the rectangular one as indicated in Fig. 4.4. The width of the shear band in the centre is wider than that near the edge. Thus, the results to be shown in the following sections, which are based on the central rectangular region, can only provide approximate information of the shear band behaviour. Nevertheless, the deformation pattern at the end of the simulated test is in excellent agreement with the experimental behaviour shown in Fig. 4.5c.

4.3.1 Theoretical aspects

The results of the simulations are analysed in terms of stresses, rather than forces. There are two ways to calculate the stress. One is that the stress tensor is calculated from the distribution of contact forces in the shaded region (shear band) using the equation:

$$\sigma_{ij} = \frac{2}{V}\sum_{l}^{c} P_i x_j \tag{4.5}$$

which is described in Chapter 2.

The other is that the stresses are calculated based on the boundary information. In laboratory experiments, the vertical normal stress σ due to a vertical load N and the shear stress τ due to the horizontal load T acting on the central horizontal plane are obtained by dividing the force N and T, by the cross-sectional area A of the sample respectively. Figure 4.6 shows the forces acting on the top part of the specimen.

The following relationships are satisfied from equilibrium:

$$N = T_1 - T_2 + N_3 \tag{4.6}$$

$$T = N_1 - N_2 + T_3 \tag{4.7}$$

where T_i and N_i (i=1,3) are the total shear forces and normal forces on each wall respectively, and are calculated by the summation of particle-wall contact forces on each wall.

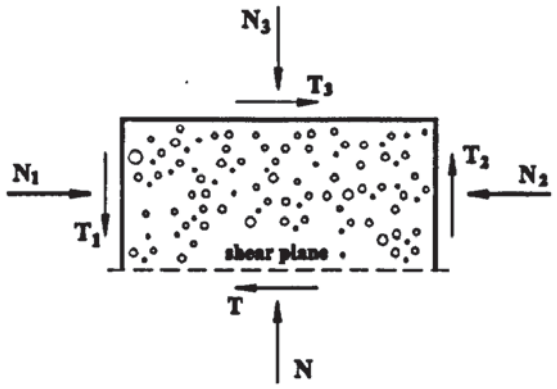

Fig. 4.6 Forces acting on the top part of the specimen

The normal stress σ and the shear stress τ are defined as

$$\tau_h = \frac{T}{A} \tag{4.8}$$

$$\sigma_v = \frac{N}{A} \tag{4.9}$$

and these stresses should satisfy Coulomb's equation, so

$$tan\varphi_c = \frac{\tau_h}{\sigma_v} = \frac{T/A}{N/A} = \frac{T}{N} \tag{4.10}$$

Equation (4.10) indicates that the ratio of horizontal to vertical load is assumed to provide an estimation of the average ratio of shear to normal stress acting in the shear band, and thereby provide a direct measurement of the Coulomb bulk friction.

4.3.2 Deformation monitoring

The deformation of the specimen is constrained by the rigid walls. A quantitative analysis method is introduced to measure the incremental displacement fields and the associated strain fields in the sample, which allows step-by-step mapping of the incremental displacement fields to be displayed. First, the whole sample is divided into $n_x \times n_y$ grids.

The particles that are the nearest to the intersections of these grids are chosen as markers, which are shown as the solid circles in Fig. 4.7.

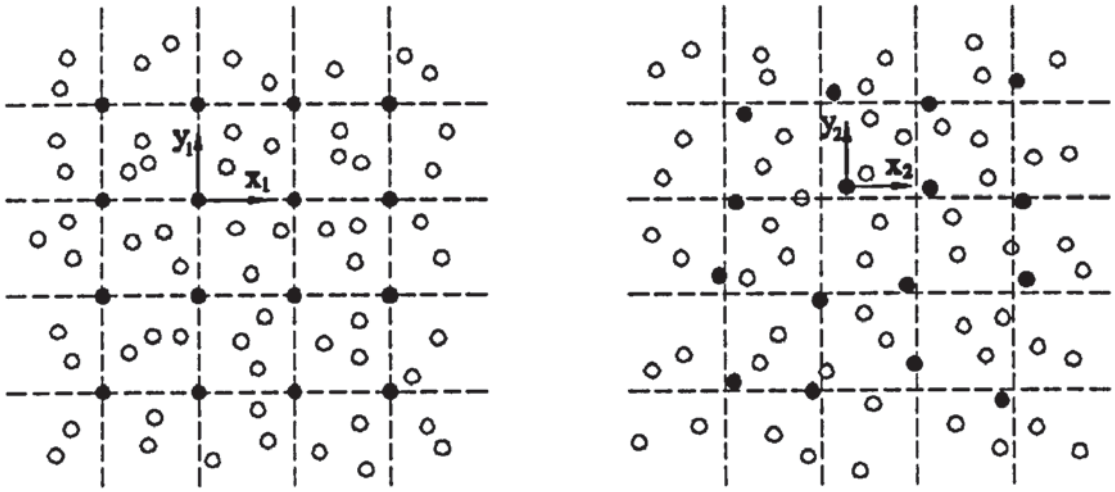

(a) t_1 stage (b) t_2 stage

Fig. 4.7 Illustration of using markers in simulation

If at instant t_1 the coordination of a marker is (x_1, y_1), then the particle moves to a new position (x_2, y_2) at instant t_2, the increment displacement between this two stages are calculated as:

$$\Delta u_x = x_2 - x_1 \tag{4.11}$$

$$\Delta u_y = y_2 - y_1 \tag{4.12}$$

A series of stages are saved to record the specimen deformation during shearing. Therefore, the internal displacements and strains within the specimen can be readily monitored by tracing the movement of the markers inside the specimen. A similar technique has been used in laboratory studies using x-ray tomography and lead shot marker particles are applied in simple shear tests (Stroud, 1971) and biaxial compression tests (Alshibli and Sture, 1999).

4.4 Constant volume (CV) tests

Three boxes of different aspect ratios were used in the present study. One with a height to length ratio (H:L) equal to 1 is a square box (Sample I). Another with a height to length ratio equal to 1/2 (Sample II) is the same as the standard Casagrande shear box. An aspect

ratio of 1/3, as used in the Jenike shear cell, is adopted for sample III, which is the thinnest one. The dimensions of these shear boxes are given in Table. 4.1. The volume and solid fraction are set to be identical for all three samples and the same boundary conditions are applied during the tests.

Table 4.1 Dimensions of three shear boxes

Sample	Aspect ratio	H (mm)	L (mm)
I	1:1	4.07 ($67.8D_{50}$)	4.07 ($67.8D_{50}$)
II	1:2	2.88 ($48.0D_{50}$)	5.75 ($96.0D_{50}$)
III	1:3	2.35 ($39.2D_{50}$)	7.05 ($117.6D_{50}$)

A series of constant volume tests were performed on the three different shear boxes described above. In order to achieve the constant volume condition, the top and bottom platen only move in the horizontal direction and cannot move in the vertical direction.

4.4.1 Effect of aspect ratio

Figure 4.8 presents the simulation results for sample I. Taking advantage of DEM the stress tensor can be calculated separately for the whole sample (W_{part}), the central part (C_{part}) which gives the state of stress inside the shear band, and the part outside the shear band (O_{part}). Fig. 4.8a shows the evolution of $\tan\varphi_c = \tau/\sigma_v$ against the horizontal displacement. It can be seen that, the maximum value of $tan\varphi_c$ within the shear band is about 0.43, which is nearly twice the value obtained for W_{part}, which is over 20% higher than that obtained for O_{part}. For all three sets of calculations, the fluctuations of $tan\varphi_c$ are very similar during the test. This demonstrates that the mobilized Coulomb friction angle φ_c inside the shear band is higher than that outside the shear band. In Fig. 4.8b, the evolution of the stress ratio calculated from the boundary information *T/N* according to (4.5) is shown together with the evolution of $tan\varphi_c$ acting on the horizontal planes in the central part of the assembly. Although the fluctuations of the two curves tend to coincide, the maximum value of force ratio *T/N*, which is measured at the wall boundaries is about 16% higher than the maximum value of $tan\varphi_c$ which is calculated in the central shear zone, a volume averaged value.

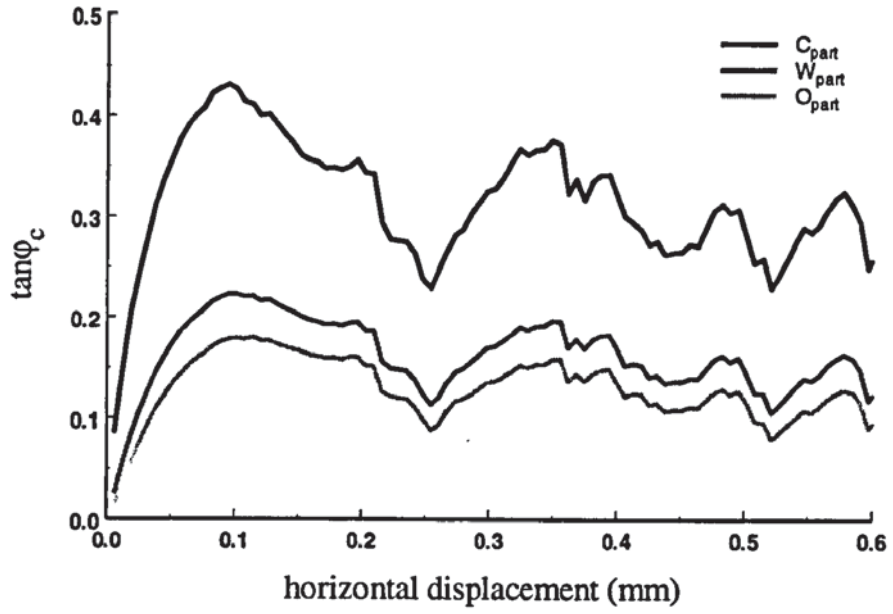

(a)

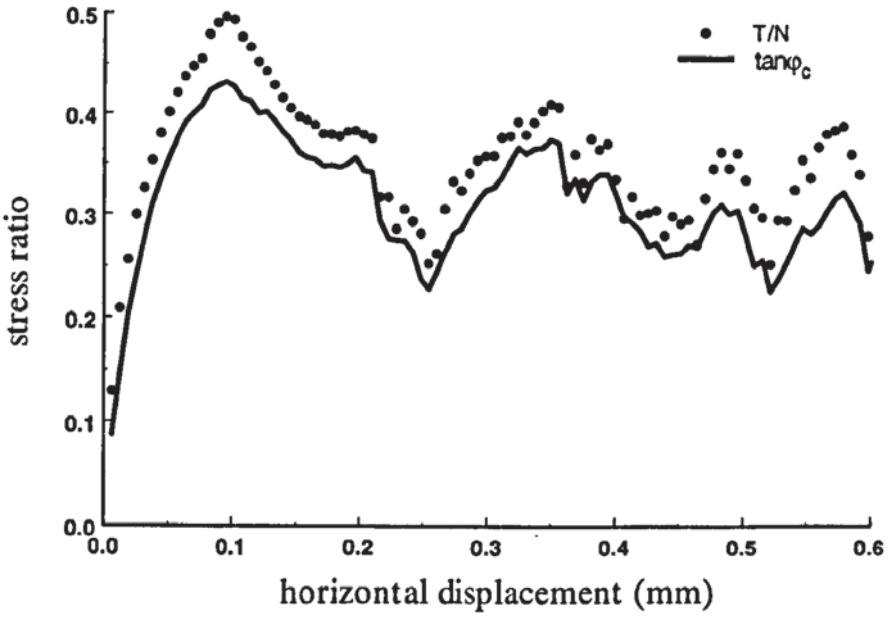

(b)

Fig. 4.8 Test results of sample I: (a) $tan\varphi_c$; (b) comparison of T/N and $tan\varphi_c$

The corresponding results for sample II with aspect ratio 1/2 are shown in Fig. 4.9. It can be seen that, the maximum values of $tan\varphi_c$ occurs at a horizontal displacement of ca. 0.1mm. The maximum value inside the shear zone is very close to the result obtained from sample I and it is almost 50% higher than that outside the shear zone (Fig. 4.9a). The stress ratio outside the shear zone is closer to that inside the central shear zone for sample II than for sample I. The maximum value of the force ratio of *T/N* is ca. 14% higher than

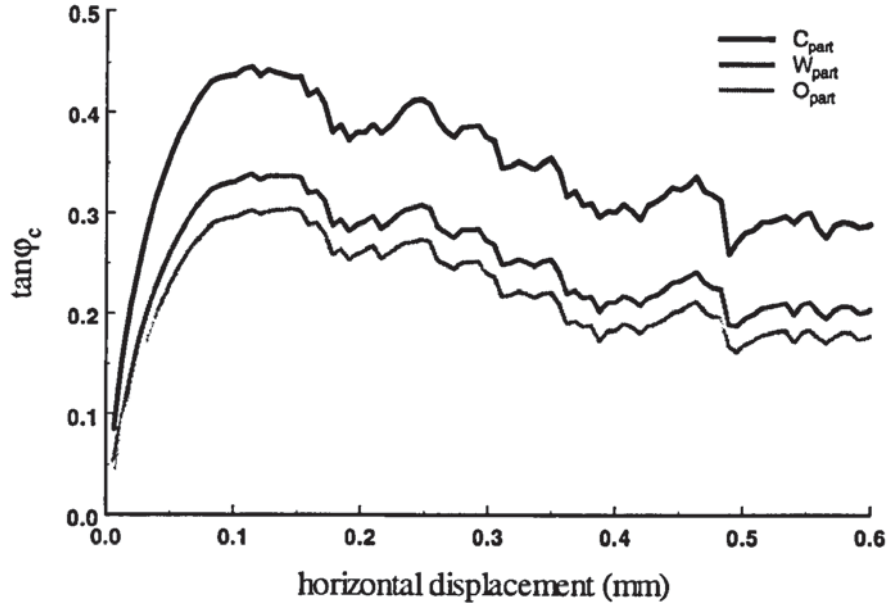

(a)

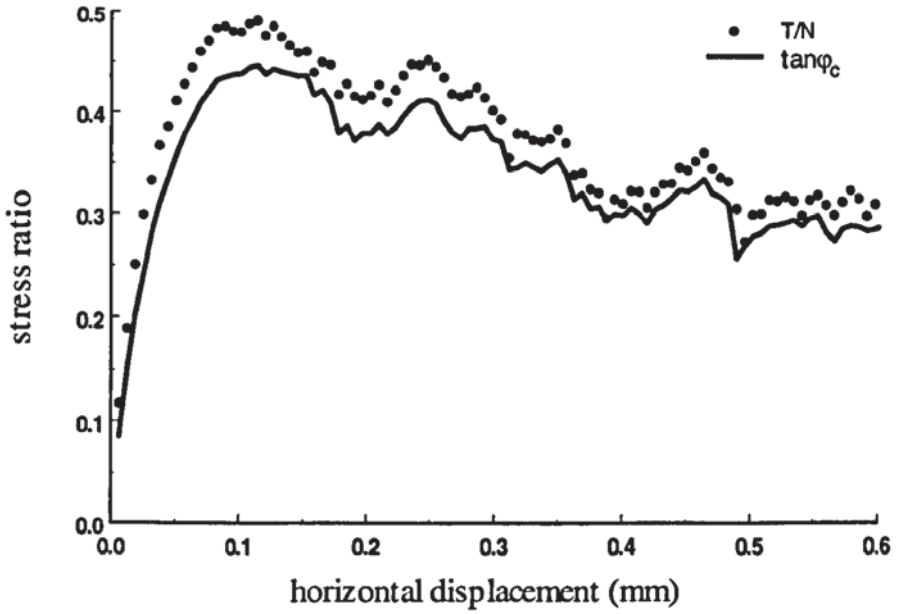

(b)

Fig. 4.9 Test results of sample II: (a) $tan\varphi_c$; (b) comparison of T/N and $tan\varphi_c$

that of $tan\varphi_c$ in the shear band as shown in Fig. 4.9b.

Figure 4.10 shows the results for sample III. Although the maximum value of $tan\varphi_c$ of C_{part} is similar to the values obtained for the other two thicker samples, the stress ratio calculated for W_{part} and O_{part} are found to be much closer to that of C_{part}. This implies that

the thinner the box used, the closer the value between the W_{part} and the C_{part}. The force ratios obtained from boundary measurements and the stress ratios calculated in the shear zone are compared in Fig. 4.10b. It can be seen that the peak value of *T/N* is just 7% greater than that of $tan\varphi_c$. When comparing *T/N* with $tan\varphi_c$ in the shear zone it was found, for all aspect ratios considered, that the wall measurements are always higher than the volume averaged values. However, as the aspect ratio is reduced the difference between the boundary measurements and the shear zone calculations become closer.

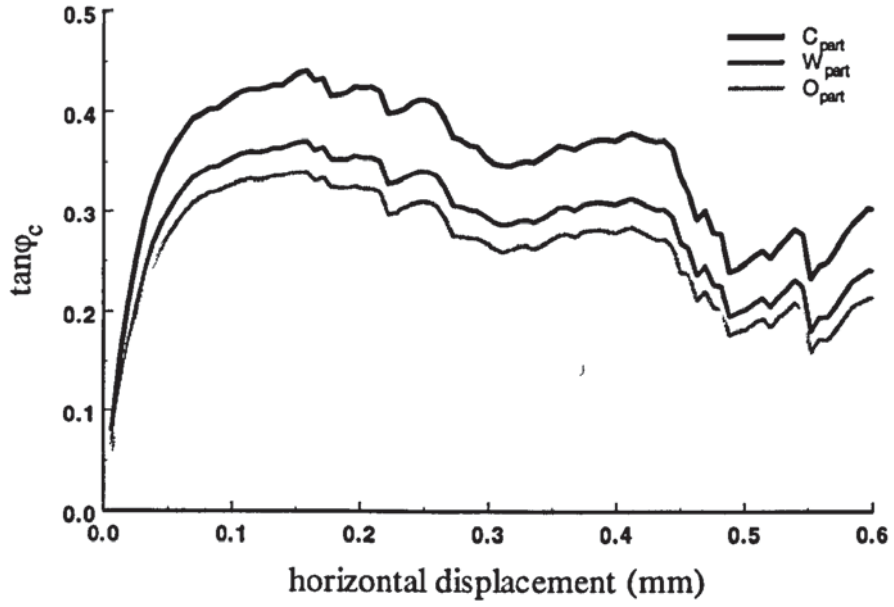

(a)

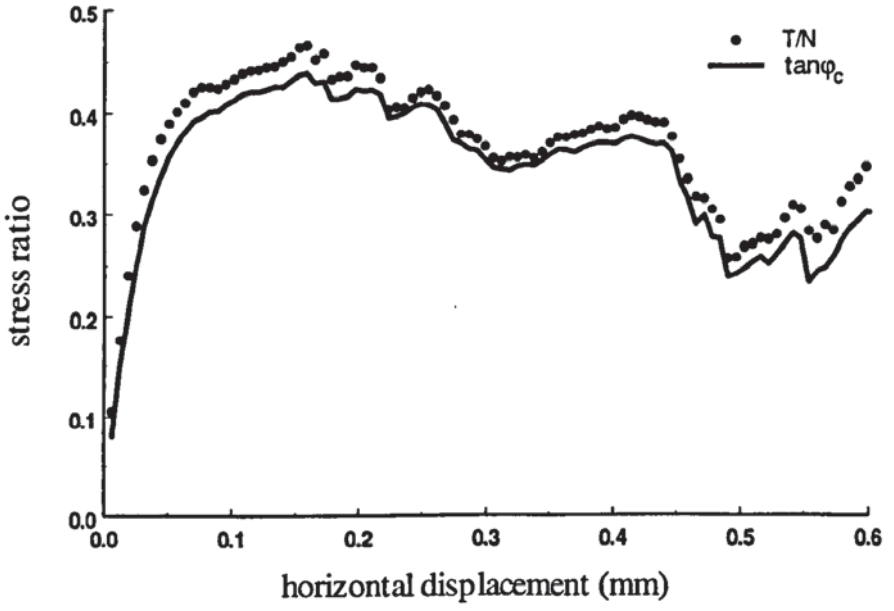

(b)

Fig. 4.10 Test results of sample III: (a) $tan\varphi_c$; (b) comparison of T/N and $tan\varphi_c$

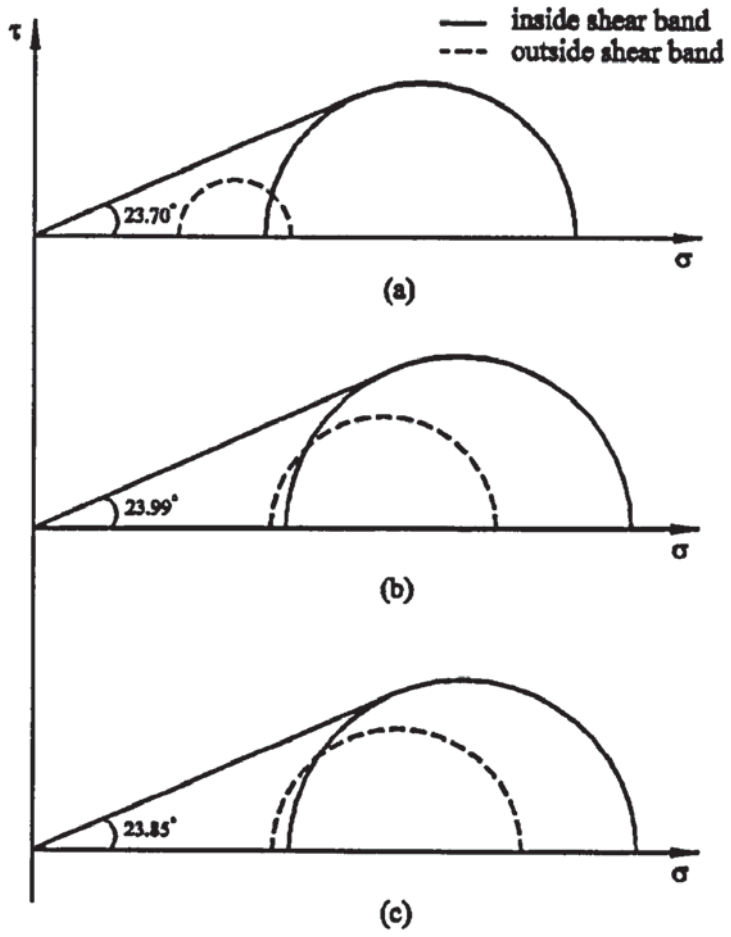

Fig. 4.11 Mohr stress circles inside the shear band and outside the shear band at peak stress ratio: (a) 1:1; (b) 1:2; (c) 1:3

The Mohr stress circles for each sample at peak stress ratio are drawn in Fig. 4.11 for both inside (solid semi-circle) and outside (dashed semi-circle) the shear band. The figure clearly shows that the mobilized angles of internal shear resistance (φ_m) are more or less the same for all three cases when the calculation is based on the information inside the shear band in spite of the different aspect ratios. The figure also shows that, as the aspect ratio is reduced, the state of stress outside the shear band becomes closer to that inside the shear band.

The evolutions of $tan\varphi_c$ obtained from the shear band and *T/N* for all three samples are compared in Fig. 4.12. By comparing Figs. 4.8-4.11, it was noted that the maximum values of $tan\varphi_c$ inside shear band for all three cases are essentially identical, which is also confirmed by Fig. 4.12a. It is found from Fig. 4.12b that the maximum values of *T/N* are 0.5, 0.49 and 0.47 for three samples respectively and they are all greater than the stress

ratios obtained from the shear band. It can be seen in Fig. 4.12 that there are occasionally very large fluctuations in both $tan\varphi_c$ and *T/N* during post-peak deformation. It is not clear why these occurred but it may be due to the contribution of a relatively small number of particles, 2D constraints on particle motion and the overall constant volume constraint. Allowing for the fluctuations, the average values of $tan\varphi_c$ and *T/N* at large displacements are similar for all aspect ratios.

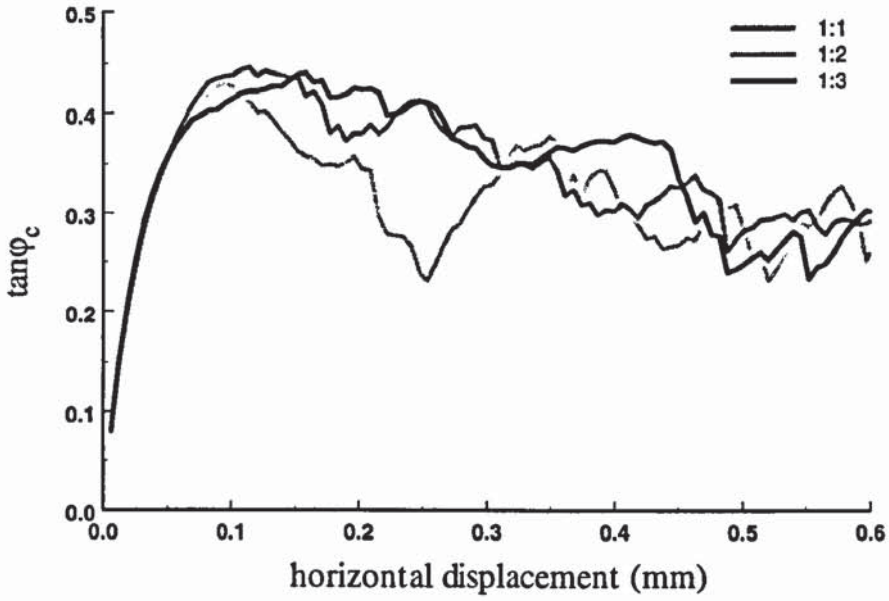

(a) $tan\varphi_c$

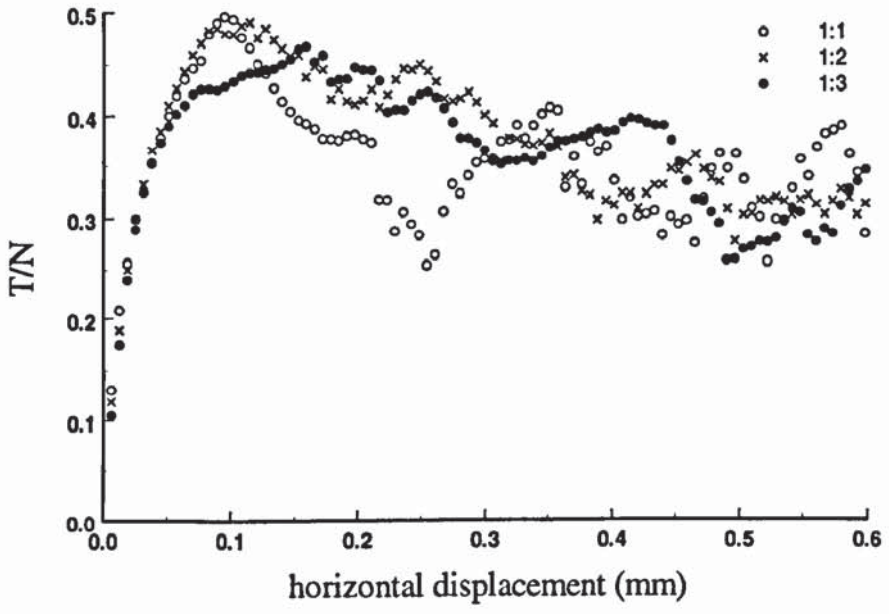

(b) T/N

Fig. 4.12 Evolution of $tan\varphi_c$ and *T/N* for different aspect ratios

4.4.2 Dilation in the shear zone

Figure 4.13 shows that, during deformation, the porosity changes inside the shear band for all three constant volume tests. Although the overall volume of the specimen is kept constant, dilation occurs inside the shear band, as indicated by the increasing porosity in the central region. The shear box with aspect ratio 1:1 exhibits the highest dilation inside the shear band. Figure 4.13 demonstrates that it is not possible to conduct a true constant volume test in the direct shear apparatus if one wishes to examine the shear behaviour of material in the shear zone.

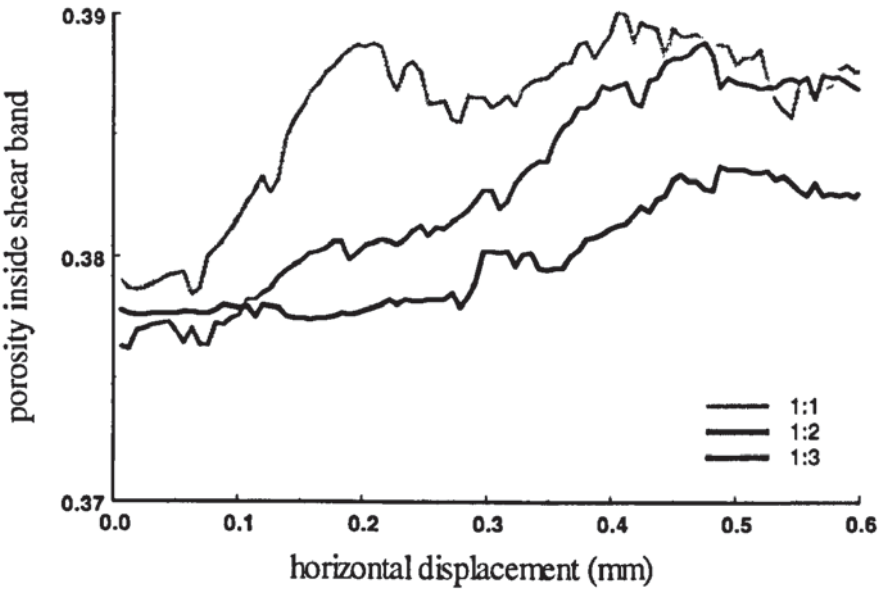

Fig. 4.13 Porosity inside shear band

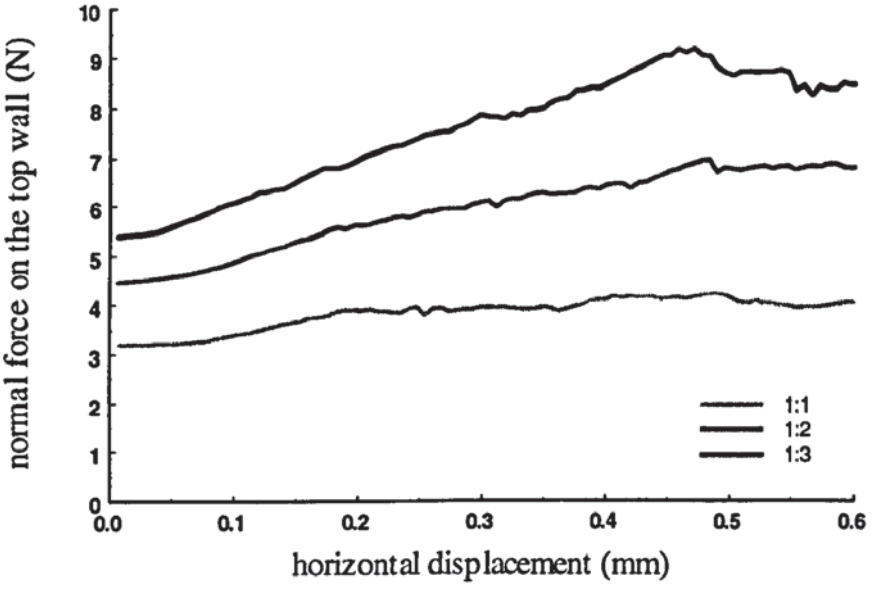

Fig. 4.14 Normal force on the top wall

The evolution of the normal force on the top wall is shown in Fig. 4.14. Since these tests are carried out under constant volume condition it can be seen that the normal force on the top boundary increases during shearing. It seems that the higher expansion inside shear band correlates with the lower normal force on the top boundary. The influence of this factor will be further investigated in constant normal stress test simulations later in this chapter.

4.4.3 Effect of wall friction

The influence of the boundary friction at particle-wall contacts was investigated using the shear box of aspect ratio 1:2. An additional constant volume test was performed with the friction parameter μ_w set to 0.1. Figure 4.15a shows the normal force on each wall during shearing of this sample with $\mu_w = 0.1$. The normal forces on the walls *AB* and *HG*, which are the walls pushing the sample to move in opposite directions, have very similar magnitudes, and increase until ca. 0.2mm horizontal displacement. They then remain approximately constant thereafter. The magnitudes of the normal forces on walls *EF* and *DC* are also similar but decrease to a minimum value at ca. 0.2mm and then remain fairly constant during continued shearing. The normal forces on the walls that push the sample are greater than the normal forces on the walls that are pushed. The magnitude of normal forces on the top and bottom walls are also very similar and increase due to the fact that the walls cannot move in the vertical direction. The tangential forces on each wall are shown in Fig. 4.15b. Before reaching 0.2mm horizontal displacement, the tangential forces on the top walls *HG* and *DC* are of similar magnitude but opposite sign to the bottom walls *AB* and *EF* respectively. During this period the ratio of the tangential to normal force on the top and bottom walls remains close to the value of $\mu_w = 0.1$ indicating that most of the contacts with these two walls are sliding. After 0.2mm displacement, the tangential forces fluctuate and change sign. At large displacements all the tangential forces are small.

The corresponding evolutions of normal and tangential forces on each wall are shown in Fig. 4.16 for μ_w set to 0.5. For each wall the magnitude of the normal force is similar to the values, obtained for $\mu_w = 0.1$. However the maximum value of the tangential force on the top and bottom walls is three times larger than that for $\mu_w = 0.1$. The peak values of

tangential force on the top and bottom walls occur at 0.15mm horizontal displacement when the ratio of tangential to normal force is ca. 0.24, which is significantly less than $\mu_w = 0.5$. This implies that friction is not fully mobilized along the top and bottom walls.

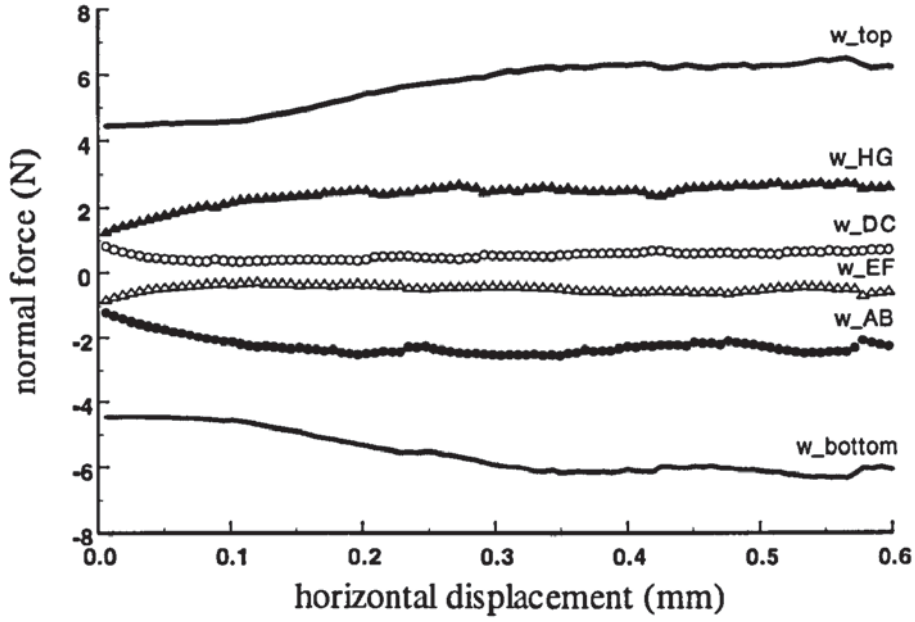

(a) normal force

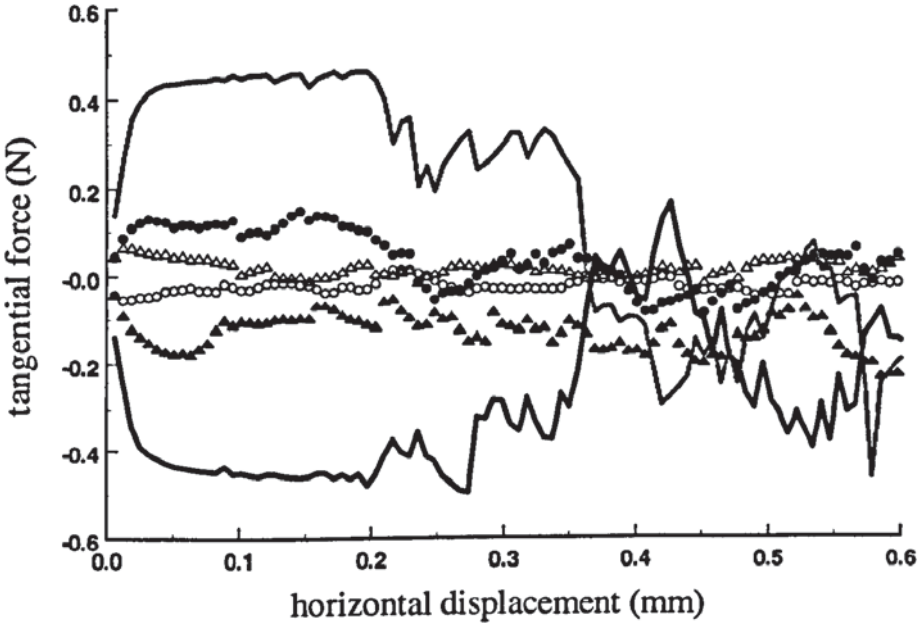

(b) tangential force

Fig. 4.15 Evolution of forces on the walls of sample with $\mu_w = 0.1$

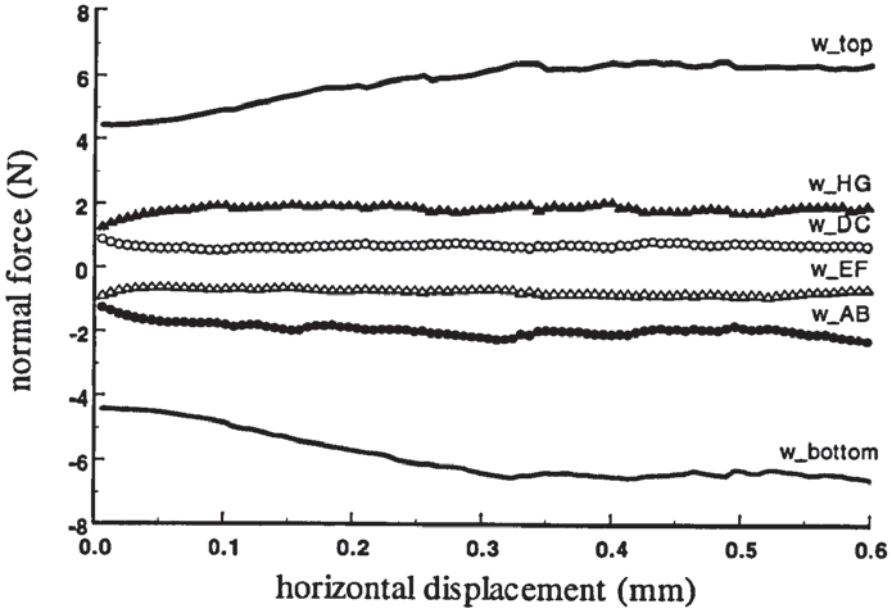

(a) normal force

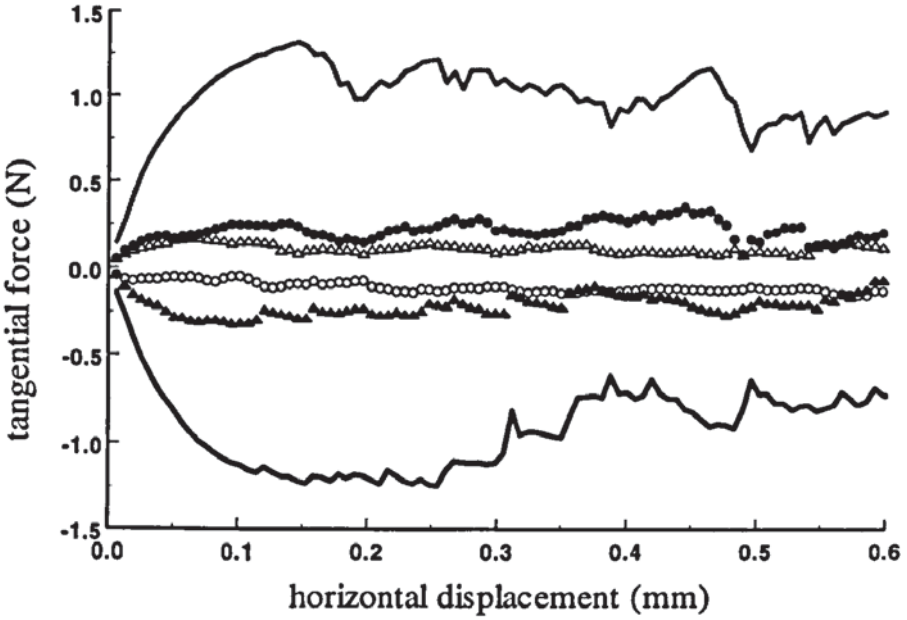

(b) tangential force

Fig. 4.16 Evolution of forces on the walls of sample with $\mu_w = 0.5$

The evolutions of $tan\varphi_c$ for these two tests are presented in Fig. 4.17a. The maximum values of $tan\varphi_c$ are nearly the same although the wall particle friction is different. Figure 4.17b shows the evolution of the force ratio *T/N* for these two cases. The maximum values and the values at the critical state are very similar. This implies that the boundary friction does not significantly affect the shear behaviour of the specimens.

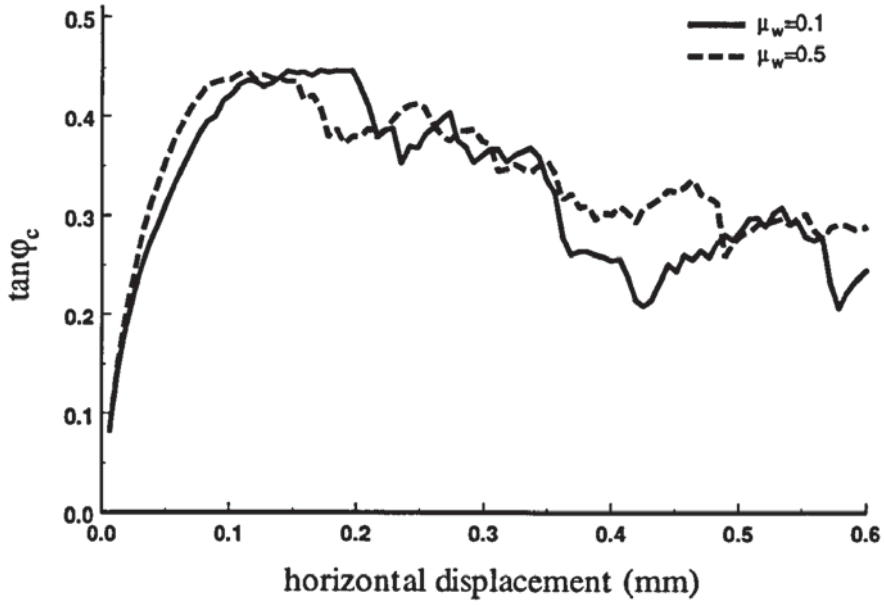

(a)

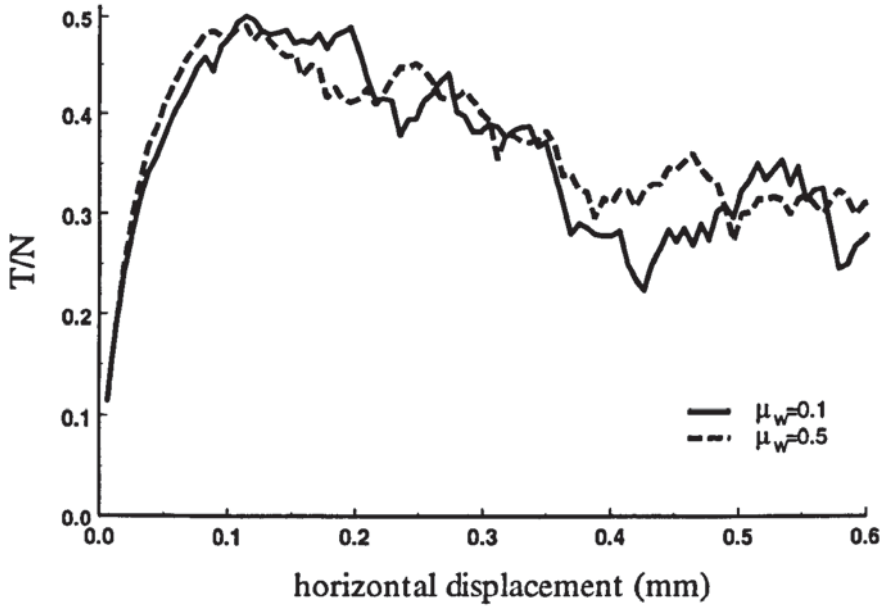

(b)

Fig. 4.17 Effect of wall friction on: (a) τ/σ ; (b) *T/N*

4.5 Constant normal stress (CN) tests

In the second series of tests the top and bottom platens are displaced in the horizontal direction but are also permitted to move in the vertical direction. Initially, tests were simulated by adjusting the vertical position of the top and bottom walls to keep the vertical

normal force N_3 constant (see Fig. 4.6). However, this did not work because the vertical tangential forces T_1 and T_2 cannot be controlled satisfactorily by moving the top wall. Ideally, one would wish to maintain constant the normal stress σ_v, acting on the shear band but this also proved to be not possible. In the tests reported here, the stress tensor for the complete specimen is calculated using (4.5) and the top and bottom walls are continuously adjusted to maintain the average vertical normal stress σ_v, for the complete specimen at a constant value. To achieve this, at each time step, the vertical velocity of the top wall is set to,

$$v^s = g(\sigma_v^d - \sigma_v^c) \tag{4.13a}$$

where σ_v^d is the desired vertical normal stress to be achieved, σ_v^c is the calculated vertical normal stress for the whole specimen and g is the gain parameter and set to 0.001. If v^s is greater than a specified maximum admissible velocity v_{max}, then

$$v^s = sign(v_{max}, g(\sigma_v^d - \sigma_v^c)) \tag{4.13b}$$

In the simulations v_{max} was set to $8.0\times10^{-6}\,ms^{-1}$. Three direct shear tests were simulated in which the average vertical normal stress for the complete specimen was maintained constant at 10MPa, 15MPa and 20MPa, respectively.

4.5.1 Force transmission

Homogeneous stress and deformation are key pre-requisites for experiments in which boundary measurements are used to deduce the material behaviour. The force transmissions through the system of particles, before shearing, at peak stress ratio and at the end of shearing, are illustrated in Fig. 4.18. Each line is drawn between the centres of two particles in contact with each other. The larger than average contact forces are indicated by black lines, and grey lines indicate less than average contact forces. The magnitude of each force is indicated by the thickness of the line, scaled to the current maximum contact force. It is clear that the force distribution before shearing is isotropic inside the sample (Fig. 4.18a). It can be seen from Fig. 4.18b that, at peak stress ratio, there are significantly large contact forces acting on the left-top end wall *A'B'* and right-bottom end wall *H'G'*. On the top and bottom walls, the large forces concentrate to the side near the end-walls, which push the sample. At the other side of the top and bottom

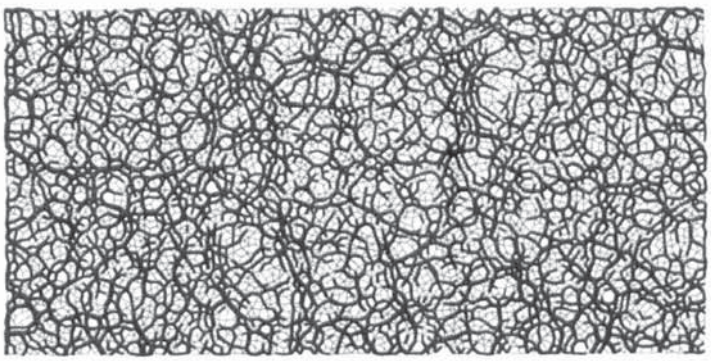

(a) before shearing

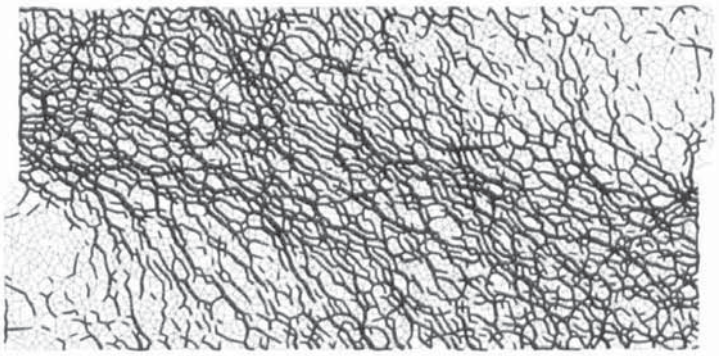

(b) at maximum stress ratio

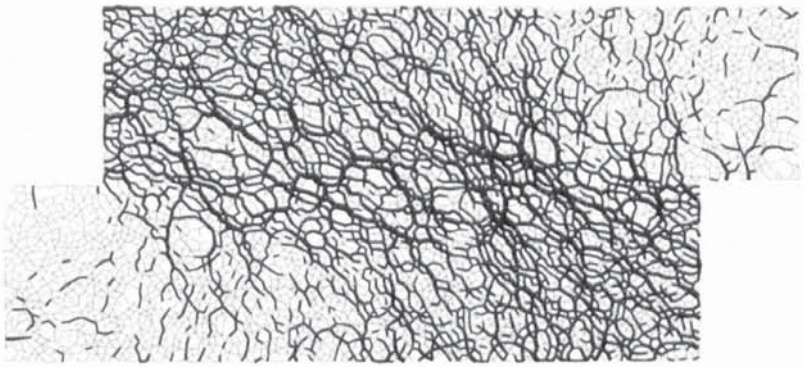

(c) at large horizontal displacement

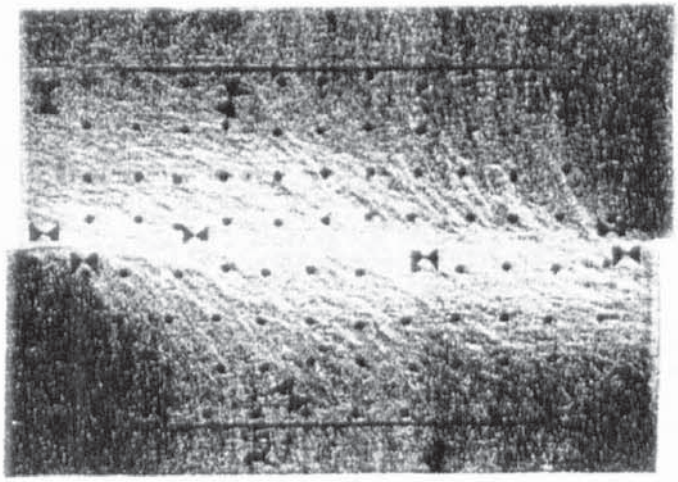

(d) Dyer and Milligan (1984)

Fig. 4.18 Force transmission patterns

walls the forces are relatively small. It is clear that the normal stress distribution along the top and bottom walls is not uniform. Only small forces are transmitted to the other two vertical end walls *E'F'*, *D'C'*. Consequently, the strong force transmission pathways are inclined as they pass through the shear zone at the mid-height of the specimen. The overall pattern shown in Fig. 4.18b clearly indicates a very heterogeneous distribution of stress. Figure 4.18c shows the force transmission diagram at large horizontal displacement. The force transmission pattern correlates well with photo-elastic observations for crushed glass reported by Dyer and Milligan (1984), see Fig. 4.18d, in which the light stripes coincide with principal stress trajectories.

4.5.2 Mobilized strength and apparent dilatancy

The evolution of the ratio of the shear stress to the normal stress (τ/σ) acting in the shear band is shown in Fig. 4.19 for the three tests carried out. It can be seen that the mobilised stress ratios are similar for all three cases with slightly decreasing maximum values of 0.46 (10MPa), 0.45 (15MPa) and 0.44 (20MPa). However, it is also clear that the peak stress ratio appears earlier when a lower stress level is applied. Although the pre-peak curves are divergent, which is merely due to the different vertical normal stress values, the initial shear moduli are in fact identical for all three tests. Nevertheless, when the horizontal displacement exceeds a certain value (say 0.45mm), all three tests indicate a value of ca. 0.3 at the critical state regardless of the stress level.

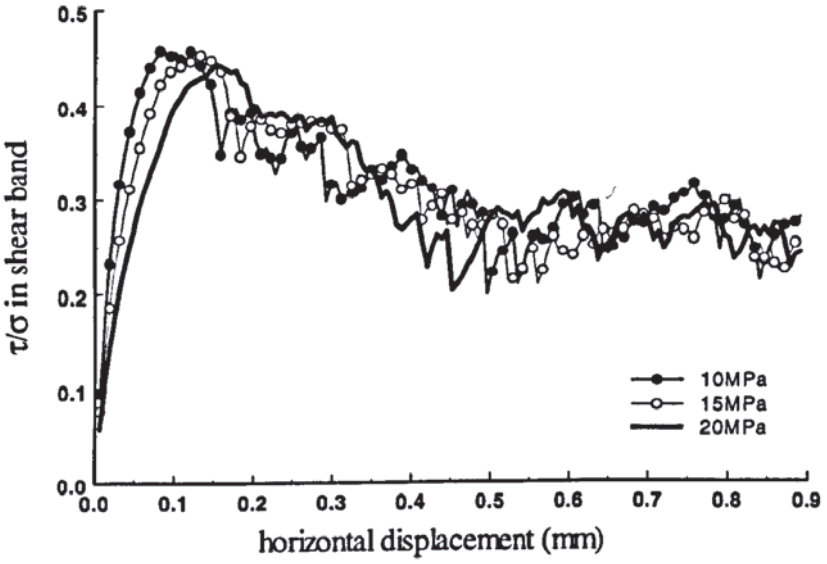

Fig. 4.19 Mobilised stress ratio τ/σ inside shear band

Figure 4.20 shows the vertical displacement (Δy), which is calculated from the change in the height of the specimen, plotted against the horizontal displacement. It can be seen that, as expected for dense granular media, volumetric expansion occurs during shear. It is also clear that, for the test with an applied stress level at 20MPa, the sample undergoes contractive behaviour at the beginning of the test, followed by dilation. When a lower stress level is applied (10MPa) expansion of the sample takes place from the very beginning of the test. Less significant dilation occurs at higher stress levels. In all three simulations, the small changes in the vertical direction after 0.6mm horizontal displacement indicate that the specimens are deforming at approximately constant volume.

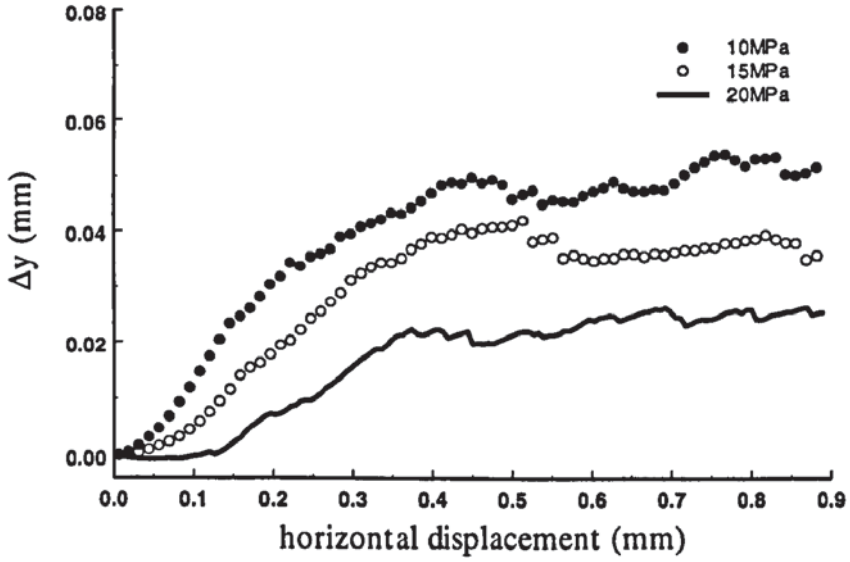

Fig. 4.20 Vertical displacement during the tests

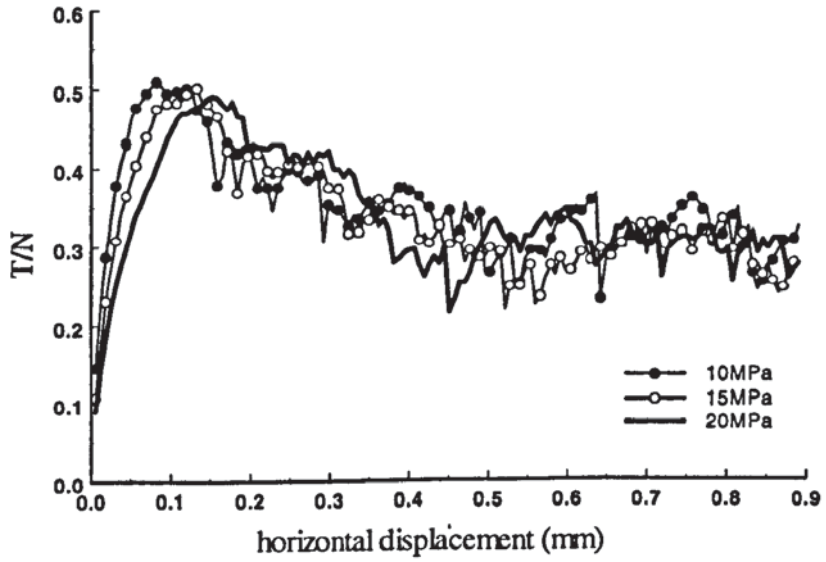

Fig. 4.21 Evolution of *T/N* with displacement

The corresponding evolution of the force ratio (*T/N*) is shown in Fig. 4.21. The results shown in the figure are qualitatively very similar to the results shown in Fig. 4.19. At critical state both figures indicate a stress ratio of ca. 0.3 but the maximum values of *T/N* are 0.53 (10MPa), 0.49 (15MPa) and 0.47 (20MPa) respectively, which are higher than the maximum values of τ/σ as shown in Fig. 4.19. It is not possible to say what corresponding values of *T/N* would be obtained in a laboratory experiment since this depends very much on the details of the equipment design (Jewell 1989).

4.5.3 Dilation in the shear zone

The evolution of porosity is illustrated in Fig. 4.22, in which both the evolution of the porosity of the complete specimen, as measured from the vertical displacements of the top and bottom walls, and the porosity changes that occurred in the central region used to approximate the shear band are shown. It is clear that the dilation is reduced by the increasing normal stress level. Furthermore, the specimens are deforming at constant volume at the critical state. Although significant fluctuations occur in the values of the calculated porosity in the shear band the rate of dilation and the final voidage in the shear band exceeds that indicated by the wall movements. This demonstrates that the dilation angle measured from the boundary displacement is not a reliable indicator of actual

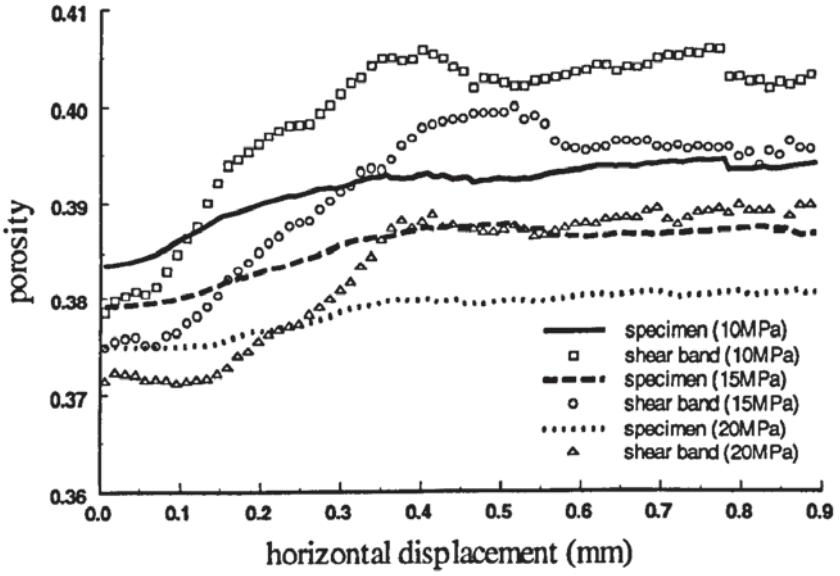

Fig. 4.22 Evolution of porosity of overall specimen and inside shear band

dilatancy inside the shear zone. It may be noted that there is an initial difference between the calculations based on the central region and the complete specimen. This is due to boundary effects on the complete specimen calculations. The difference would be significantly reduced if more (orders of magnitude) particles had been simulated.

4.5.4 Evolution of normal stresses

Figure 4.23 shows the evolution of the vertical and horizontal normal stresses (σ_v, σ_h) acting in the central part of the specimen, which approximates to the shear band, for the three cases. Although the average vertical normal stress over the complete specimen is controlled to remain constant, it can be seen that the vertical normal stress in the shear band gradually increases by about ten percent during the simulations. As the relative displacement between the upper and lower parts of the specimen increases, the horizontal normal stress in the shear band increases until the stress ratio τ/σ reach its maximum (see Fig. 4.19). At this stage the horizontal normal stress is greater than the vertical normal stress, which reflects the fact that the strong force chains shown in Fig. 4.18 are inclined at an angle less than 45° to the horizontal. After peak stress ratio the horizontal normal stress decreases and, significantly, becomes approximately equal to the vertical normal stress when the critical state is attained. The consequence of this condition will be discussed in the next section.

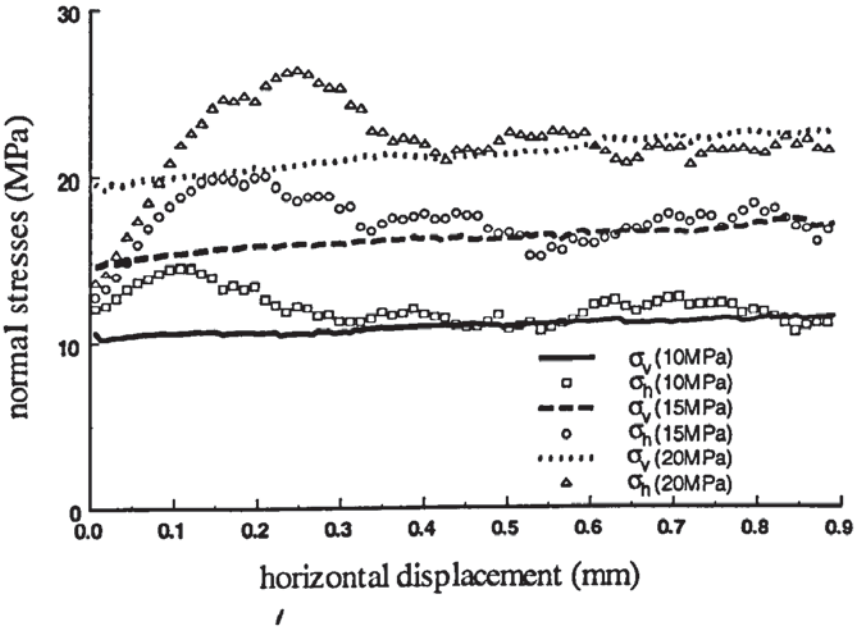

Fig. 4.23 Evolution of normal stresses in the shear band

4.5.5 Stress conditions at the critical state

Since the vertical and horizontal normal stresses in the shear band are equal, $\sigma_h = \sigma_v = \sigma_n$ defines the centre of the Mohr circle at critical state and the radius is equal to τ. As illustrated in Fig. 4.24, the stress combination (τ, σ_n) is given by point *P*, which is also the pole of the circle since the plane on which this stress combination acts is horizontal (Schofield and Wroth, 1968). This demonstrates that the principal stresses at the critical state are inclined at ±45° to the horizontal. At critical state, the shear deformation in the shear band occurs under constant volume conditions as shown in Fig. 4.22 and, therefore, the directions of the principal strain rates are also inclined at ±45° to the horizontal. Consequently, the directions of principal stress and strain rate are coaxial at the critical state. It can also be seen from Fig. 4.24 that the Coulomb friction angle φ_c is less than the angle of shearing resistance φ_m defined by Mohr's criterion.

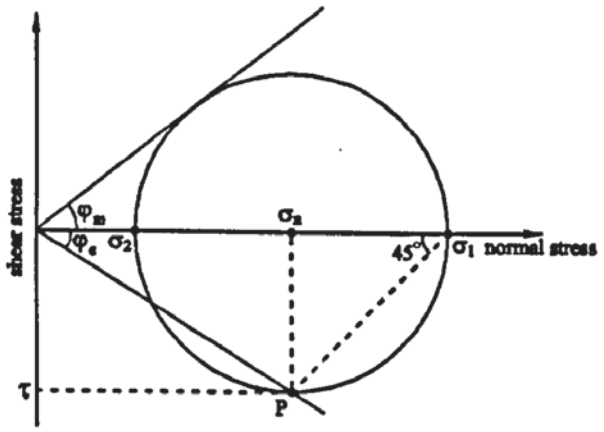

Fig. 4.24 Stress condition inside shear band at critical state

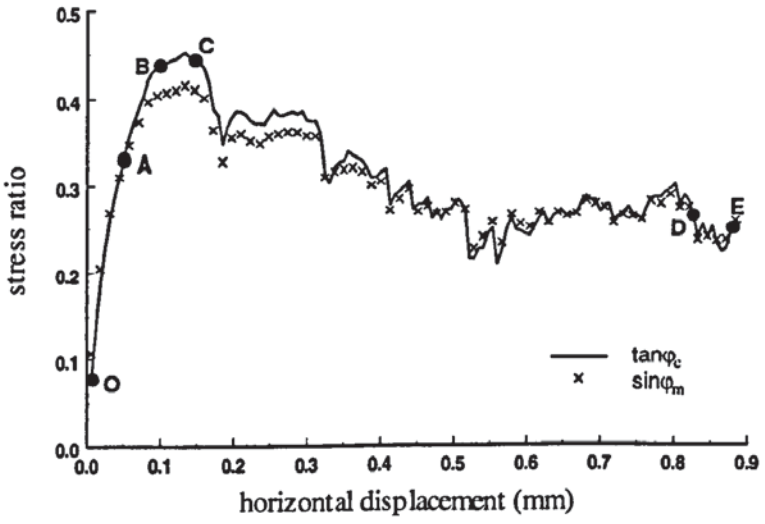

Fig. 4.25 Evolution of $tan\varphi_c$ and $sin\varphi_m$

From the geometry of the diagram, $tan\varphi_c = sin\varphi_m$ and this is also demonstrated by Fig. 4.25, in which the evolution of $tan\varphi_c$ and $sin\varphi_m$ are compared. The difference between the Coulomb friction angle (φ_c) measured from experiments and the Mohr friction angle (φ_m) at the critical state based on the simulations are shown in Fig. 4.26. It is clear that the difference becomes more and more significant as φ_c increases.

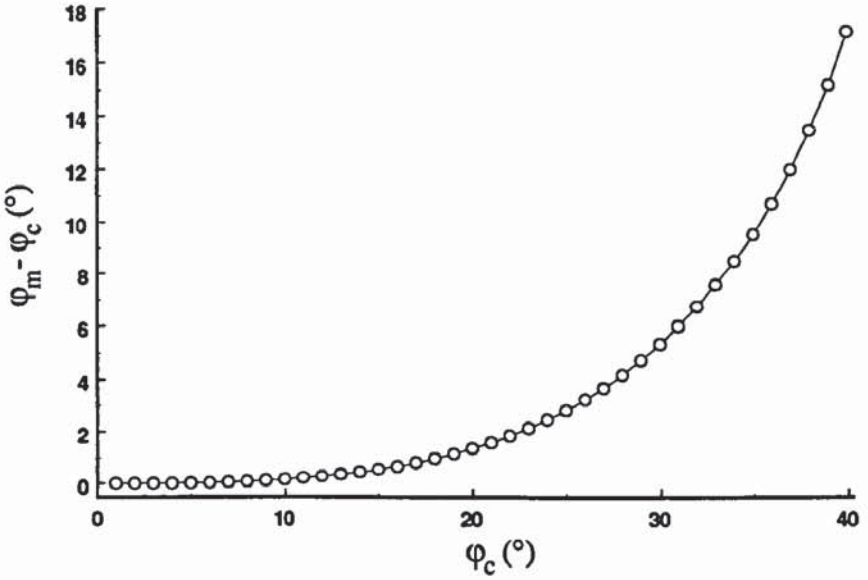

Fig. 4.26 The relationship between φ_m and φ_c

In the direct shear test, the problem is that experimentalists attempt to measure the shear and normal stresses acting on the failure plane (shear band), which satisfies Coulomb's criterion. Unfortunately, the location of the corresponding Mohr circle of stress is not known since the horizontal normal stress (σ_h) in the shear band cannot be measured directly. Consequently, the magnitude and directions of the principal stresses are unknown. However, in DEM simulations all components of the stress tensor can be calculated for any specified volume as mentioned before. It has been shown in Fig. 4.24 that σ_n is the centre of the Mohr circle. In Fig. 4.27 the small dark semi-circle is drawn based on calculations from the simulations. However, in the Standard Shear Testing procedures using the Jenike shear cell (1989) the sample is sheared in two steps. In the first, the sample is 'presheared' under a constant normal stress σ until steady flow is established and τ = *constant*. It is normal practice to assume that the measured values of σ and τ define a point on the 'effective yield locus', as shown in Fig. 4.27.

From the experimental data the location of the corresponding Mohr circle of stress is not known. It is conventionally assumed that the 'effective yield locus' is the same as the Mohr-Coulomb line traditionally used in soil mechanics thereby implying that, in the Mohr criterion (4.1) and Coulomb criterion (4.2), $\varphi_c = \varphi_m$. Consequently, the Mohr circle is drawn tangent to the effective yield locus, as illustrated by the grey semi-circle shown in Fig. 4.27, with the 'major consolidation stress' $\sigma_1 = \sigma_1^M$. However, the DEM results show that the actual Mohr circle is the dark semi-circle in Fig. 4.27 and the 'major consolidation stress' $\sigma_1 = \sigma_1^C$. From Fig. 4.27 the relationship between the major principal stresses based on the simulation calculation (σ_1^C) and deduced from experiment measurement (σ_1^M) can be determined as follows.

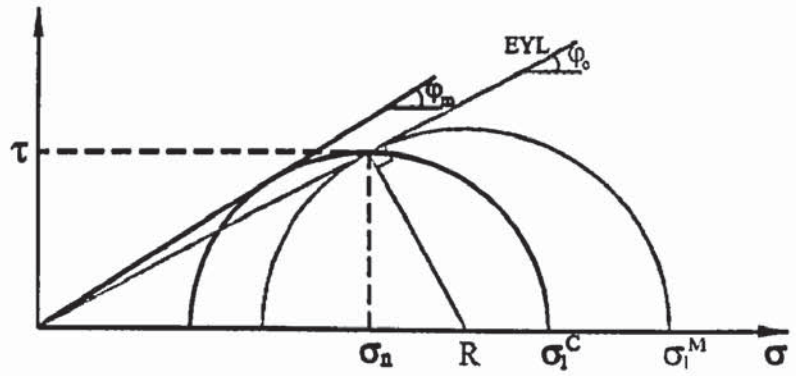

Fig. 4.27 Mohr circles based on different measurements

From the geometry of the dark circle,

$$\sigma_1^C = \sigma_n + \tau \tag{4.14}$$

$$tan\varphi_c = \frac{\tau}{\sigma_n} \tag{4.15}$$

Using (4.14) and (4.15),

$$\frac{\sigma_1^C}{\sigma_n} = 1 + \frac{\tau}{\sigma_n} = 1 + tan\varphi_c \tag{4.16}$$

From the geometry of the grey circle,

$$\sigma_1^M = R + R\,sin\varphi_c = R(1 + sin\varphi_c) \tag{4.17}$$

and $R = \sigma_n + \tau\,tan\varphi_c$ (4.18)

Combining (4.17) and (4.18),

$$\sigma_1^M = (\sigma_n + \tau \tan\varphi_c)(1+\sin\varphi_c) \tag{4.19a}$$

Rewriting (4.19a), yields

$$\frac{\sigma_1^M}{\sigma_n} = (1+\tan^2\varphi_c)(1+\sin\varphi_c) \tag{4.19b}$$

and combining (4.16) and (4.19b) we obtained:

$$\frac{\sigma_1^M}{\sigma_1^C} = \frac{(1+\tan^2\varphi_c)(1+\sin\varphi_c)}{1+\tan\varphi_c} \tag{4.20}$$

which indicates that the Mohr interpretation overpredicts the major principal stress and that, as a consequence, the corresponding flow function underpredicts the unconfined yield stress for a given value of major principal stress. The ratio of these two principle stresses according to (4.20) as a function of the Coulomb friction angle is shown in Fig. 4.28. It can be seen that the principle stress assumed in the experiment becomes more and more greater than that calculated from the simulation as φ_c increases. For example, if φ_c is 40°, σ_1^M is about 1.55 times greater than σ_1^C.

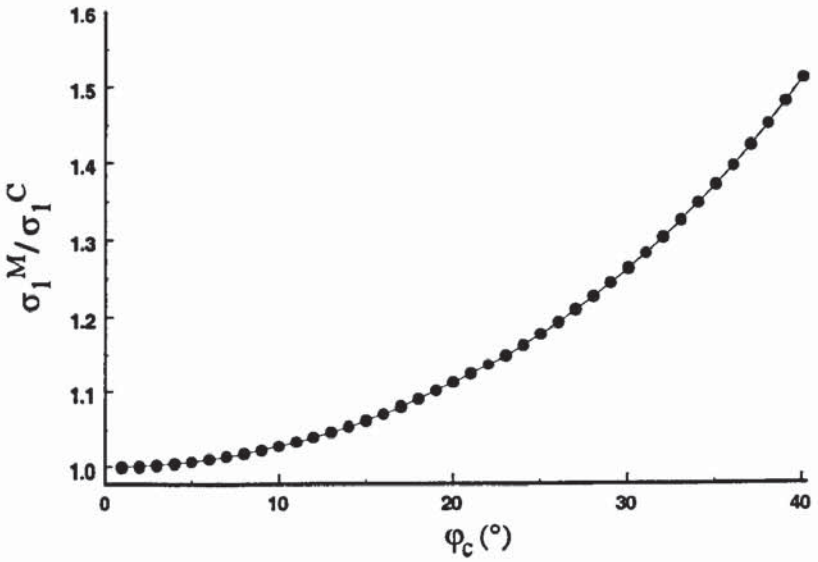

Fig. 4.28 The variation of σ_1^M / σ_1^C with different φ_c

4.5.6 Strain analysis

Fig. 4.29 shows a number of horizontal incremental displacements Δu_x of the markers set within the sample before shearing. The displacement increments are taken between the

successive steps labelled in Fig. 4.25. The contour lines show the locations where the displacement increments have the same magnitude. For stage O to A the displacement contours are shown in Fig. 4.29a. Since large horizontal displacement gradients occur at mid-height and the space between the lines increases gradually towards the top and bottom edges, no significant strain localization is revealed. Fig. 4.29b indicates that strains start to localize at the edges of the mid-plane of the specimen, while the stress-strain response is strain-hardening. A hint of the onset of localization appears at this stage. During the peak strength stage (B-C), the gradient of displacement increases and more and more strain is concentrated along the mid-height of the sample (Fig. 4.29c). Finally, a shear band is clearly visible at large displacements, as seen in Fig. 4.29d. It also can be seen from 4.29d that the horizontal displacement increments are localized into a band between the heights of 0.9mm and 1.6mm. This means that the shear band develops between these two heights. The width of this band is about $W_{SB} \approx 0.7mm$ (see Fig. 4.29d). Since the average particle diameter D_{50} is $60\mu m$ the ratio $W_{SB}/D_{50} \approx 11.6$. This value is consistent with the analysis of Muhlhaus and Vardoulakis (1987), who reported W_{SB}/D_{50} in the range of 11-12.

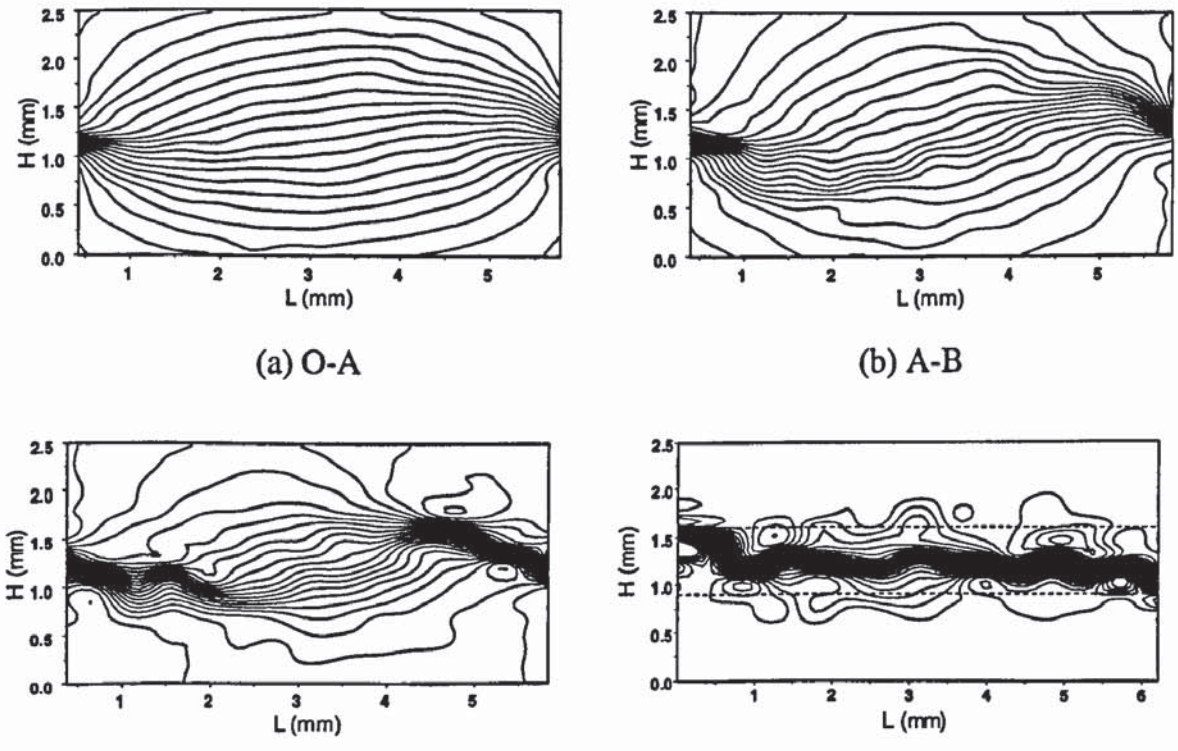

Fig. 4.29 Horizontal displacement contours during successive displacement increments

4.5.7 Particle rotation

The continuous field of average particle rotation distributions $\langle\theta\rangle$ of the whole sample are presented in Fig. 4.30. The whole sample is divided into many small boxes and $\langle\theta\rangle$ is the average rotation of all the particles in each box. Thus,

$$\langle\theta\rangle = \frac{\sum_{i=1}^{C} \varpi_i}{C} \tag{4.21}$$

where ϖ_i is the rotation of particle i and C is total number of particles in each box.

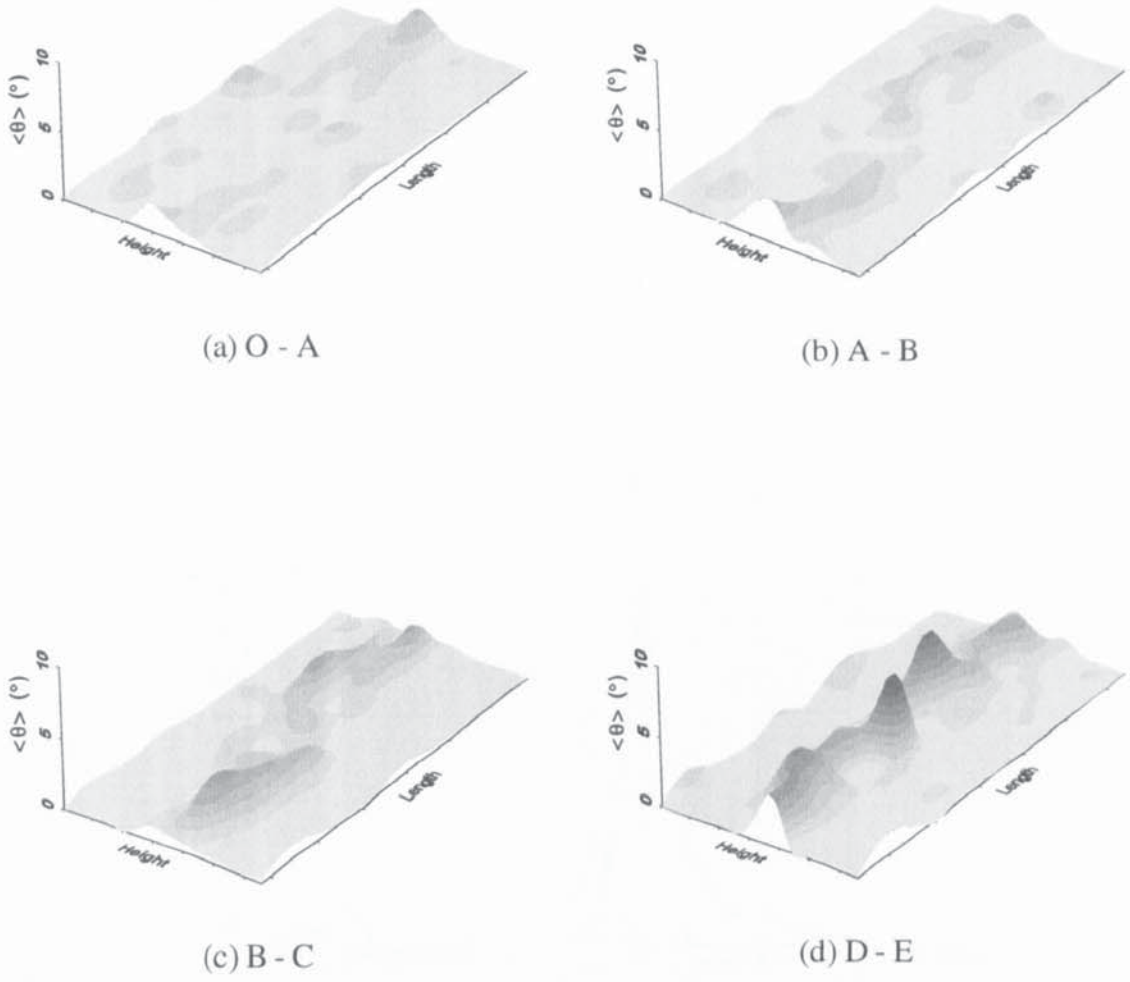

(a) O - A

(b) A - B

(c) B - C

(d) D - E

Fig. 4.30 Particle rotation distribution

It is clear from Fig. 4.30a that the average rotation field forms a smooth platen with only a few undulations in the early stage of shearing. During stage A to B some dark colour area,

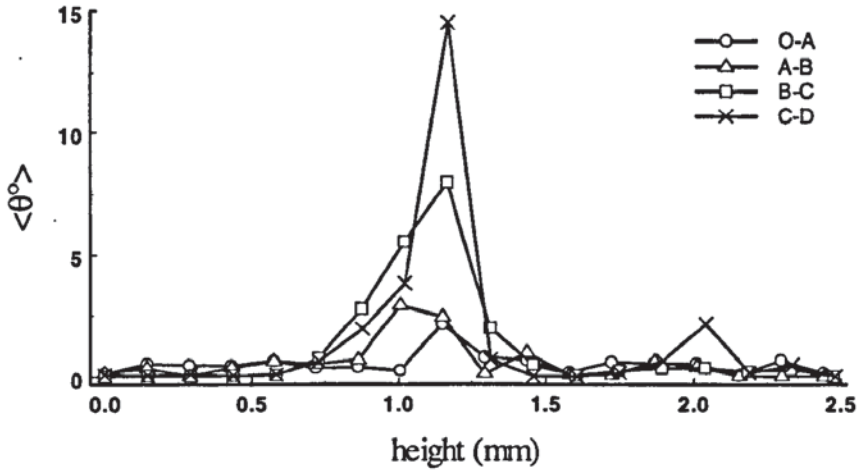

(a) 10 MPa

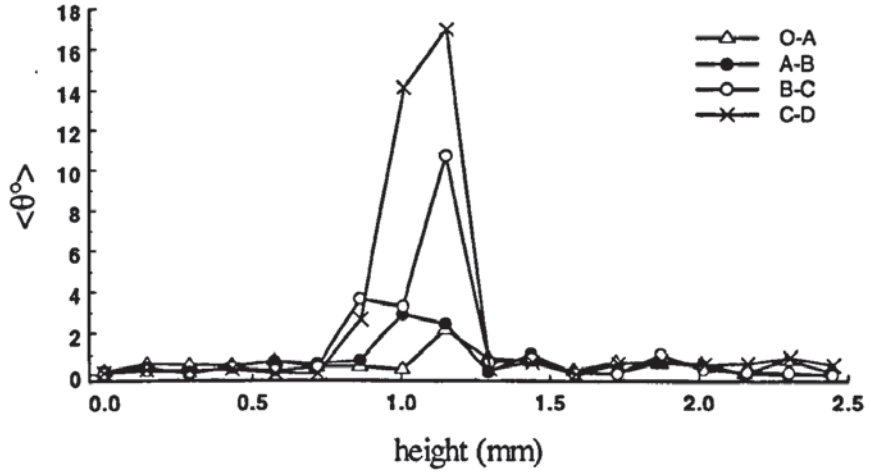

(b) 15MPa

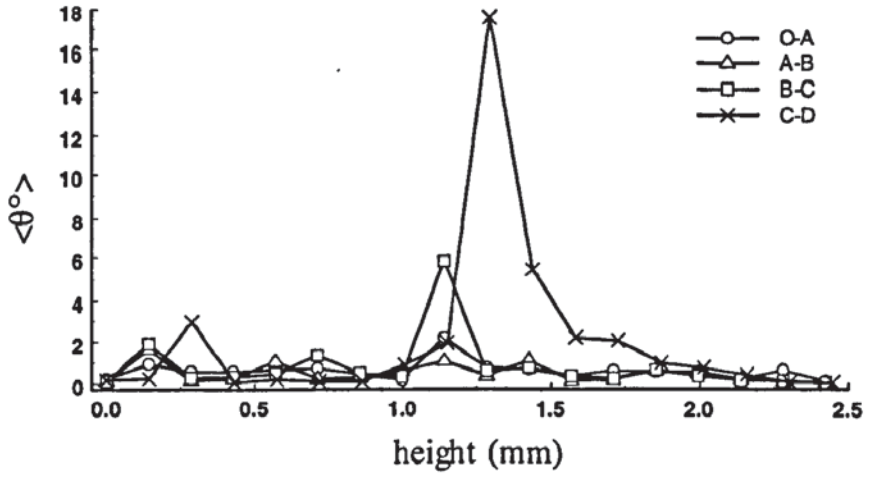

(c) 20 MPa

Fig. 4.31 Particle rotation along the height of specimen

which stand for large rotation, appear in the sample (Fig. 4.30b). During the peak strength period, these dark areas concentrate significantly into a central band as shown in Fig. 4.30c and it can be seen that a distinct ridge appears at mid-height of the specimen when the shear band is fully developed at large strain (see Fig. 4.30d). This demonstrates that during shearing the particles inside the central shear zone rotate more significantly (about 10°) than the particles outside the band (lower than 1°).

The average particle rotations along the height of the specimen for these three CN tests during four different stages are shown in Fig. 4.31, in which the average rotation is defined in (4.21). It is clear that the rotation changes significantly along the height of the specimen and reaches the highest value at the mid-height of the sample. During stage O-A the maximum rotation at the mid-height of the specimen is relatively small when compared to that of the other three stages. It is clear that the rotation becomes more significant when more shear deformation is induced.

For the simulation with a constant normal stress of 15MPa, the average rotation in the central shear zone is plotted against the horizontal displacement in Fig. 4. 32. It is clear that the evolution of the average rotation with shear strain is essentially linear. This observation is consistent with the experimental and simulation results obtained by Janssen (2001) for the same displacement range.

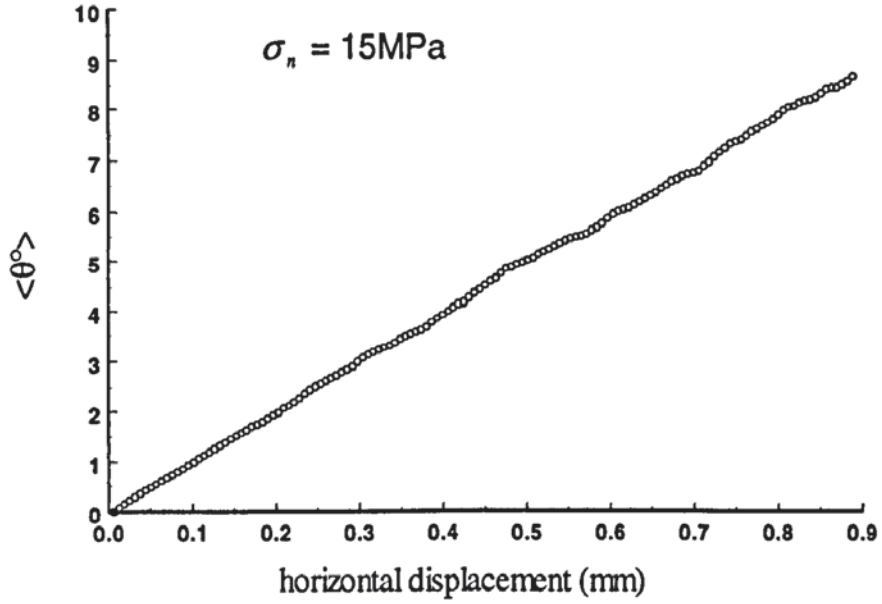

Fig. 4.32 Evolution of the average rotation in the central shear zone

4.6 Non-coaxiality

Non-coaxiality between the principal axes of stress and incremental strain is one of the possibilities for causing inaccurate test results. Detailed measurements on sand in simple shear have shown that, the theoretical value of φ_c calculated by using φ_m (4.3a) is slightly larger than the measured values (Stroud, 1971; Tatsuoka *et al.*, 1988). This is due to the fact that the inclination of principal stress σ_1 is slightly higher than the inclination of principal incremental strain $d\varepsilon_1$. This means that during the monotonic rotation of principal axes, the principal axes of stress often lags behind the principal axes of incremental strain. Consequently, the measured Coulomb friction angle for the specimen is in error. By denoting the difference between the direction of principal incremental strain and that of principal stress as the angle of non-coaxiality i (Fig. 4.33), equation (4.3a) is modified to

$$\tan\varphi_c = \frac{\sin\varphi_m \cos(\psi+2i)}{1-\sin\varphi_m \sin(\psi+2i)} \tag{4.22}$$

which implies the measured Coulomb friction angle is lower than the theoretic value when the principal axis of stress has not rotated as far as the principal axis of incremental strain (positive i).

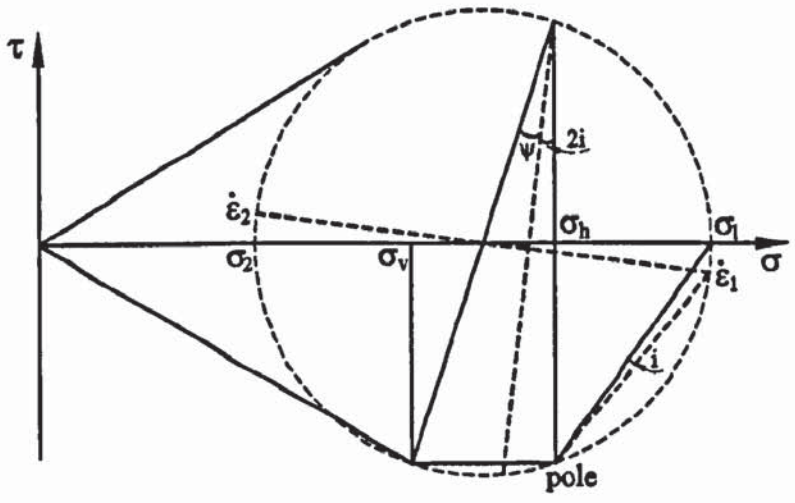

Fig. 4.33 The Mohr circle

As shown in Fig. 4.33 the angle of non-coaxiality is related to the difference between the vertical and horizontal normal stresses and the dilation angle. As mentioned in section 4.3, in the simulation of the direct shear test the results based on the centre part is a kind of

approximation for the shear band. Since there are only a small number of particles within this region very large fluctuations appear in the calculation of the dilation angle (not shown), which makes the analysis of non-coaxiality very difficult in the direct shear simulations. It is expected that better results can be obtained from the simple shear test since there are more particles involved in the shear plane. Thus, the angle of non-coaxiality will be examined further in the next chapter.

4.7 Influence of different shear schemes

Experimental direct shear tests have revealed that the measured properties are significantly influenced by the test configuration (Assadi, 1975; Shibuya *et al*, 1997). In simulations the constant normal stress in the vertical direction can be achieved by either of the following four schemes (Fig. 4.34): a) only move either top or bottom wall vertically (1wall); b) move both top and bottom walls vertically (2walls); c) only move either top or bottom box vertically (1box); d) move top and bottom box vertically together (2boxes). In the first two schemes the top or bottom platen and the end walls move independently. In the last two shear schemes the end walls are screwed to the top or bottom platen so that they are fixed together. In this way they will move together as a unit not only in the horizontal direction but also in the vertical direction. The first two schemes refer to the conventional arrangement and the last two schemes refer to the improved arrangement according to Jewell (1989). One will expect that schemes 'b' and 'd' will create a more symmetrical deformation condition in the sample. Bearing this in mind, four more constant normal stress tests were carried out in order to investigate the influence of the different shear schemes.

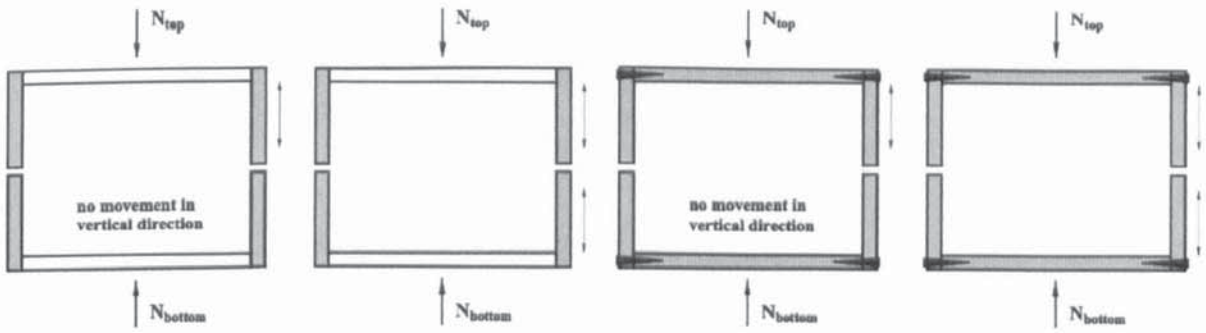

(a) 1 wall (b) 2 walls (c) 1 box (d) 2 boxes

Fig. 4.34 Different shear schemes

Figure 4.35 shows the evolution of normal forces for the four different schemes, in which N represents the normal force on the central shear plane calculated from (4.6) and N_3 measured from the top platen (see Fig. 4.6). It is clear that if the constant normal stress tests are carried out by using 1 wall or 2 walls the normal force N is much higher than the normal force N_3. If the same tests are simulated by using 1 box or 2 boxes the normal force N is close to the normal force N_3. This indicates that effect of the tangential force caused by the friction on the two end walls is more significant in schemes 'a' or 'b' than in schemes 'c' or 'd'. This is because the effect of friction on the end walls becomes very small when the end walls are fixed to the top or bottom walls.

The corresponding evolution of tangential force T and T_3 (see Fig. 4.6) are presented in Fig. 4.36. It can be seen that before 0.2mm horizontal displacement the tangential forces T according to (4.7) and the tangential forces T_3 measured from the boundary for all the cases are very similar though the tangential force T is about 2.5 times higher than the tangential force T_3. As shearing continues, they begin to diverge slightly. As Shibuya *et al* (1997) pointed out, the conventional measurement of vertical load in their shear box involved a considerable error in estimating the average normal stress on the horizontal shear plane, owing to the interface friction developed on the vertical faces of the specimen. Therefore, if the normal and tangential force on the central shear plane cannot be measured correctly, the reliability of the shear strength and other properties of the specimen, which are calculated based on these two forces, obtained by experimentalists is very much questionable.

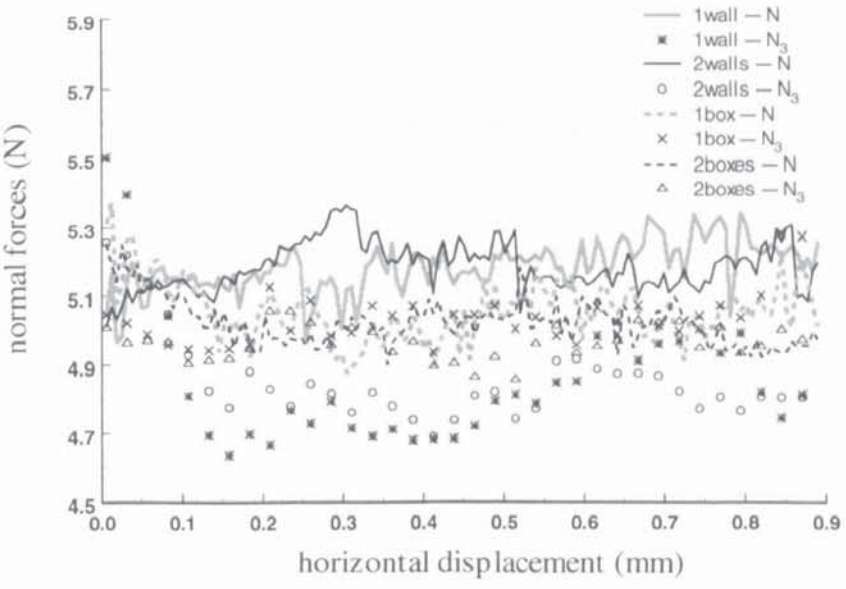

Fig. 4.35 Normal force evolutions

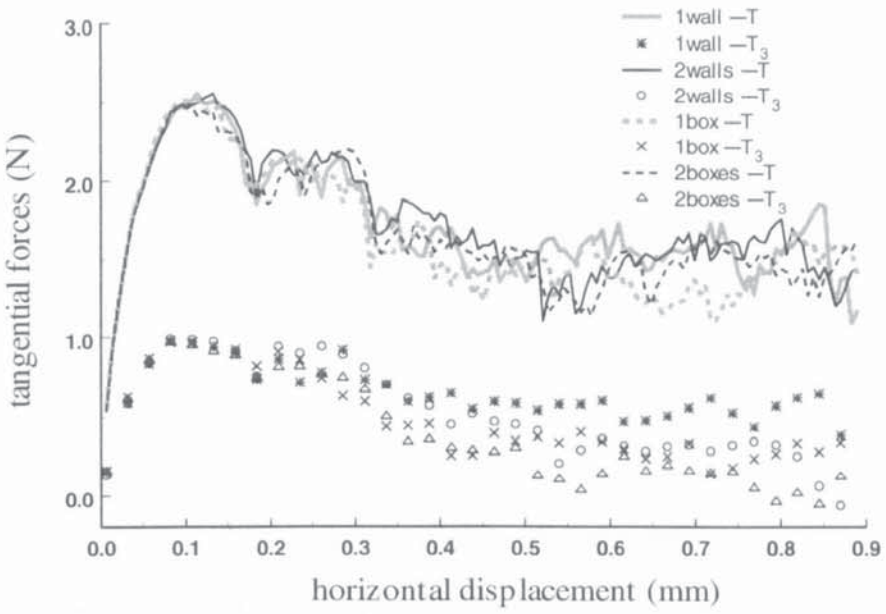

Fig. 4.36 Tangential force evolutions

Figure 4.37 shows the evolution of porosity inside the shear band. For the four cases considered the evolutions are very similar. The porosity increases quickly until the horizontal displacement reaches 0.4mm. Thereafter, they remain nearly constant. Figure 4.38 shows the stress ratio τ/σ inside the shear band for all the cases according to (4.5). It can be seen that the peak shear strength and the complete evolution of the stress ratio are essentially the same for all the schemes.

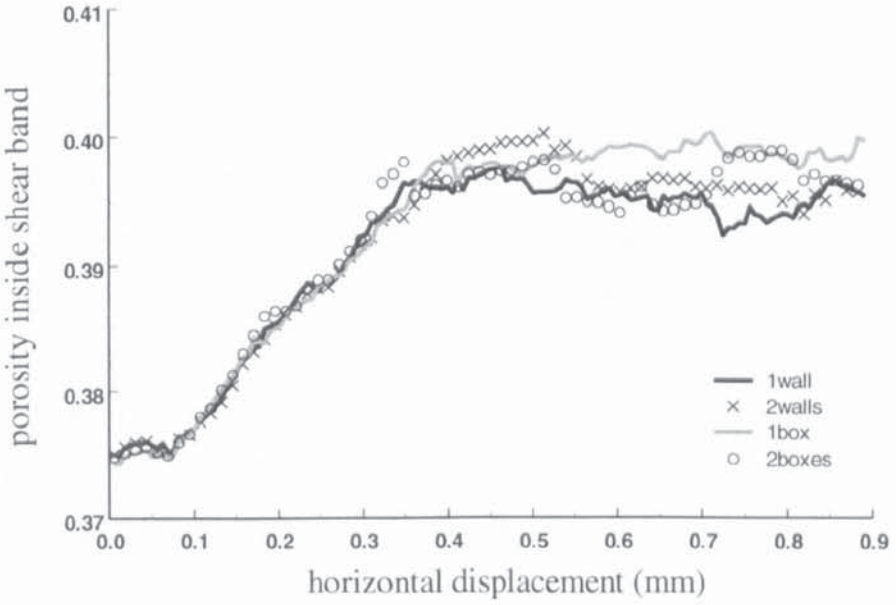

Fig. 4.37 Evolution of porosity inside shear band

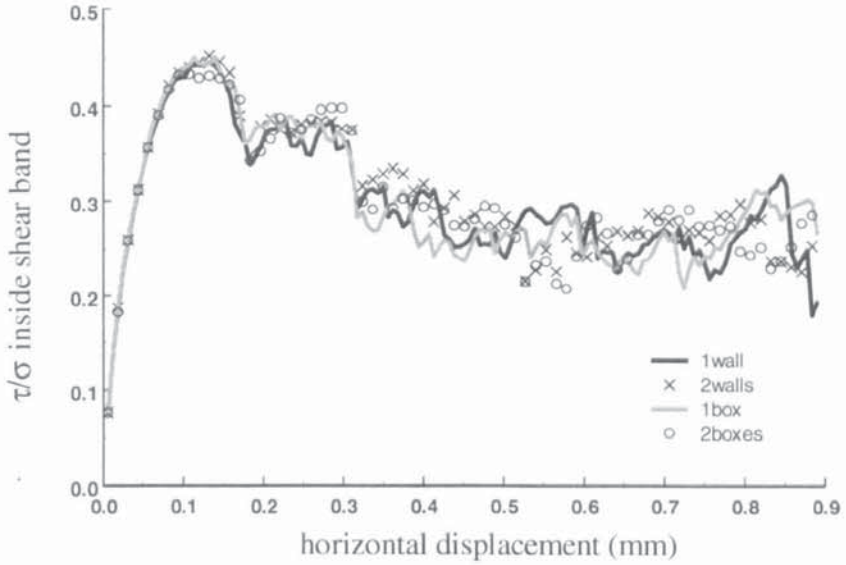

Fig. 4.38 Evolution of stress ratio inside shear band

Since it is hard to say what force is measured exactly in the laboratory test the force ratio *T/N* can be calculated by either of following ways,

$$tan\varphi_c = T/N \text{ , according to (4.10)} \tag{4.23a}$$

$$tan\varphi_c = T_3/N_3 \text{ , purely based on the boundary forces} \tag{4.23b}$$

$$tan\varphi_c = T_3/N \tag{4.23c}$$

$$tan\varphi_c = T/N_3 \tag{4.23d}$$

The evolutions of force ratio from the above calculations are presented in Fig. 4.39. It can be seen from Fig. 4.39a that all the four different shear schemes show essentially the same results. Nevertheless, they are still 10% higher than the results obtained from the central shear zone (Fig. 4.38). If the force ratio obtained based on (4.23d) (see Fig. 4.39d) the results from 1 box and 2 boxes are similar to the results shown in Fig. 39a. However the peak force ratio of schemes 1 wall and 2 walls are higher than the results calculated using (4.23a). This is because the normal force N is close to N_3 in schemes 1 box and 2 boxes but N is higher than N_3 in the other two schemes. The force ratios based on (4.23b) or (4.23c) are similar (see Fig. 4.39b and c) but they are much lower than the ratios shown in Fig. 4.39a. Also, significant divergence can be observed at critical state. Therefore accurate measurement of the tangential force is crucial for determining the shear properties of the specimen correctly and the results also imply that no matter what scheme is chosen the pre-peak behaviour is essentially the same.

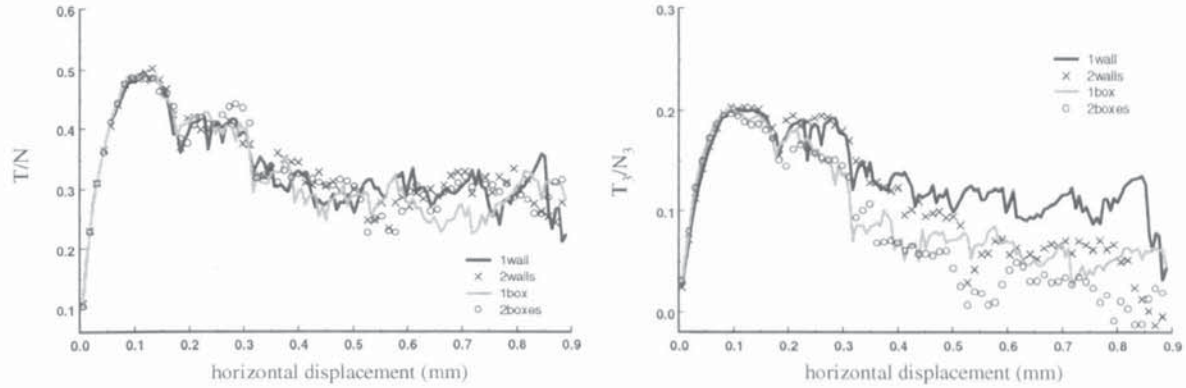

(a) $tan\varphi_c = T/N$ (b) $tan\varphi_c = T_3/N_3$

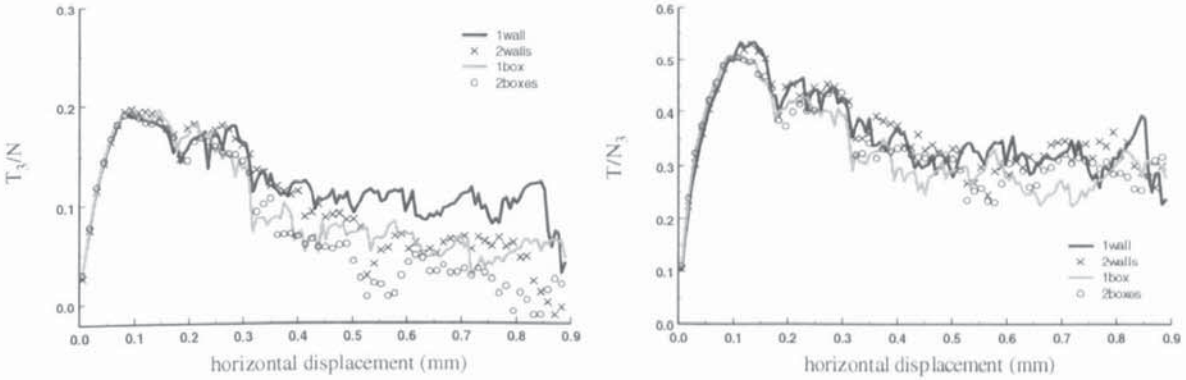

(c) $tan\varphi_c = T_3/N$ (d) $tan\varphi_c = T/N_3$

Fig. 4.39 Evolution of force ratio based on different measurements

Based on the above analysis it is clear that by using either the 1 box or 2 boxes scheme the effect of friction on the vertical face of the specimen can be minimised. It also shows that the normal force and tangential force on the horizontal shear plane are independent of the shear schemes. The same results will be obtained if one can measure these forces correctly. Even if these forces can be measured correctly the force ratio is still slightly higher than the stress ratio calculated from the central shear zone.

4.8 Summary

Two series of numerical simulations of the direct shear test have been performed. The intrinsic drawbacks involved in conventional direct shear tests have been identified through a comprehensive investigation. Taking advantage of the numerical simulation

technique, the stress tensor and the voidage inside and outside of the shear zone have been examined. In the first series, three boxes with different aspect ratio were employed to simulate tests under constant volume conditions. Test results calculated from wall boundaries and from different stress tensors have been compared. In terms of the shear strength $tan\varphi_c$, if it is calculated from the stress tensor inside the shear band, the pre-peak behaviours are not significantly influenced by the difference in aspect ratio of the shear box. However, the post-peak behaviours are affected by this kind of boundary condition. The stress ratio reduces after the peak very sharply and early for the thickest sample. The thinnest sample tends to maintain the peak strength until a large horizontal displacement is reached. The stress ratio inside the shear band is higher than the stress ratio outside of shear band. When a thinner box is used this difference becomes smaller. It is found that dilation occurs inside shear band though the total volume of the sample is kept constant. Therefore, concerning examination of the shear behaviour on the central shear plane it is not possible to perform a true constant volume test in the direct shear test.

In the second test series the sample with aspect ratio 1:2 was subjected to different constant normal stresses in order to examine stress and strain distributions and the effect of stress level in the direct shear test. By using the markers pre-selected in the specimen the incremental horizontal displacement contours were plotted. It was illustrated that the shear strain is highly non-uniform. The shear strain appears to concentrate in the mid-plane of the sample as shear deformation develops. Correspondingly, significant particle rotations localize into the shear band. It was also shown that the evolution of the average rotation with shear strain is essentially linear. Although the stress distribution within the specimen is heterogeneous, as indicated by the force transmission pattern, it has been shown that the evolution of the stress ratio inside the shear band is similar to that inferred from the boundary force calculations except that the peak value based on the boundary information is a slightly higher than that obtained from the shear band.

The results suggest that different normal stress levels do not significantly affect the maximum value of φ_c. It was found that the porosity measured from the shear band is much greater than that obtained from boundary observations. This means that the dilation angle determined from movement of the top boundary of the sample cannot reflect the real dilatancy inside the shear band.

The simulations have demonstrated that under critical state conditions the vertical and horizontal normal stresses in the shear band are equal and that the directions of principal stress and strain rate are coaxial. The important conclusions arising from this discovery are:

(i) It is the Coulomb friction angle φ_c that is measured in the experimental direct shear test.

(ii) The Coulomb friction angle φ_c is less than the angle of shearing resistance φ_m defined by Mohr's criterion.

(iii) The conventional interpretation of the location of the Mohr stress circle at the critical state results in an over prediction of the major principal stress.

Finally, the examinations of four different shear schemes show that the influence of the friction on the vertical face of the specimen can be eliminated if the loading platen is fixed to the end walls. However, the numerical simulations reveal that calculations based on information from the shear band show essentially the same results regardless of the different shear schemes. Therefore, if one can accurately measure the stresses acting on the central shear plane, the choice of scheme is irrelevant.

CHAPTER 5: SIMPLE SHEAR TESTS

5.1 Introduction

For the simulations presented in the last two chapters, shear tests were carried out with walls that translated. In order to simulate simple shear, the same sample as prepared for the biaxial compression test with wall boundaries is used. However, the two vertical walls are rotated at a constant angular velocity about a certain point along the side-walls. Simultaneously the top and bottom walls are translated using a compatible horizontal velocity in opposite directions. This is also the principle of the simple shear test employed in the laboratory. The aims of the analysis are: (1) to explore the effect of the wall friction and the initial ratio of horizontal to vertical stress, K_0 on the results obtained; (2) to compare the difference between the results obtained from plane strain biaxial compression, direct and simple shear tests; (3) to investigate the correlation of the angle of non-coaxiality with (i) the difference between the two orthogonal normal stresses and (ii) the rate of dilation.

In this chapter three series of simple shear tests have been conducted. First, constant volume (CV) tests with various boundary friction are considered in order to show the comparison between the average internal state of stress and the measurement at the boundaries. Secondly, constant normal stress (CN) tests, in which the sample is subjected to different constant normal stresses, are simulated to examine the effect of stress level. Finally the simple shear tests are carried out on three samples with different initial stress ratio K_0. Based on the calculations of the stress tensor, the principal stress directions are identified and the effect of K_0 on the behaviour of the material are examined. Investigations have also been carried out on the local void cell deformation and particle rotation during the simple shear test.

5.2 Brief literature review

The objective of laboratory testing is to study the behaviour of a given soil under

conditions similar to those encountered in the field and to obtain material parameters, which describe the behaviour in a set of constitutive equations. In a laboratory test the specimen is intended and generally assumed to represent a single point in a soil medium. The validity of this assumption relies on the uniformity of stress and strain distributions within the soil samples. Moreover, the uniformity depends on the configuration of the specimen and the control and measurement of stress and strain on its surface. The states of stress and strain in the aforementioned direct shear devices are not uniform, and the cross section of the soil sample between the top and bottom box changes continuously.

Various attempts were made to modify the direct shear device in order to impose a uniform condition of simple shear to the soil specimens. One of the earliest attempts was made by Kjellman (1951) who developed the Swedish Geologic Institute (SGI) Box in the 1950's. The SGI box encases the specimen laterally in a heavy rubber tube. The tube is prevented from expanding under pressure by closely spaced, but separated, aluminium rings. Shear is applied to the top of the box, and the shear strain is assumed to be distributed uniformly between the top and bottom of the box. Due to the compression of the rubber tube between the soil and the rings, there is some lateral deformation of the soil, so that the lateral stresses will be even more indeterminate than in the ordinary direct shear test. Another solution to the same problem was developed at Cambridge by Roscoe (1953), who employed rigid but hinged plates for the ends of the shear box. These plates tilt during shear so as to maintain a constant specimen length parallel to the direction of shear. Thus a uniform shear strain is imposed on the specimen while lateral deformation is prevented. Hence such a box provides improvements on the SGI apparatus, but still has many drawbacks such as non-uniformity of boundary stresses, uncertainty about the stress tensor because no information was available about the horizontal normal stress. In 1966 the Norwegian Geotechnical Institute (NGI) refined the SGI device by replacing the rings with thin wires embedded in the rubber membrane (Bjerrum and Landva, 1966) and a large amount of research and testing was carried out on the NGI device that showed a more uniform straining of the specimen was obtained in the NGI type device than in the SGI one.

The Cambridge and NGI devices are the two main types of simple shear devices, which have been used to study the quasi-static behaviour of soils. Studies have shown that neither the vertical normal stresses nor the shearing stresses are uniformly distributed in

the simple shear test (Cole, 1967; Stroud, 1971; Budhu, 1979). Thus it is inevitably subject to criticisms because of the non-uniformity of stresses and strains, which may facilitate the occurrence of progressive failure along the potential shear plane (Airey *et al*, 1985). A critical review of the various theoretical analyses for the Cambridge and NGI apparatuses was presented by Saada and Townsend (1981). They dismissed these simple shear devices by using the results of photoelastic studies carried out on flanged circular and rectangular photo-elastic models and remarked that these apparatuses "cannot claim to yield either reliable stress-strain relations or absolute failure values." They concluded that "simple shear tests are of no value for research purposes." Results of drained simple shear tests in the Cambridge and NGI type simple shear apparatuses were compared by Budhu (1984), who showed that the rigid boundaries of the Cambridge type apparatus impose a definite simple shear configuration to the sample. The flexible boundary of the NGI type apparatus provides less restraint, which allows out-of-plane movements to occur. He concluded that the Cambridge apparatus can be expected to give an accurate estimation of the behaviour of sand in monotonic loading if stress measurements are taken at the centre of the sample.

A further development of the Cambridge simple shear apparatus, which was initiated by Roscoe, was described by Bassett (1967). It permitted the measurement of the magnitude and direction of the principal stresses within the sample at all stages of a test. Based on the test data, the hypothesis of Wroth and Bassett (1965) for predicting the behaviour of materials in the early models of the simple shear apparatus (in which only the stresses on horizontal planes were measured) was subjected to critical examination. Discrepancies were found between prediction and the observations and then the hypothesis was modified to incorporate several new parameters, which were applicable to all plane-strain problems. The new revised hypotheses were in excellent agreement with experimental observations. However, the shortcoming of the apparatus, such as the unmeasured side and end wall friction forces, the sensitivity and rigidity of the side load cells and the non-uniformities of stress distribution inside the specimen, were still not overcome by the new design.

The Cambridge simple shear apparatus built by Bassett (1967) and modified by Cole (1967) showed significant non-uniformities developed within the samples, which gave rise to large underestimates of both stress and strain quantities measured at the boundaries. The causes of this non-uniform behaviour were investigated and the major fault was found

to lie in the weak contact between sand grains at the top of the sample and the upper boundary of the sample container. In order to overcome this Stroud (1971) designed special new load cells to be incorporated in the simple shear apparatus. Based on the new apparatus a comprehensive study on the simple shear apparatus itself and its influence on the soil properties was carried out and the behaviour of Leighton Buzzard sand at low stress levels was presented and discussed in detail. In a critical assessment of the development of boundary stresses around samples tested in the new apparatus, and by using X-ray methods, the local strains within these samples were also examined. It was demonstrated that conditions were vastly improved and that the behaviour was remarkably uniform up to the point of failure.

Dyvik *et al.* (1987) described a laboratory-testing device developed from the NGI apparatus, which enables simple shear tests to be performed under undrained conditions with pore pressure measurement. The results were compared with the conventional constant volume simple shear test. Good agreement between these two techniques was obtained for all practical purposes. The assumption that the change in applied vertical stress is equal to the pore pressure, which would have developed in an undrained test, was validated by the experimental evidence.

Airey *et al.* (1985) presented the findings of research work at Cambridge using the simple shear apparatus on both soil and clay. The detailed study identified non-uniformity of boundary stresses and the development of internal inhomogeneities as the principal shortcomings in the simple shear test. It was found that uniformity of boundary stresses and internal deformations were very much better in the tests on clays than those on sands. The results suggested that, in routine tests, the presence of non-uniformities would be undetectable and care should be taken in the interpretation of the experimental results.

Dounias and Potts (1993) compared the results for a direct shear box test and simple shear test on a soil, which is assumed to be elastoplastic, with and without dilation using the finite element method. In direct shear, large stress and strain nonuniformities were observed, which reached a maximum as peak conditions were approached. In simple shear, deviatoric strains were fairly uniform during the initial loading stages, but as peak conditions were approached they became highly nonuniform. The conditions in the shear box were found to be similar to those of simple shear, except for behaviour beyond peak

strength.

In the simple shear test the increase in shear stress on the horizontal plane will cause a rotation of the principle stresses and a change of their magnitudes. Owing to the fact that the stress conditions are unknown, the interpretation of the test results is limited to a consideration of the shear stress and normal stress on the horizontal plane. Simple shear devices have been introduced as an improvement over direct shear devices. The results of simple shear tests are interpreted as a model test illustrating the conditions in a narrow shear zone separating two rigid bodies which move relative to each other, which is equivalent to the central shear zone in the direct shear test. Are the simple shear tests better than the direct shear tests and could they produce more reliable results than direct shear tests? If it is accepted that the simple shear test produces data of reasonable quality the question arises as to how the data can be related to the results obtained from other laboratory tests. This is of interest because the design procedures for many field problems are based on the results from triaxial tests, but the soil response often bears more resemblance to simple shear. Unfortunately it is difficult because in the laboratory simple shear test the principal stresses cannot be determined; only the normal and shear stresses on the horizontal boundaries are measured and it is not possible to construct a Mohr circle of stress. To construct a Mohr's circle of stress, the lateral stress σ_{11} must be estimated using certain assumptions. For sands this has been achieved (Budhu, 1979) by assuming coincidence of the principal axes of stress and strain increment. However, it was shown by Borin (1973) that no such coincidence exists for normally consolidated Kaolin. In DEM simulations all the components of the stress tensor and all the forces on the boundaries can be measured directly. In this Chapter, an investigation of granular material behaviour in the simple shear test is reported. The stress and strain distributions, shear strength and dilatancy are examined.

5.3 Two typical stress-strain conditions in the shear test

5.3.1 Pure shear deformation

The term "pure shear", when used for a state of stress in a solid, is often described by an element *abcb* subjected only to shear stresses on the four side faces (Fig. 5.1a). The state of stress can be presented by,

$$\begin{bmatrix} 0 & -\tau & 0 \\ -\tau & 0 & 0 \\ 0 & 0 & 0 \end{bmatrix}$$

Another state of pure shear in which two principal stresses are in perpendicular directions and equal in magnitude and opposite in sign without any shear stresses is shown in Fig. 5.1b. Thus the above matrix becomes:

$$\begin{bmatrix} \sigma_x & 0 & 0 \\ 0 & -\sigma_y & 0 \\ 0 & 0 & 0 \end{bmatrix}$$

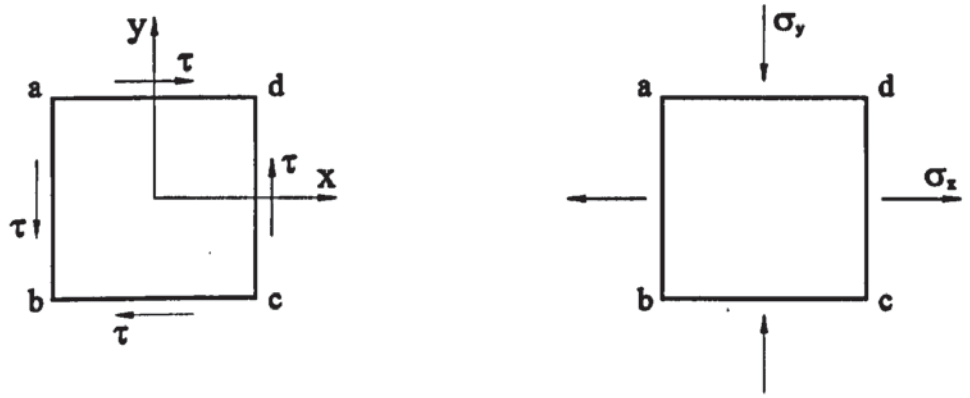

(a) state 1 (b) state 2

Fig. 5.1 Stress in pure shear on the element *abcd*

In terms of a state of strain at a point for the element *abcd* under pure shear condition, the corresponding shear strains are shown in Fig. 5.2. Considering the element in pure shear condition shown in Fig. 5.1a, with $\varepsilon_x = 0$, $\varepsilon_y = 0$, and a shear strain $\gamma \neq 0$ corresponds to a change in the angle between two lines that are originally perpendicular to each other. Therefore, the element changes its shape from a rectangle (dashed line) to a parallelogram (continues line) as shown in Fig. 5.2a. Next, consider the strains that occur in Fig. 5.1b, which consists of a uniform extension in the tensile stress direction, and a uniform contraction in the compressive stress direction by the same amount so that the volume remains unchanged. These dimensional changes are shown in Fig. 5.2b, in which the dashed lines show the original element. As in the biaxial compression test described in Chapter 3 there is no rotation in principal stress or strain rate directions thus the principal directions of stress and strain rate are coaxial throughout the test.

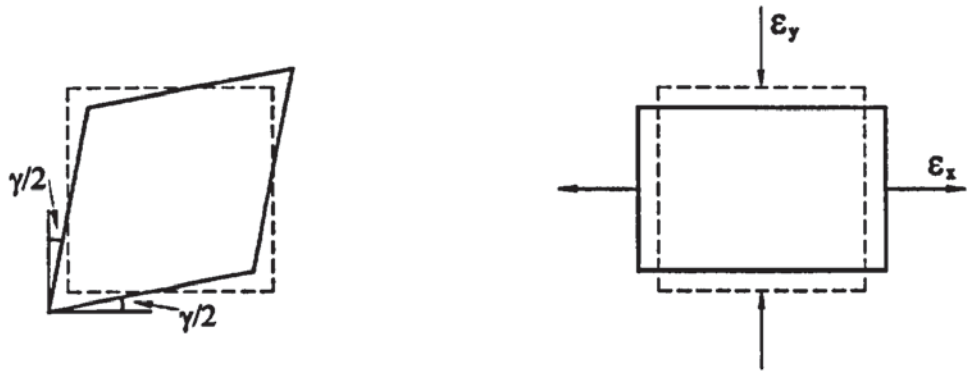

(a) state 1 (b) state 2

Fig. 5.2 Strain in pure shear on the element *abcd*

5.3.2 Simple shear deformation

The term "simple shear" refers strictly to a state of strain rather than to a state of stress. It is such a state of plane strain that $\varepsilon_z = 0$. It is also an inextensional mode of shear so that $\varepsilon_x = 0$. In this case all planes parallel to the *xz*-plane move in the direction of the *x*-axis, and the displacements are proportional to their distance from the *xz*-plane. All horizontal planes do not change in length. Therefore the *x*-direction coincides with a line of zero extension. Any change in volume is due to length changes in the *y*-direction, vertical strain ε_y, and the corresponding angle of dilation ψ is shown in the Fig. 5.3. Simple shear can be regarded as a pure shear plus a rotation. Though simple shear applies a uniform strain to the element from its boundary there is no guarantee of internal homogeneity and the uniformity of the state of stress.

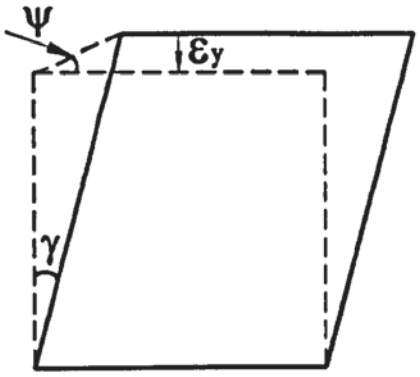

Fig. 5.3 Simple shear strain condition

5.4. DEM model of the simple shear test

For DEM simulations of the simple shear test, the sample used in the biaxial compression test with wall boundaries (see Chapter 3) is selected in order to make direct comparisons. The simulation model is illustrated in Fig. 5.4, in which the dashed lines show the initial position of the specimen. The stresses can be calculated from the stress tensor by averaging all the contact forces inside the sample in the same manner as used in the previous simulations. In the simulation the normal forces (N_T, N_B, N_L and N_R) and the shear forces (T_T, T_B, T_L and T_R) on the boundaries can be calculated (Fig. 5.4).

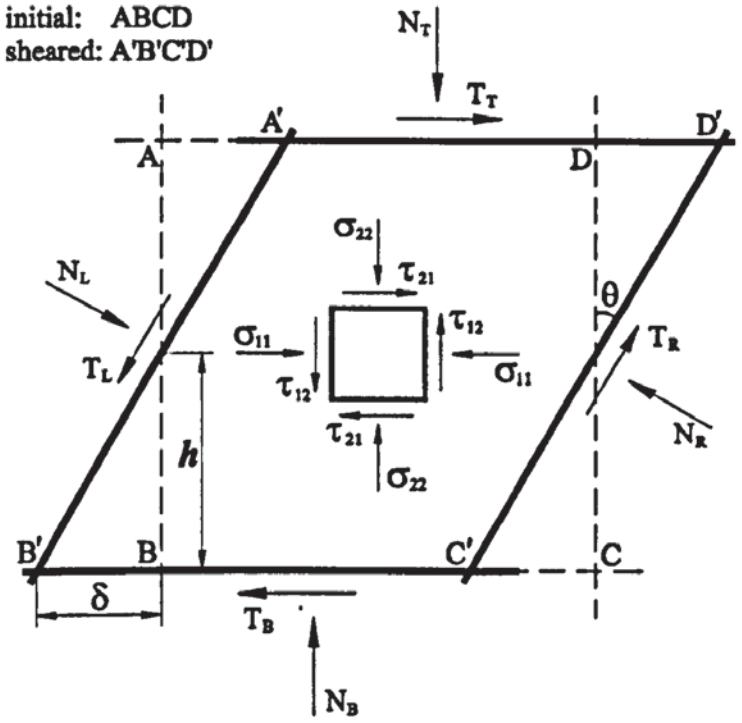

Fig. 5.4 Scheme of DEM model in simple shear test

By dividing these forces by the areas on which they act, the average normal stresses σ_L, σ_R, σ_T, σ_B and shear stress τ_L, τ_R, τ_T, τ_B can be obtained from the wall forces as follows,

$$\sigma_L = \frac{N_L}{l_{AB} D_{50}}, \quad \sigma_R = \frac{N_R}{l_{AB} D_{50}} \tag{5.1}$$

$$\sigma_T = \frac{N_T}{l_{AD} D_{50}}, \quad \sigma_B = \frac{N_B}{l_{AD} D_{50}} \tag{5.2}$$

$$\tau_L = \frac{T_L}{l_{AB} D_{50}}, \quad \tau_R = \frac{T_R}{l_{AB} D_{50}} \tag{5.3}$$

$$\tau_T = \frac{T_T}{l_{AD} D_{50}}, \quad \tau_B = \frac{T_B}{l_{AD} D_{50}} \tag{5.4}$$

where l_{AB} and l_{AD} are the current lengths of the wall AB and wall AD, respectively.

The initial configuration of the specimen at equilibrium is shown in Fig. 5.5a. Two different schemes can be used to perform the simple shear test. The vertical walls can be rotated either about the mid-point of the vertical walls (AB, CD, see Fig. 5.4, scheme 1) or the intersections of vertical wall and bottom wall (point B and C, see Fig. 5.4, scheme 2). The comparisons of the macroscopic and microscopic results obtained from these two schemes are provided in Appendix D and it is shown that the results obtained from scheme 1 and scheme 2 are essentially the same. In the simulations reported in this chapter, the two vertical walls AB and DC rotate at a constant angular velocity about the midpoints of the walls. The top and bottom walls are translated using a compatible horizontal velocity in opposite directions. The solid thick lines $A'B'C'D'$ (Fig. 5.4) show the position at the end of shearing. Figure 5.5b shows the corresponding particle configuration at the end of shearing from a simple shear test simulation. The figure shows that uniform simple shear deformation is reasonably achieved throughout the specimen.

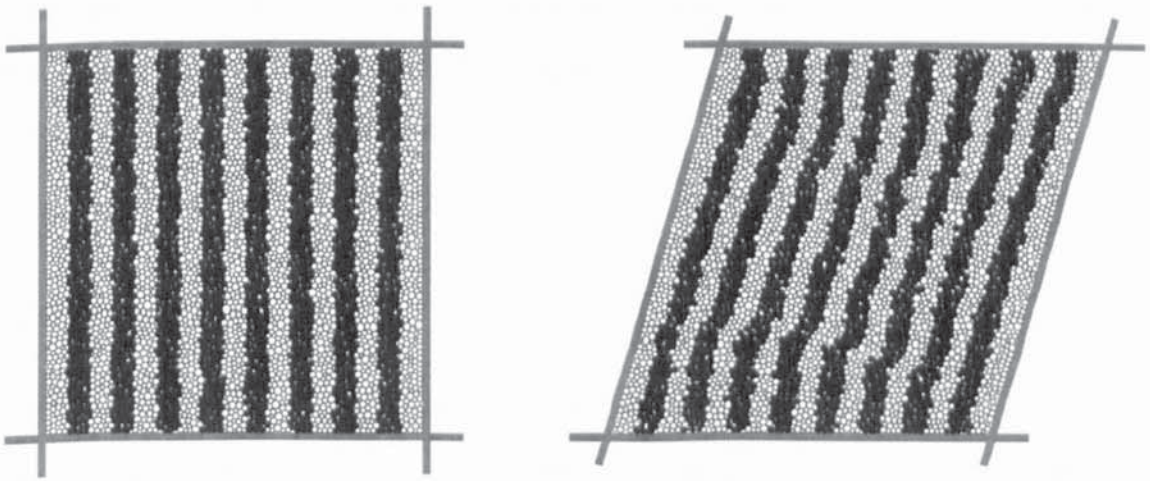

(a) before shearing (b) after shearing

Fig. 5.5 Particle configurations

Shear strain is defined as,

$$\gamma = tan\theta = \frac{\delta}{h} \tag{5.5}$$

where θ is the angle of inclination of the rotating walls (Fig. 5.4).

The shear strength can be determined, according to Coulomb, by

$$tan\varphi_c = \frac{\tau}{\sigma} = \frac{\tau_{21}}{\sigma_{22}} \tag{5.6}$$

where σ and τ are average vertical normal stress and average shear stress obtained from the ensemble stress tensor. If the calculation is based on the boundary information the shear strength can also be expressed as,

$$tan\varphi_c = \frac{T_T}{N_T} = \frac{\tau_T}{\sigma_T} \tag{5.7}$$

5.5 Constant volume (CV) tests

In the constant volume test the height of the sample has to be maintained constant in order to achieve the constant volume condition. Therefore, when the two vertical walls (*AB* and *CD*) rotate about their mid-points, the top and bottom boundaries (*BC* and *AB*) are displaced horizontally by δ in opposite directions and are constrained not to move in the vertical direction. In this test series, three samples are investigated with the wall friction μ_w set to 0.1, 0.5 and 0.8, respectively.

5.5.1 Forces on the walls

The normal forces (N_T, N_B, N_L and N_R) and tangential forces (T_T, T_B, T_L and T_R, see Fig. 5.4) acting on each wall for all three samples are shown in Fig. 5.6. The normal force and tangential force of each pair of opposite walls have essentially the same magnitude and opposite sign for all three samples considered. Although the tangential forces for sample I are lower than the results obtained from the other two samples, the evolution of the normal forces are quite similar for all three samples.

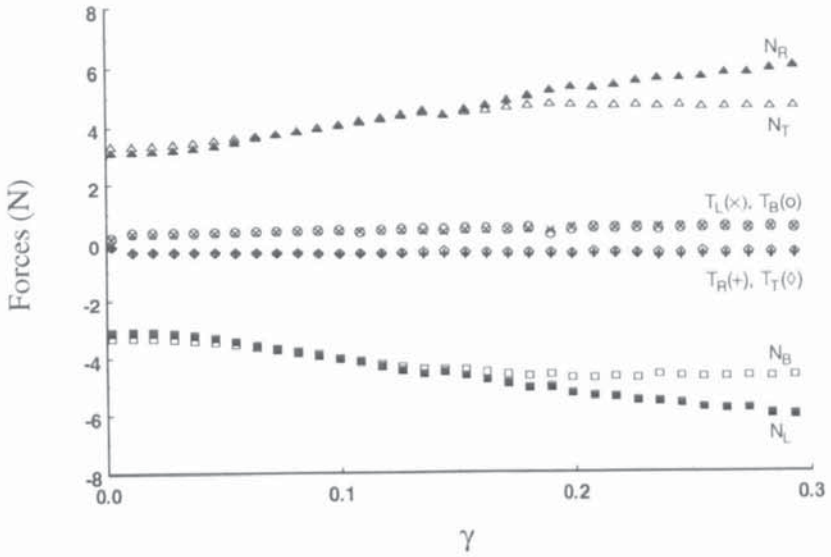

(a) $\mu_w = 0.1$

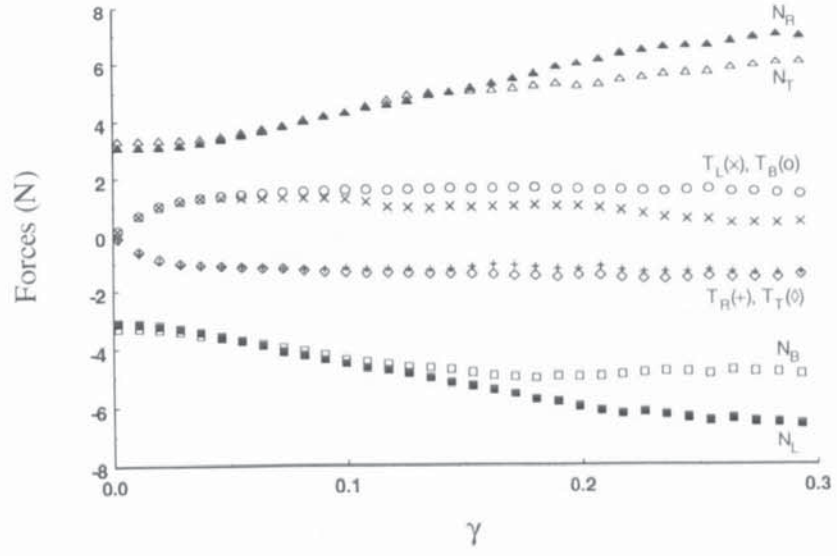

(b) $\mu_w = 0.5$

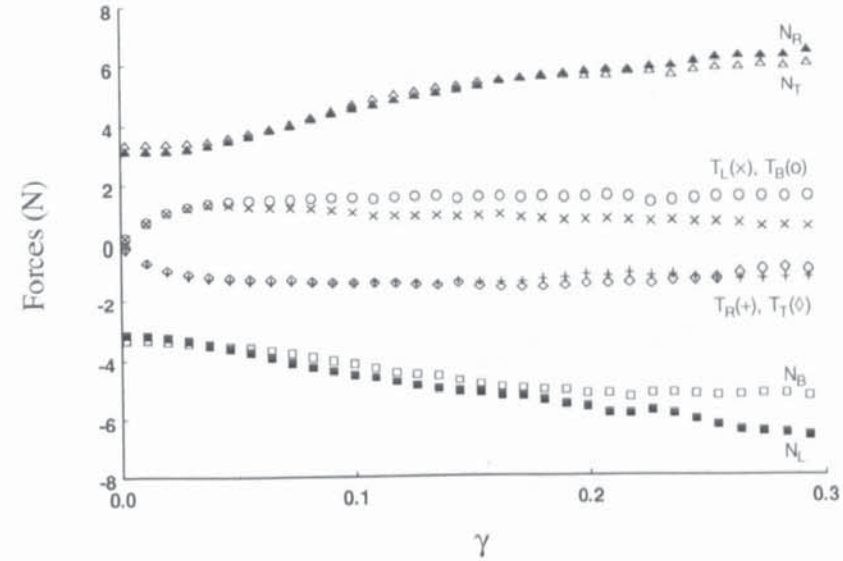

(c) $\mu_w = 0.8$

Fig. 5.6 Evolution of wall forces

5.5.2 Stresses

The normal stress and shear stress measured from the boundaries (σ_R, σ_T, τ_R and τ_T) and the stress components calculated from the stress tensor (volume averaged, σ_{11}, σ_{22}, τ_{12} and τ_{21}) for all three samples are shown in Figs. 5.7 - 5.9, respectively. It can be seen from Fig. 5.7a that the volume averaged normal stress σ_{11} is greater than σ_R before 15% shear strain, afterwards σ_R becomes greater than σ_{11}. The normal stress σ_{22} is significantly greater than σ_T throughout shearing. In addition, the volume average shear stresses τ_{12}

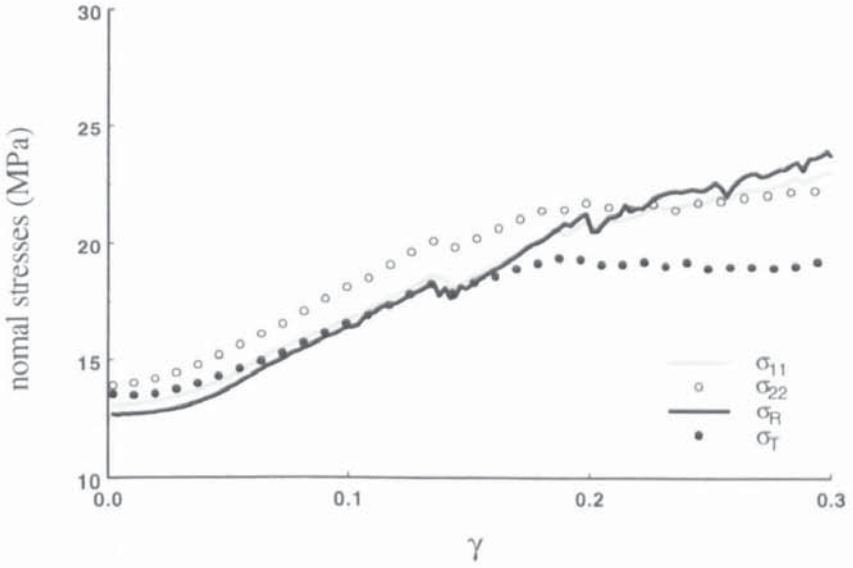

(a) normal stress

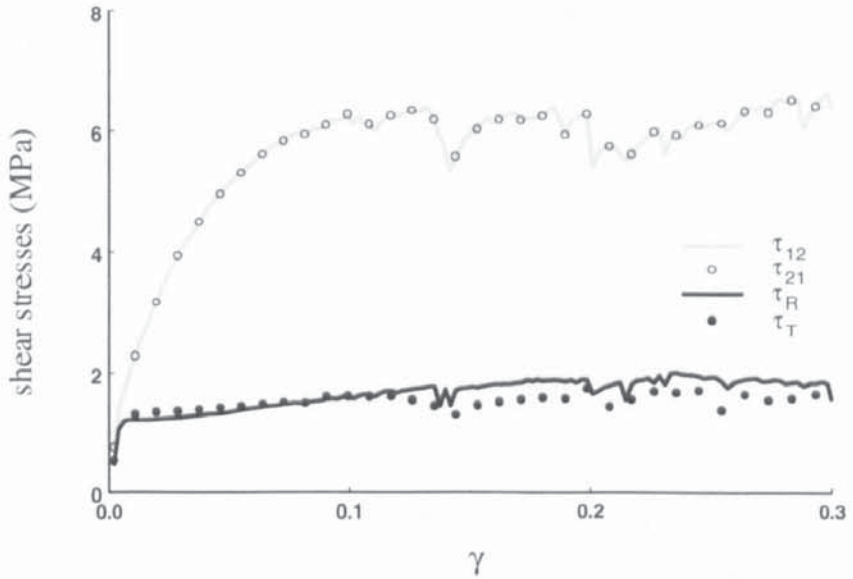

(b) shear stress

Fig. 5.7 Evolution of stresses for $\mu_w = 0.1$

and τ_{21} are identical throughout test, which means that the stress tensor is symmetrical. After 10% strain these values are ca. 3 times greater than the shear stresses τ_R and τ_T which are calculated from boundary measurements (Fig. 5.7b).

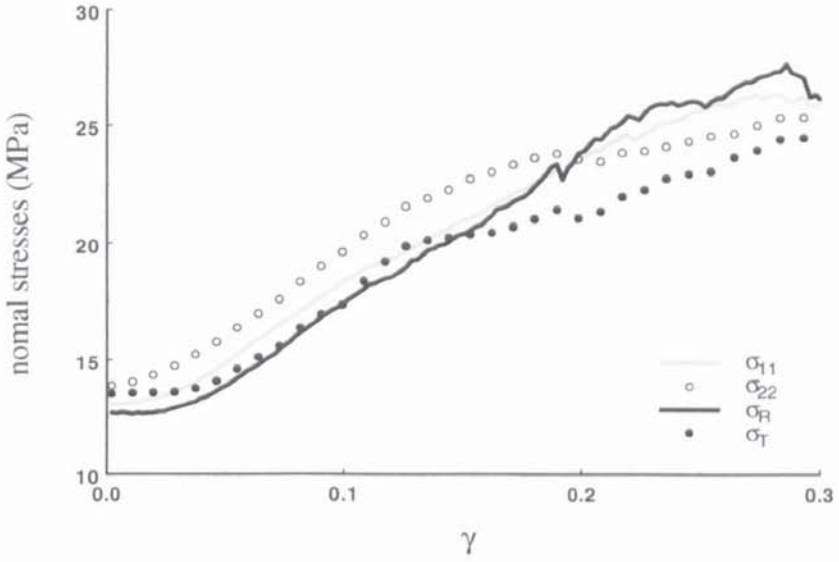

(a) normal stress

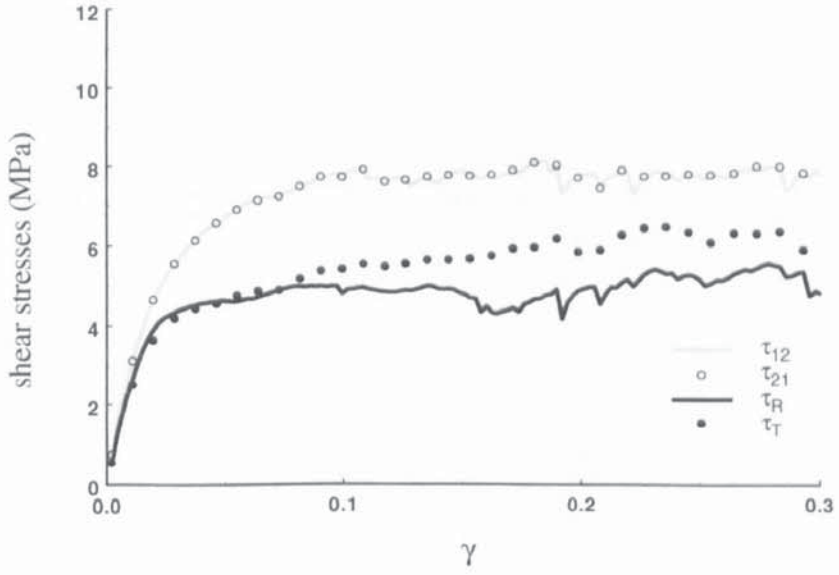

(b) shear stress

Fig. 5.8 Evolution of stresses for $\mu_w = 0.5$

For the samples with higher wall friction (say 0.5), the evolution of the normal stress measured from both wall and volume average information (see Figs. 5.8-9) are similar to those for the sample with the lowest wall friction. However, τ_R and τ_T fluctuate above 5.0MPa for the two samples with higher wall frictions, while for the lowest wall friction

sample they fluctuate around 1.5MPa. Although the shear stresses obtained from the boundaries are lower than τ_{12} and τ_{21} they become closer to the volume averaged values when a higher wall friction value is chosen.

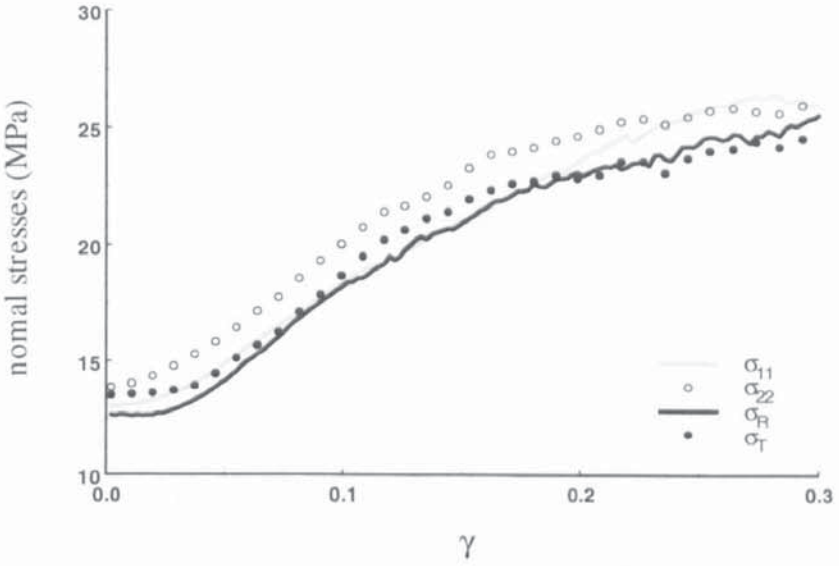

(a) normal stress

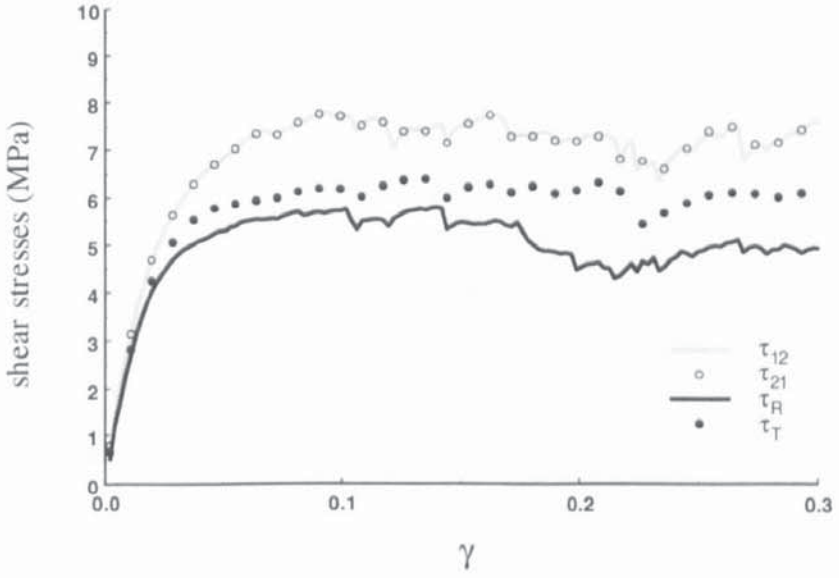

(b) shear stress

Fig. 5.9 Evolution of stresses for $\mu_w = 0.8$

5.5.3 Stress ratios

The evolutions of stress ratios $sin\varphi_m$ and $tan\varphi_c$, together with the force ratio T/N defined by (2.10), (5.6) and (5.7) respectively, are presented in Fig. 5.10. For all three

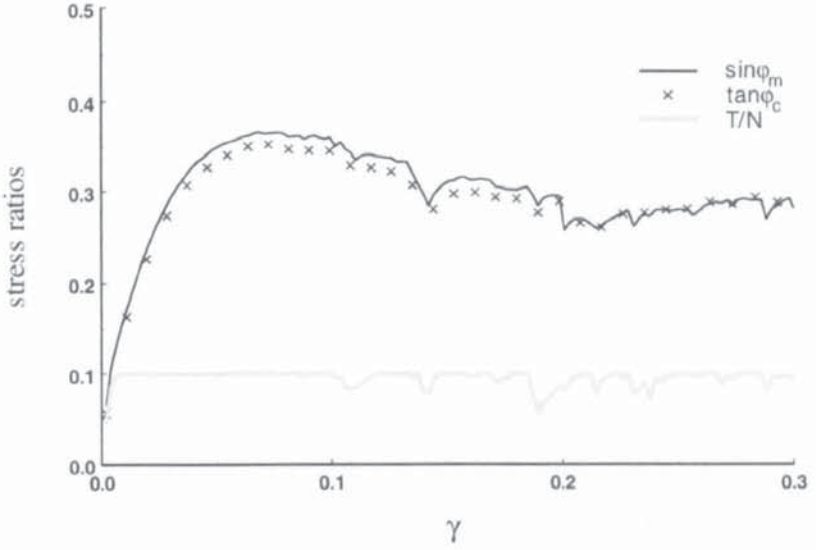

(a) $\mu_w = 0.1$

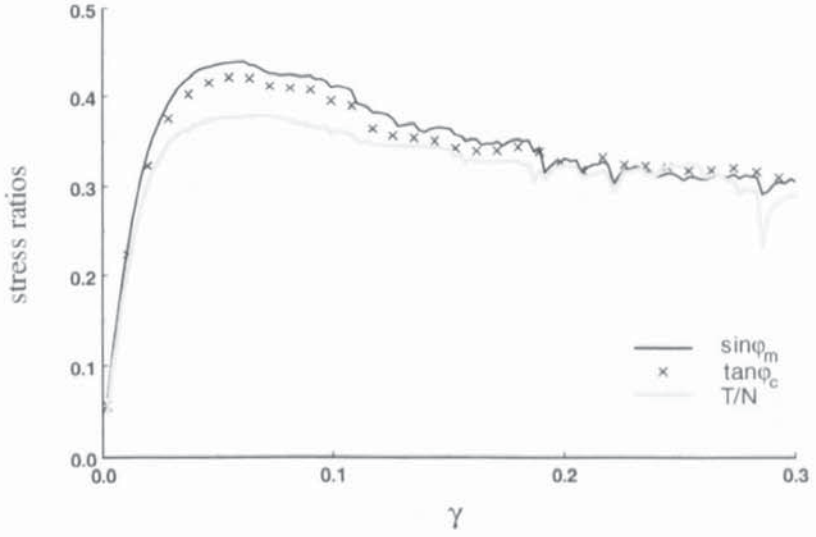

(b) $\mu_w = 0.5$

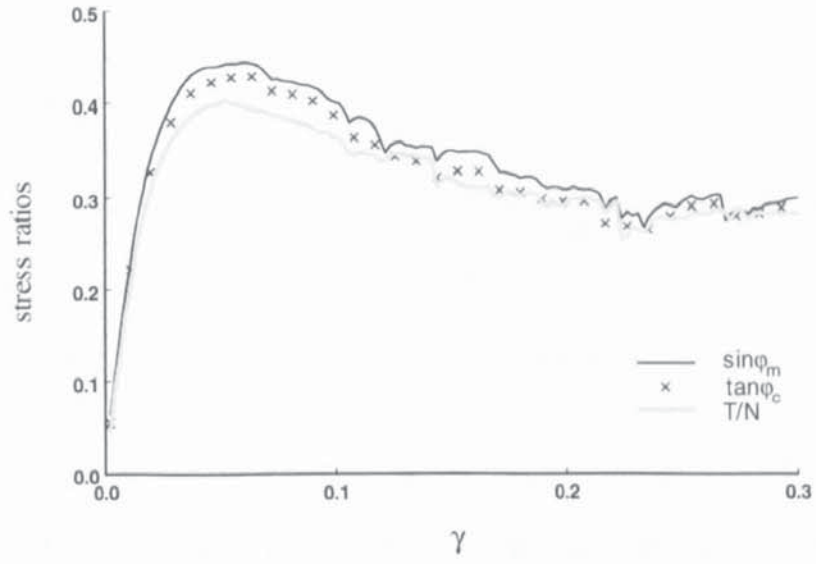

(c) $\mu_w = 0.8$

Fig. 5.10 Evolution of stress ratios

samples $sin\varphi_m$ exhibits the highest value. The maximum value of $sin\varphi_m$ is about 0.37 when $\mu_w = 0.1$, but it reaches a value of ca. 0.44 for samples with higher boundary friction. This implies that boundary friction can significantly affect the measurement of the shear strength of the specimen. When $\mu_w = 0.1$ (Fig. 5.10a) the ratio of *T/N* is essentially equal to the specified wall friction. For $\mu_w = 0.5$ and $\mu_w = 0.8$ the peak values of the ratio *T/N* are about 0.38 and 0.40 respectively. It is interesting to note that for the high wall friction values the three ratios fluctuate around the same value at large strains (Figs. 5.9b and 5.9c). This implies that the critical state shear strength calculated from volume averaging and boundary information are essentially identical, although the peak values of shear strength obtained from boundary information (*T/N*) are lower than the volume averaged values ($sin\varphi_m$, $tan\varphi_c$). Figure 5.10 indicates that the wall stress measurements do not reflect the true internal state of stress but merely provide information about the average mobilised wall friction coefficient. However, the simulations show that the critical state shear strength can be determined from wall measurements provided that the wall friction is sufficiently high.

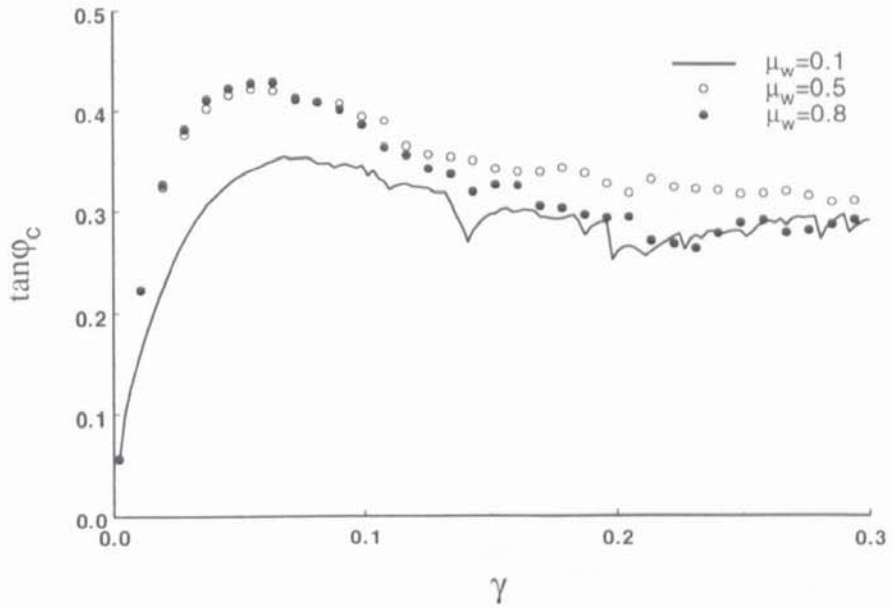

Fig. 5.11 Effect of wall friction on evolution of $tan\varphi_c$

The evolutions of $tan\varphi_c$ for the three samples are shown in Fig. 5.11. The peak values of $tan\varphi_c$ for the two samples with higher wall friction values are very similar and they are 22% higher than that obtained when $\mu_w = 0.1$. After 20% shear strain, $tan\varphi_c$ for all three samples fluctuates about 0.32. It has been shown from Figs. 5.10 – 5.11 that a low peak

value of shear strength is obtained for the sample with a low wall friction. If μ_w is higher than 0.5, the peak shear strength is independent of μ_w. However, essentially the same critical state shear strength is obtained regardless of the wall friction.

5.6 Constant normal stress (CN) tests

The sample with wall friction $\mu_w = 0.5$ was chosen to perform three constant normal stress tests, in which the tests are repeated with different applied constant normal stresses on the top boundary of 10MPa, 15MP and 20MPa respectively. In order to achieve this, the top wall is allowed to move vertically but still has to remain horizontal. Hence the height of the sample changes continuously during the test. The servo control used to adjust the velocity of the top boundary is the same as that used in constant normal stress direct shear tests, which were described in section 4.5.

The vertical displacement of the top wall is shown in Fig. 5.12. The samples contract slightly at the beginning of shearing and, as the sample is sheared further, it starts to expand. For a lower normal stress level the sample contracts less and starts to expand at a smaller shear strain. It is also noted that the sample expands more when a lower normal stress is specified. In all three cases the rate of expansion increases to a maximum value and then decreases until the volume remains constant at large strains, as observed in laboratory tests.

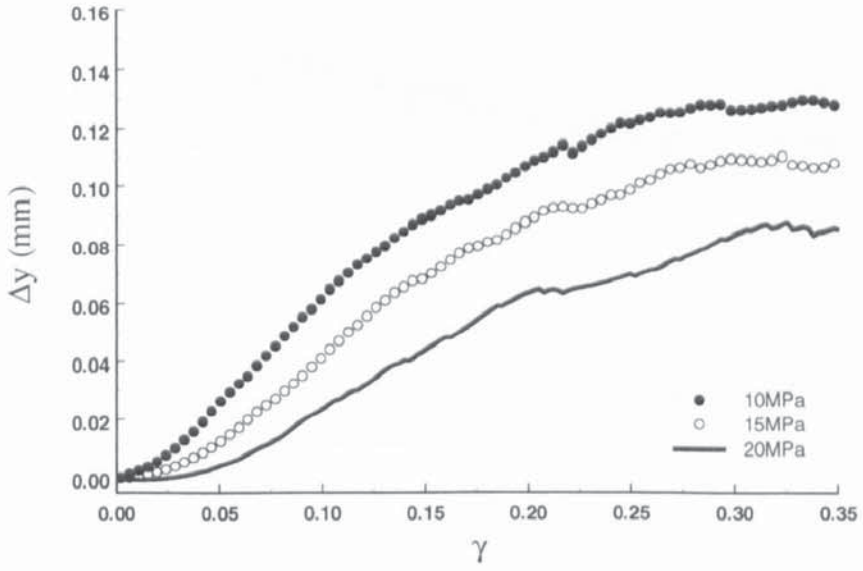

Fig. 5.12 Evolution of vertical displacement

The variation of the ratio of shear to normal stress ($tan\varphi_c = \tau/\sigma$) with shear strain is shown in Fig. 5.13. The maximum stress ratio decreases when the normal stress level increases but all three cases indicate a value around 0.3 at the end of shear. The same trends are obtained for the corresponding tangential to normal force ratio (*T/N*) on the boundary of the samples as shown in Fig. 5.14, except that the maximum values of the force ratios are lower than that of the stress ratios. Therefore the boundary measurements underestimate the shear strength of the sample.

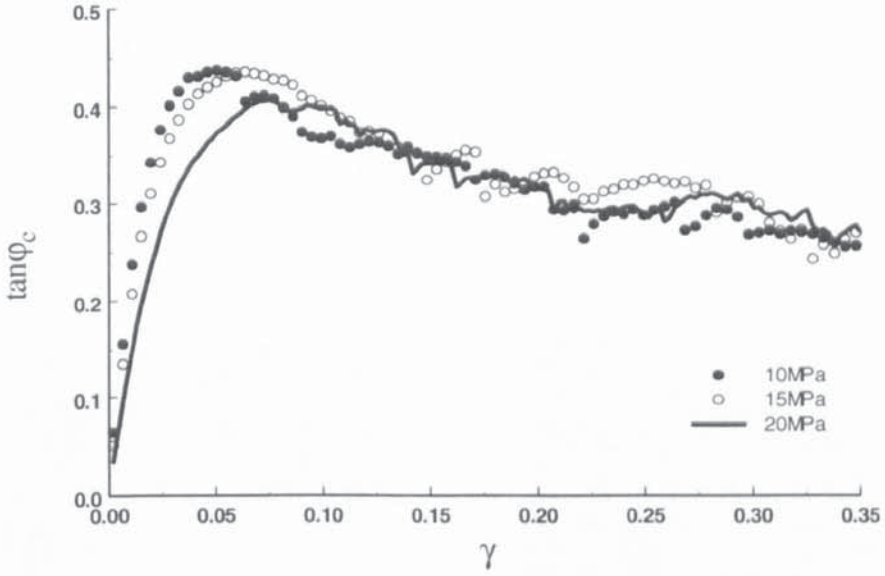

Fig. 5.13 Evolution of $tan\varphi_m$

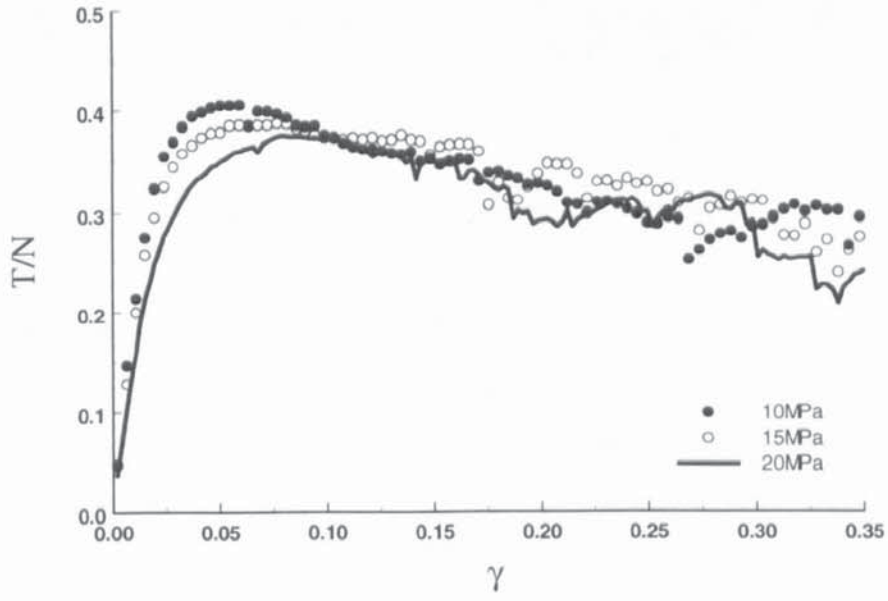

Fig. 5.14 Evolution of force ratio

5.7 Distribution of stress and strain

5.7.1 Distribution of stress

The simple shear apparatus has been particularly criticized because it cannot impose uniform stresses on the specimen. Figure 5.15 examines the force transmission during a simple shear test for a constant top normal stress of 15MPa. Before shearing ($\gamma = 0\%$) the whole sample is stressed uniformly as shown in Fig. 5.15a. As shearing continues the larger than average forces are inclined in order to align with the direction of the major principal stress. Consequently, it is clear from Fig. 5.15b that the normal forces at the contacts with the wall at the left hand side of the top wall are much greater than those at wall contacts at the right hand side; and that it is not clear what the average values of the wall stresses mean exactly in terms of the state of stress in the assembly since the stresses are not distributed uniformly on each boundary or inside the specimen.

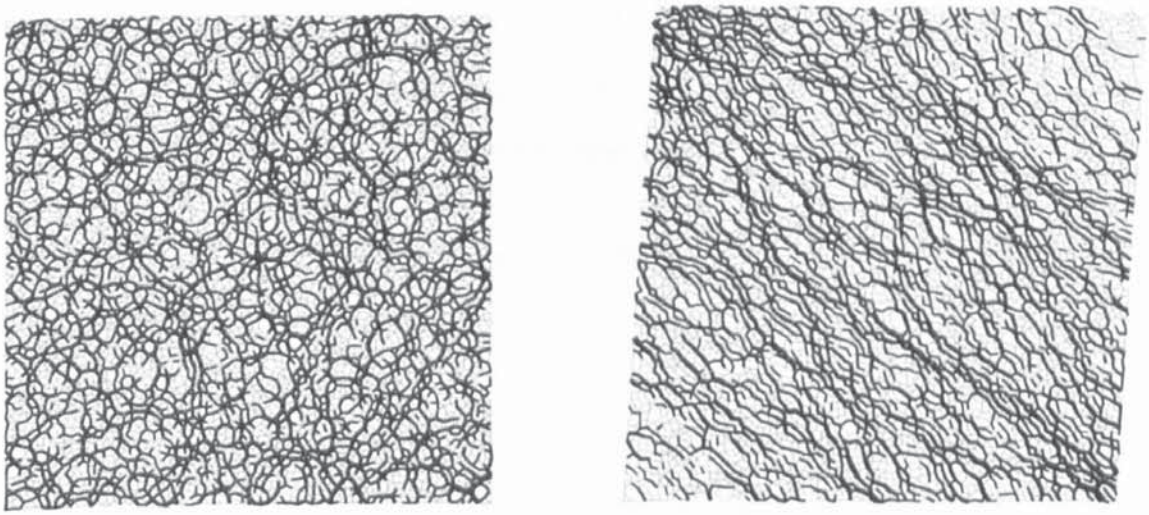

(a) $\gamma = 0\%$ (b) $\gamma = 6.6\%$

Fig. 5.15 Force transmission diagram

In order to further examine the stress distribution inside the sample and its effect on the mobilized shear strength, the sample was divided into three parts (A, B and C) as shown in Fig. 5.16. The stress tensors for each part are calculated separately based on the contact forces within each region.

The evolutions of mean stress for three specified parts of the sample together with the measurement for the whole sample are shown in Fig. 5.17. It is clear that the mean stress

measured from the separate parts fluctuate around the measurement for the whole sample and the maximum difference between the whole sample measurement to three local measurements are normally within 1MPa. The corresponding results of shear strength evolutions are compared in Fig. 5.18. It can be seen that, before peak shear strength, except the result for part *A* that is slightly higher than the others, the measurements from parts B and C are essentially the same as the measurement for the whole sample. After peak, the different measurements start to diverge from each other. At the critical state, the result for part B, which is the middle part of the sample, gives the highest strength at about 0.39 and the others fluctuate around 0.31.

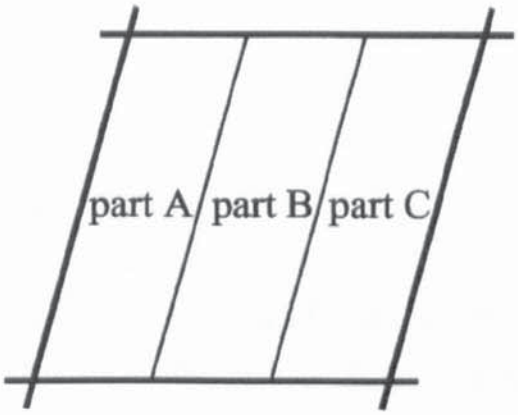

Fig. 5.16 Sub-regions used for stress calculations

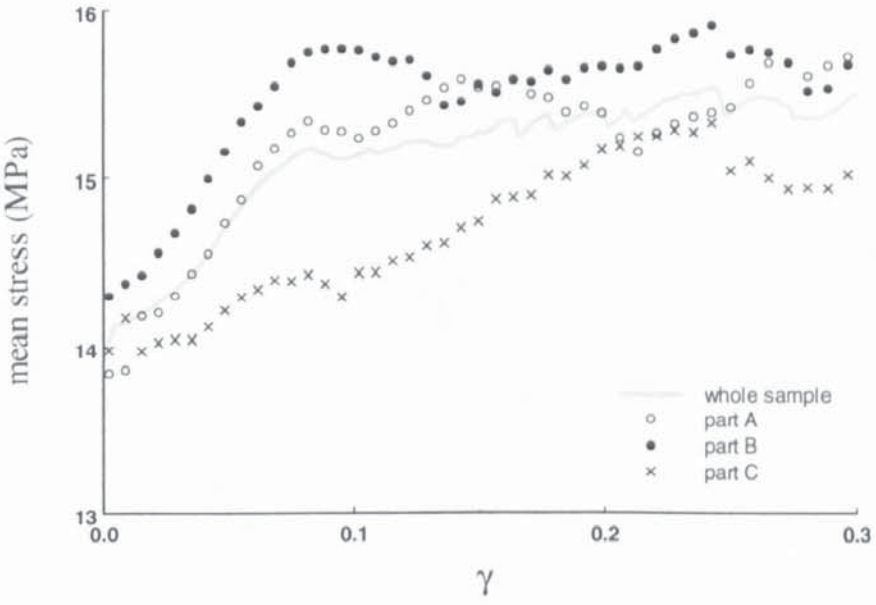

Fig. 5.17 The measurement of mean stress at different locations of the specimen

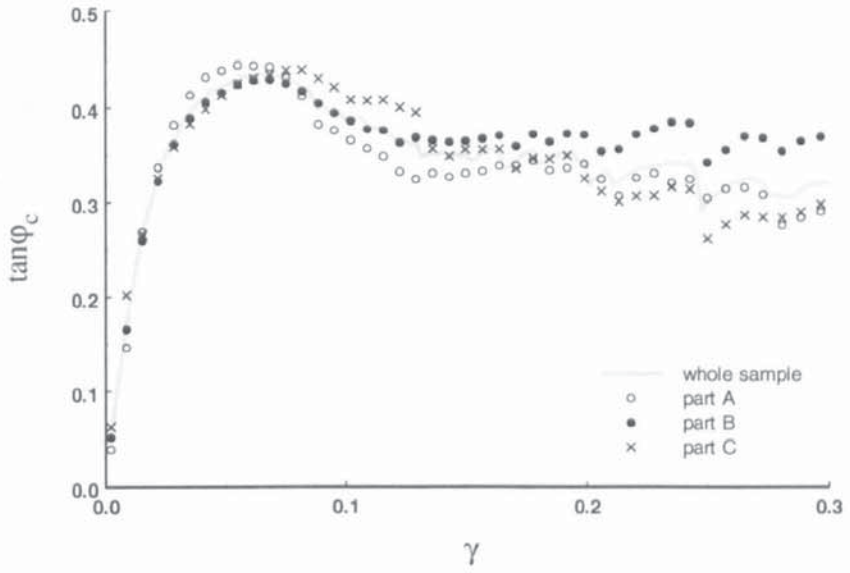

Fig. 5.18 The measurement of $tan\,\varphi_c$ at different locations of the specimen

The aspect ratio of the specimen used in the laboratory is normally less than 1:1. Therefore a simple shear simulation was also carried out on another sample with aspect ratio 1:3. The evolutions of mean stress measured from the different sections of the sample are shown in Fig. 5.19. Before 2% shear strain the different measurements are very close. After 5% shear strain the mean stresses in parts *A* and *B* start to jump sharply. The maximum difference between the whole sample measurement to the three local measurements exceeds 2MPa. Therefore the stress distributions become more non-uniform in such a specimen.

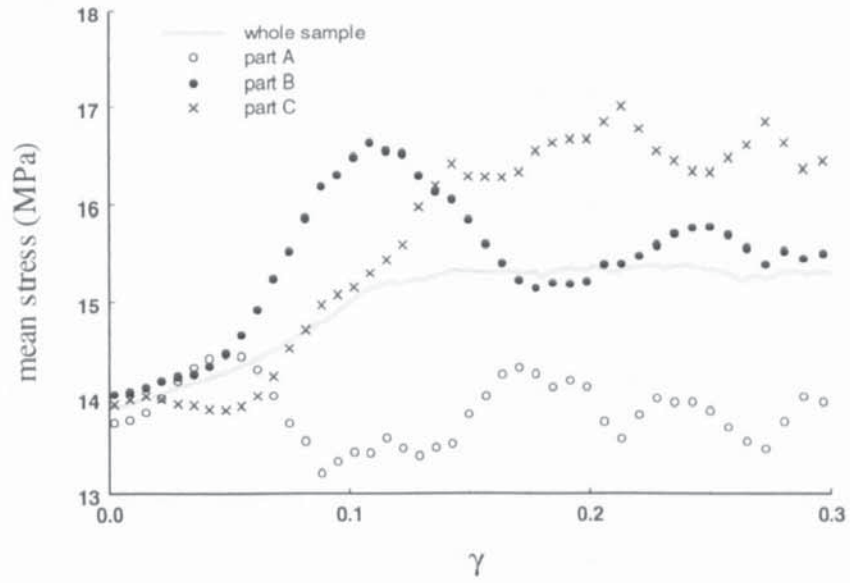

Fig. 5.19 The measurement of mean stress at different locations of the specimen

The relationships between shear strength with shear strain for the same sample are shown in Fig. 5.20. It is clear that the measurement from part A gives the largest peak shear strength at 0.44 and the other measurements give values below 0.4. It also can be seen that the difference between each part are greater when compared to the same set of results shown in Fig. 5.18. The results presented in Figs. 5.17- 5.20 illustrate that if the aspect ratio of the specimen becomes less the stress distribution inside the sample would be more non-uniform. Therefore, it suggests that small aspect ratio specimens should be avoided in the simple shear tests.

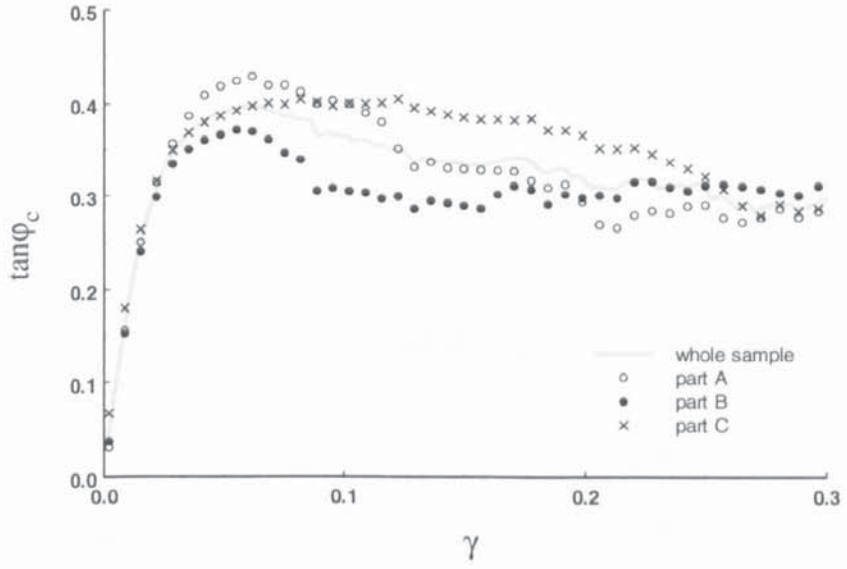

Fig. 5.20 The measurement of $tan\,\varphi_c$ at different locations of the specimen

5.7.2 Distribution of strain

In order to examine the strain distribution in the simple shear test the horizontal displacement increment was measured for every 2.2% increment of shear strain. Figure 5.21 shows the distributions of the horizontal displacement increments during the test. Before 6.6% shear strain the strain is distributed uniformly over the whole sample (pre-peak stage) and is in agreement with the results reported by Budhu (1984) by using radiographic technique. As the sample is sheared further, non-uniformities appear at the top and bottom boundaries and gradually develop into the centre. This is consistent with the numerical analysis of Shen *et al* (1978), who carried out a parametric study and showed that major non-uniformities occur in the specimen near the boundaries. Uniform strain inside the specimen can only be associated with a uniform stress state. Hence,

according to the analysis presented in the last section, the non-uniform stress distribution on the top and bottom wall will be the major cause of such strain localization initiated from the boundaries.

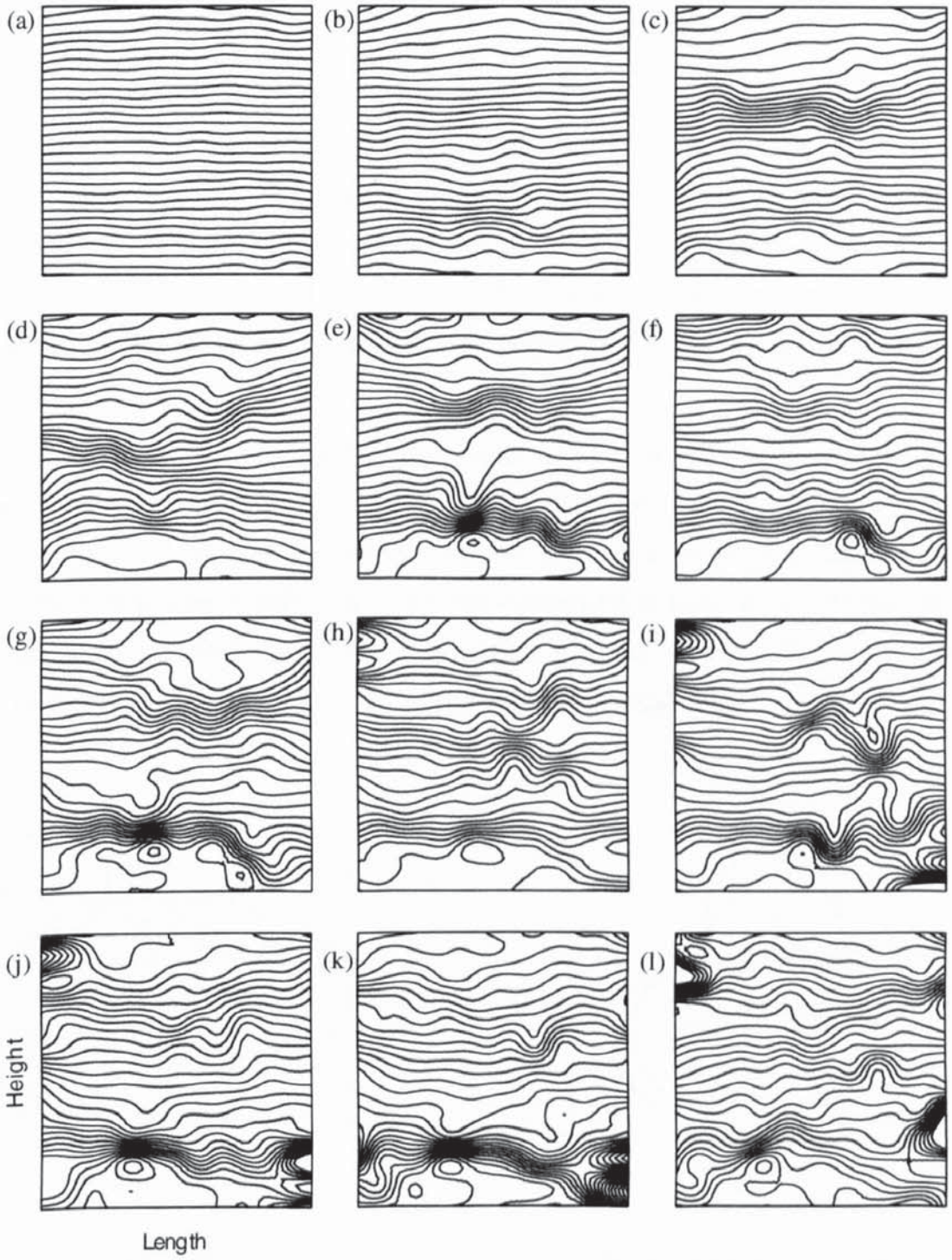

Fig. 5.21 Contour lines of horizontal displacement increments during simulation: (a) 0% - 2.2%; (b) 2.2% - 4.4%; (c) 4.4% - 6.6%; (d) 6.6% - 8.8%; (e) 8.8% - 11%; (f) 11% - 13.2%; (g) 13.2% - 15.4%; (h) 15.4% - 17.6%; (i) 17.6% - 19.8%;(j) 19.8% - 22%; (k) 22% - 24.2%; (l) 24.2% - 26.4%

Although stress and strain non-uniformities are observed inside the sample during the simple shear test, they are not as significant as in the direct shear test, in which the central shear zone is very distinct and extends from one end to the other end of the sample as described in Chapter 4. Therefore the stress and strain distributions in the simple shear test are far more uniform than in the direct shear test.

It has been shown in Fig. 5.5 that deformation causes changes in the particle configuration. At the local scale, rearrangement of the particle locations cannot occur without changes in volume. Therefore, the local expansion and contraction will happen simultaneously with the sample deformation and the balance between expansion and contraction will be reflected in the overall volume change. In the following, the deformation at the local scale is examined by using the graph-theoretical approach.

The graph-theoretical approach has been used to examine the mechanics of granular materials (Satake, 1993b; Bagi, 1996b; Kuhn, 1999). By using such an approach, a granular assembly can be described by a particle graph as shown in Fig.22a. In a particle graph there exist large numbers of loops that correspond to local void cells that are each surrounded by the branch vectors of contacting particles. These cells are used in the simulation to examine the local deformation within individual voids.

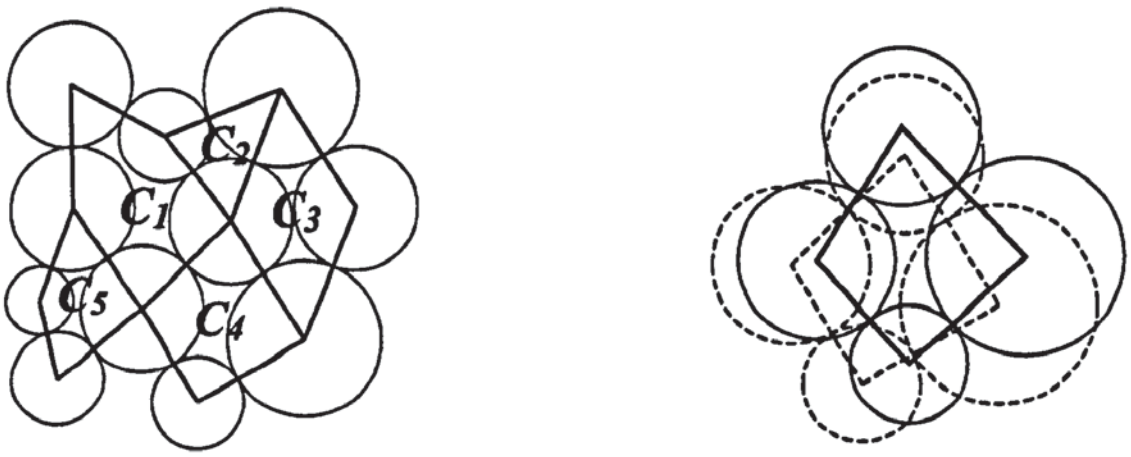

(a) void cell (b) void cell deformation

Fig. 5.22 Particle graph

Let us consider that at instant t_1 the area of void cell C_i is A_i^1 (dashed area in Fig. 5.22b). After an increment of shear strain, the branch vectors forming this void cell have moved to

new positions at instant t_2 (continuous line in Fig. 5.22b). The current area of the void cell C_i is A_i^2, then the difference of the area between this two stages is calculated as:

$$\Delta A_i = A_i^2 - A_i^1 \tag{5.8}$$

If $\Delta A_i > 0$, it means the void cell C_i expands and the difference is noted as ΔA_i^e. In contrast, if $\Delta A_i < 0$, the void cell C_i contracts and the change is referred to ΔA_i^c. Hence, based on this calculation the dilation of local regions can be examined. The summation over all the individual area differences will give the total area of expansion or contraction during this period,

$$\Delta A_e = \sum_{i=1}^{N_e} \Delta A_i^e \tag{5.9}$$

$$\Delta A_c = \sum_{i=1}^{N_c} \Delta A_i^c \tag{5.10}$$

where N_e and N_c are the number of the expanding and contracting void cells, respectively.

The differences in area for local void cells were measured for every 2.2% increment of shear strain and are shown on the left hand side of Fig. 5.23. The black shaded areas represent void cells, which expand with ΔA_i^e over 1/120 times the average single particle area. The other expanding void cells are indicated by the grey shaded areas. For the contracting void cells the areas are not shaded and only the branch vectors are shown. In addition, the values of ΔA_e and ΔA_c during every period are calculated and listed under each diagram. The evolutions of particle rotation during the simple shear test are shown on the right hand side of Fig. 5.21, in which only rotations larger than two degrees are shown. The negative rotations (clockwise rotation) are shown by circles and the solid discs represent the positive rotations (counter-clockwise rotation). The investigation is carried out on the previous constant normal stress test of 15MPa on the top boundary, which was reported in Section 5.6.

It can be seen that during the initial stage up to 2.2% shear strain the contracting void cells are more than the expanding ones (Fig. 5.23a), and the total contracting area is larger than the total expanding area. Recalling Fig. 5.12, the whole sample contracts during this stage.

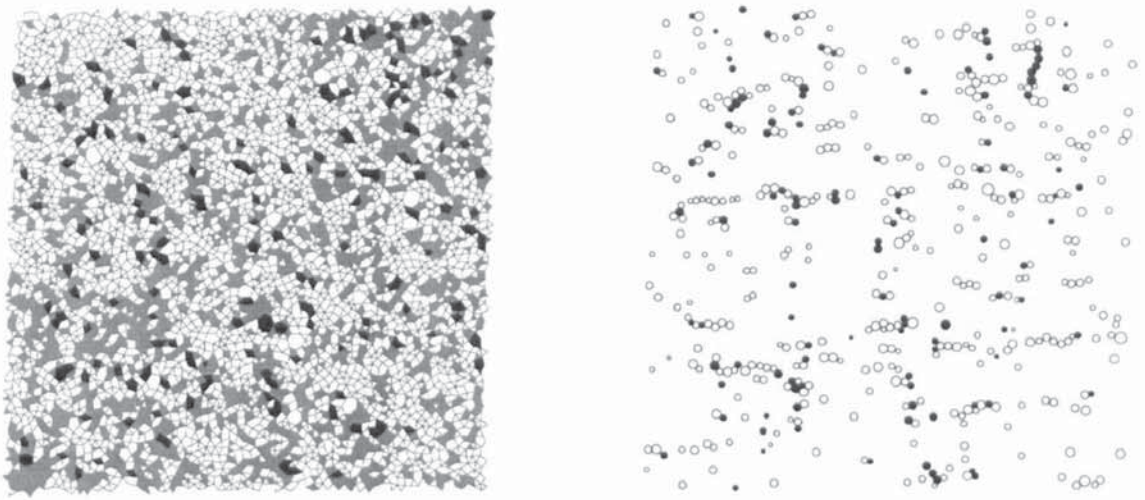

$\Delta A_e = 0.01915mm^2$, $\Delta A_c = 0.03249mm^2$

(a) 0%-2.2%

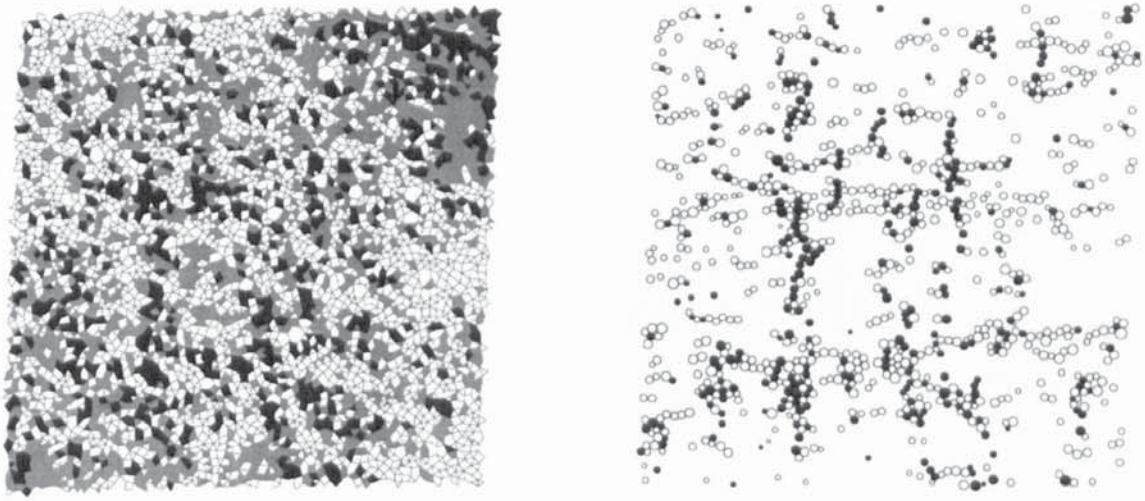

$\Delta A_e = 0.05539mm^2$, $\Delta A_c = 0.03874mm^2$

(b) 2.2%-4.4%

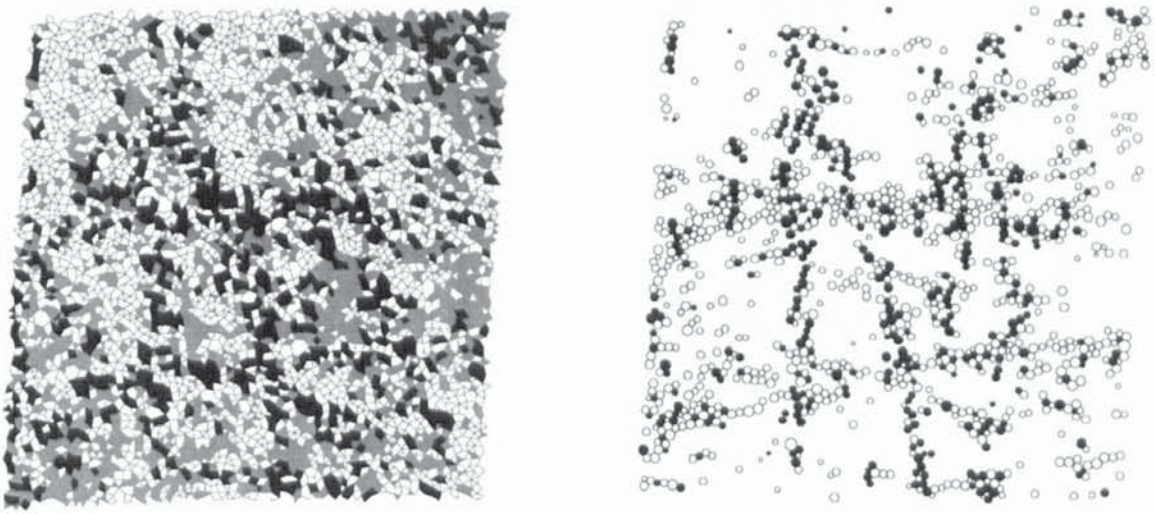

$\Delta A_e = 0.07369mm^2$, $\Delta A_c = 0.04370mm^2$

(c) 4.4%-6.6%

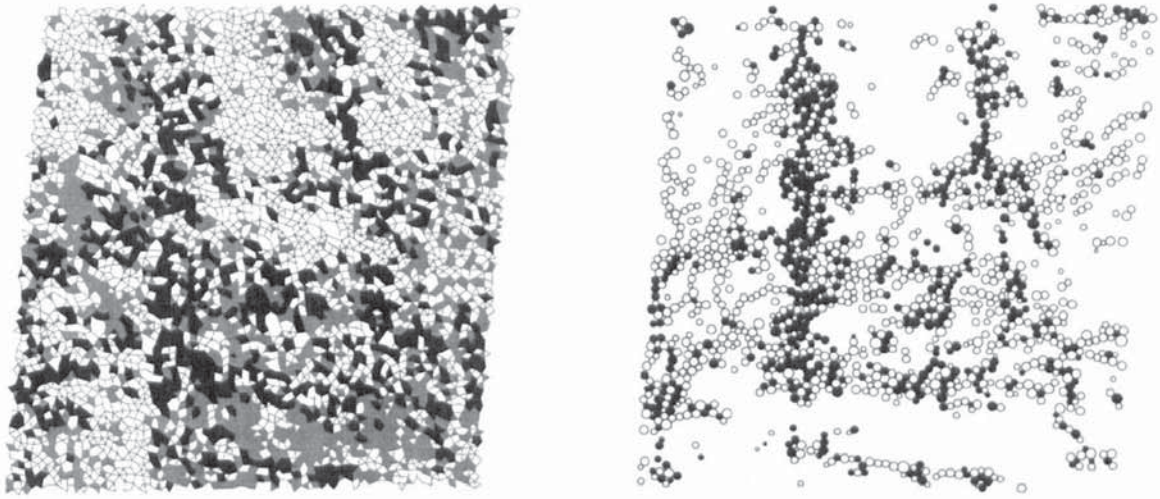

$\Delta A_e = 0.09482mm^2$, $\Delta A_c = 0.06181mm^2$

(d) 6.6%-8.8%

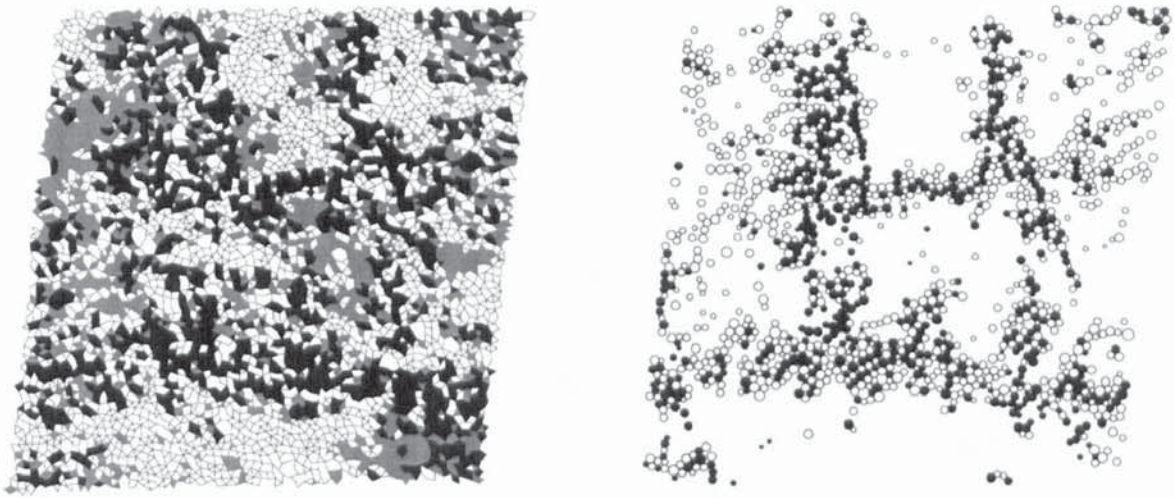

$\Delta A_e = 0.10924mm^2$, $\Delta A_c = 0.06621mm^2$

(e) 8.8%-11.0%

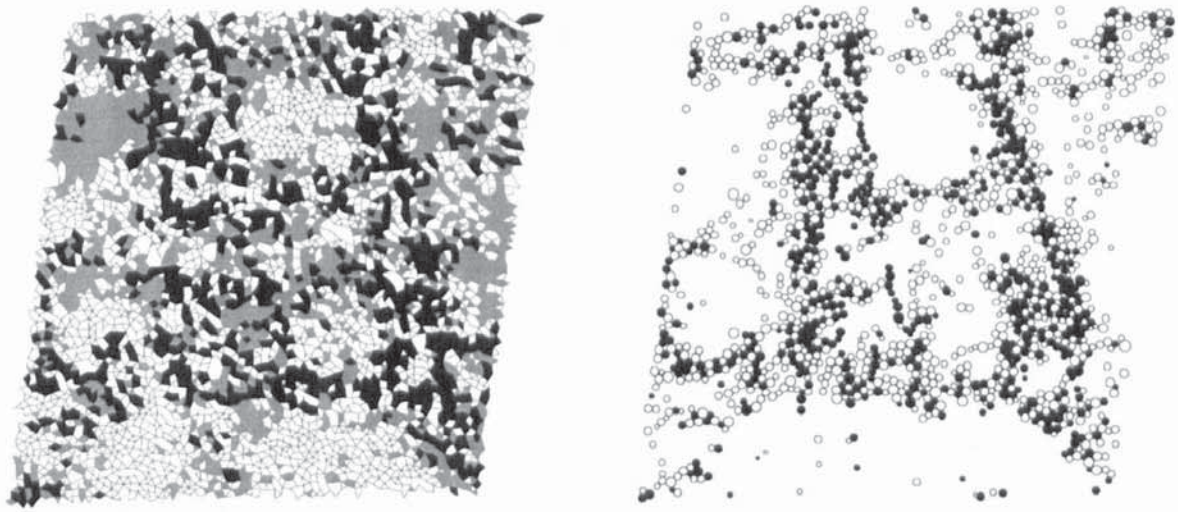

$\Delta A_e = 0.10853mm^2$, $\Delta A_c = 0.06540mm^2$

(f) 11.0%- 13.2%

Fig 5.23 Void cell deformation and particle rotation (constant normal stress of 15MPa)

In addition, the large particle rotations occurred randomly within the sample and most of them are negative rotations, which is in the same direction as the body rotation of the sample. It can be seen from Fig. 5.23 that the number of dark and grey cells increases with strain. The total area of expansion becomes larger than the total contracting area corresponding to expansion of the whole sample. Interestingly, the number of discs in the rotation diagram also increases and large particle rotations occur almost at the same locations as where the large void cell dilations occur. It is clear from Fig. 5.23 that the contracting void cells almost correspond to the area where particle rotations are less than the average rotation. This means that when the void cell dilates it facilitates the particle rotation; on the contrary if the void cell contracts it restricts the particle rotation. In addition, the particles within the big expanding void cells have more freedom to rotation in the opposite direction to the body rotation.

5.8 The effect of initial stress ratio K_0

It has been suggested that the stress-strain response of an elastoplastic material under ideal simple shear is significantly influenced by the initial ratio of horizontal to vertical stress, K_0, and by the degree of dilation, ψ, assumed for the plastic region (Hansen, 1961; Potts *et al*,. 1987). In order to examine the dependence of the results of simple shear tests on these two parameters and the non-coaxial phenomenon of the directions of principal stress and strain rate, three samples were prepared to perform simple shear simulations under both constant volume and constant normal stress conditions. The difference in these three samples is the initial stress ratio $K_0 = \sigma_h/\sigma_v$, which was equal to 0.5, 1.0 and 2.0 respectively.

5.8.1 Stress-strain relationship

Figure 5.24 presents the evolution of the horizontal (σ_h) and vertical (σ_v) normal stresses for both CV and CN tests. The initial states of stress for all cases are clearly shown in this figure. The initial vertical normal stresses for samples with $K_0 = 1.0$, $K_0 = 2.0$ are 12MPa and 10MPa respectively and for the sample with $K_0 = 0.5$ it is 20MPa. They are kept perfectly constant in CN tests. It also illustrates that the two normal stresses σ_h and

σ_v always converge to a same value at the critical state no matter what the initial condition is and which type of test is performed.

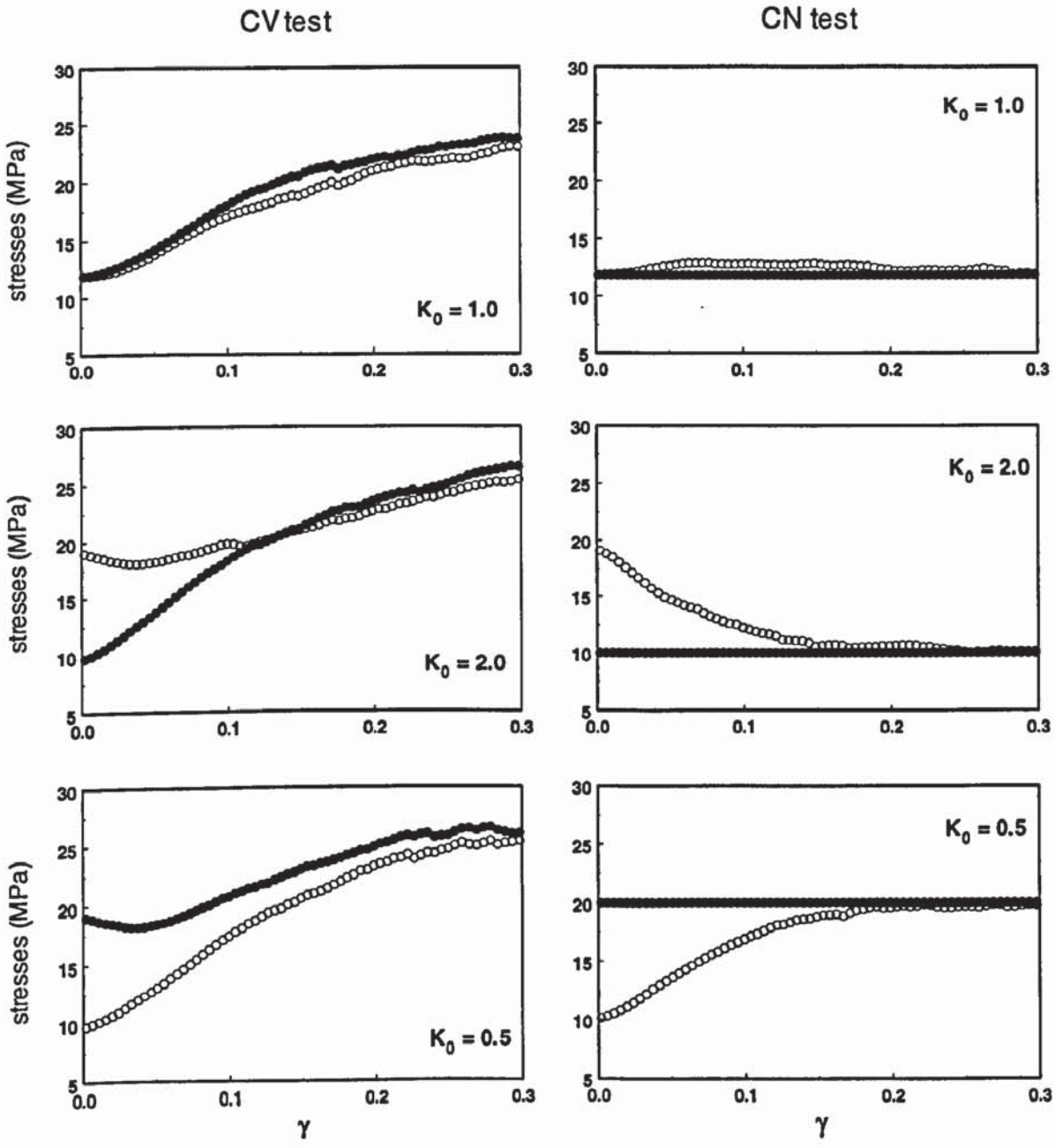

(a) CV test (b) CN test

Fig. 5.24 Development of normal stresses (•: σ_v, ∘: σ_h)

The variations of mean stress with shear strain for all three samples during constant volume tests are shown in Fig. 5.25. The corresponding variations of $tan\varphi_c$ are shown in Fig. 5.26. It can be seen that the mean stresses increase during shearing for all cases. The

samples with $K_0 \neq 1.0$ have the same mean stress both at the beginning and end of test, with a slight divergence around 20% shear strain (Fig. 5.25). It is clear that the sample with lower value of K_0 gives the lower peak stress ratio (Fig. 5.26). Although the evolution of mean stress for the two samples with $K_0 \neq 1.0$ is essentially the same, the evolution of $tan\varphi_c$ is totally different. For the sample with $K_0 = 0.5$ the maximum mobilised stress ratio (about 0.37) is not achieved until 9% shear strain and subsequently

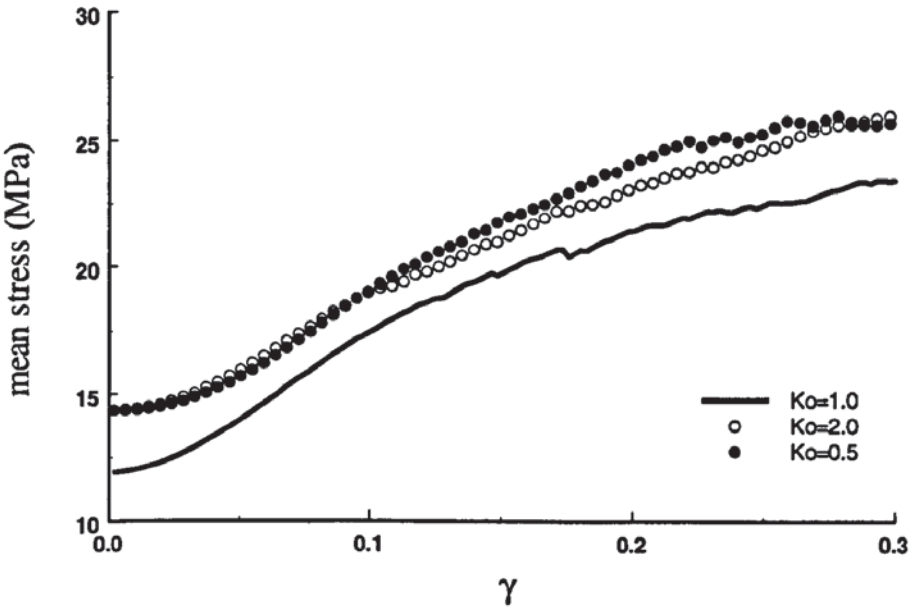

Fig. 5.25 Evolution of mean stress in CV tests

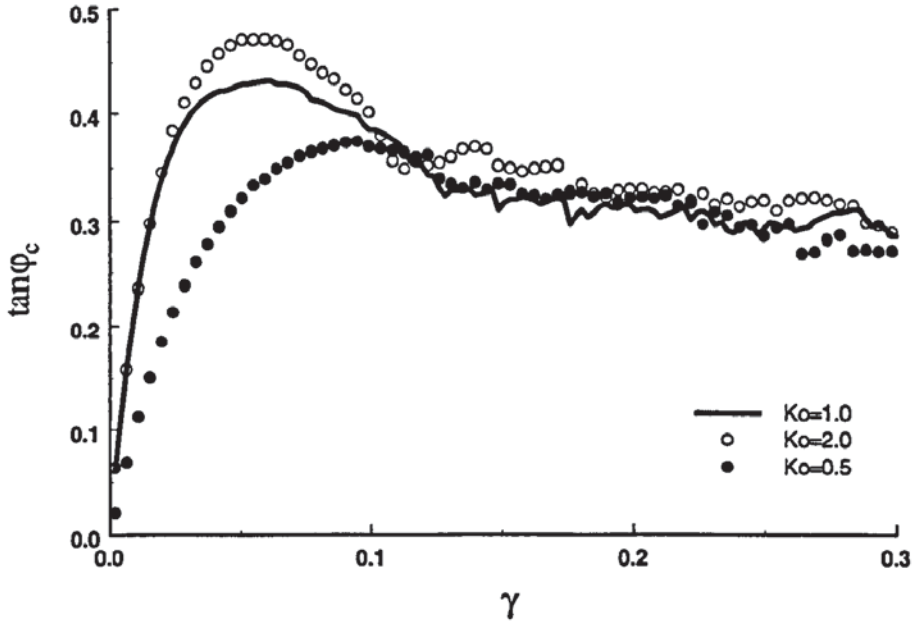

Fig. 5.26 Evolution of $tan\varphi_c$ in CV tests

there is a gradual reduction until the critical state is reached. The peak stress ratios for the other two samples are 0.43 and 0.48 respectively. After reaching the peak at about 5% strain, these samples show a pronounced reduction in mobilised shear strength. The stress-strain relationships of these two cases are similar to the behaviour for the dense sample shown in Fig. 2.2. Nevertheless, there is close agreement for all three cases after 12% shear strain. The results indicate that the parameter K_o plays a very important role in the shear behaviour of the granular materials prior to the critical state.

Figure 5.27 shows the changes in the vertical sample dimension during shear in the constant normal stress tests. It is clear that the sample with the least K_o value shows the greatest contraction at the beginning of the test and least expansion by the end of test, when compared to the other two cases. The evolutions of $tan\varphi_c$ for all cases are shown in Fig. 5.28. It is interesting to note that the results of samples with $K_o \leq 1.0$ are quantitatively similar to the results observed in the constant volume test. However, the peak stress ratio for the sample with the highest K_o decreases 9% in the constant normal stress test. It is conventional to expect that low sample dilation corresponds to low peak stress ratio. This is true for the sample with $K_o = 0.5$ in the simulation. However, for the two samples with $K_o \geq 1.0$, the peak values of stress ratio are almost identical but the sample with the higher K_o exhibits significantly greater expansion.

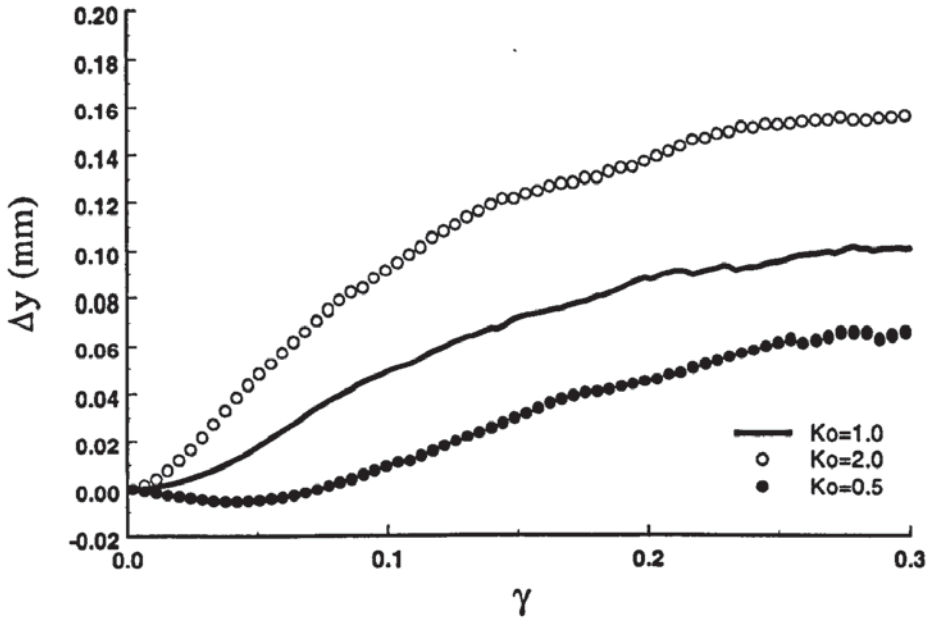

Fig. 5.27 Evolution of Δy in CN tests

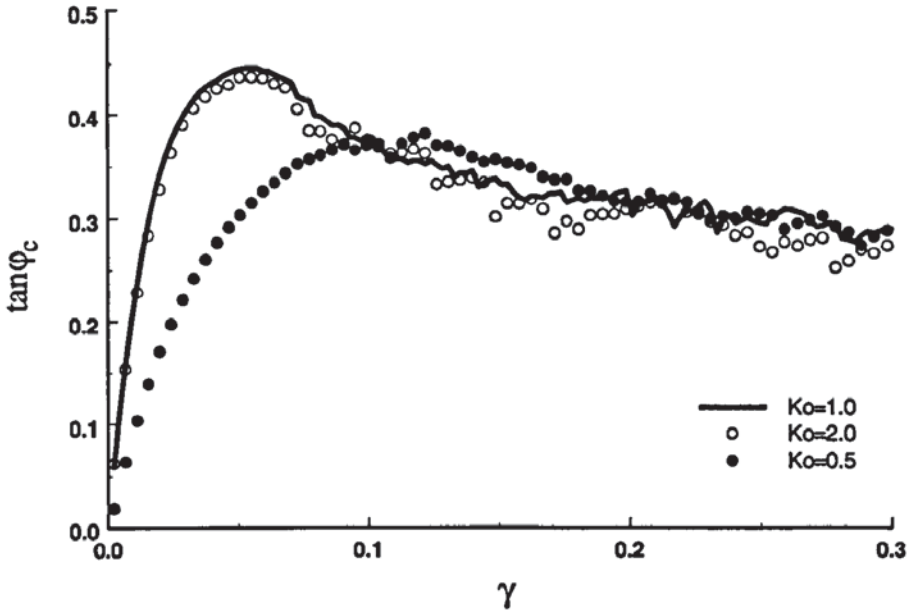

Fig. 5.28 Evolution of $tan\varphi_c$ in CN tests

The correlation between the average particle rotation and the sample body rotation ($\theta/2$), see Fig.5.4, for all three samples is shown in Fig. 5.29, in which the dashed line denotes the condition where the average particle rotation is equal to $\theta/2$. It can be seen that, for the sample with initial $k_0 = 0.5$, the average particle rotation is slightly larger than $\theta/2$. For the other two samples the average particle rotations are less than $\theta/2$.

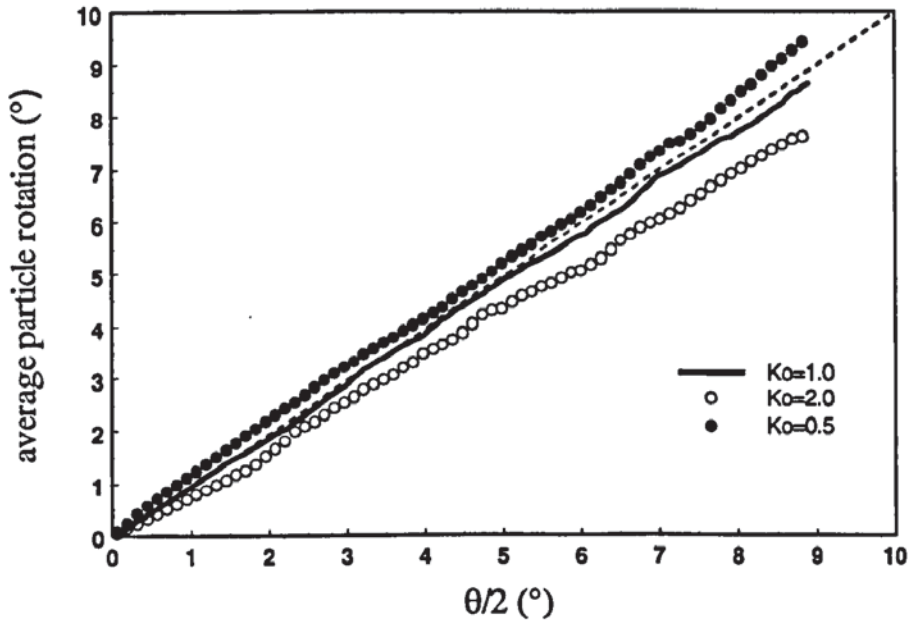

Fig. 5.29 Relationship between average particle rotation and body rotation

5.8.2 Deformation patterns

In the traditional experiment, the uncertainty about the stress tensor arises because no information is available about the horizontal normal stress σ_h or σ_{II}. It can be assumed that at failure the horizontal plane on which the stress combination (σ_v, τ) acts could be any of the following three cases (Airey *et al.*, 1985):

(a) It could be a plane of maximum stress obliquity so the Mohr friction angle (Fig. 5.30a) is,

$$tan\,\varphi_m = \frac{\tau}{\sigma_v} \tag{5.11}$$

(b) Alternatively, it also could be a plane of maximum shear stress (Fig. 5.30b) so that

$$sin\,\varphi_m = \frac{\tau}{\sigma_v} \tag{5.12}$$

(c) A further possibility was proposed by de Josselin de Jong (1972, 1988) using a book-stack analogy. Externally observed simple shear deformation of a pile of books can be produced by the sliding of each book on a horizontal plane (Fig. 5.31a), but the same external effect is found when each book in a row of the same books is allowed to slide on a vertical plane and then the whole row is rotated (Fig. 5.31b). The sliding mode shown in Fig. 5.31a corresponds to the state of stress illustrated in Fig. 5.30a. The mode of sliding shown in Fig. 5.31b corresponds to the state of stress illustrated in Fig. 5.30c and the Mohr friction angle is obtained from

$$\frac{sin\,\varphi_m\,cos\,\varphi_m}{1+sin^2\,\varphi_m} = \frac{\tau}{\sigma_v} \tag{5.13}$$

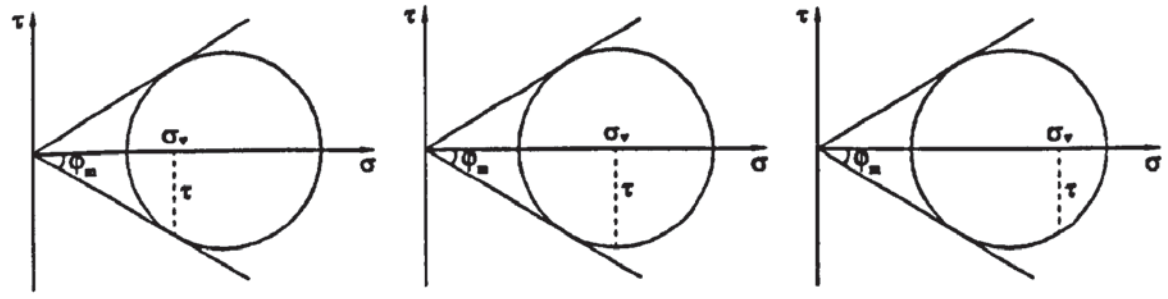

(a) (b) (c)

Fig. 5.30 Possible Mohr circles for simple shear state of stress

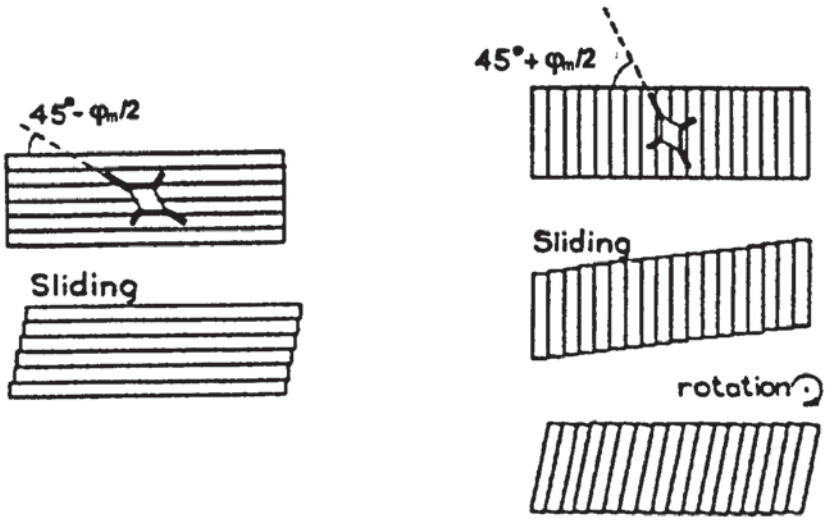

(a) (b)

Fig. 5.31 Book-stack analogy of simple shear deformation proposed by de Josselin de Jong (1972)

De Josselin de Jong suggested that the vertical failure planes plus rotation mode would usually be the easiest one for the soil to choose. This conclusion is to some extent governed by the initial stress state (K_0 condition) of the sample at the start of the simple shear deformation.

In order to examine the simple shear deformation pattern proposed by de Josselin de Jong the sample with $K_0 = 0.5$ is colour-banded in both the horizontal and vertical directions before shearing. The particle configurations at the end of the simulation are illustrated in Fig. 5.32, from which it not very clear whether the deformation follows the pattern shown in Fig. 5.31a or Fig. 5.31b. It is also noted that the particle configuration at the end of shearing for this sample is very similar to the result shown in Fig. 5.5.

The evolution of horizontal displacement increments during the test is presented in Fig. 5.33. The contour lines of horizontal displacement increment shown in this figure are similar to those shown in Fig. 5.21, which is from the simulation on a sample with $K_0 \approx 1.0$. It is clear that no significant strain localization in the vertical direction can be observed. Therefore the initial stress condition does not appear to affect the deformation pattern in simple shear test, as implied by de Josselin de Jong.

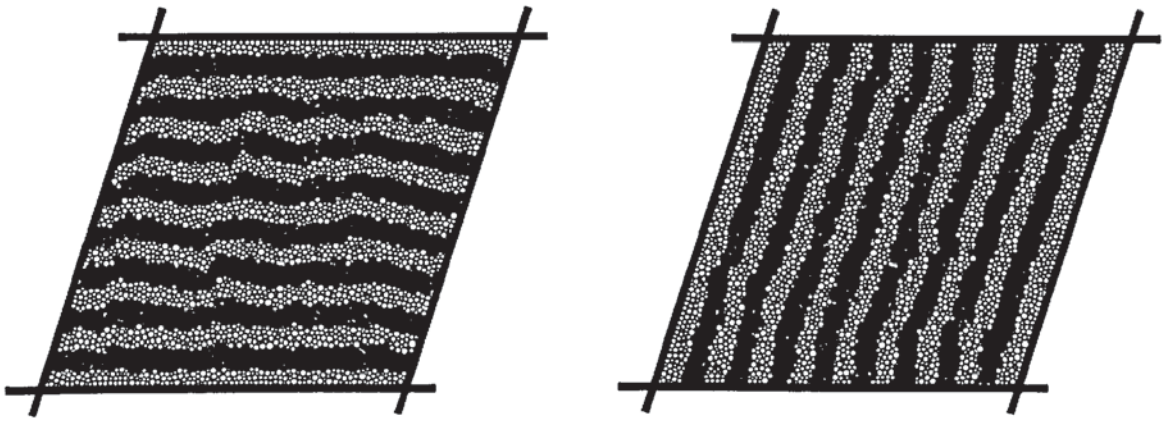

(a) horizontal colour banded (b) vertical colour banded

Fig. 5.32 Particle configuration for the sample of $K_0 = 0.5$

From the previous analysis in Chapter 4 it was found that particle rotations are high within shear bands and low everywhere else. The evolution of particle rotation during the above test carried out on the sample with $K_0 = 0.5$ is shown in Fig. 5.34. In this figure only the rotations greater than 1° are shown. It can be seen that most of the particle rotations are negative at the initial stage. Particles with positive rotations become more prevalent when the sample is sheared further. It becomes clear that the negative rotations are concentrated into horizontal bands and the positive particle rotations appear in vertical bands. There is no single strong strain localization that can be observed inside the specimen from both the contours of horizontal displacement increments and the evolution of particle rotations. Hence, based on the above results it is suggested that during simple shear deformation the sample does not have a preferred deformation pattern. For the samples with different initial values of K_0 the deformation patterns are essentially the same. In addition, the uniformity of strain distribution is much better in the simple shear test than in the direct shear test.

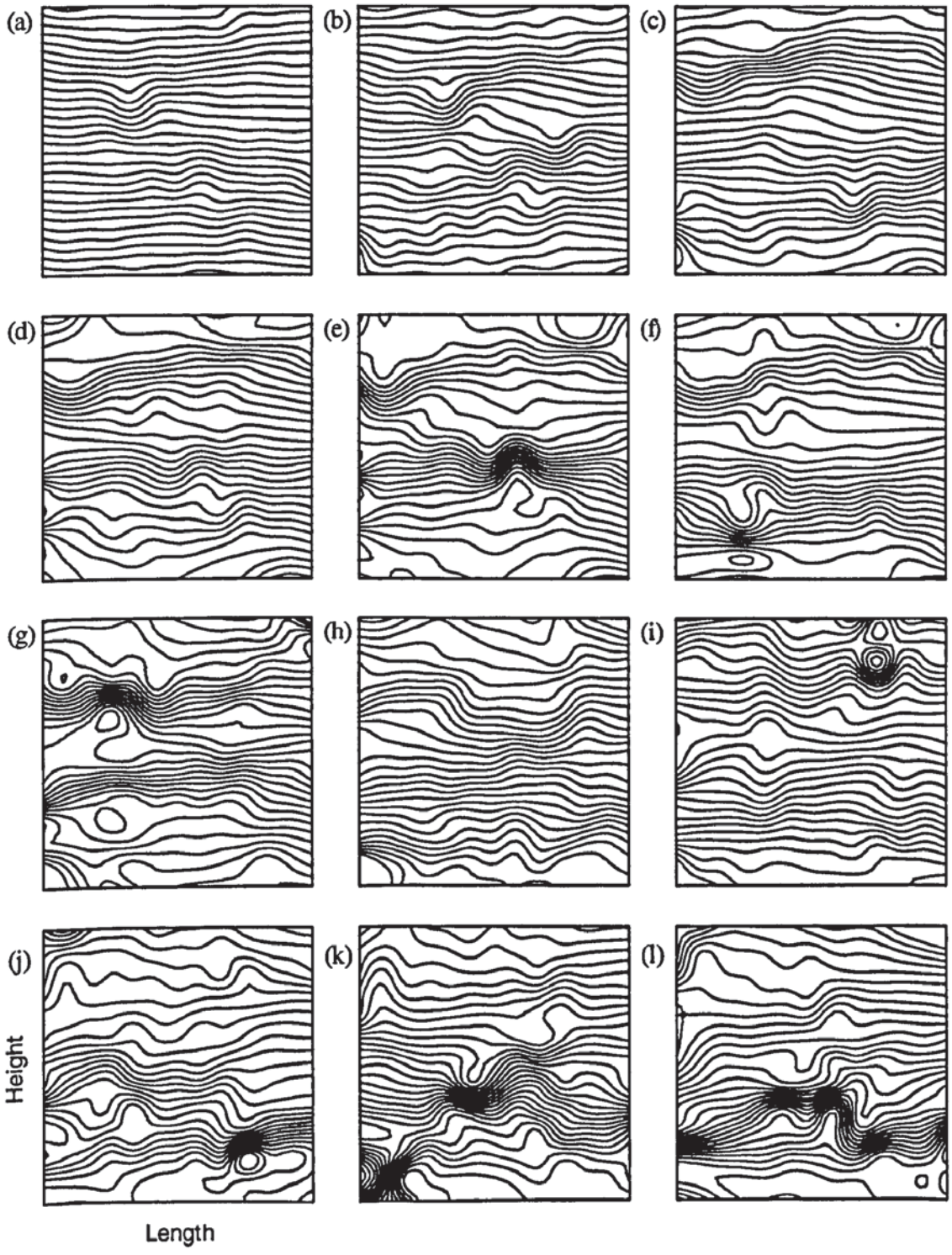

Fig. 5.33 Horizontal displacement increments during the test for $K_o = 0.5$:
(a) 0% - 2.2%; (b) 2.2% - 4.4%; (c) 4.4% - 6.6%; (d) 6.6% - 8.8%; (e) 8.8% - 11%;
(f) 11% - 13.2%; (g) 13.2% - 15.4%; (h) 15.4% - 17.6%; (i) 17.6% - 19.8%;
(j) 19.8% - 22%; (k) 22% - 24.2%; (l) 24.2% - 26.4%

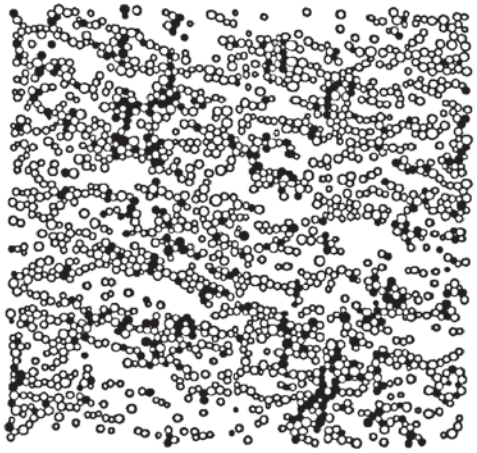

(a) 0% - 2.2%

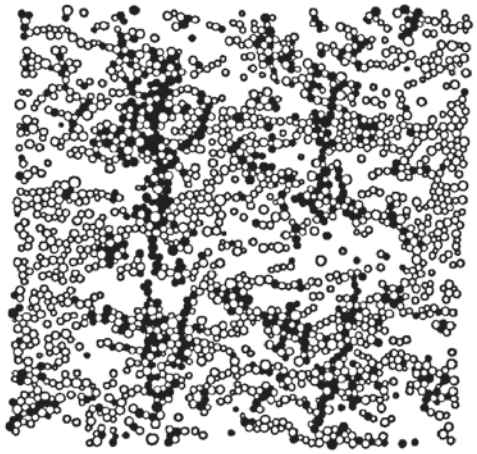

(b) 2.2% - 4.4%

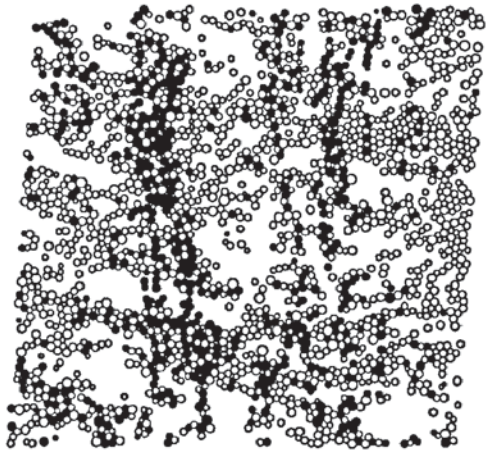

(c) 4.4% - 6.6%

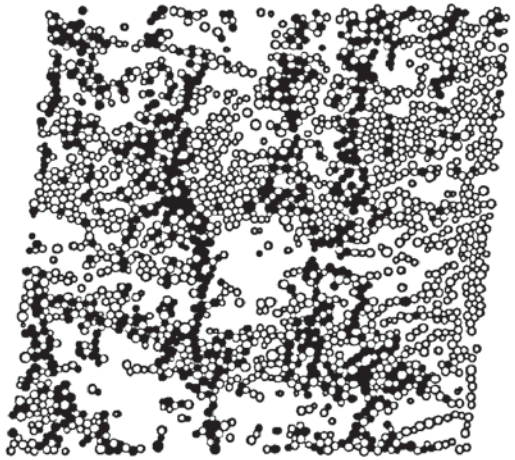

(c) 6.6% - 8.8%

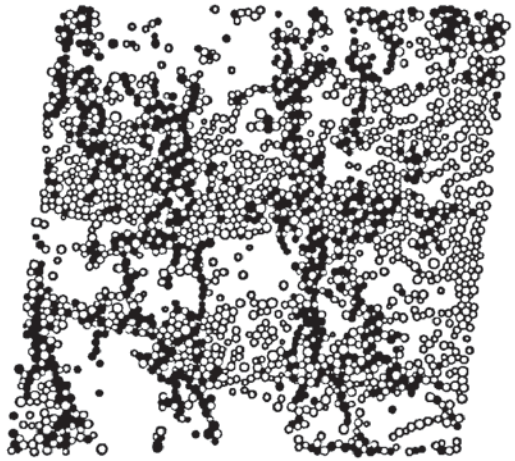

(d) 8.8% - 11%

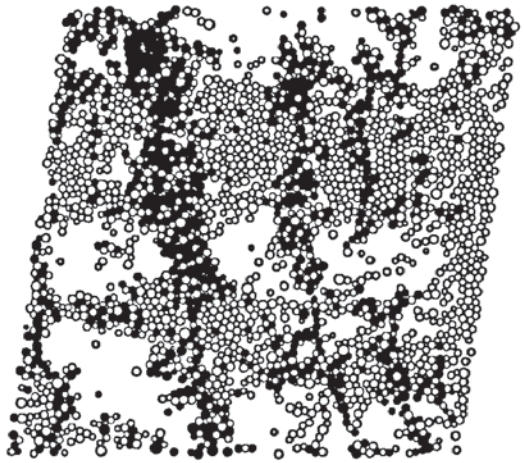

(c) 11% - 13.2%

Fig. 5.34 Particle rotation

5.8.3 Non-coaxiality

The orientations of the major principal stress σ_1 and major principal strain rate $\dot{\varepsilon}_1$ to the horizontal direction during the test are presented in Fig. 5.35 for all the samples. For $K_0 = 1.0$, the direction of principal stress essentially matches the direction of strain increment (Fig. 5.35a). Initially, the σ_1 direction is horizontal (0° to the horizontal) for $K_0 = 2.0$ and is vertical for the sample with $K_0 = 0.5$ (90° to the horizontal). The major principle stress direction rotates at a decreasing rate for both cases: rotating clockwise if $K_0 = 2.0$ (Fig. 5.35b) and counter-clockwise if $K_0 = 0.5$ (Fig. 5.35c). Eventually, for all cases, the principal stress directions are inclined at 45° to the horizontal at the critical state, as shown in Fig. 5.35.

As shown in Fig. 5.35, at the critical state, the major principal stress is always inclined at 45° to the horizontal plane, which is the same as the results obtained from the simulations of the direct shear test. Therefore, the Mohr circle interpretation presented in Fig. 5.30b correctly defines the stress state for the specimen at the critical state.

Figure 5.36 shows the evolution of the angle of non-coaxiality i (the difference between the direction of principal strain rate and principal stress) for each test. For the sample with $K_0 = 1.0$ the non-coaxiality is not significant as the angle i fluctuates around 0° throughout the tests. However, for the other two samples, non-coaxiality is very significant before 10% shear strain. Eventually, the principal stress direction matches the principal strain rate direction at the critical state for all the cases.

The evolutions of the dilation angle are shown in Fig. 5.37. It is clear that before 10% shear strain the sample with the highest initial K_0 has the highest dilation angle. At the critical state, in all cases, the dilation angle fluctuates around zero. It is clear from Figs. 5.36-37 that not only the angle of non-coaxiality but also the rate of dilation are affected by the initial difference between the two orthogonal normal stresses. In the laboratory, during the sample preparation stage, the sample is consolidated before it is used to perform a shear test. Therefore, the initial stress state of the sample is more likely to be $K_0 < 1.0$. Since the non-coaxiality is significant at strain less than 10%, as shown in

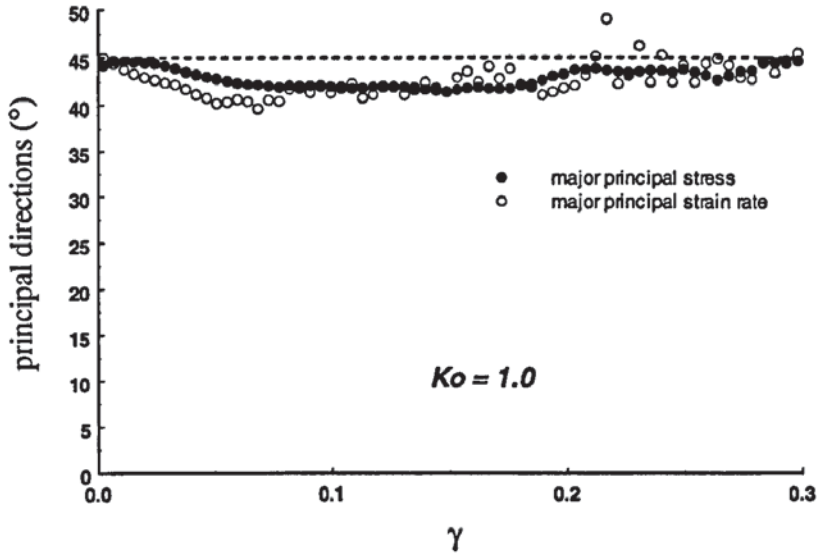

(a)

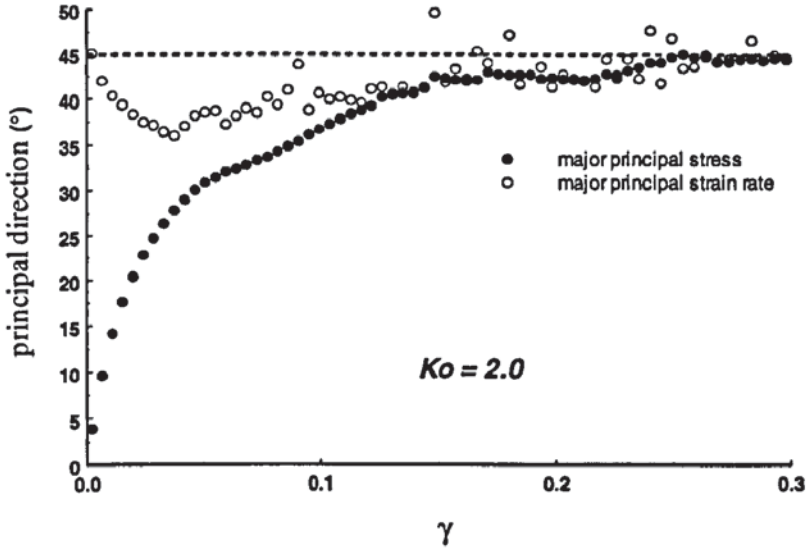

(b)

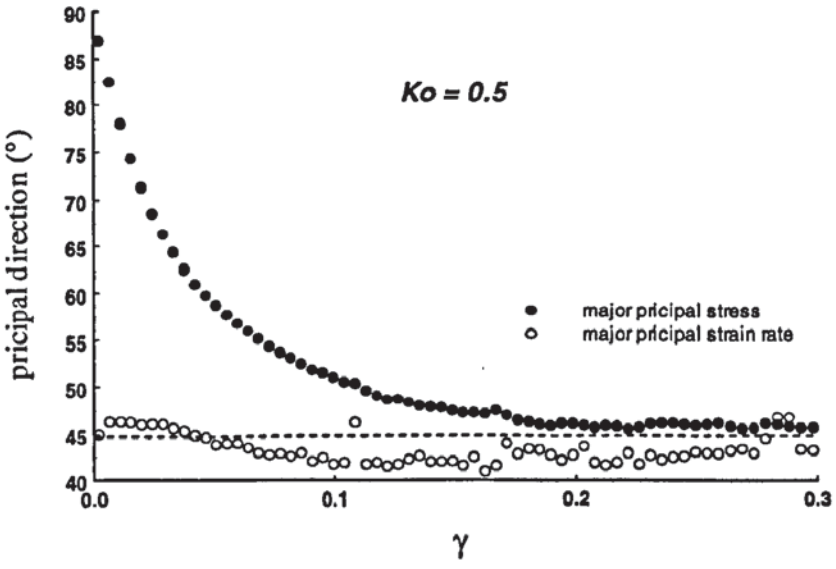

(c)

Fig. 5.35 Major principal stress and strain rate orientations

Fig. 5.36, the traditional soil mechanics interpretation based on the assumption of coaxiality between the principal stress and principal strain rate direction cannot reliably determine the maximum stress ratio.

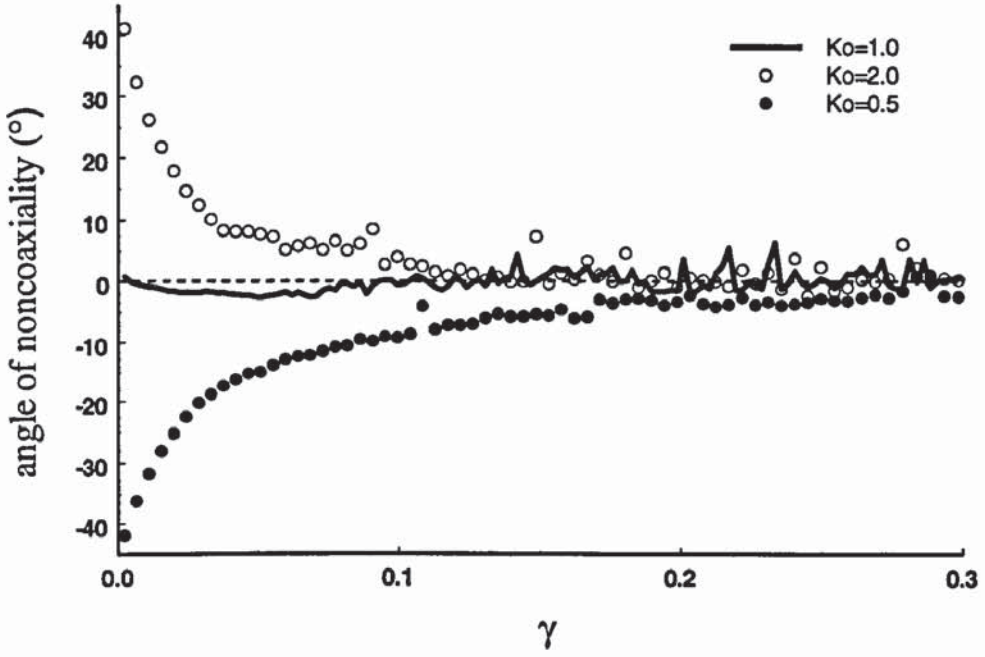

Fig. 5.36 Variation of non-coaxiality angle

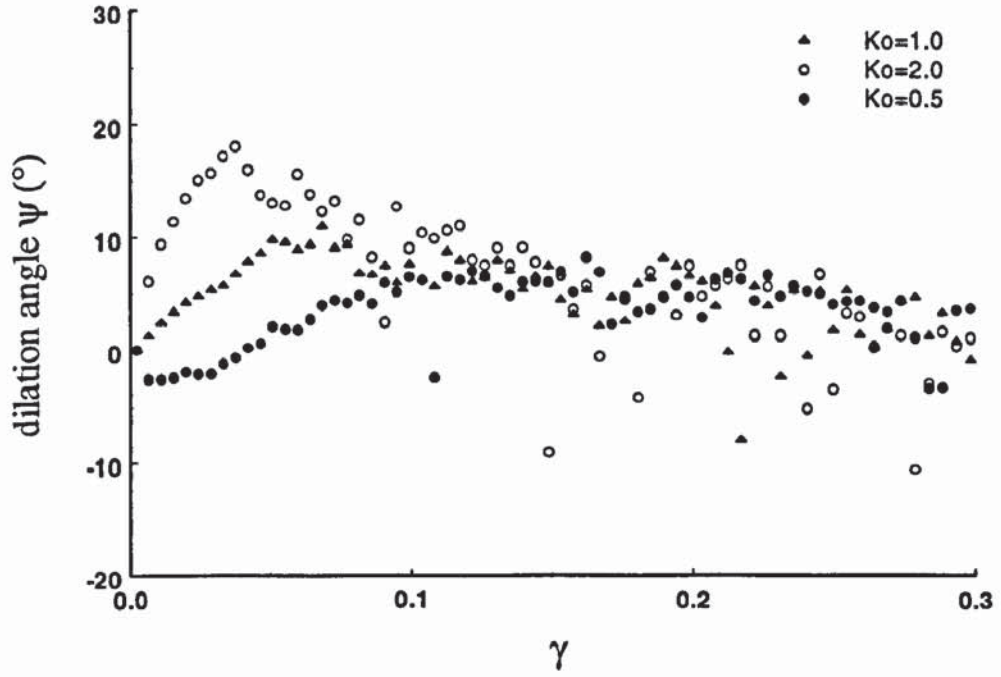

Fig. 5.37 Variation of dilation angle

As described in Chapter 4, by assuming that the direction of the major principal stress σ_1 coincides with the direction of major principal strain increment $\dot{\varepsilon}_1$, the relationship between φ_m and φ_c is given by (4.3). However, the principal axis of stress is not necessarily coincident with the principal axis of incremental strain, as reflected by Figs. 5.35-36. Taking account of this fact, equation (4.3) is modified to (4.22). The angle of non-coaxiality i is defined as the difference between the direction of principal strain rate and principal stress. If let $\theta = \psi + 2i$, Equation (4.22) can hence be rewritten as,

$$\tan\varphi_c = \frac{\sin\varphi_m \cos\theta}{1 - \sin\varphi_m \sin\theta} \tag{5.14}$$

The Mohr's circles for the samples with different initial K_o and different dilation angles are drawn in Fig. 5.38. In each diagram the Mohr strain rate circle is superimposed on the Mohr stress circle according to the different angle of non-coaxiality and dilation angle, in which the strain rate axes are indicated by dashed lines. For the case $K_0 > 1.0$ (see Fig. 5.38a and b), the theoretical value of φ_c (for a given φ_m and ψ) obtained from (4.3a), which assumes coaxiality, is smaller than that obtained from (5.14). When $K_0 < 1.0$ (see Fig. 5.38c and d), the value of φ_c obtained using (4.3a) becomes greater than that obtained using (5.14). If $K_0 = 1.0$ (see Fig. 5.38e and f) $\tan\varphi_c = \sin\varphi_m$ since $\theta = 0$. In this case the value of φ_c calculated from the (4.3a) can be either greater or less than $\sin\varphi_m$ depending on the sign of dilation angle. However, Fig. 5.38e and 5.38f demonstrate that $\tan\varphi_c = \sin\varphi_m$ unexpective of the sign of ψ since the necessary requirement is that $2i = -\psi$ and hence θ is always zero. Based on the above analyses, it is clear that the value of φ_c based on the flow rule (5.14) is very much dependent on the value of K_0, the dilation angle and the angle of non-coaxiality. Since $\theta = \psi + 2i$ cannot be measured experimentally the theoretical value of φ_c can either underestimate or overestimate the 'measured' value of the Coulomb friction angle depending on the value of K_0.

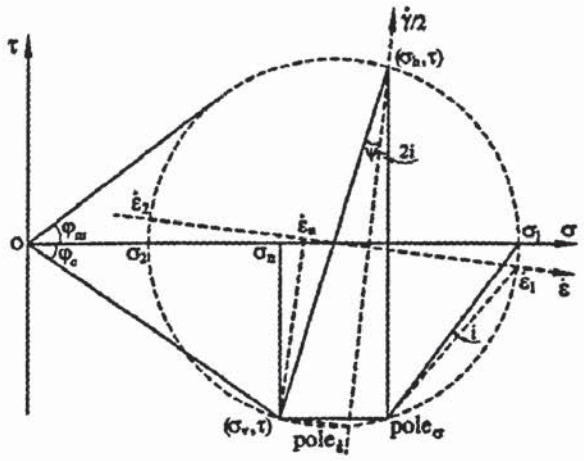

(a) $K_o > 1.0$, $\psi > 0$, $i > 0$, $\theta > 0$

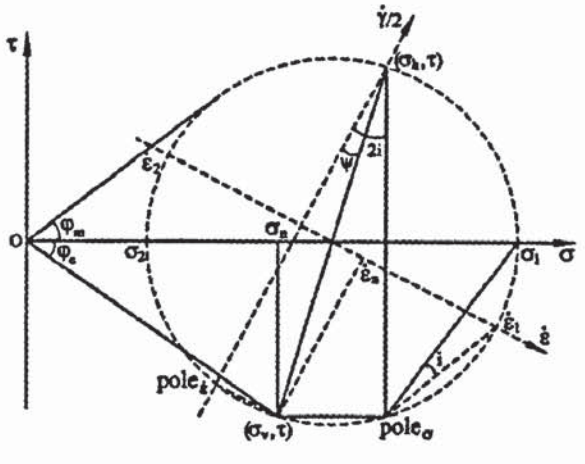

(b) $K_o > 1.0$, $\psi < 0$, $i > 0$, $\theta > 0$

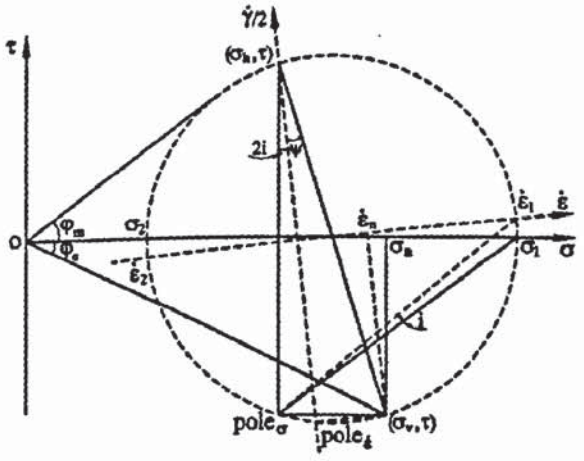

(c) $K_o < 1.0$, $\psi < 0$, $i < 0$, $\theta < 0$

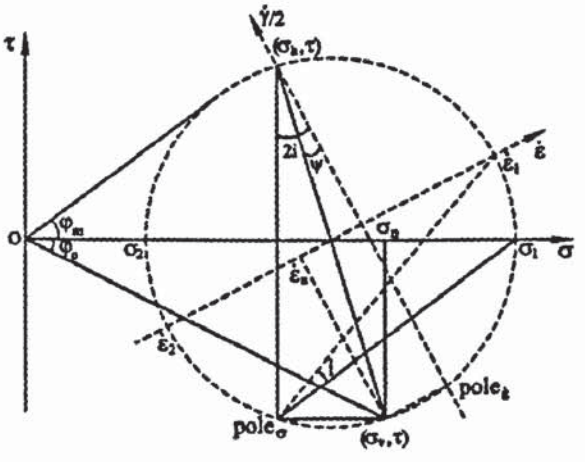

(d) $K_o < 1.0$, $\psi > 0$, $i < 0$, $\theta < 0$

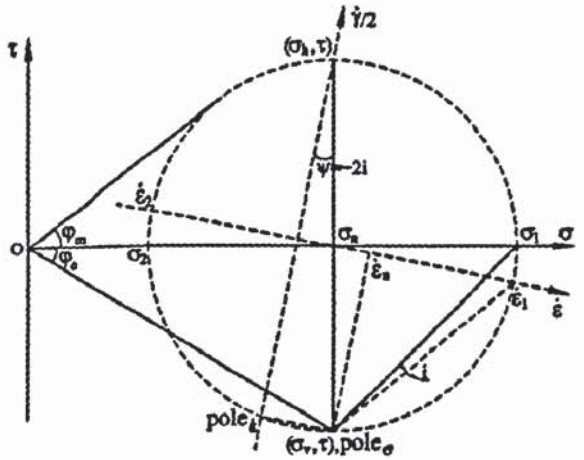

(e) $K_o = 1.0$, $\psi < 0$, $i > 0$, $\theta = 0$

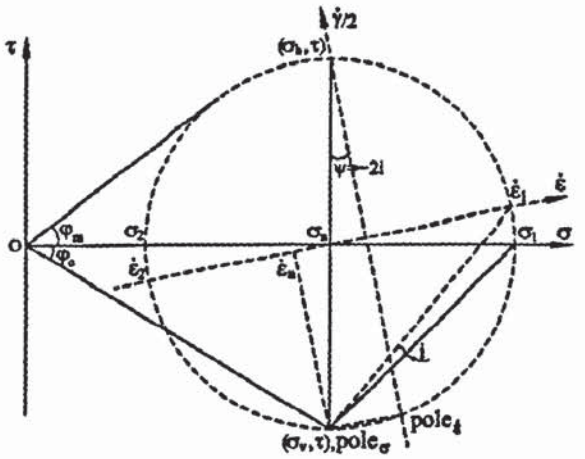

(f) $K_o = 1.0$, $\psi > 0$, $i < 0$, $\theta = 0$

Fig. 5.38 Mohr circles for different K_o

5.9 Comparisons of material behaviour during simple and pure shear deformation

The material behaviour during the simple shear test (**SST**) with $K_0 = 1.0$ and the biaxial compression test with wall boundaries (**BCW**), as defined by the volume-averaged calculations, are compared in this section. The comparison is made for the constant volume tests only. The evolutions of deviator stress and mean stress for both tests are shown in Figs. 5.39-40. The figures show that the evolution of deviator stress and mean stress of **BCW** and **SST** are similar. Figure 5.41 shows the evolution of $sin\varphi_m$. It can be seen that the mobilised angle of internal shearing resistance is independent of the type of test.

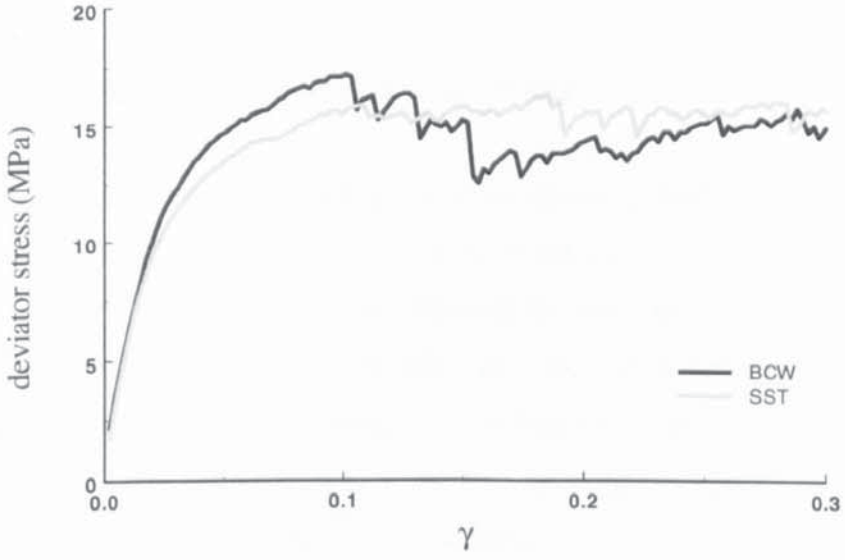

Fig. 5.39 Comparison of the evolution of deviator stress

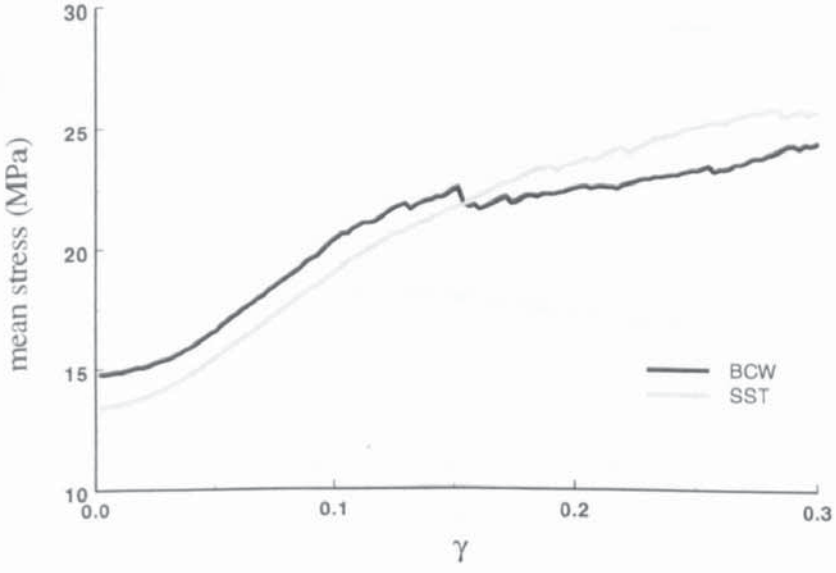

Fig. 5.40 Comparison of the evolution of mean stress

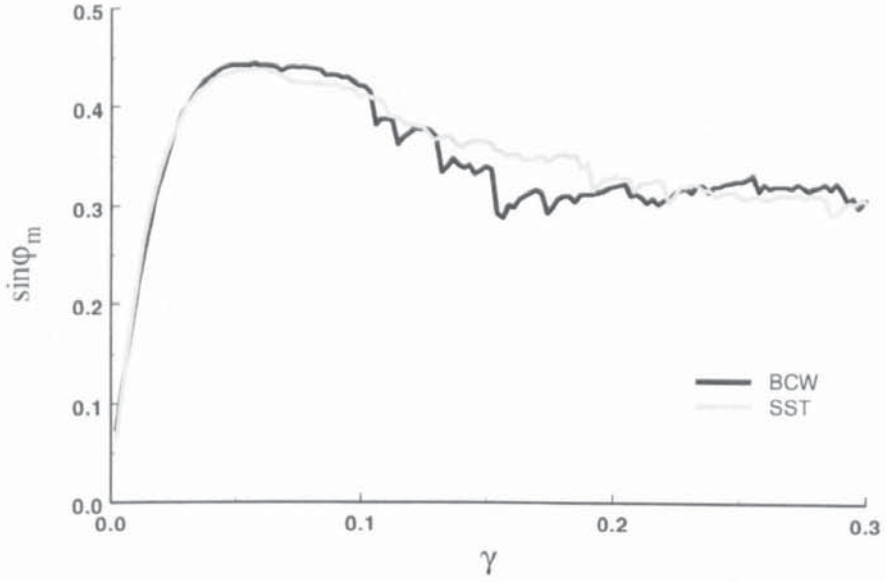

Fig. 5.41 Comparison of the evolution of $sin\,\varphi_m$

The evolutions of internal variables during the simulations of both types of test are shown in Figs. 5.42-44. Figure 5.42 shows the evolution of the mechanical coordination number, Z_m. It can be seen that similar results are obtained for both tests. Figure 5.43 shows the evolution of structural anisotropy in the two tests and very similar results are again obtained. The evolutions of the percentage of sliding contacts are also similar in both tests, as shown in Fig. 5.44. The reduction in the percentage of sliding contacts is due to the increase in mean stress developed during the tests.

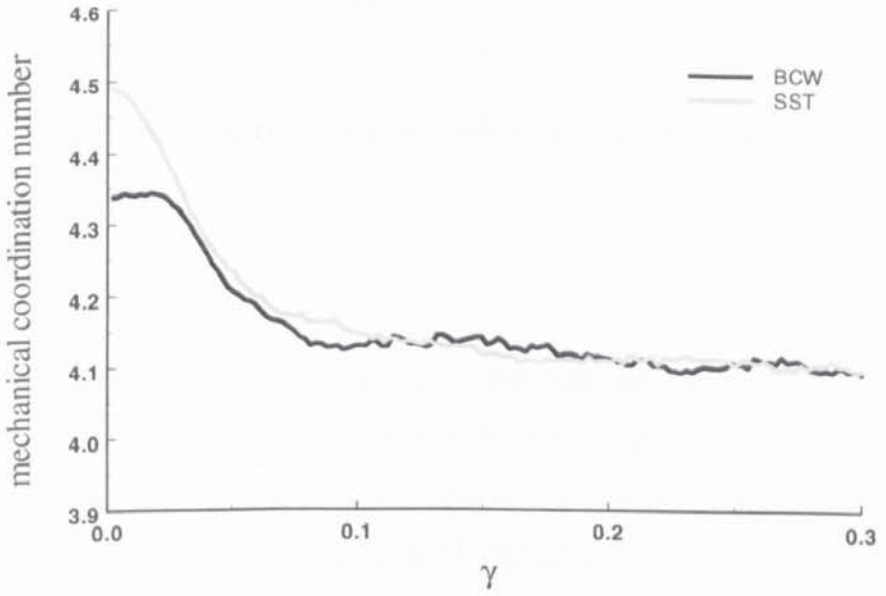

Fig. 5.42 Comparison of the evolution of Z_m

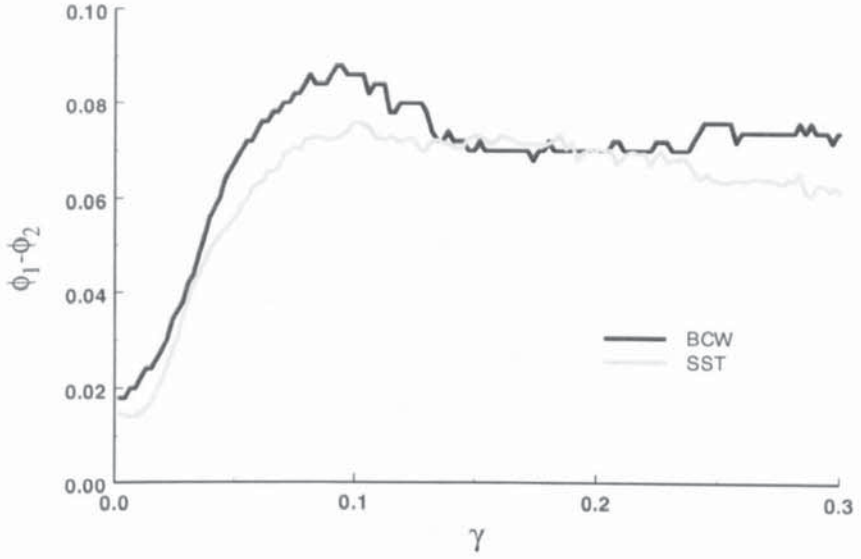

Fig. 5.43 Comparison of the evolution of deviator fabric

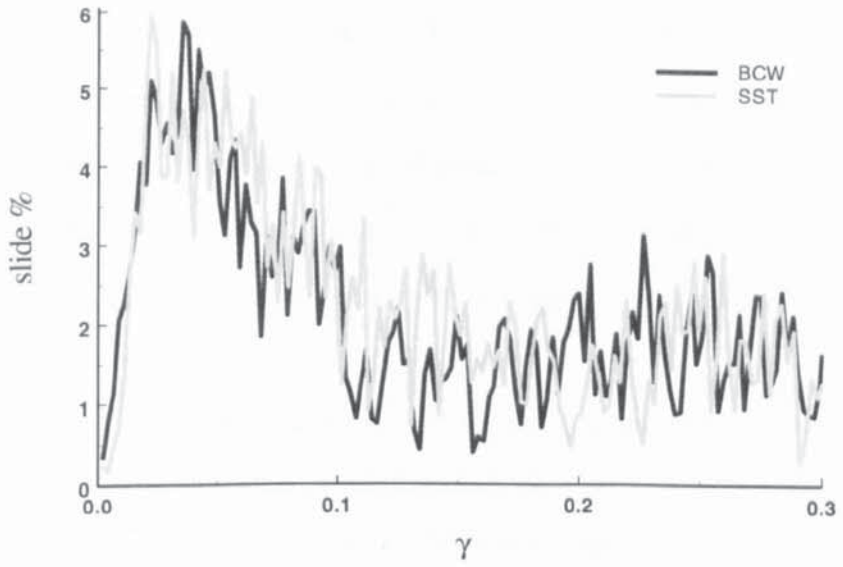

Fig. 5.44 Comparison of the evolution of percentage sliding

5.10 Summary

The investigations of simple shear tests have been carried out using DEM simulations. The tests with different wall frictions demonstrate that experimental measurements of wall stresses do not reflect the internal state of stress but merely provide information about the average mobilized wall friction. The detailed examination of stress distribution reveals that the stress distribution inside the sample and on the boundaries are nonuniform from the beginning of the test, the average stress obtained from the boundary information

cannot represent the real state of stress for the whole assembly. It is found that the strain distributions are uniform before peak strength, thereafter hints of nonuniformities appear near the top and bottom boundaries. Nevertheless, they are less significant than in the direct shear test. Therefore, the simple shear test can impose more uniform distribution of stress and strain to the specimen than direct shear tests. However, in simple shear tests performed in the laboratory the horizontal normal stress cannot be measured directly, which is the same problem as encountered in the direct shear test. Consequently, the Mohr stress circle cannot be drawn correctly and this makes the interpretation of the results from simple shear test experiments also unreliable.

It has been shown that the ratio of the two orthogonal normal stresses at the initial state has a strong influence on both the non-coaxiality between the direction of major principal stress and strain rate and the rate of dilation. At peak strength, the samples with $K_0 \neq 1.0$ show significant non-coaxiality between the directions of principal stress and strain rate but the non-coaxiality is not significant for the sample with $K_0 = 1.0$. In the laboratory the simple shear tests are most likely to carried on a sample with initial $K_0 < 1.0$, so the assumption of coaxiality of the direction of principal stress and strain rate is not valid when determining the peak strength in such a test. The results indicate that the initial K_0 state, the dilation and the angle of non-coaxiality all significantly affect the value of φ_c.

The overall behaviour of a particle assembly is believed to be strongly related to the local deformation of the specimen. Through the examination of the expansion/contraction of the local void cells it was found that large expansion of the void cell encourages particle rotation. When the void cell contracts it restricts the particle rotation. The simulation results also suggest that the sample does not have a preferred deformation pattern during simple shear deformation and the pattern is not governed by the initial stress state (K_0 condition) as suggested by de Josselin de Jong.

Excellent agreement was obtained between the results of the simple and pure shear test simulations based on the volume-averaged data. In terms of macro- and microscopic behaviour, both tests exhibit similar responses of the specimen. This demonstrates that DEM simulations can provide reliable test results, unlike laboratory experiments, in which different tests generally show significant differences in the material behaviour.

CHAPTER 6: PERIODIC CELL SIMULATIONS

6.1 Introduction

Granular materials are composed of discrete particles that interact only through the contacts between particles. Recent research has shown that the overall mechanical properties of granular materials are significantly dependent on the micro-scale geometric arrangement and the contact stiffnesses between interacting particles. It is desirable to describe the macro-scale constitutive law for granular materials using suitable continuum variables, and to derive the macro-scale continuum variables explicitly from the micro-scale discrete variables. Therefore, it is fundamental to understand the macroscopic mechanical behaviour of granular materials from a microscopic point of view.

This chapter reports the results of numerical simulations that have been carried out to investigate the quasi-static shear characteristics of granular media at both the macro- and micro- scales. The objective is to examine in detail the spatial distribution and temporal evolution of contact force transmission, inter-particle sliding and structural anisotropy in order to better understand the correlation of the physics observed at the micro-scale with the macro-scale mechanics of granular media. Some simulation results presented in this chapter were first reported in Thornton and Zhang (1999).

Simulations of isotropic compression followed by biaxial compression are carried out using a periodic cell. Samples with a wide range of packing density are sheared under constant volume and constant mean stress conditions. The sample preparation method is described in Section 3.3.1. Aspects of both the macroscopic and microscopic responses are presented and visualisations of force transmission patterns are provided.

6.2 Brief literature review

The stress-strain behaviour of granular media depends upon both the stress level and stress path due to the fact that the ensemble macroscopic behaviour is closely related to the

distribution of the constituent particles of different size and shape, the distribution of other internal variables and the interaction between contiguous particles. Traditionally, a macroscopic approach is used to model a granular medium as a continuum whose mechanical behaviour is described in terms of a stress tensor, a strain-rate tensor and some internal variables. However, two important discoveries have revived interest in the microscopic aspects of granular materials: (a) the contact network is generically anisotropic, which means that the contact normals are not randomly directed in space; (b) in contrast to the highly uniform density of a well packed assembly, the distribution of contact forces is highly heterogeneous. These observations suggest that the mechanical state of the granular system may be governed by several internal variables associated with the fabric and the modes of the force transmission inside the system.

Thornton and Barnes (1986) reported that the macroscopic state of stress is a function of the distribution of contact forces and Thornton (1993) showed that the ensemble moduli are related to the distribution of contact stiffness. For any ensemble of discrete particles subjected to external loading, the transmission of force from one boundary to another can only occur via the inter-particle contacts. Therefore, it is expected that the distribution of contacts will determine the force distribution inside the assembly. Direct observations of stress distribution via photo-elastic studies of two-dimensional arrays of discs have been reported by Dantu (1957), Drescher and de Josselin de Jong (1972) and Oda and Konishi (1974). Using dynamic photo-elastic studies of regular arrays of elliptical discs, the dynamic stress wave propagation in disc assemblies have been investigated by Zhu *et al.* (1996). It has been observed from all static photo-elastic studies of disc assemblies that the load is largely transmitted by relatively rigid, heavily stressed chains of particles forming a relatively sparse network of larger than average contact forces. The other contacts separating the strong force chains are only lightly loaded. Liu *et al.* (1995) have demonstrated the existence of strong force chains in three-dimensional packings of spheres and they also proposed a simple model that can reproduce many aspects of the experiments and simulations.

Traditional theoretical and experimental investigations of the mechanical behaviour of granular materials are restricted by the limited quantitative information about what actually happens internally. Laboratory experiments on real materials rely on estimates of the macroscopic stress and strain states from boundary measurements, which themselves

depend on assumptions made about the material behaviour. Information on the internal mechanisms is rare, since any attempts at direct observation and measurement intrude upon the material response. In addition, comparisons between sets of test data are uncertain due to the inability to prepare exact replicas of the physical system. Traditional attempts to mathematically model the mechanical behaviour of granular media are normally based on intuitive speculation as to how the observed experimental behaviour might be modelled by modifying existing continuum mechanics theories. However, the resulting theories invariably include new parameters, the precise physical meaning of which is relatively obscure. This leads to difficulties in selecting appropriate experiments to rigorously justify a theory.

As an alternative approach to investigate the mechanical behaviour of granular materials, computer simulations have become more and more attractive in the last ten years. This technique can determine not only the overall behaviour of the granular assembly but also the evolution of internal variables associated with the micromechanical processes occurring at the particle scale. In addition to the direct observations of force transmission in two-dimensional arrays of photo-elastic discs, numerical simulations of quasi-static shear deformation of particle systems with visualisation of the force transmission patterns have been reported by many researchers. Computer simulations of general three-dimensional quasi-static shear deformations have been performed over the complete range of deviatoric radial loading paths from axisymmetric compression to axisymmetric extension, for both dense and loose polydisperse systems by Thornton and Sun (1994). The reported macroscopic behaviour was in good qualitative agreement with results obtained from real experiments on sand and also demonstrated that computer simulated experimentation is a versatile and convenient technique that may be used to examine complex 3D loading histories, which are necessary to check the detailed formulation of continuum models. Further examinations of shear deformation of three-dimensional disperse systems of elastic spheres subjected to different complex loading histories have been reported by Thornton and Antony (1998) and Thornton (2000a). The results of numerical simulations of planar assemblies of elliptical particles were presented by Rothenburg and Bathurst (1992). Qualitative features of these systems that are similar to real sand behaviour were identified and the influence of particle eccentricity on peak friction angle and peak dilation rate was explored in a systematic manner. The results also showed that the stress-force-fabric relationship verified for planar assemblies of discs

(Rothenburg and Bathurst, 1989) was also valid for assemblies of elliptical particles.

Research on granular media has also attracted the attention of many physicists. Radjai *et al.* (1996) examined force networks in numerical simulations of two-dimensional systems of rigid discs. The simulation technique is known as the Contact Dynamics Method, which was described by Moreau (1994). From the obtained probability distributions, it was found that although the above-average normal contact forces exhibited an exponential decay, the smaller than average normal contact forces had a power-law distribution. Radjai *et al.* (1997) performed Contact Dynamics simulations of quasi statically driven assemblies of rigid particles and suggested that the contact network at every stage of deformation is composed of two sub-networks: a 'strong' sub-network of contacts carrying forces larger than the mean force, and a 'weak' sub-network of contacts carrying forces lower than the mean force. In addition the strong sub-network supports all the deviatoric load, whereas the weak sub-network contributes only to the mean pressure. The stress propagation characteristics of granular materials when they are subjected to increasing pressures were investigated by Nguyen and Coppersmith (2000). They characterized the statistical properties of forces by using the force histogram and a two-point spatial correlation function of the forces. The comparisons of results of a two-dimensional scalar lattice model with those of a molecular dynamics simulation of slightly polydisperse discs showed that when the pressure is increased the changes in the force histogram obtained from the molecular dynamics simulations are very similar to those obtained from the lattice model. In contrast, the spatial correlations evolve qualitatively differently in the lattice model and in the molecular dynamics simulations.

It has been shown from previous numerical simulations that there is a multiplicity of pathways along which force transmission may be achieved in order to establish a stable stress state. In order to achieve a stable state of stress the system does not use all the potential pathways but naturally optimises the selection to match the loading direction. In terms of statistical physics, this is a percolation problem and the system can be considered to be self-organising. This self-organised optimisation of the force transmission is reflected by a critical value of the mechanical coordination number, which corresponds to a percolation threshold (Thornton, 1997). In this chapter the percolation phenomena of granular media and its correlation to the mechanical coordination number is further examined by performing numerical simulations of biaxial compression on ten different

polydisperse systems. There are two test series that have been carried out. The simulation results of constant volume tests will be presented first followed by the results obtained from constant mean stress tests.

6.3 Constant volume (CV) tests

The relationship between the isotropic stress and solid fraction obtained at the end of the isotropic compression stage is shown in Fig. 6.1. The stress level varied from 12.8kPa for the loosest sample to 30.6MPa for the densest sample when samples were prepared in the manner described in Chapter 3. The corresponding mechanical coordination number, Z_m, plotted against solid fraction is shown in Fig. 6.2. It is noted that the value of Z_m increases rapidly as the solid fraction is increased from 0.584 to 0.598.

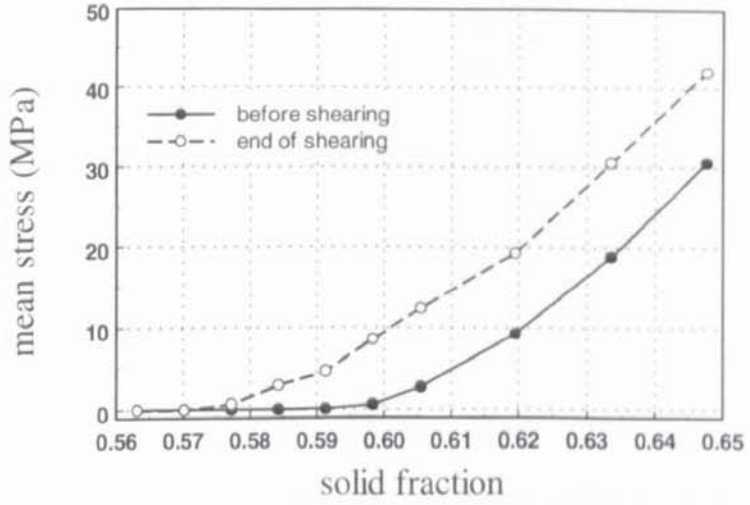

Fig. 6.1 Mean stress vs. solid fraction

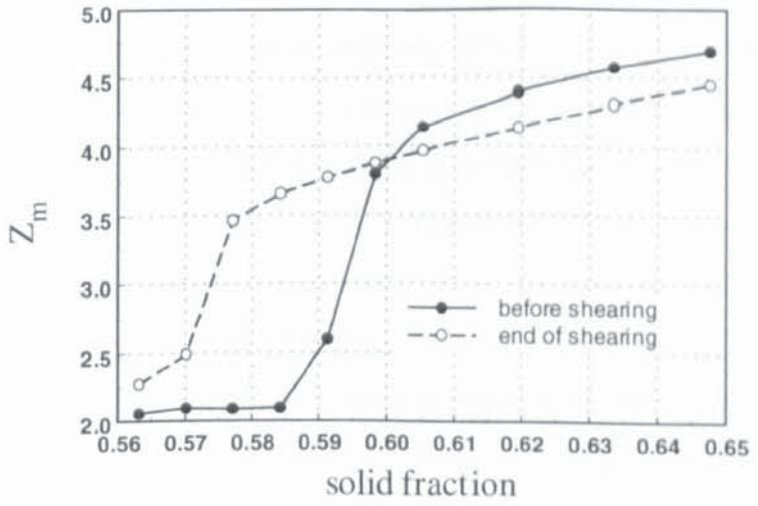

Fig. 6.2 Mechanical coordination number vs. solid fraction

Figure 6.3 shows the distributions of contact normal orientations of the samples prior to shearing. It can be seen that at low solid fractions (0.564 - 0.585) the samples are slightly anisotropic, but at high solid fractions (0.599 – 0.635) the samples are reasonably isotropic.

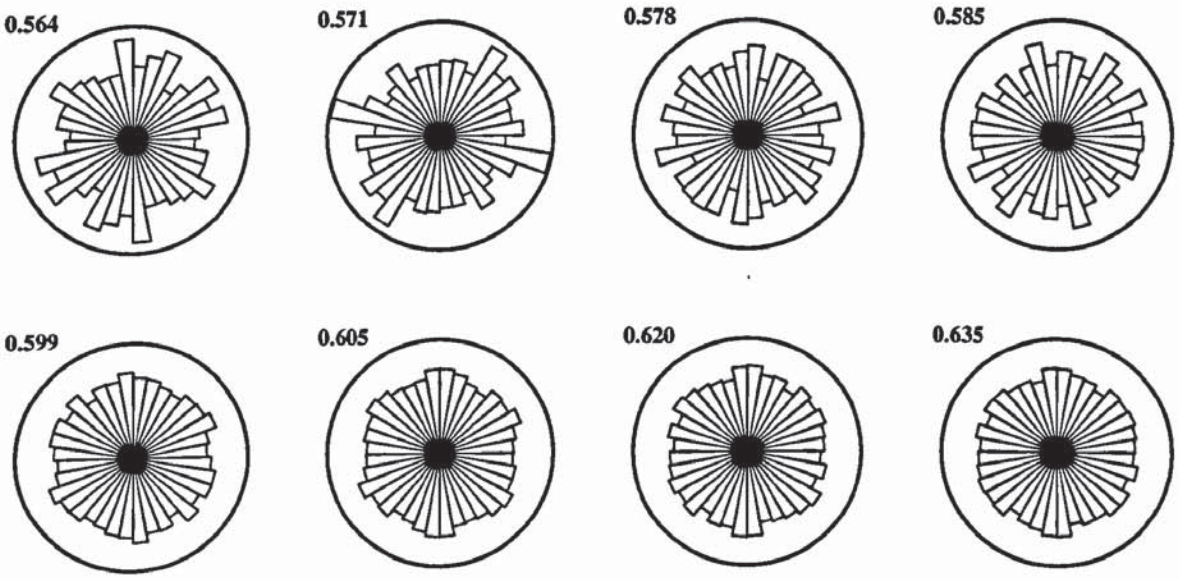

Fig. 6.3 Contact normal orientations before shearing

6.3.1 Macroscopic behaviour

Figure 6.4 shows the variation of the deviator stress $(\sigma_1 - \sigma_2)$ with deviator strain $(\varepsilon_1 - \varepsilon_2)$ during biaxial compression under constant volume conditions for various systems with different initial solid fractions. It can be seen that, for the systems with low initial solid fractions of 0.564 and 0.571, no significant shear stress is developed. For the systems with intermediate initial solid fractions (0.578, 0.585 and 0.592), a significant deviator stress is only developed after a certain amount of deviator strain is reached (Fig. 6.4a). For those systems with high initial solid fractions (larger than 0.599), the deviator stress increases from the start of shear until an approximately constant value is maintained after about 10% deviator strain (5% axial strain), as can been from Fig. 6.4b. The magnitude of the deviator stress developed is, however, also dependent on the magnitude of the isotropic stress. For all but the two loosest systems, deformation at constant volume was accompanied by an increasing isotropic stress, as can be seen from Fig. 6.5 which shows the evolution of mean stress $(\sigma_1+\sigma_2)/2$ against deviator strain for all ten systems

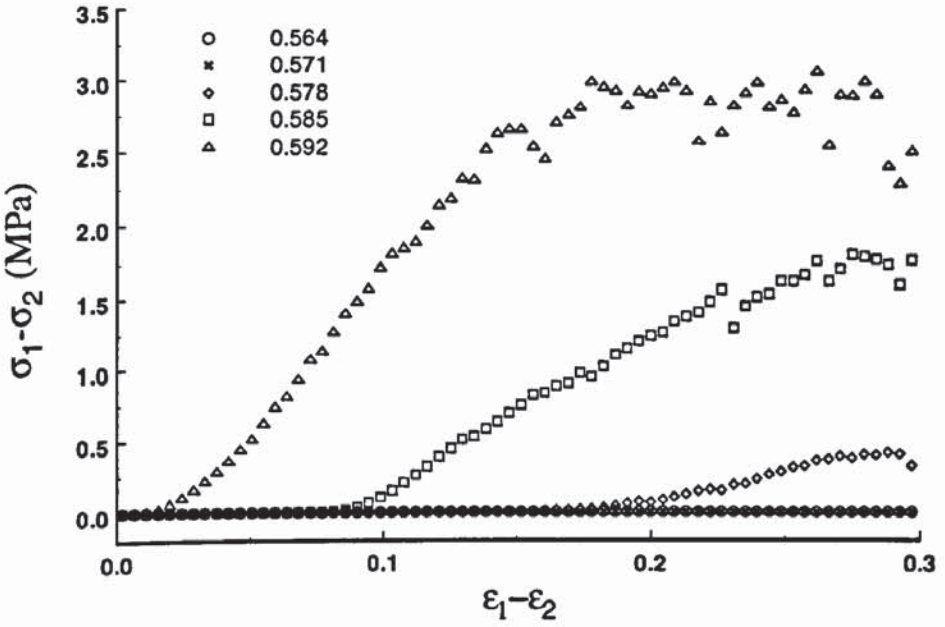

(a)

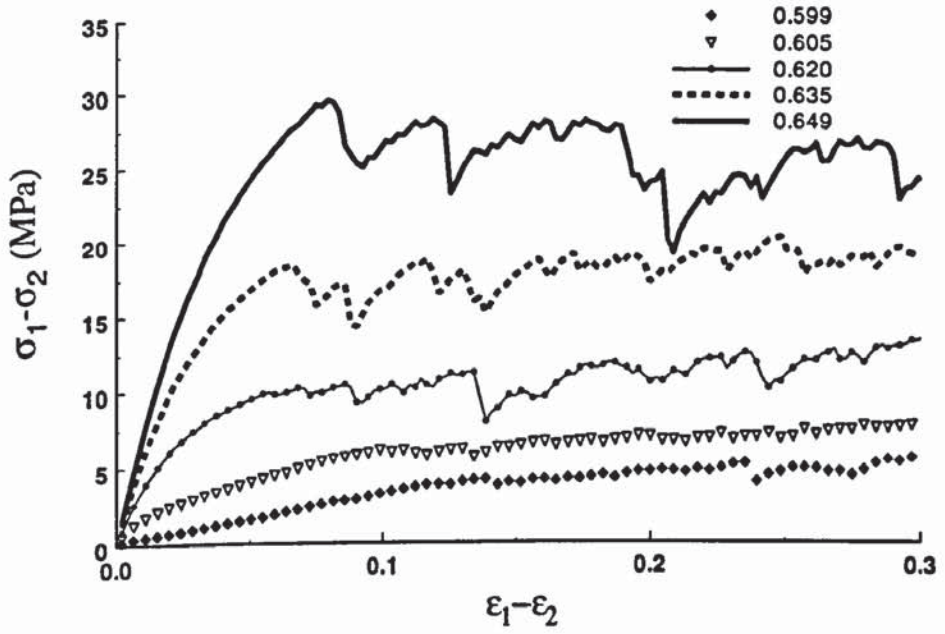

(b)

Fig. 6.4 Evolution of deviator stress

considered. For the two loosest samples of solid fraction 0.564 and 0.571 the mean stress decreased from 4.22kPa and 4.39kPa to just 0.057kPa and 0.053kPa, respectively.

Figure 6.6 shows the variation of $sin\varphi_m$ with deviator strain for all the systems considered. It is clear that, for solid fractions greater than 0.578, the magnitude of $sin\varphi_m$

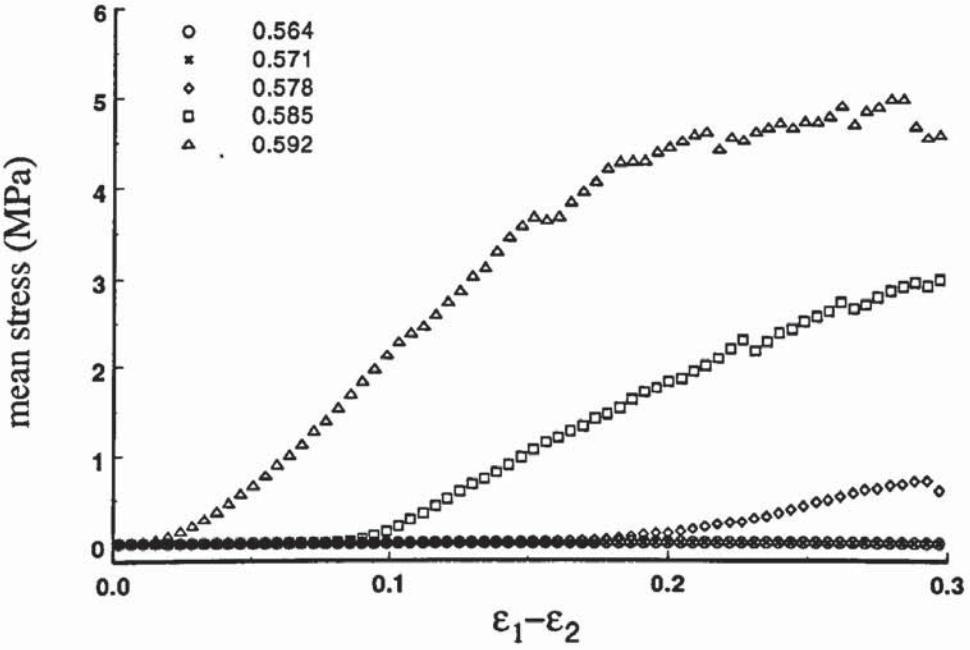

(a)

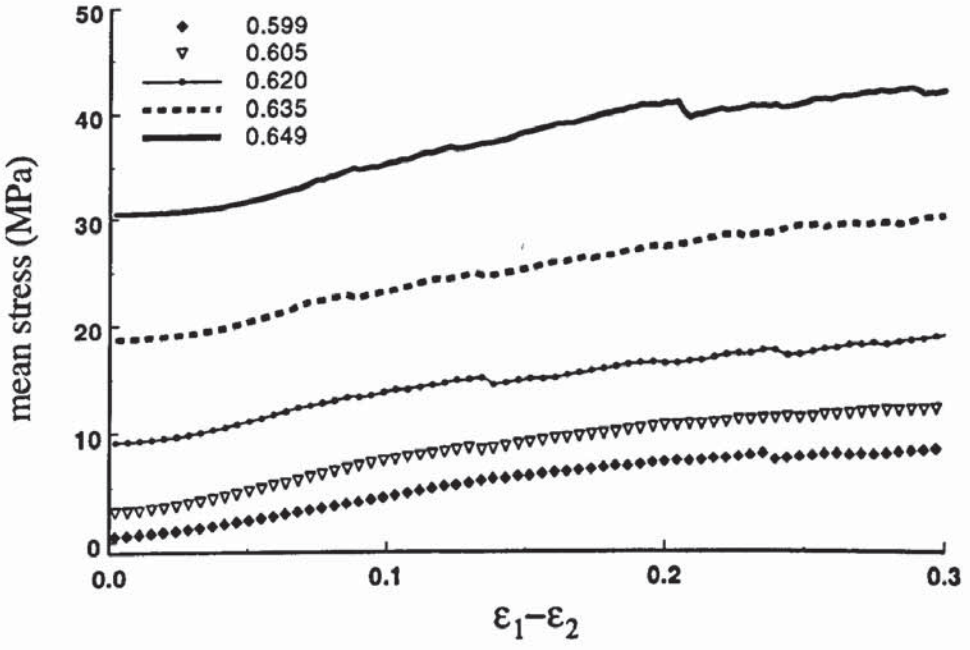

(b)

Fig. 6.5 Evolution of mean stress

increases with increasing deviator strain at low strains and then decreases with further increase of deviator strain until, finally, a constant value is reached. The value of $sin\varphi_m$ for the system with a solid fraction of 0.578 increases initially, but with significant fluctuations, until a maximum value is reached just before 10% shear strain, then remains

essentially constant thereafter. Systems with solid fraction less than 0.578 exhibit significant fluctuation in the value of $sin\varphi_m$ throughout the simulation (Fig. 6.6a). Nevertheless, the results shown in Fig. 6.6 demonstrate that the mobilized value of $sin\varphi_m$ at large strains is independent of the initial packing density.

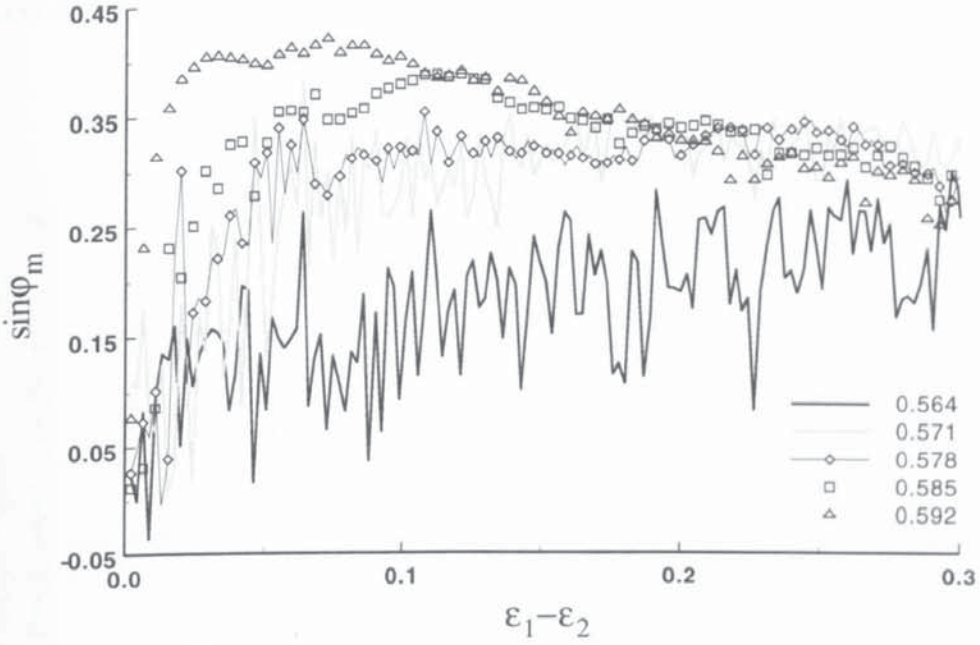

(a)

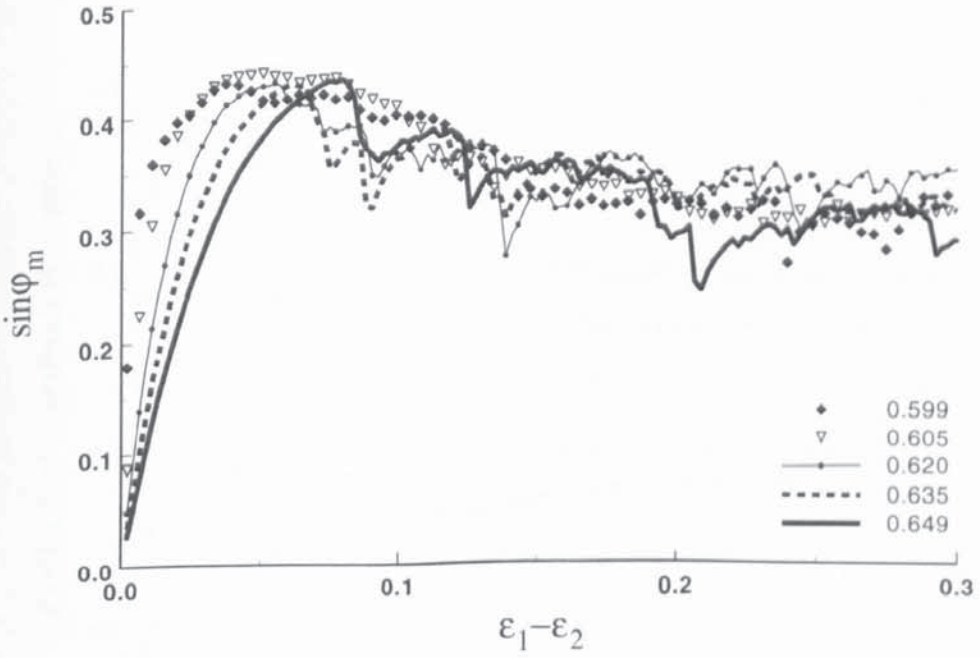

(b)

Fig. 6.6 Evolution of $sin\varphi_m$

6.3.2 Microscopic behaviour

Generally, three microscopic features play key roles in the mechanics of granular media: the mutual exclusion of particles, which can be reflected by the mechanical coordination number; the dissipative nature of interactions due to plastic deformation during collisions or sliding friction; and dynamically-induced randomness which is related to the fabric. The observed microscopic behaviours are shown in the following figures.

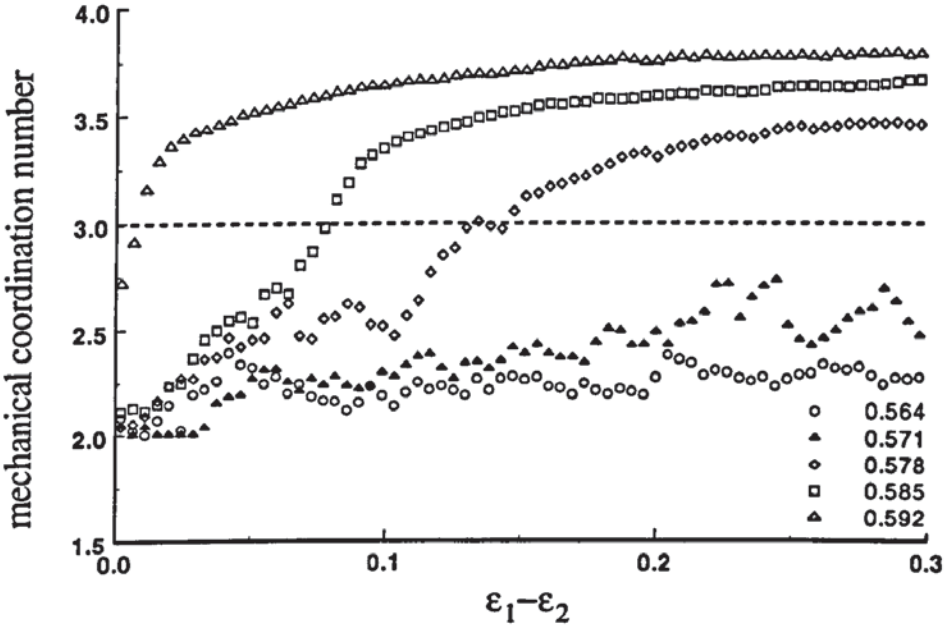

(a)

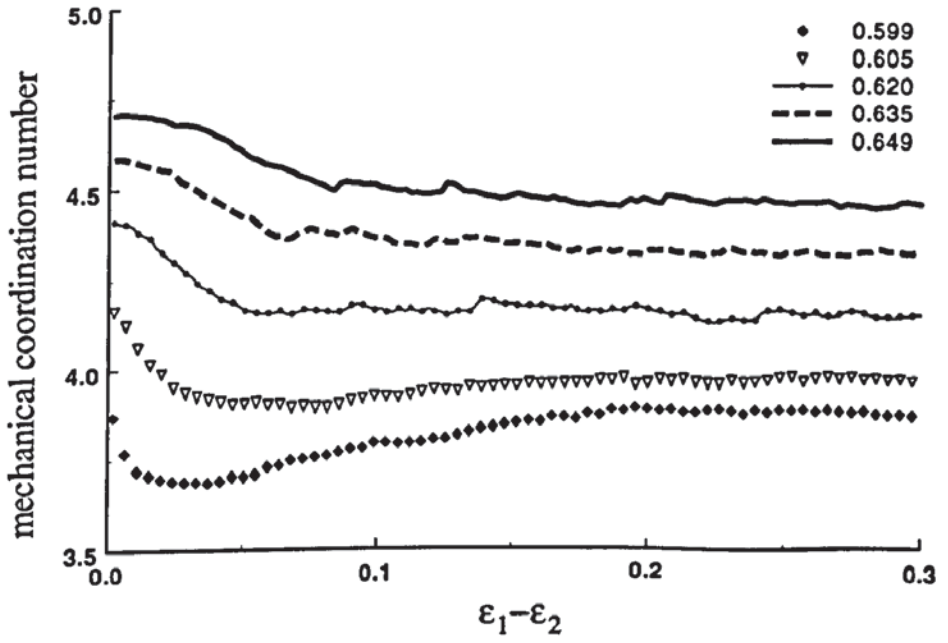

(b)

Fig. 6.7 Evolution of mechanical coordination number

The evolution of the mechanical coordination number, Z_m, is shown in Fig. 6.7. For the three densest systems, as shown in Fig. 6.7b, the mechanical coordination number decreases until a critical value is attained and remains essentially constant thereafter. For solid fractions of 0.599 and 0.605, Z_m initially decreases but then increases a little until a constant value is maintained at large strain. The mechanical coordination number remains very low during the deformation of the two loosest systems. However, for the other three systems shown in Fig. 6.7a, the mechanical coordination number increases from the start of shear until a constant value is reached at large strains. The relationship between the final value of the mechanical coordination number and solid fraction is shown on Fig. 6.1. Comparing Figs. 6.4a and 6.7a, it is interesting to note that the deviator stress begins to increase only when the mechanical coordination number reaches a value of ca. 3.0. A closer look at the evolution of deviator stress together with mechanical coordination number for a solid fraction of 0.585 during the period when the deviator stress starts to develop is shown in Fig. 6.8. It is clear that the deviator stress (black line) starts to increase from a low level at 7.8% deviator strain and at this stage the mechanical coordination number (grey line) is ca. 3.0. This implies that a certain degree of connectivity is necessary before a stable arrangement of particles can be created sufficiently for the system to develop a shear modulus. Therefore, we may infer that $Z_m = 3.0$ is indicative of an elastic percolation threshold.

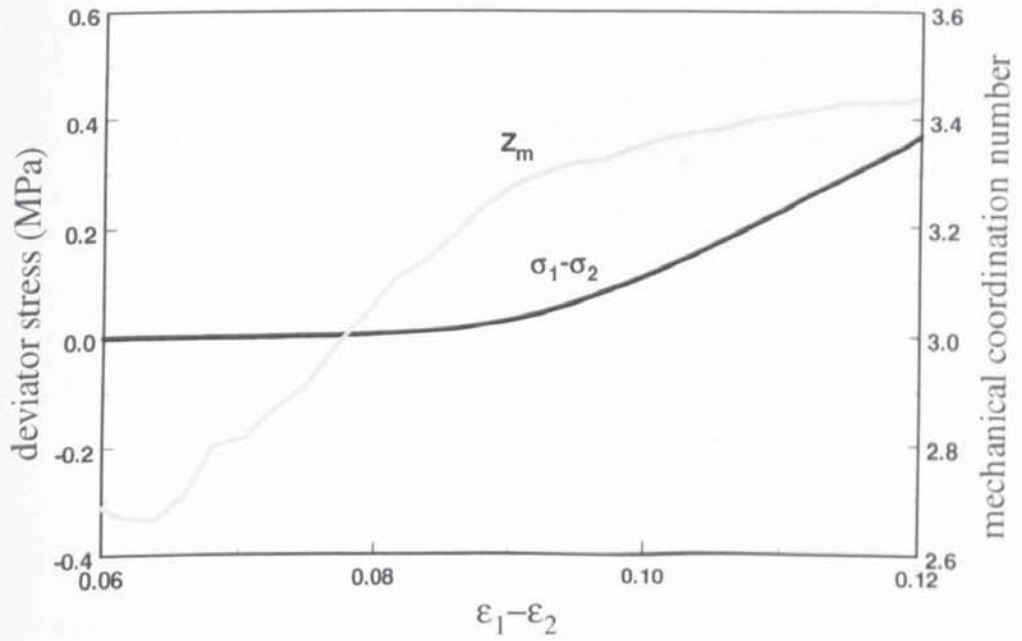

Fig. 6.8 Evolution of $\sigma_1 - \sigma_2$ and Z_m during a short period for solid fraction 0.585

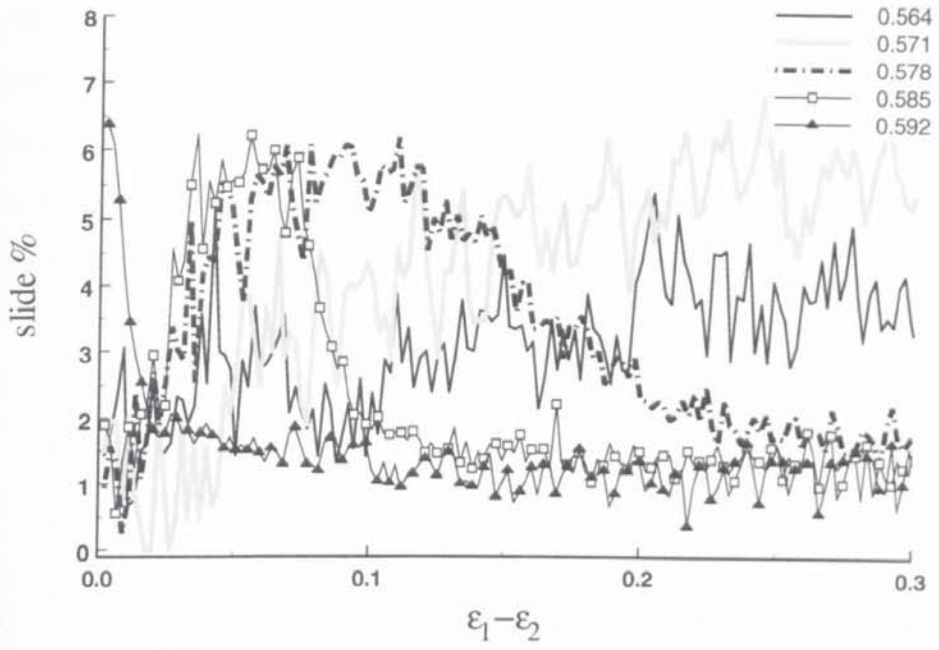

(a)

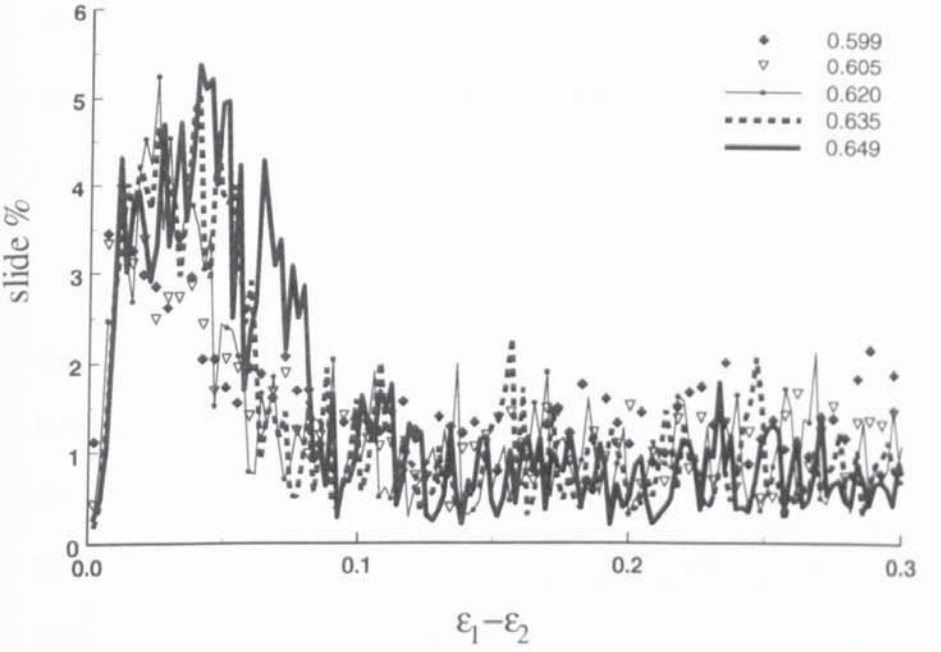

(b)

Fig. 6.9 Evolution of sliding contact

Figure 6.9 shows the evolution of the ratio of sliding contacts during biaxial compression for all ten systems. It can be seen that, for dense systems, the ratio of sliding contacts changes dramatically at the beginning of shear, but remains essentially constant after about 10% deviator strain with ca. 1% of contacts sliding, independent of the initial solid fraction (Fig. 6.9b). However, for the two loosest systems, the percentage of sliding

contacts quickly increases to between 4% and 6% and remains, essentially constant but with strong fluctuations. Interestingly, for intermediate solid fractions of 0.578, 0.585, and 0.592, the percentage of sliding contacts is comparable with the loosest system in the early stages of shear. When the mechanical coordination number increases to a value greater than 3.0 (see Fig. 6.7a) the percentage of sliding contacts falls until, at large strains, it is similar to that observed for the dense systems.

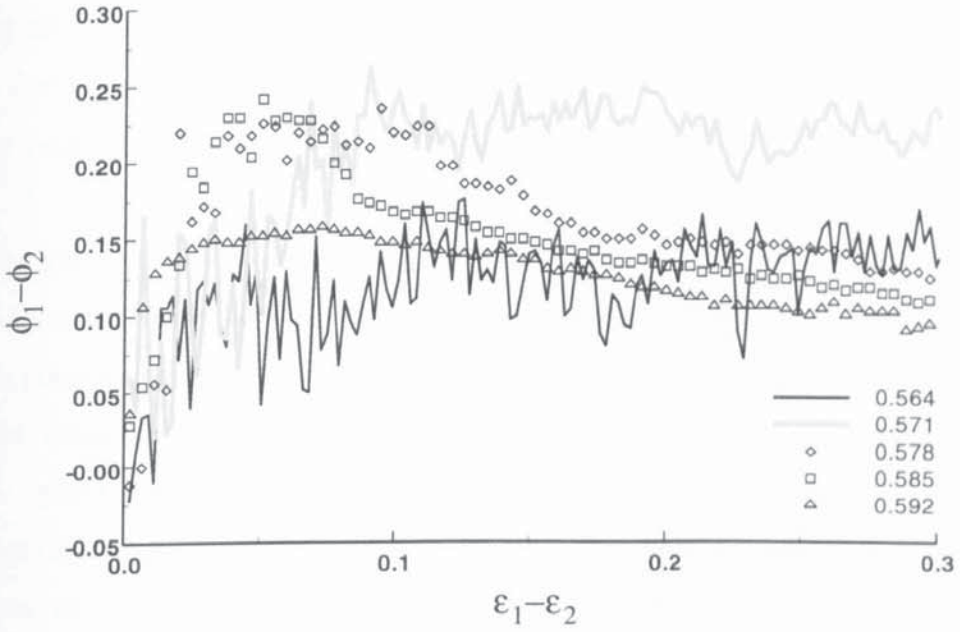

(a)

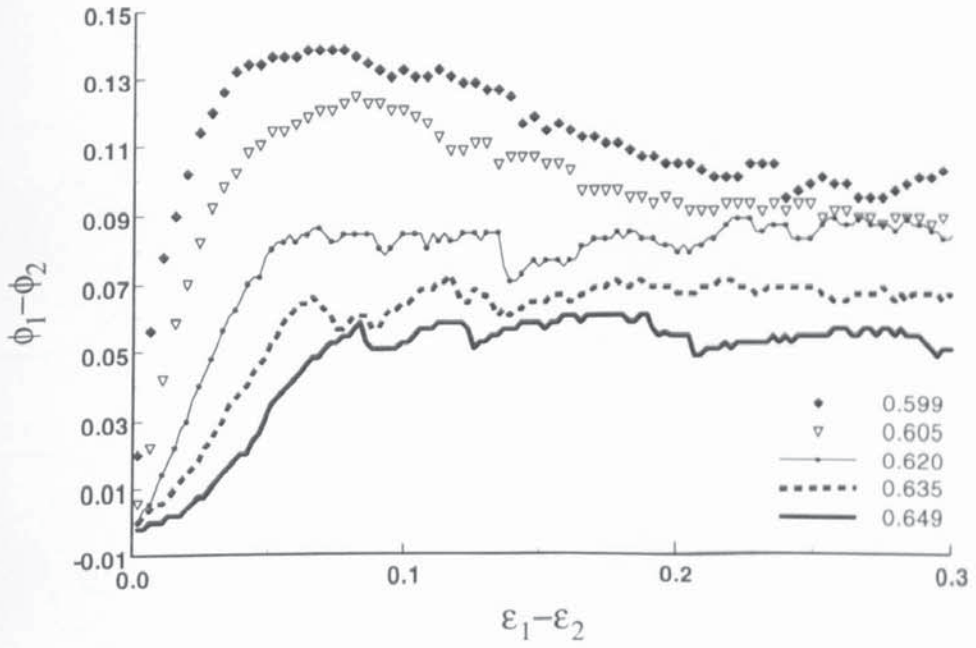

(b)

Fig. 6.10 Evolution of deviator fabric

The evolution of the deviator fabric ($\phi_1 - \phi_2$) is shown in Fig. 6.10. For solid fractions of 0.599 and 0.605, the deviator fabric rapidly increases to attain a maximum value prior to 10% deviator strain and then reduces until an essentially constant value is maintained at large strains. No peak in the evolution of the deviator fabric is observed for solid fractions greater than 0.605. Comparing Fig. 6.10a with Fig. 6.7a, it can be seen that a similar evolution of the deviator fabric occurs once the mechanical coordination number is greater than 3.0. The two loosest systems exhibit high values of deviator fabric, but with significant fluctuations, and there is no reduction in deviator fabric at large strains. However, for these systems, which fail to develop a significant shear stress, Fig 6.4a, and have a low number of contacts, the relevance of the deviator fabric is unclear.

An examination of Fig. 6.10 might suggest that the deviator fabric at large strain decreases as the solid fraction increases. However, it was demonstrated by Thornton and Sun (1993) that, in constant mean stress tests, the deviator fabric at large strains is independent of the initial solid fraction. Therefore, what Fig. 6.10 illustrates is that, the degree of induced structural anisotropy is suppressed by increasing the mean stress since the mean stress increases with increase in solid fraction in constant volume tests (Fig. 6.1). The distributions of contact normal orientations for all samples at the end of shearing are presented in Fig. 6.11. It is clear that the contact normals have a preferred orientation along the horizontal direction, which is also the direction of compression. In addition, the loose systems show stronger anisotropy than the dense systems.

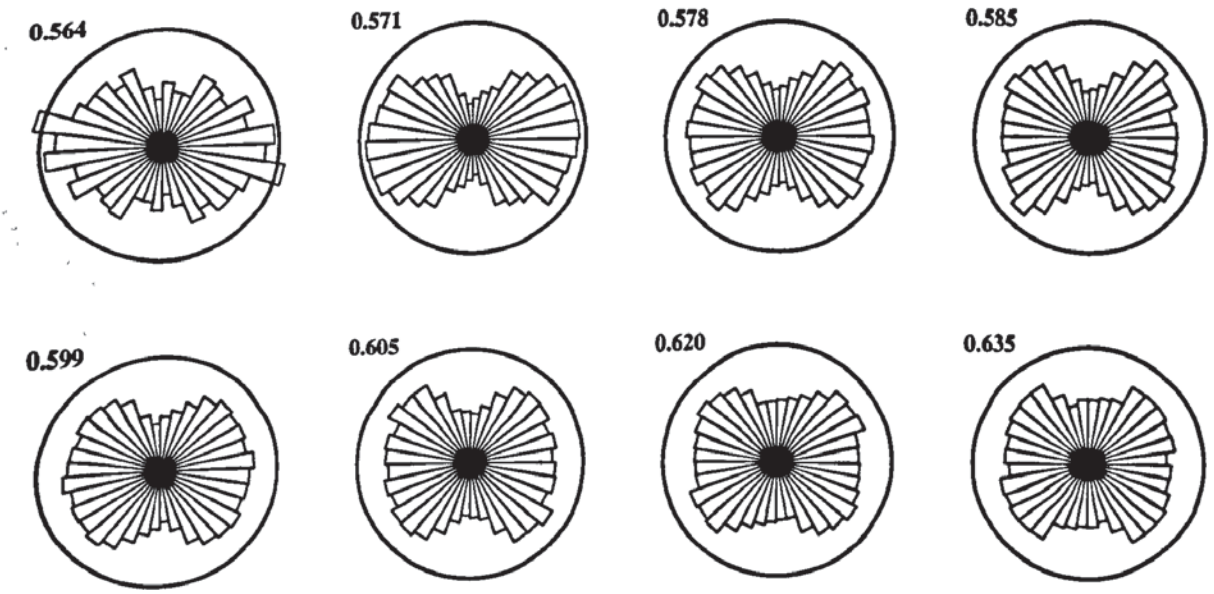

Fig. 6.11 Contact normal orientations at the end of shearing

6.3.3 Force transmission

In order to understand how the macroscopic behaviour relates to the behaviour at the grain scale during shearing, visualisations of force transmission are presented in this section. The connection and force diagram of the sample with a solid fraction of 0.635 is shown in Fig. 6.12. Figure 6.12a shows the force transmission pattern before shearing. At this stage both the structure and the applied stress field are isotropic. After the system has been subjected to 30% deviator strain, there is a distinct preferred orientation of the large contact forces, as can be seen in Fig. 6.12b. It is clear that the large forces are oriented in the direction of the major compressive principal stress. The contact force orientations of the loosest system with a solid fraction of 0.563 are shown in Fig. 6.13. It can be seen from Fig. 6.13a that the system does not percolate in either direction, indicating collisional behaviour. In contrast to Fig. 6.12, Fig. 6.13 shows that the loosest system never establishes continuous force transmission pathways between the boundaries of the periodic cell, although some degree of connectivity in certain regimes of the sample can be seen in Fig. 6.13b, which is indicative of clustering. Figure 6.14 shows the force transmission for a sample with a solid fraction of 0.585. At the beginning of shearing, the system is very similar to the loosest one (Fig. 6.13a) in that there is no connectivity across the system. At the end of shearing, Fig. 6.14c, strong force transmission pathways are evident, similar to those shown in Fig. 6.12b. Figure 6.14b shows the connection diagram at 7.8% deviator strain when the mechanical coordination number is ca. 3.0 (Fig. 6.6a) just prior to the development of a significant shear modulus (Fig. 6.4a). Figure 6.14b, therefore, illustrates the force transmission pattern near the elastic percolation threshold when enduring connectivity is being established.

Video clips of the evolution of the connectivity and contact force transmission throughout the biaxial compression tests for the system with solid fractions of 0.585 and 0.635 are provided at http://www.iem.bham.ac.uk/computation/granular/microevo.htm and also described in Appendix C. It is clearly seen from these videos that the ability for a system to develop a significant shear modulus is determined by whether enduring connectivity (percolation) is established, which is reflected in a critical value of the mechanical coordination number.

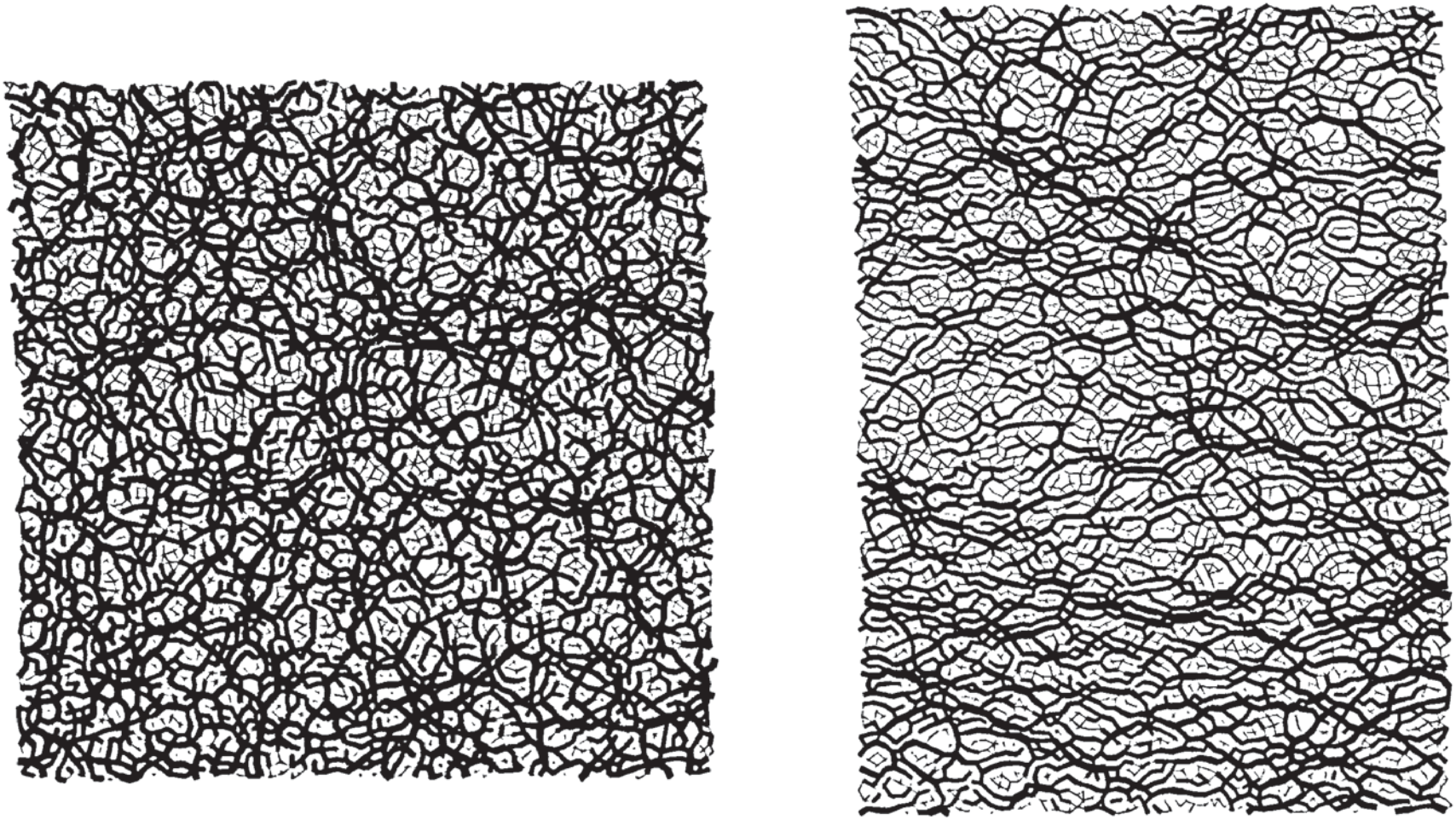

(a) before shearing (b) end of shearing

Fig. 6.12 Force transmission diagram for sample with solid fraction 0.635

(a) before shearing

(b) end of shearing

Fig. 6.13 Force transmission diagram for sample with solid fraction 0.564

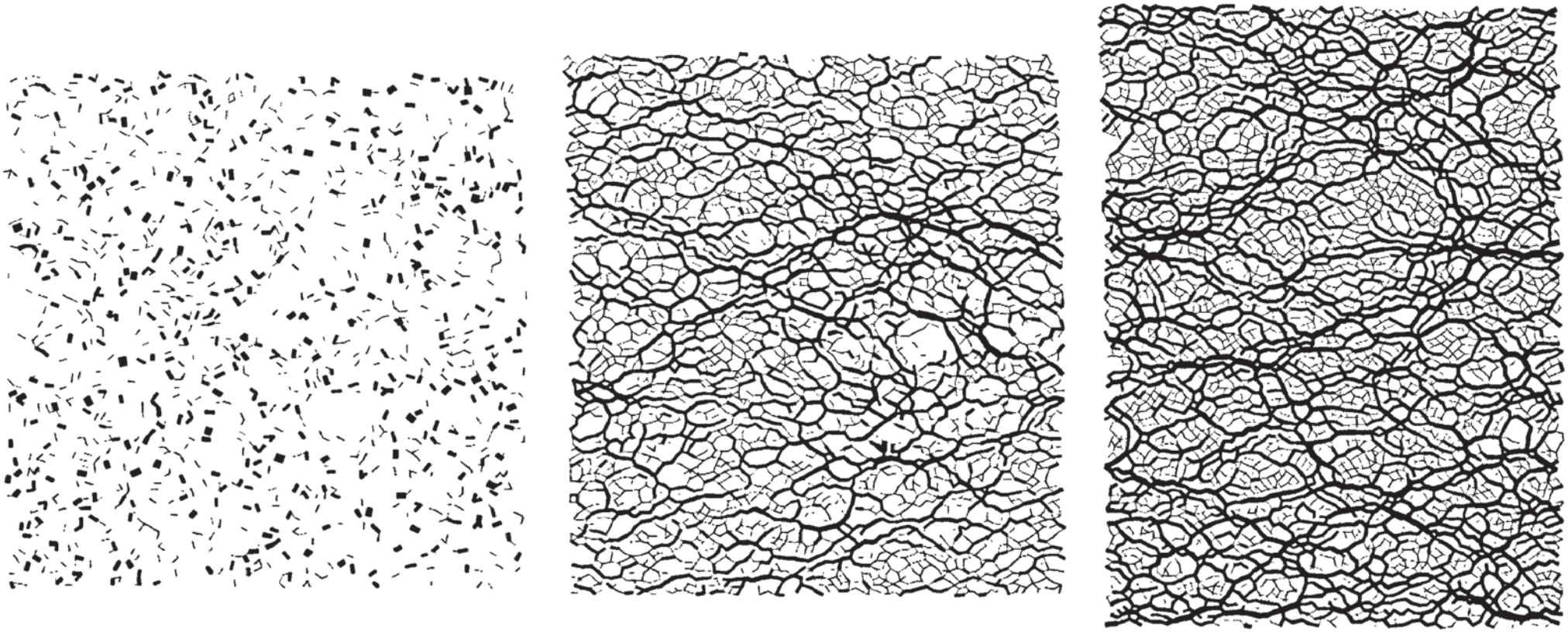

(a) before shearing (b) at 7.8% deviator strain (c) end of shearing

Fig. 6.14 Force transmission diagram for sample with solid fraction 0.585

Following the recent research work on granular materials by physicists (Radjai *et al.*, 1996), the simulation data in terms of strong and weak networks are re-examined. The ratio of the number of contacts in the strong sub-network (C_s) to the number of total contacts (C) is defined as,

$$P_s = \frac{C_s}{C} \tag{6.1}$$

The evolution of P_s is shown in Fig. 6.15. It can be seen that, for dense systems, the ratio P_s decreases continuously until 10% shear strain, thereafter it remains essentially constant ca. 0.365 independent of the initial solid fraction (Fig. 6.15b). It can be seen from Fig. 6.15a that for the two loosest systems, the ratio decreases at the beginning of shearing and fluctuates about 0.15 and 0.25 at the end of shearing, respectively. For the intermediate solid fraction of 0.578, 0.585, and 0.592 the ratios also decrease initially then increase. Eventually, when each mechanical coordination number increases to a value greater than 3.0 at 14.5%, 7.8% and 0.8% deviator strain, Fig. 6.7a, the ratios P_s remain constant at a value of 0.365, similar to that observed for the dense systems. Radjai *et al.* (1996) found in their simulations that there were 60% of contacts carried forces less than the average force. Hence, in their simulation P_s was 40%, which is close to the results shown in Fig. 6.15.

In addition, the fabric tensor is calculated for the weak and strong networks separately. For the sample with solid fraction 0.635 the evolutions of the corresponding deviator fabrics are shown in Fig. 6.16 together with the overall deviator fabric. It can be seen that the contacts within the strong sub-network exhibit a much stronger anisotropy than the overall anisotropy of the sample. It is also noted that the deviator fabric of the weak sub-network is negative.

The corresponding polar diagrams of the contact normal orientations of the two sub-networks are shown in Fig. 6.17. Figure 6.17a shows the polar diagrams before shearing. It is clear that at this stage the contacts in both sub-networks are isotropic. However, at the end of shearing both distributions are strongly anisotropic as shown in Fig. 6.17b. It is also noted that the majority of contact normals in the strong sub-network tend to align with the principal direction of compression, whereas in the weak sub-network, there is a majority of contact normals that tend to be aligned with the principal direction of extension.

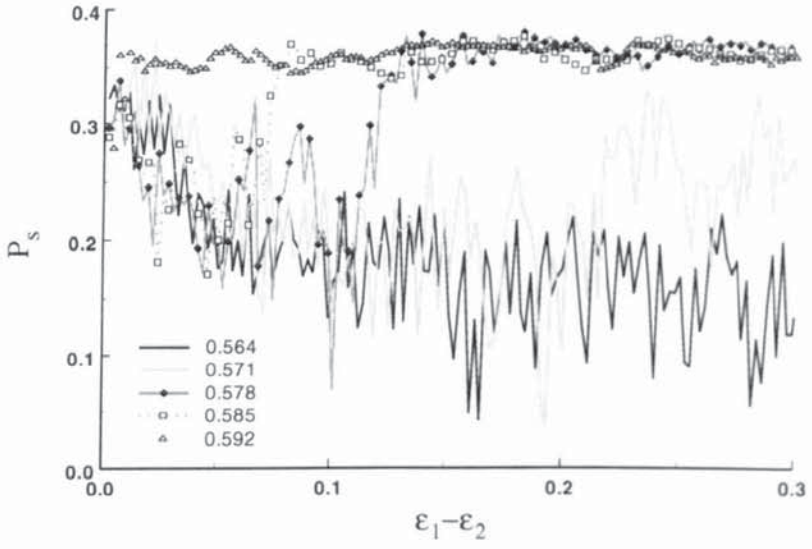

(a)

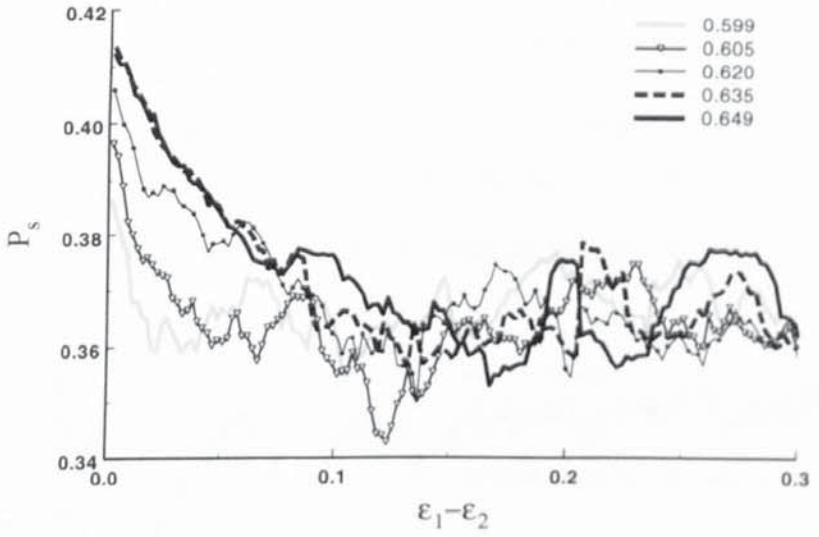

(b)

Fig. 6.15 The evolution of ratio P_s

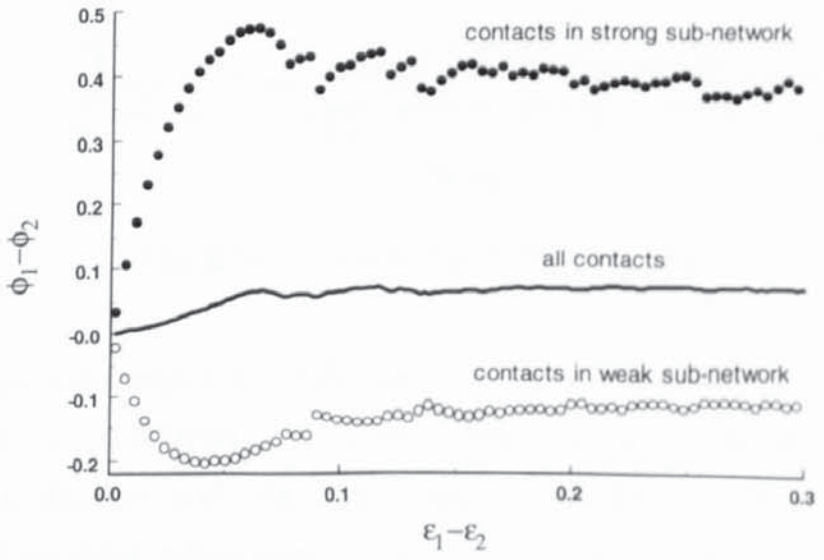

Fig. 6.16 The evolution of deviator fabric

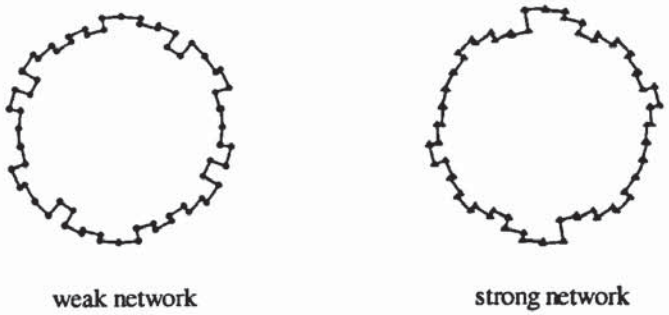

(a) before shearing

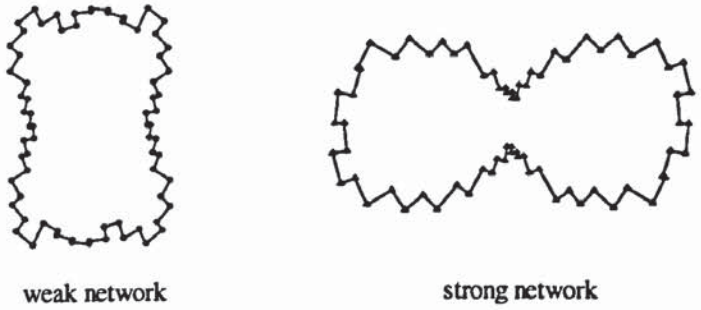

(b) at the end of shearing

Fig. 6.17 Polar diagrams of the contact normal orientations in the two sub-networks

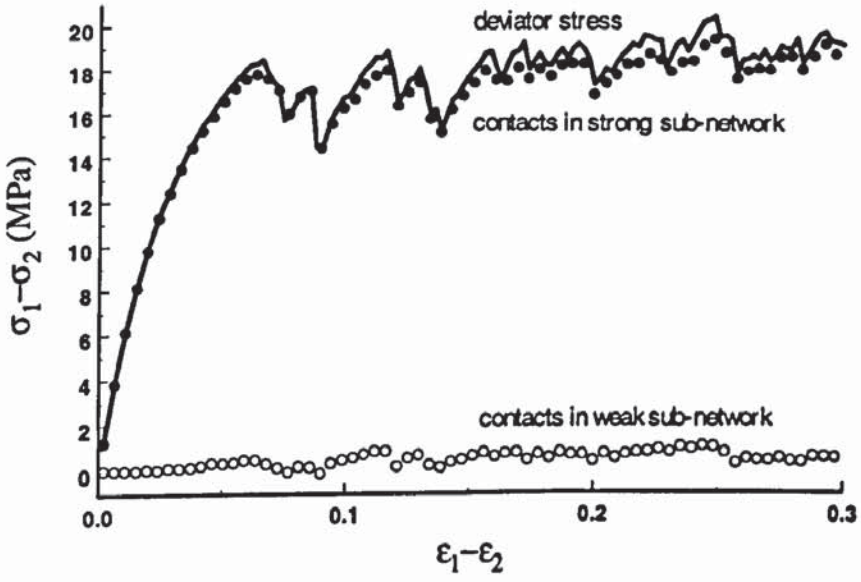

Fig. 6.18 The evolution of deviator stress

The stress tensor is decomposed into the contribution due to the contacts in the strong sub-network and weak sub-network, respectively. Figure 6.18 illustrates the evolution of the deviator stress together with the corresponding contributions. It is clear that the contribution of the weak sub-network to the deviator stress is very small and always less than 5%, although there are ca. 63.5% of the contacts within this sub-network (Fig. 6.15b).

In Fig. 6.19, the evolution of the deviator fabric in the strong sub-network $(\phi_1 - \phi_2)^s$ is plotted against $\sin\varphi_m$. It can be seen that the variation of $(\phi_1 - \phi_2)^s$ with $\sin\varphi_m$ is essentially linear up to the peak value. It also shows that the results plot above the line $(\phi_1 - \phi_2)^s = \sin\varphi_m$, which means that the value of $(\phi_1 - \phi_2)^s$ becomes higher than $\sin\varphi_m$ after certain strain. This can be further confirmed by Fig. 6.20, in which the evolutions of both $\sin\varphi_m$ and $(\phi_1 - \phi_2)^s$ with the deviator strain are shown. It is clear that after 5% deviator strain, the evolution of $\sin\varphi_m$ becomes lower than that of $(\phi_1 - \phi_2)^s$ by 10%.

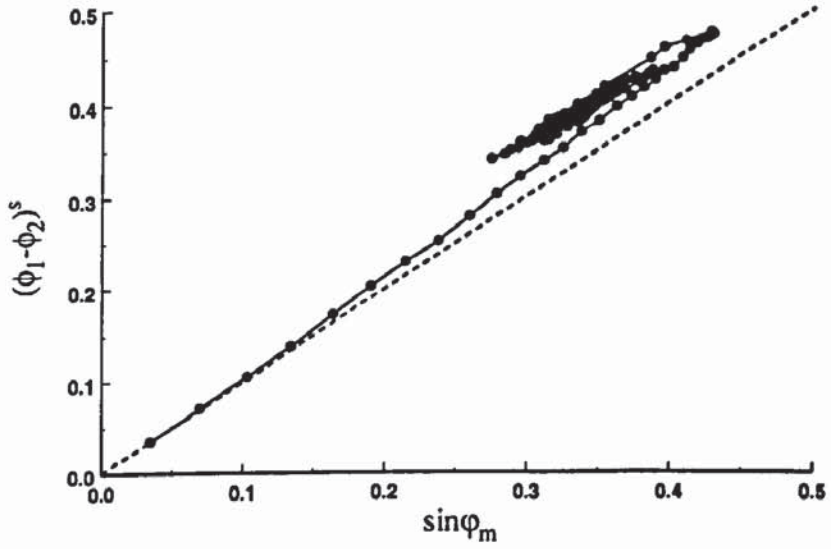

Fig. 6.19 The evolution of deviator fabric in the strong sub-network vs. $\sin\varphi_m$

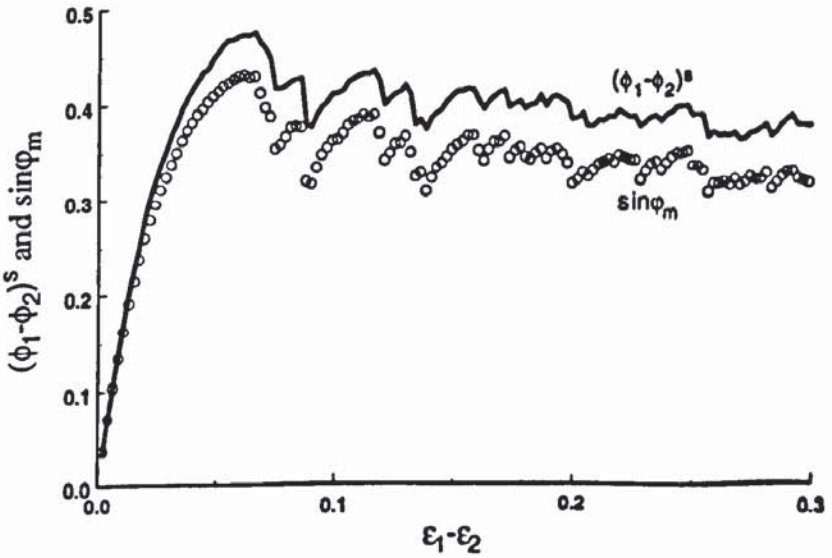

Fig. 6.20 The evolution of deviator fabric in the strong sub-network and $\sin\varphi_m$

The force transmission diagram for this sample at the end of shearing is re-plotted in Fig. 6.21, in which the force transmission in the two sub-networks is plotted separately. In addition, sliding contacts are superimposed on the weak sub-network as solid circles. It can be seen that the contacts within weak sub-network tend to align with the vertical direction and the contacts in strong sub-network tend to align with the horizontal direction. Therefore, this figure explains the orientations of the contact normals in the two sub-networks, which was shown in the Fig. 6.17b. In Fig. 6.9b,it was showed that nearly 1% of contacts are sliding in the whole system. Specifically, there are a total of 84 sliding contacts at this stage and only 12 of them transmit a force larger than the average contact force, which means that 86% of the sliding contacts are in the weak sub-network. This indicates that nearly all the strong contacts are non-sliding and almost all the frictional dissipation occurs within the weak sub-network.

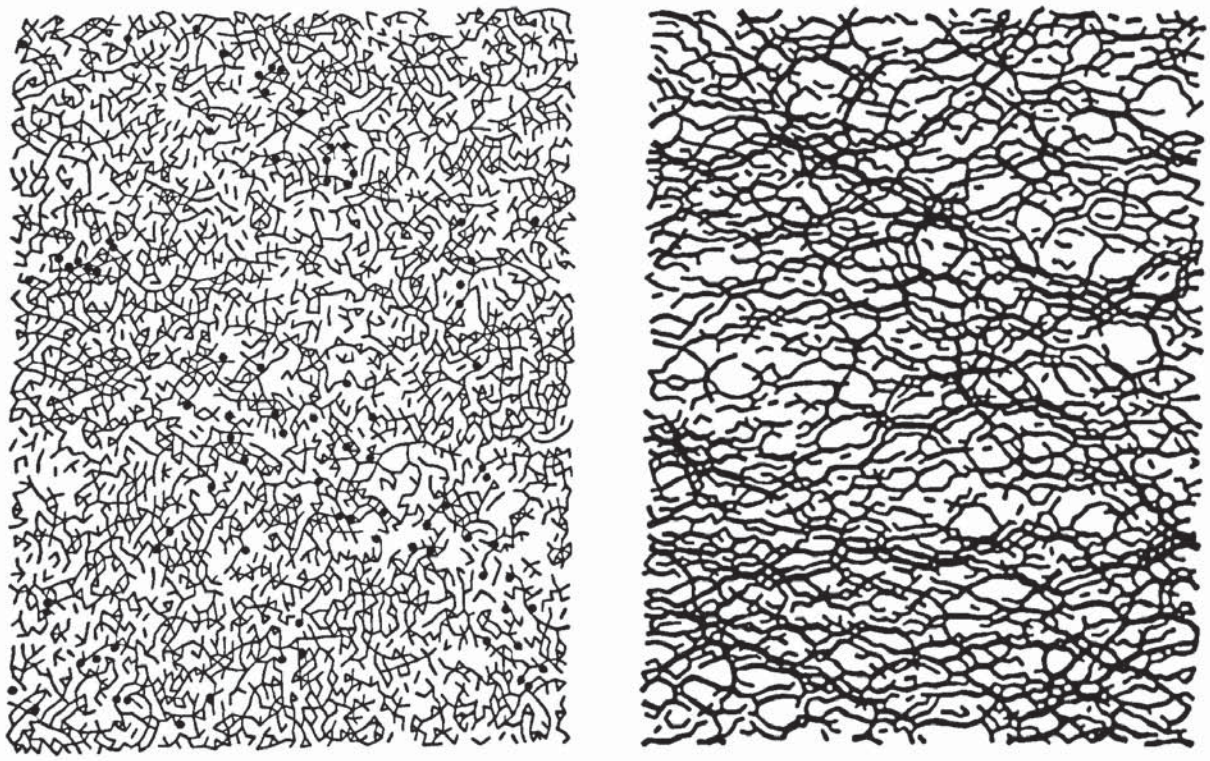

(a) weak sub-network (b) strong sub-network

Fig. 6.21 Force transmission diagram

6.4 Constant mean stress (CM) tests

The change in solid fraction during biaxial compression tests in which the mean stress is held constant is shown in Fig. 6.22. It can be seen that the solid fractions at the end of

shearing are lower than those before shearing except for the two loosest samples. Figure 6.23 shows the corresponding changes in mechanical coordination number. It is noted that the values of Z_m at the end of shearing are all above 3.2 when the mean stress remains constant.

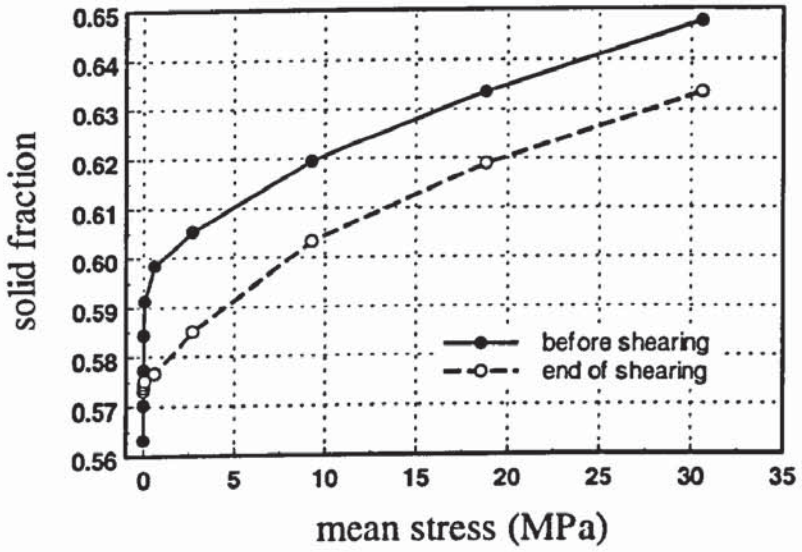

Fig. 6.22 Solid fraction vs. mean stress

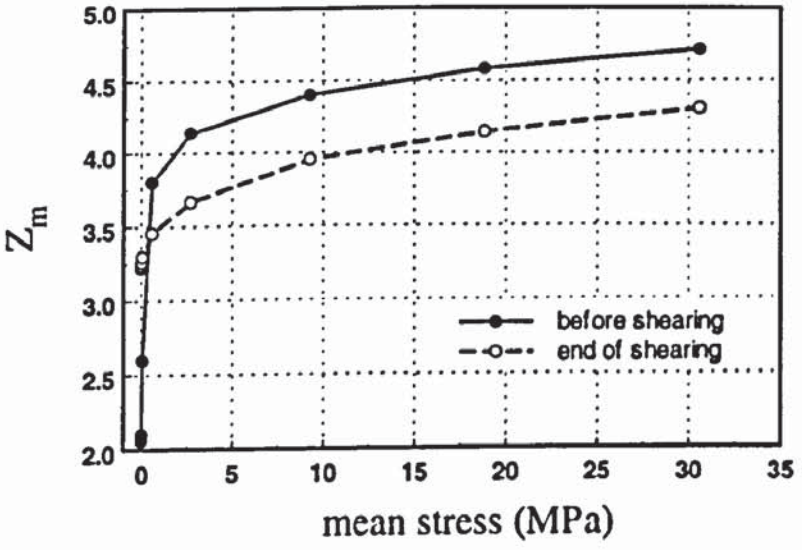

Fig. 6.23 Z_m vs. mean stress

6.4.1 Macroscopic behaviour

Figure 6.24 shows the evolution of the deviator stress against deviator strain. It can be seen that, for the four loosest systems, shear stresses are very small and all below 20kPa. For the system with an initial solid fraction of 0.592, a significant deviator stress is

developed, which is three times higher than the other four looser samples (Fig. 6.24a). For those systems with a high initial solid fraction (larger than 0.599), the deviator stresses increase from the beginning of shear and slightly decrease after peak until an approximately constant value is maintained at large strains (Fig. 6.24b).

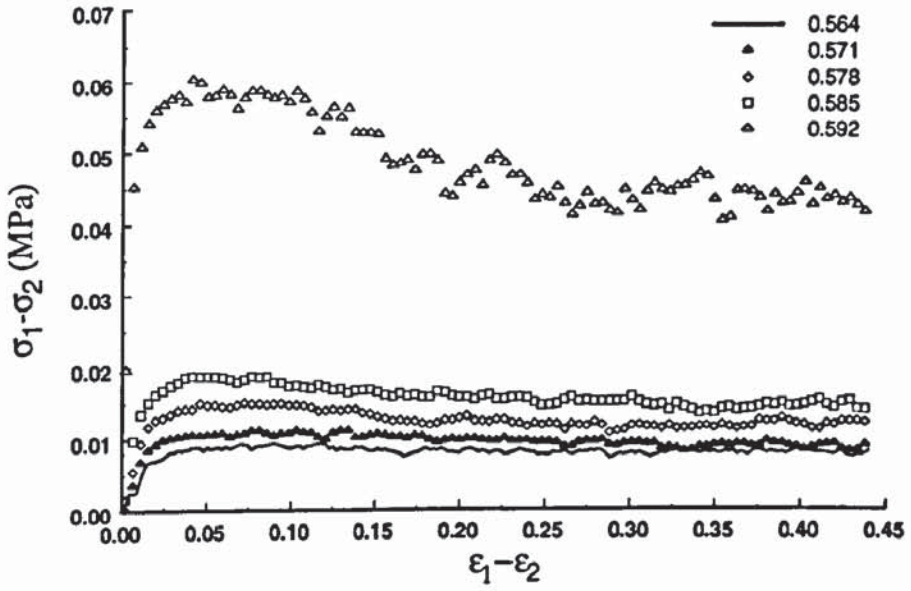

(a)

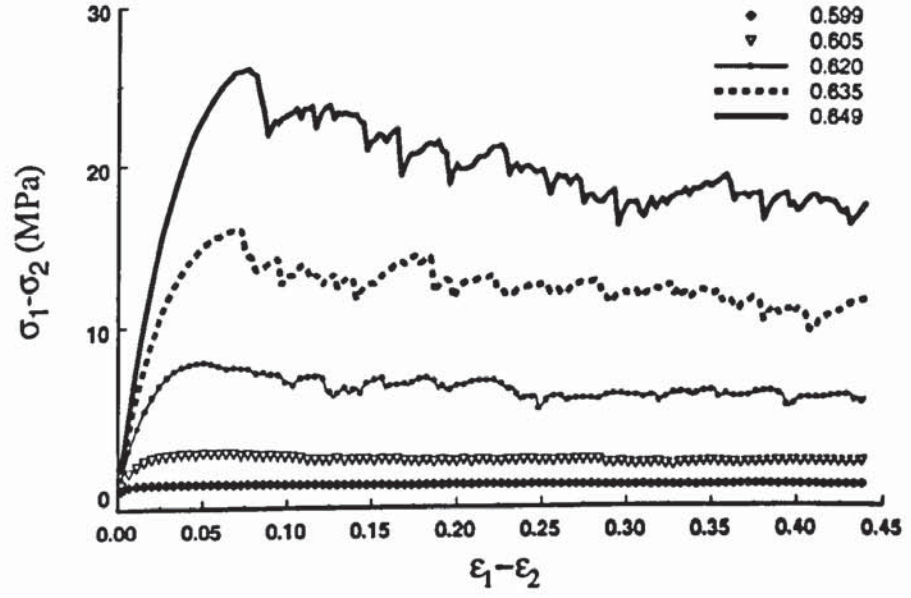

(b)

Fig. 6.24 Evolution of deviator stress

The evolution of volume strain ε_v during biaxial compression under constant mean stress conditions for all ten systems is shown in Fig. 6.25. It can be seen that the five loosest systems contract initially then expand and at large strain deform at approximately constant

volume. At the end of shearing, the volumes of the loosest samples are less than its original volume. Since these five curves are almost parallel after a certain amount of strain, the dilation angles of the five systems are essentially the same. However, the sample with the lowest initial density has the lowest maximum degree of dilation. The five dense systems do not show significant contraction at the beginning of shearing and they dilate almost throughout the test (Fig. 6.25b). In contrast to the loose systems shown in Fig. 6.25a for which expansion increases with increasing initial solid fraction, the degree of expansion of the five dense systems decreases with increasing initial solid fraction.

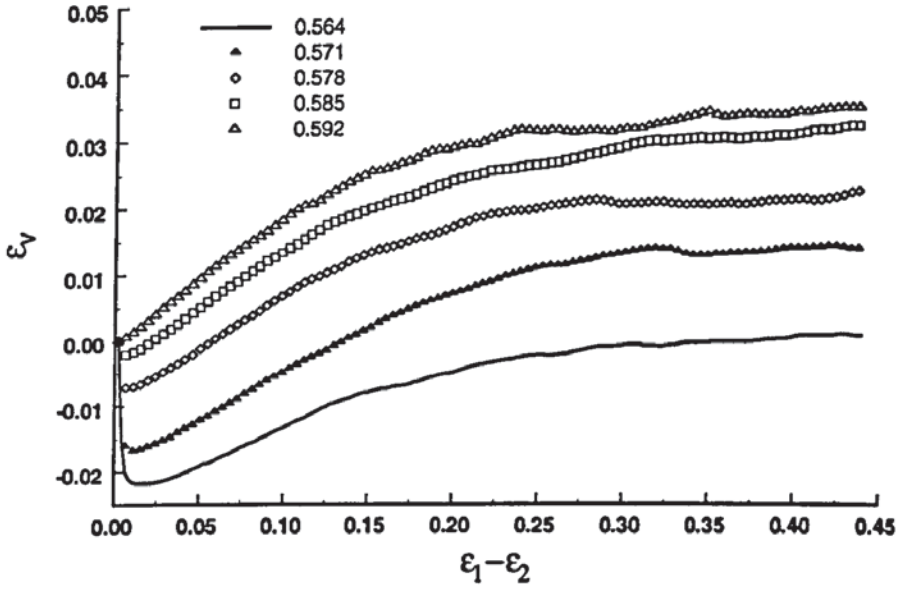

(a)

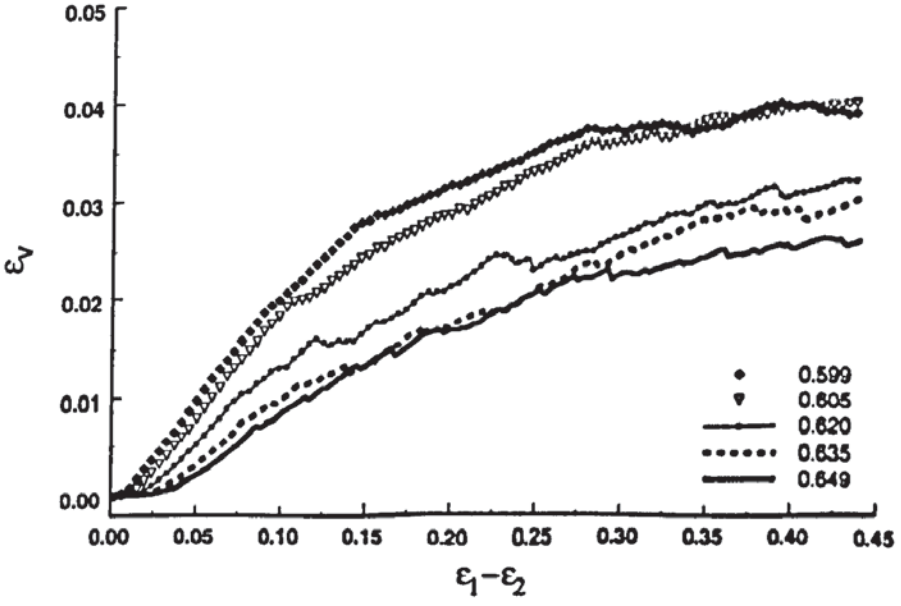

(b)

Fig. 6.25 Evolution of volumetric strain

Figure 6.26 shows the variation of $sin\varphi_m$ with deviator strain for all the systems. It is clear that a similar shear strength is developed for all but the loosest of the ten systems. Allowing for the fluctuations, it is also noted that the mobilised shear strength during the strain softening regime (e.g. after 10% deviator strain) is essentially the same for all initial packing densities. Fig. 6.26 also indicates that, at large strain, the 'critical state' value of φ_m is essentially the same for all ten system.

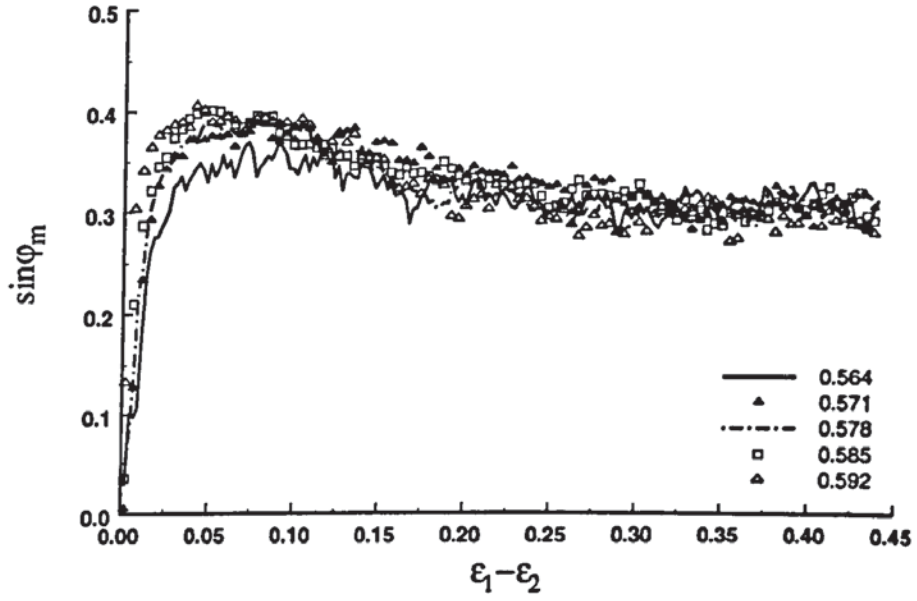

(a)

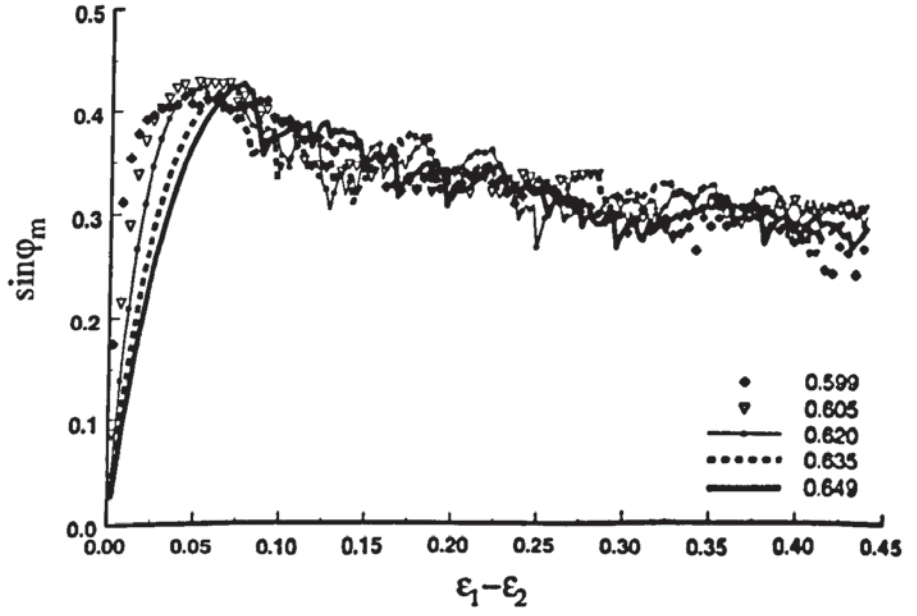

(b)

Fig. 6.26 Evolution of $sin\varphi_m$

The maximum values of $t=(\sigma_1-\sigma_2)_{max}/2$ for all ten samples in both constant volume and constant mean stress tests are plotted against the corresponding mean stress $s=(\sigma_1+\sigma_2)/2$ in Fig. 6.27. It is clear that they all lie on the same line even though there are ten different densities and the samples were deformed under different conditions. By using linear regression, the relation between these two parameters can be written as $t=0.43*s$, which is also superimposed in Fig. 6.27 by the dashed line. Hence, the maximum shear strength defined by $sin\varphi_m=0.43$ ($\varphi_m=25.5°$) is the same for all specimens.

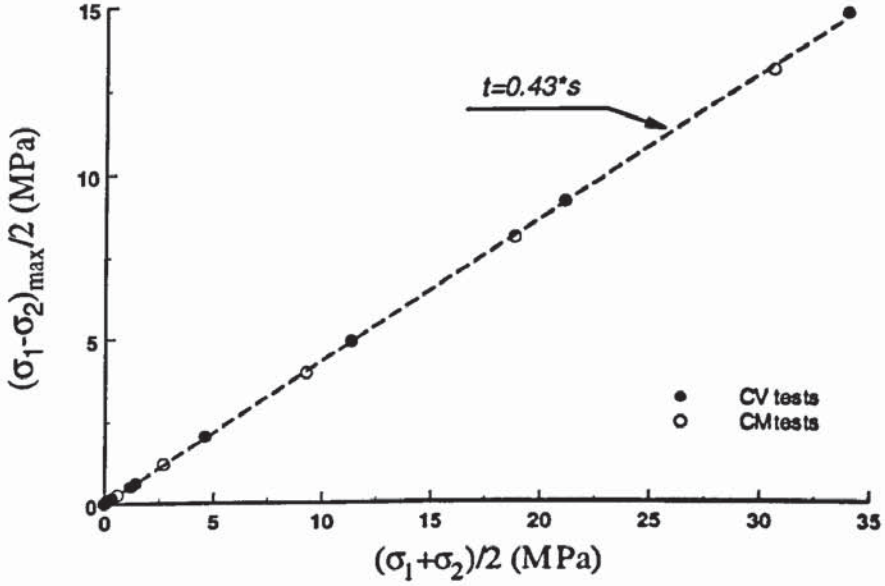

Fig. 6.27 $(\sigma_1-\sigma_2)_{max}/2$ vs. $(\sigma_1+\sigma_2)/2$

6.4.2 Microscopic behaviour

The evolution of the mechanical coordination number is shown in Fig. 6.28. For the four loosest systems, Z_m increases sharply to the value ca. 3.2 and then remains essentially constant at this value. The behaviour of the dense systems is similar to the results obtained from constant volume tests (Fig. 6.7b) in terms of the overall trends, although the final values are different.

Figure 6.29 shows the evolution of deviator fabric for all systems. Again, the overall trends exhibited by the five densest systems are similar to those observed for constant volume tests (Compare Fig. 6.10b and Fig. 6.29b). However, unlike constant volume tests,

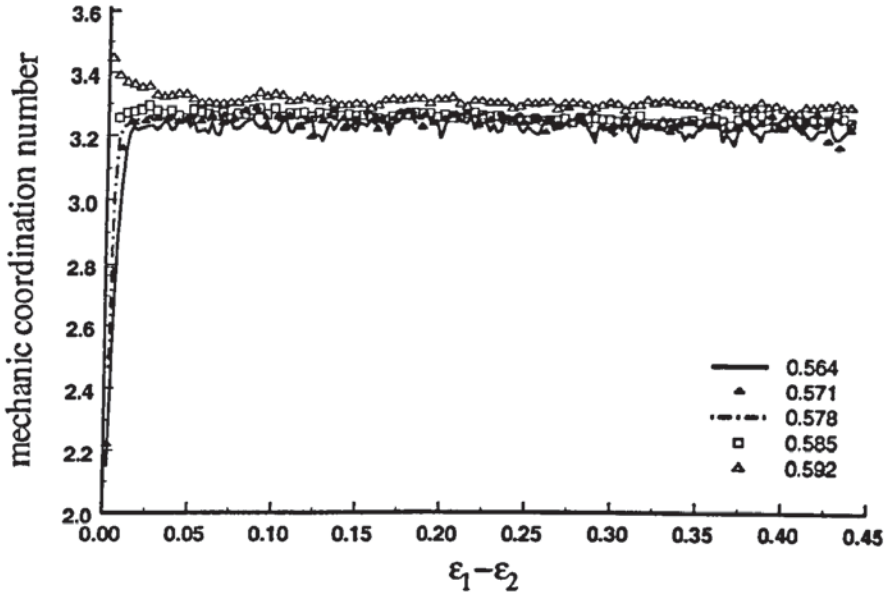

(a)

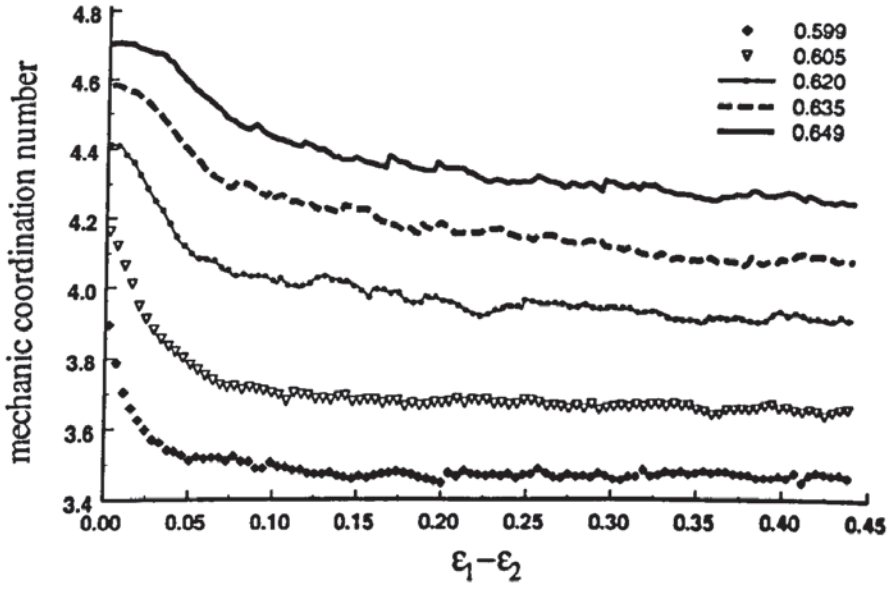

(b)

Fig. 6.28 Evolution of mechanical coordination number

it can be seen that the evolution of deviator fabric does not show strong fluctuations during constant mean stress tests on the loose samples (Fig. 6.29a). This is due to the fact that, when the mean stress of each sample is maintained constant, the five loosest systems contract initially and a mechanical coordination number above 3.0 is quickly established, thereby ensuring enduring connectivity across the specimen. Although at the end of shearing the five loosest systems have essentially the same degree of structural anisotropy, the five dense systems show a decreasing degree of structural anisotropy with increasing

initial packing density. The mean stresses of the loose systems are very close and all under 1.0MPa throughout shearing. However, the mean stresses of the dense systems vary from 6MPa for the sample with a solid fraction of 0.599 to 30.6MPa for the densest sample (Fig. 6.1). This suggests that increasing stress level suppresses the degree of structural anisotropy developed.

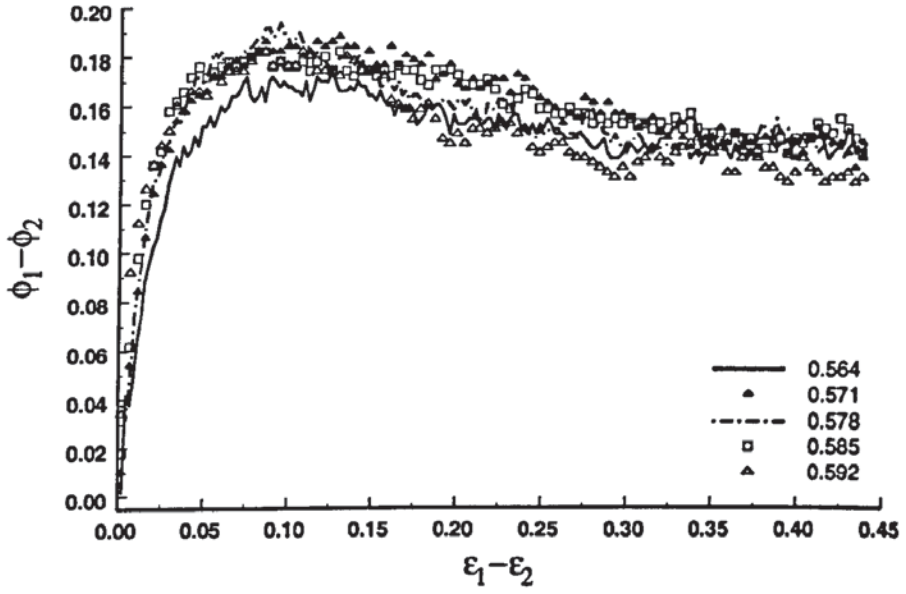

(a)

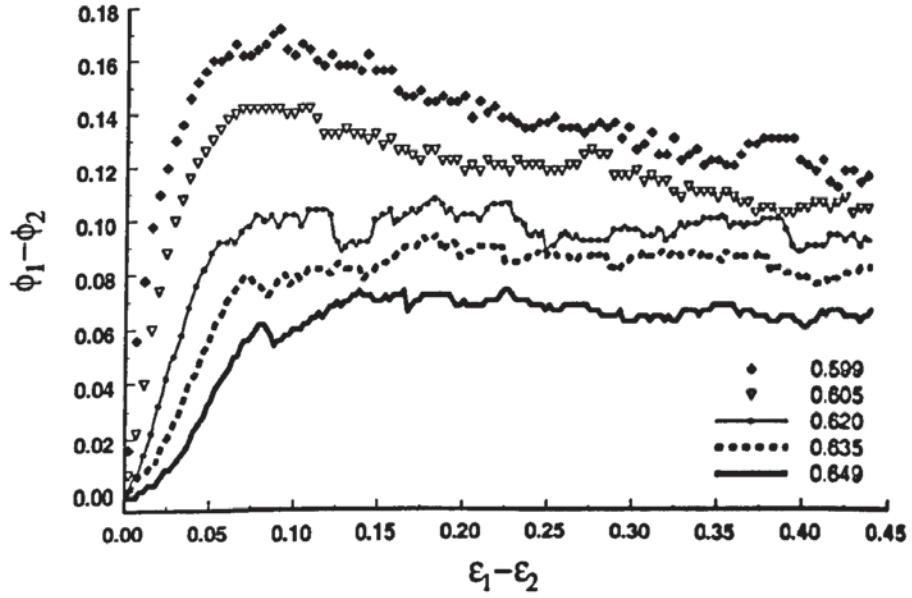

(b)

Fig. 6.29 Evolution of deviator fabric

The evolution of the ratio of sliding contacts is shown in Fig. 6.30. It is clear that two different behaviours can be identified depending on the initial density of the sample. For

the samples with low solid fractions (Fig. 6.30a) the percentage of sliding contacts fluctuate around 3% throughout the test. In addition, for these samples (solid fraction ≤ 0.592), the amplitude of the fluctuations increases with decreasing initial packing density. For the samples with higher initial densities (Fig. 6.30b), the percentage of sliding contacts increases sharply at the beginning of the test, thereafter it reduces to a value ca. 1-2% after 10% shear strain.

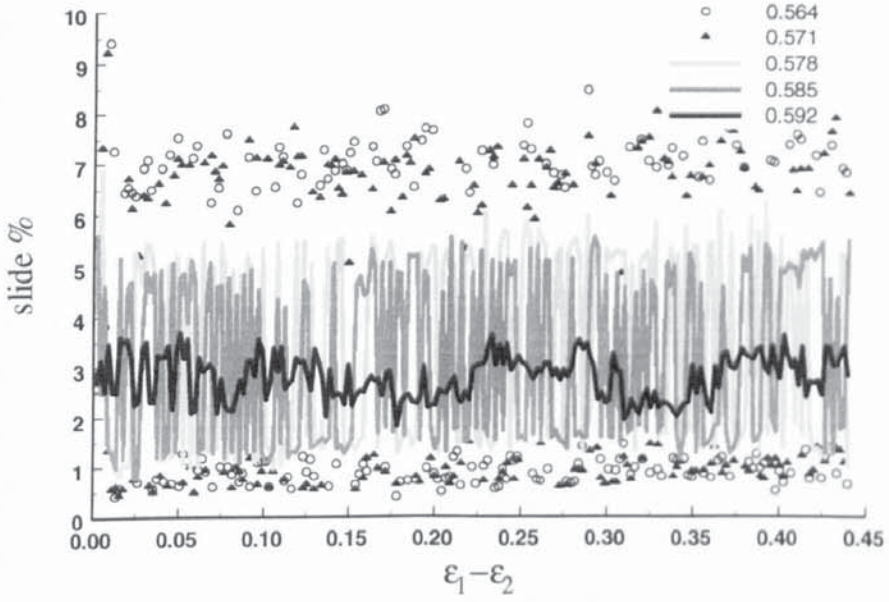

(a)

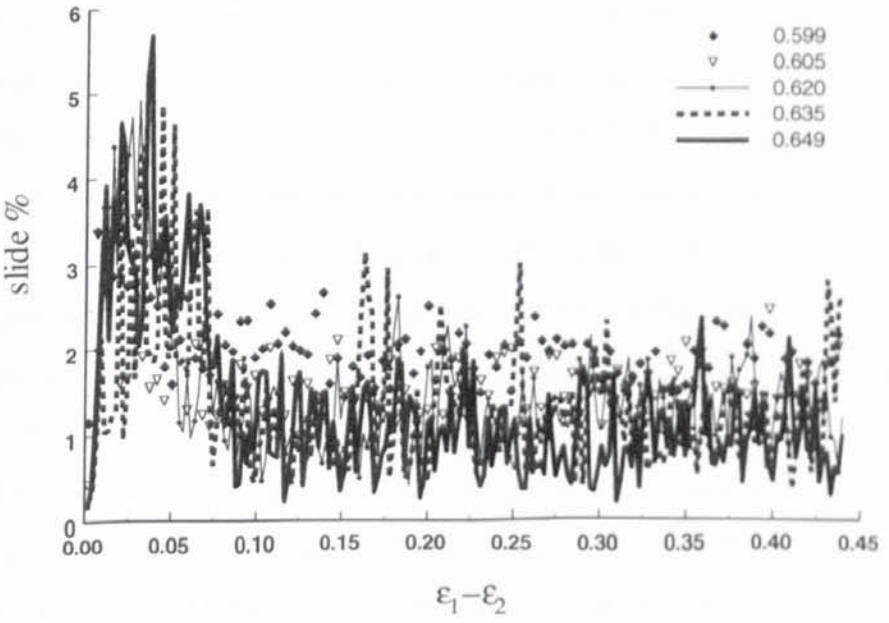

(b)

Fig. 6.30 Evolution of sliding contact

6.5 Fully developed flow (the so-called 'critical' state)

There is a special interest in the behaviour of granular media at large strain when fully developed flow has been established. This is true both in soil mechanics and particle technology. As demonstrated by results presented in this Chapter, at the 'critical state' when fully developed flow has been established then, for a given mean stress p, (i) the shear strength remains constant, (ii) all systems continue to deform at constant volume and (iii) the void ratio is independent of the initial packing density. This confirms with the established concepts of traditional soil mechanics (Schofield and Wroth, 1968). In this section, the data obtained from both constant volume tests and constant mean stress tests are re-examined to focus on the conditions during fully developed flow.

In the context of soil mechanics, it is more traditional to define the packing density in terms of the void ratio e (volume of voids/volume of solids) rather than the solid fraction (volume of solids/ total volume). The data from various tests over a wide stress range are compared and shown in $e-p$ space in Fig. 6.31. The isotropic compression line is denoted as 'ICL', which presents the relationship for all ten samples at the initial state after isotropic compression. The critical state line is defined as 'CSL', which shows the relationship at fully developed flow. It can be seen that the shape of the critical state line is very similar to the results reported by experimentalists.

It is clear that, except for the two loosest samples, the void ratio of the sample increases in the constant mean stress tests (see path a). Also, except for the two loosest samples, the mean stress increases in the constant volume tests (see path b). It can be seen that, the CSLs of constant volume and constant mean stress tests coalesce onto a common curve. Hence, it suggests that whether the test is performed under constant volume or constant mean stress does not have any influence on the location of the CSL. It is noted that the curvature of the CSLs changes abruptly at a stress level ca. 1MPa and some authors have simplified this by means of a bilinear critical state line (Been *et al.*, 1991). In addition, the slope of the CSL for constant volume tests changes at stress levels lower than 1kPa as well. Tatsuoka *et al.* (1986) carried out a large number of tests at stress levels of 5kPa and showed that the CSL became flatter at low stress levels. In this study, the stress levels are all greater than 10kPa initially and at the critical state only the two loosest samples developed stress levels lower than 1kPa in constant volume tests. However, it should be noted that there is no gravity field in the simulations.

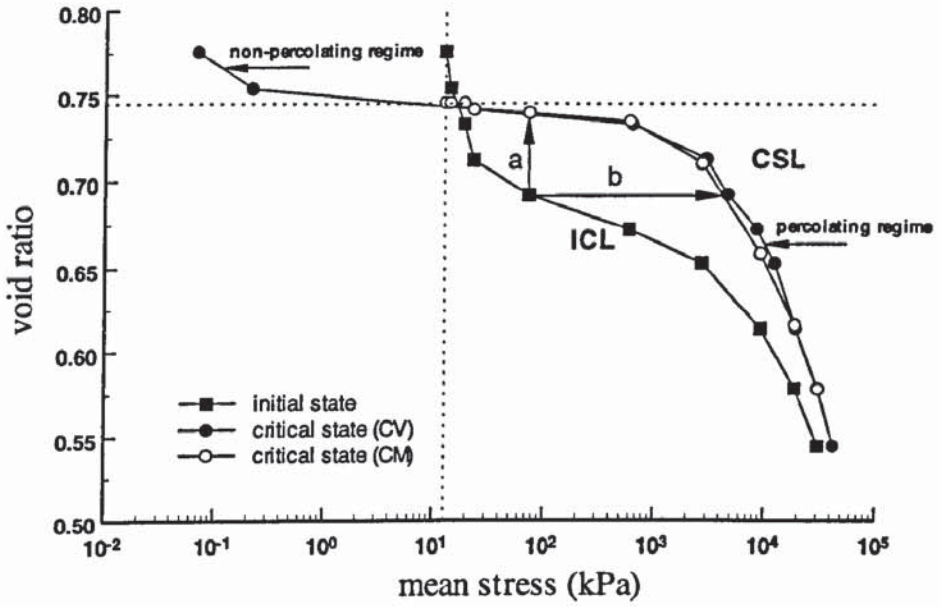

Fig. 6.31 $e-p$ plane

In Fig. 6.31, the vertical reference line (dashed) divides the CSL into two regimes. To the left there are two samples with mean stress lower than 10kPa and with void ratio higher than 0.745 (corresponding to a solid fraction of 0.573). According to the behaviour of the two samples at the critical state, this part of CSL corresponds to the non-percolating regime. The regime to the right of the vertical reference line corresponds to the percolating regime in which, at the critical state, all the samples within this regime behave similarly. The intersection of the two reference lines hence indicates the percolation threshold.

In most research into the critical state, only limited information can be provided in the context of the macroscopic scale. However, by using DEM simulations more information can be provided about the microscopic scale. The relationship between mechanical coordination number and the mean stress is shown in Fig. 6.32. Figure 6.33 shows the relationship between the mechanical coordination number and void ratio. It is clear that at the critical state, for both types of test, similar critical state behaviour can be observed except for the two loosest samples. For the constant volume tests, the two loosest samples cannot develop a mechanical coordination number higher than 3.0 and consequently, at the critical state, the stress levels are much lower and void ratios are much higher, compared to the tests on other samples. This implies that at the critical state, for samples at relatively low stress levels, the material behaviour depends on whether the sample percolates or not. As indicated by the reference line in Fig. 6.32 and 6.33 that the mechanical coordination

number at the percolation threshold is ca. 3.2. Recalling Fig. 6.28a in which the evolution of mechanical coordination number of constant mean stress tests are shown for the five low solid fraction samples, it can be seen that the mechanical coordination number rapidly increased to a certain value above 3.2 after which all the curves showed the same trend.

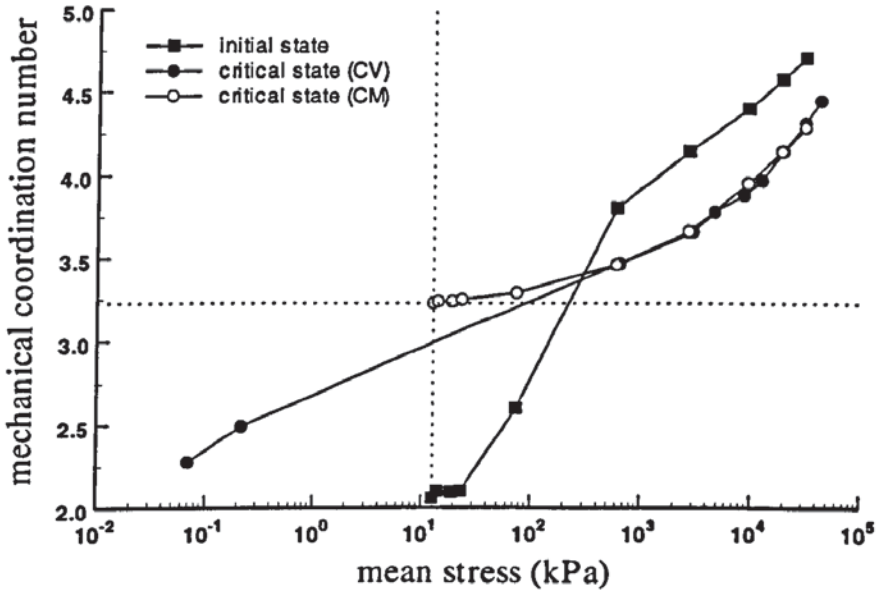

Fig. 6.32 Mechanical coordination number vs. mean stress

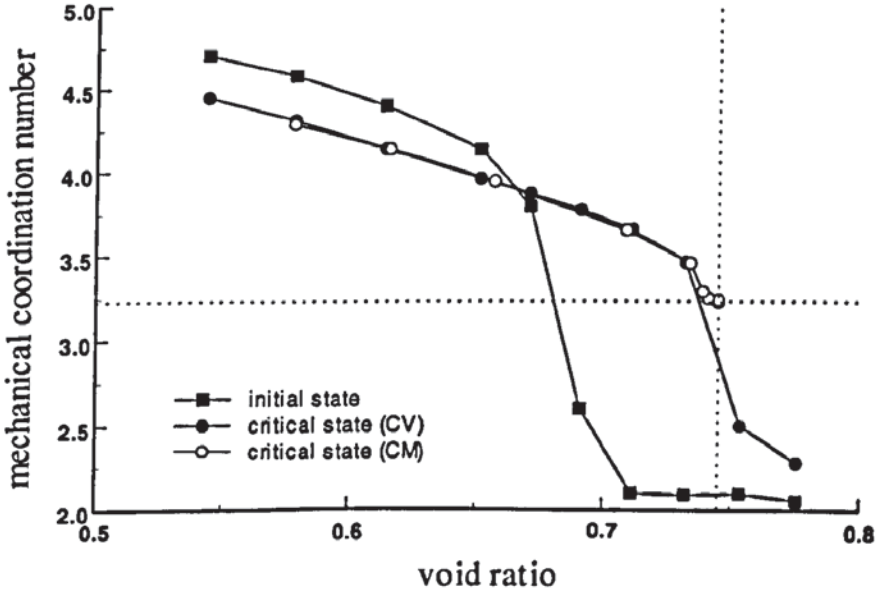

Fig. 6.33 Mechanical coordination number vs. void ratio

It is recognized that the shear response is fabric-dependent. Hence, some aspects of material behaviour related to the structural anisotropy at the critical state are presented in

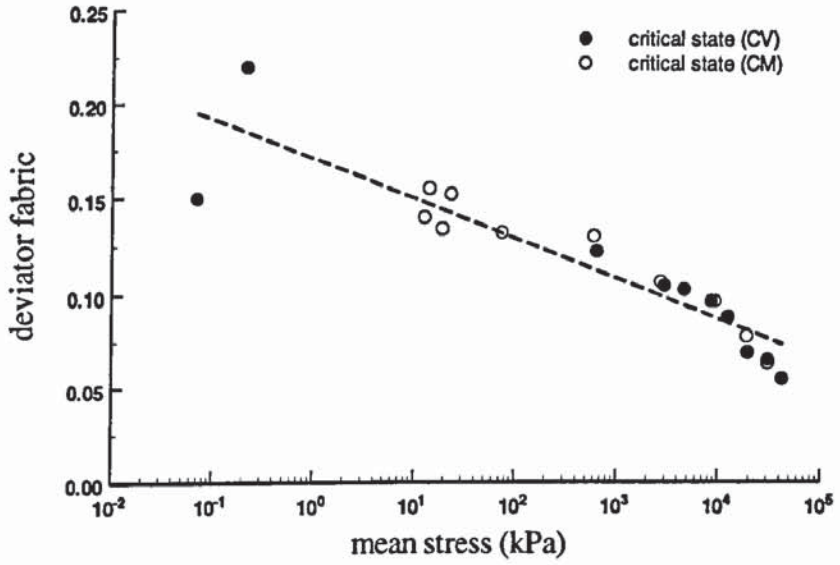

(a) deviator fabric vs. mean stress

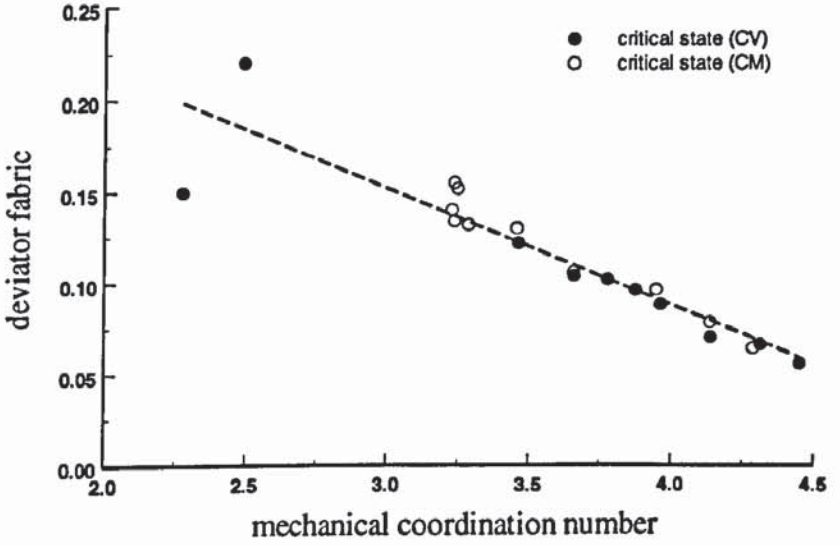

(b) deviator fabric vs. mechanical coordination number

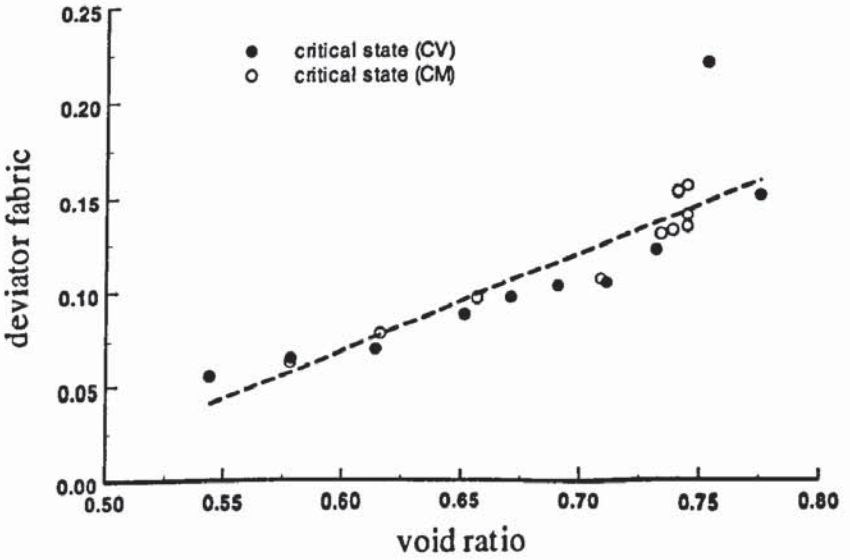

(c) deviator fabric vs. void ratio

Fig. 6.34 Comparison of deviator fabric at the critical state from CV and CM tests

Fig. 6.34, in which the relationship between deviator fabric against mean stress, mechanical coordination number and void ratio are shown, respectively. The best-fit lines are superimposed on each figure. It is clear that, except for the two loosest samples in the constant volume tests, all the results from the other tests exhibit strong correlations between the various parameters at the critical state. It can be seen from Fig. 6.34 that at the critical state a decreasing deviator fabric is accompanied by a increasing mean stress and mechanical coordination number, and a decreasing void ratio.

6.6 Summary

Biaxial compression of 2D systems of elastic spheres in a periodic cell have been simulated using the Discrete Element Method. The systems were deformed under both constant volume and constant mean stress conditions. The simulation results of constant volume tests have revealed that the characteristic behaviour at both the macroscopic and microscopic scales is distinguished by whether or not the system percolates, i.e. enduring connectivity is established in all directions. Dense systems, which percolate from the start of shear, generally exhibit the typical stress–strain response of soil mechanics. Very loose systems never percolate during shear and are unable to develop significant shear stresses. Systems with intermediate packing fractions are initially non-percolating but develop a shear modulus once enduring connectivity (percolation) is established, and thereafter the behaviour is similar to that of dense systems. The transition from non-percolating to percolating systems correlates well with the establishment of a mechanical coordination number of ca. 3.0. This transition is reflected in the change in the evolution of internal variables, such as the induced structural anisotropy and the ratio of sliding contacts.

For the dense systems, the mechanical behaviour in constant mean stress tests is similar to those of constant volume tests. However, for the loose systems, the macro- and micro-behaviour depends on the test conditions. In the constant mean stress tests, all the loose systems mobilised significant shear strength at small strain, and the evolution of the mechanical coordination number and structural anisotropy are also similar. This is attributed to the fact that, in the constant mean stress tests, the mechanical coordination number increased rapidly to a value higher than 3.0 for all the loose systems. This indicated that the samples changed from non-percolating to percolating systems almost immediately after shear deformation was applied.

The investigation of force transmission illustrates that there are two distinct separate networks within the system: a strong network composed of contacts carrying forces larger than the average force, and a weak network of contacts carrying forces less than the average force. It has been shown that the major principal direction of contact normal orientations in the strong sub-network coincides with the principal compression direction, whereas the major principal direction of the contact normal orientations in the weak sub-network is in the principal extension direction. In addition, most sliding contacts occur in the weak sub-network. Consequently, the dissipation due to sliding takes place primarily inside this weak network.

The examination of the critical state shows that a unique critical state line can be obtained for the material regardless of the type of test. The critical state behaviour can be divided into three groups according to the stress level experienced. For stress levels less than 1kPa and the system is non-percolating the slope of the CSL is steep. For stress levels between 1kPa and 1MPa the CSL is almost horizontal. If the stress levels are greater than 1MPa, the slope of the CSL steepens again. It has been shown that if a system can achieve percolation at large strain then the critical state point would fall on this unique critical state line for the material. The CSL can be divided into two regimes at the percolation threshold when the mechanical coordination number is ca. 3.2. The systems with a mechanical coordination number higher than 3.2 at the critical state fall into the percolating regime. Otherwise it will be in the non-percolating regime. Since all the samples used in this investigation had an initial mean stress that was higher than 10kPa, in order to examine the critical state behaviour at very low stress levels more samples need to be generated within this regime. However, one may argue this is not of practical importance.

CHAPTER 7: ANALYSIS OF SHEAR BAND FORMATION

7.1 Introduction

The failure of granular material is often accompanied by the occurrence of shear bands, i.e., the localization of deformation into thin zones. Localization phenomenon and subsequent shear band formation in granular materials can be observed when they are subjected to various loading conditions such as biaxial compression tests and direct shear tests. It is recognised that when a shear band is generated inside a specimen, heterogeneity is so dominant that quantities, such as stress and strain, lose their physical meaning if averaged over the specimen. Hence, quantitative prediction and accurate description of shear band formation is necessary to predict the failure of granular materials. Shear bands are generally characterised by the orientation angle, surface shape, and thickness. It has been shown in previous chapters that shear bands occurred in three types of shear test simulations: biaxial compression tests with periodic and wall boundaries and direct shear tests. In each type of test the bands had different appearance and inclination angle.

In this chapter, biaxial compression tests with periodic boundaries are re-examined to investigate the micromechanical deformation behaviour of shear band formation. Firstly, particle kinematics, i.e. displacements, velocity and rotations, are determined during the tests. Then the particle kinematics together with the distribution of sliding contacts are analysed to study deformation patterns and micro-deformation mechanisms. Finally, the measured shear band inclination angles are presented and compared with the classical Mohr-Coulomb and Roscoe solutions. The measurements of shear band thickness are also presented.

7.2 Brief literature review

It is well known that the formation of shear bands leads to the development of slip surfaces. The onset of slip surfaces in soil is strongly related to the stability of geostructures. Once shear bands are formed, they are persistent and finally lead to

progressive failure. This type of phenomenon has been studied as a bifurcation problem for many years. The localization theory developed by Hadamard (1949) for elastic bodies was extended to inelastic materials by Thomas (1961), Hill (1962), Rudnicki and Rice (1975) and Rice (1977). A bifurcation problem is referred to as a material subjected to static uniform deformation with a shear band mode. Although the velocity is continuous, the deformation and the velocity gradient are discontinuous across the shear band. The usual approach to this problem involves the consideration of a particular constitutive equation that describes material behaviour and the examination of such discontinuity planes, which are in turn identified with shear band boundaries and orientations.

Only in recent year has it been established via theory and accurate experiments that failure in frictional materials is often characterized by bifurcation and spontaneous localisation of deformations into rupture zones. These zones typically have a certain thickness and inclination angle. Although shear bands have been observed frequently within the scale of geotechnical structures and in laboratory tested soil specimens, it was only recently that systematic studies were undertaken to analyse and describe the occurrence and patterns of shear bands. The localization phenomenon in granular material is usually investigated by laboratory and numerical experiments. Morgenstern and Tchalenko (1967) studied the behaviour of thin sections of Carbowax impregnated clay in a direct shear device. They defined two types of discontinuities (strain and displacement), and showed that the kinematic restraint imposed by the testing configuration has a marked influence on the shear bands. Scarpelli and Wood (1982) used radiography to study the orientation of shear bands in direct shear tests of sand. They suggested that the degree of constraint experienced by the sand would influence the particular bifurcation that it adopts at a particular location. Where the sand sees freedom, it may adopt the Arthur solution. Where the imposed constraint is greater, as in the direct shear device, the shear band will tend towards the Roscoe solution, and follow directions of zero extension.

Stereophotogrammetry was used to investigate the progression of strain localization in plane strain compression tests on loose saturated sand under globally undrained and drained conditions (Harris *et al.*, 1995; Finno *et al.*, 1997). It was found that shear banding occurred in both undrained and drained experiments. Generally, a number of parallel, temporary bands gave away to a single persistent shear band. A clear pattern of the onset of the formation of persistent shear bands, mobilization of the maximum effective friction

and complete formation of the band were observed in all tests. It was found that the persistent shear bands evolved with varying width and orientation.

A study of strain localization in triaxial tests on sand was investigated by Desrues *et al.* (1996) by using computer tomography. The complex geometrical structures of the localization patterns were described and the evolution of the local void ratio in the localization zone(s) was determined. It was shown that strain localization patterns depend on test conditions. The comparison of the local void ratio in the shear zones with the global void ratio measurements demonstrated that a limit void ratio is reached in the shear zones that is significantly different from the final void ratio defined from the global measurements.

Digital image analysis was used to study localized deformation in granular materials by Alshibli and Sture (1999, 2000). A series of biaxial experiments were conducted on three sands: fine-, medium-, and coarse-grained uniform silica sands with rounded, subangular, and angular grain shapes, respectively. Different confining pressure conditions were applied to investigate the effects of specimen density, confining pressure, and sand grain size and shape on the shear band formation. It was found that the normalized shear band thickness decreases as grain-size increases and as specimen density decreases. The measured dilatancy angles increased as the grain angularity and size increased and shear band thickness was dependent on the dilatancy angle.

From a series of novel experiments using X-radiography and direct microstructural observation, shear strain localisation was studied in drained and undrained cohesionless granular materials by Nemat-Nasser and Okada (2001). In drained tests, shear localisation produced by monotonic deformation could be directly observed. In undrained tests, the local deformation during liquefaction, induced by cyclic shearing, was examined. It was directly observed that shear localisation does occur in liquefied specimens. They also found that at the centre of a fully developed shear band, the shear strains can exceed 500% although the overall nominal sample strain is about 10%.

Much of the previous research efforts were focused on describing shear bands by measuring or predicting the orientation angle and comparing it with the classical Mohr-Coulomb and Roscoe (1970) solutions. Due to the difficulty of experimentally measuring

the shear band thickness few studies have extended shear band description to include thickness measurements in addition to the orientation angle. Recently theoretical studies, which incorporated bifurcation theory, have been used to predict and describe the occurrence and pattern of shear bands. Vardoulakis and his co-workers have analysed the shear band bifurcation problem theoretically under plane strain conditions (Vardoulakis 1980, Vardoulakis and Graf 1985, Muhlhaus and Vardoulakis 1987). The predictions of shear band orientation and the evolution of its thickness were given. The theoretical solution obtained for the shear band inclination was a geometrical mean of the classical Mohr-Coulomb and Roscoe solutions and was in good agreement with the experimental data. It was found that the thickness of a shear band is a small multiple of the mean grain size. In addition, the width of shear bands was not affected by any geometrical dimensions of the specimen other than its grain sizes.

A theoretical analysis for the onset of shear banding which allowed for elastic unloading in a biaxial test was given by Vermeer (1990). It was shown that the orientation of shear bands varies within a wide range of admissible directions between the limits of the Coulomb and Roscoe solutions. Post bifurcation, for situations well beyond incipient shear banding, was also analysed in order to determine the type of shear band that is most likely to occur. For fine sands, which will tend to fail corresponding to the weakest failure mode, Coulomb type shear banding was found to be the preferred failure mechanism. Nevertheless, less inclined Roscoe type shear bands are likely to occur for coarse sands.

Apart from theoretical and experimental studies, shear band initiation and propagation have been numerically investigated by a number of researchers. Kuhn (1999) studied micro-structure deformation in granular materials using DEM simulations, in which experiments on a large two-dimensional assembly of discs was subjected to quasi-static biaxial loading. It was found that the deformation was very nonuniform at the microscale of individual voids. The predominant deformation structures were thin oblique microbands of void cells within which slip deformation was most intense. The thickness of these microbands was in the range between one and four particle diameters. Unlike shear bands, the microbands were neither static nor persistent and their orientation angle increased as deformation proceeded. In addition, dilation was slightly larger within the microbands than in the surrounding material.

Shear band formation was numerically investigated with the finite element method using a polar hypoplastic constitutive model by Tejchman and Bauer (1996). The biaxial tests were performed for two different meshes and two different mean grain diameters. Initiation of shear bands was triggered by a small inhomogeneity of the initial material properties. The calculated thickness of the shear zones was almost independent of the spatial discretisation if the size of the finite elements was not greater than five characteristic lengths. The numerical results showed that the polar effect manifested by the appearance of grain rotations is significant in the shear zone.

The structure of persistent shear bands in granular materials was investigated by numerically simulating an idealized assembly of 2D particles by Bardet and Proubet (1991, 1992). In the simulations, flexible stress-controlled boundaries were used instead of periodic boundaries to avoid constraining the motion of particles within the shear bands. The width of a shear band was found to decrease from 18 to 15 times the average particle radius with axial strain. The numerical simulations showed that the rotation of particles, the gradient of their rotation, and rotations of their neighbourhoods are concentrated inside the shear bands. The importance of rotation inside shear bands justifies the micropolar description of granular materials.

A modified distinct element method (MDEM), in which rolling resistance can be applied, was developed to study the microstructure of shear bands in granular materials (Iwashita and Oda, 1998; Oda and Iwashita, 2000). They found that the formation of column-like structures grow parallel to the major principal stress direction during strain hardening. The column-like structures kink as they pass through the shear band during strain softening. After failure, the column-like structures are reconstructed during strain softening by means of rolling so that a high gradient of particle rotation is generated in a relatively narrow shear zone. It was also demonstrated that shear bands can form irrespective of the value of rolling resistance applied and increased rolling resistance resulted in narrower shear bands. Large voids appear inside the shear band and the resulting local void ratio can exceed the corresponding maximum value determined from the overall system response.

Williams and Rege (1997a and b) described the formation of microstructures within a granular material subjected to biaxial compression using DEM. From the numerical simulations the formation of coherent vortex-like structures was observed in the

fluctuating velocity field and these structures were named circulation cells because the particles instantaneously translate and rotate as a rigid body about a common centre. These circulation cells migrate and coalesce to form larger structures during the test. Eventually a global shear band forms at the boundary of two or more of the circulation cells.

7.3 Shear band inclination angle

A shear band is always described as a thin layer of intensively sheared material with a certain width (d_b) and a certain inclination (θ) as shown in Fig. 7.1. There are two classical solutions for shear band inclination in frictional granular materials subjected to plane strain, namely the Mohr-Coulomb (static) and Roscoe (1970) (kinematic) solutions.

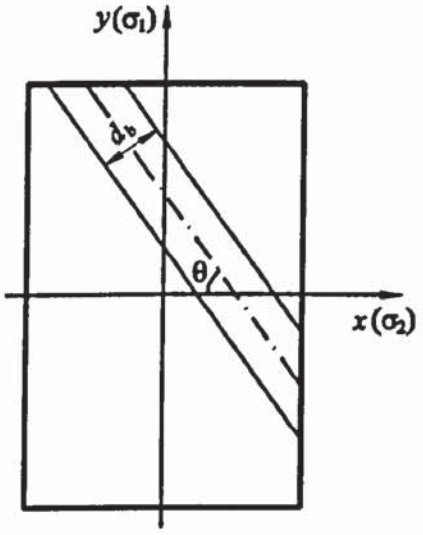

Fig. 7.1 Specimen with a shear band

(a) Mohr-Coulomb theory

According to the Mohr-Coulomb criterion, the inclination angle of the shear band is given by:

$$\theta_C = \pm\left(45° + \frac{\varphi_m}{2}\right) \tag{7.1}$$

where θ_C is the angle measured from the direction of the minor principal stress. This equation is a purely static statement defining a plane of maximum stress obliquity (i.e., the ratio of shear stress to normal stress is a maximum possible value, see Fig. 7.2a). Only one

static constitutive parameter, the angle of shear resistance φ_m, is contained in (7.1) and no deformation variables or parameters are involved.

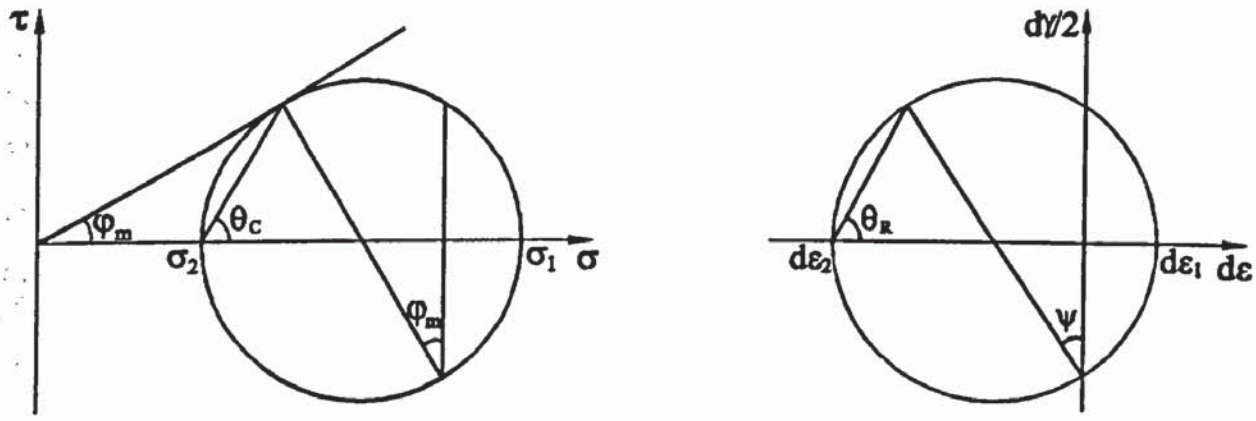

(a) stress (b) strain increments

Fig. 7.2 Mohr circles

(b) Roscoe theory

Roscoe (1970) argued that the inclination of the shear band should coincide with directions along which the rate of extension is equal to zero. Therefore, from Fig. 7.2b, the lines of zero extension should be inclined at an angle,

$$\theta_R = \pm\left(45° + \frac{\psi}{2}\right) \tag{7.2}$$

where θ_R is the angle between the shear band and the direction of the minor principal strain increment. The angle of dilatation ψ is defined by

$$\sin\psi = -\frac{d\varepsilon_v}{d\gamma} = -\frac{d\varepsilon_1 + d\varepsilon_2}{d\varepsilon_1 - d\varepsilon_2} \tag{7.3}$$

where $d\varepsilon_v$ is incremental volumetric strain, $d\gamma$ is the corresponding incremental shear strain and ε_1 and ε_2 are the major and minor principal strains, respectively. In the case of associated plasticity theories, the direction of the maximum stress obliquity plane and the zero extension direction coincide (i.e., $\varphi_m = \psi$), and thus the Mohr-Coulomb and Roscoe planes coincide. However, most researchers recognized that this is not the case for granular materials. Based on experimental observations, Arthur *et al.* (1977) obtained another result which is a combination of the two previous ones and supported by Vardoulakis (1980):

$$\theta_A = \pm\left[45° + \frac{1}{4}(\varphi_m + \psi)\right] = \pm\frac{1}{2}(\theta_C + \theta_R) \tag{7.4}$$

In the literature, experimentally measured shear band inclination angle values are widely scattered with values ranging from 55 to 70 degrees to the minor principal stress direction. Vardoulakis *et al.* (1978) found that the measured values of the shear band inclination angle θ are extremely sensitive to boundary conditions, and loose specimens are more sensitive than dense ones. For a loose, fine-grained, water-saturated sand tested under both undrained and drained conditions, Finno *et al.* (1996) found that the measured shear band orientation angle lies between the Coulomb and Arthur solutions and the inclination angle changed during strain softening.

7.4 Results and observations

It was found in Chapter 3 that the shear band deformation patterns were different when the biaxial compression tests were performed with periodic boundaries or wall boundaries. In order to avoid the sensitivity to the boundary conditions, the localization phenomena of granular material will be investigated for tests carried out with periodic boundaries in this chapter. In this study, the shear band inclination angle θ is measured with respect to the direction of the minor principal stress and is measured at the onset of the shear band since it changes as the compression proceeds, due to the change in the height of specimen, as will be shown in the following analysis.

7.4.1 Influence of packing density

In granular materials irreversible deformations take place even under very small stresses. The particles move relative to each other during deformation. The placement of different layers of coloured particles allows such deformation to be clearly observed in the simulations. In Fig. 7.3, the particle configurations at the end of shearing are shown for several samples with different solid fraction in the constant volume tests. It is clear that the deformation patterns are different. The pattern of the particle configuration for the loosest sample ($sf = 0.564$, Fig. 7.3a) looks distinct from the others. The coloured layers appear to be convex from the bottom to the top of the sample. However, no noticeable shear band

can be observed. For the sample with solid fraction 0.571, the bottom layers are essentially parallel while the top several layers become concave (Fig. 7.3b).

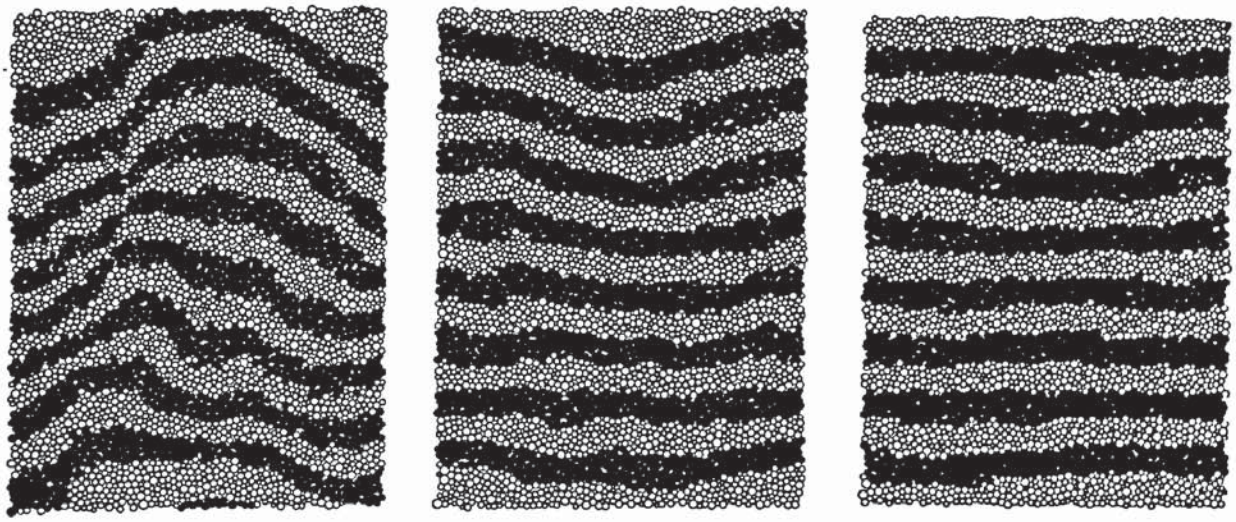

(a) $sf = 0.564$ (b) $sf = 0.571$ (c) $sf = 0.585$

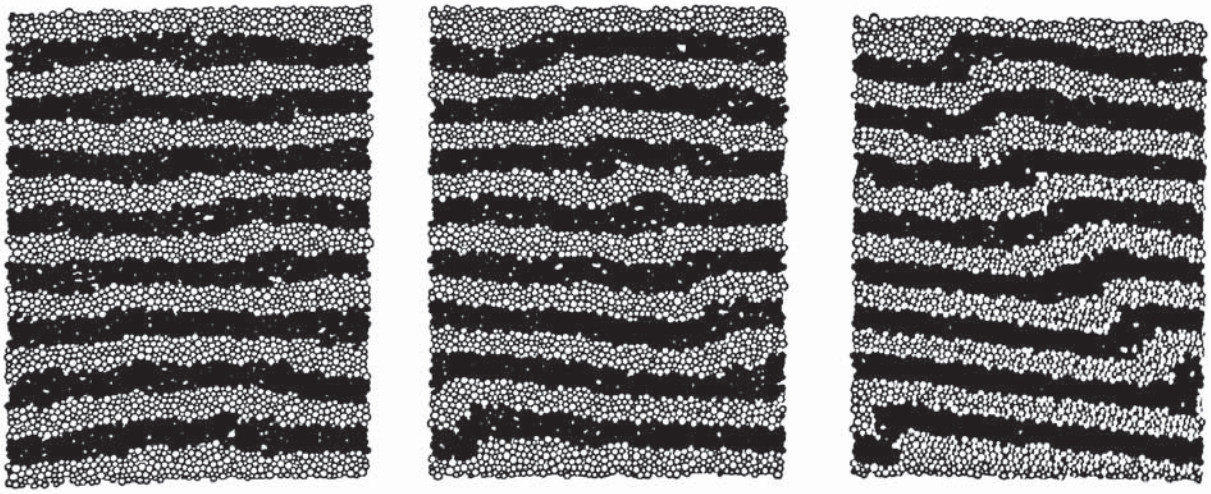

(d) $sf = 0.599$ (e) $sf = 0.606$ (f) $sf = 0.635$

Fig 7.3 Particle configuration at the end of tests with different solid fraction samples

The patterns of the samples with intermediate densities ($sf = 0.585$, 0.599, Fig. 7.3c, d) are similar and the layers are almost parallel. If the sample becomes denser a hint of a shear band starts to appear during shearing as shown in Fig. 7.3e. It can be seen that a very clear shear band formed in the sample with the highest initial solid fraction of 0.635 (Fig. 7.3f). It is therefore concluded that a dominant and persistent shear band can only be generated if the sample is dense enough. Although the loosest sample appears to have an irregular pattern at the end of shearing this is clearly not a shear band. It is only because the sample is so loose that it behaves like a fluid, as described in the previous chapter. Since the

sample with initial solid fraction 0.635 shows clear evidence of shear band formation, the following analyses are carried out on the results of this sample.

7.4.2 Shear band initiation, orientation and thickness

Figure 7.4 presents the stress-strain response of the sample during the constant volume and constant mean stress tests. The corresponding evolution of vertical displacement increment contours within the sample for the constant volume test is shown in Figs. 7.5. The displacement increments are taken between two steps that are marked in Fig. 7.4. The dimension of the diagram is drawn according to the current sample aspect ratio.

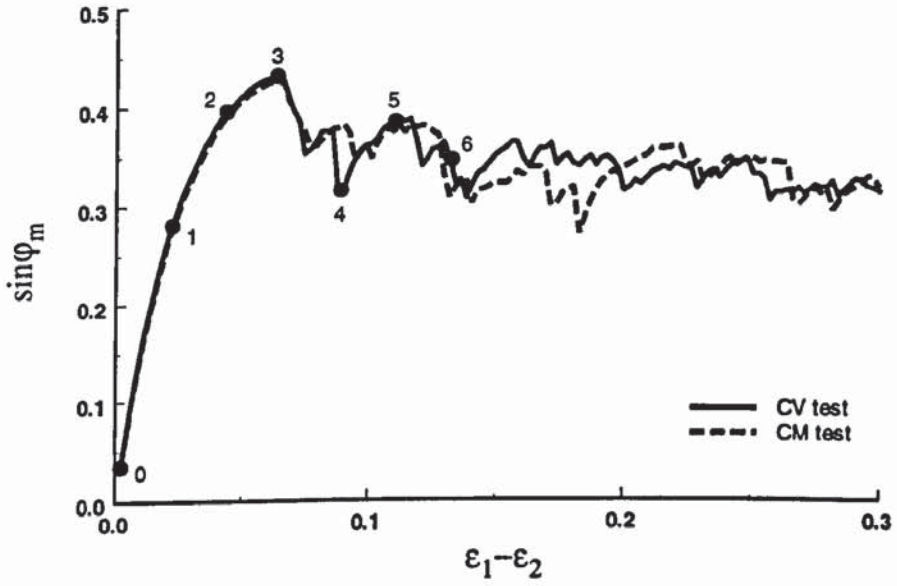

Fig. 7.4 Stress-strain curves in two biaxial compression tests

In Figs. 7.5a and b no localized deformation can be identified and the displacement field appears reasonably uniform within the specimen during these stages. Figure 7.5c indicates that the strain starts to localize into several conjugate shear bands inclined at ca. 45°, while the stress-strain response is strain hardening. However, these strain localisation bands are transient since they disappear and reappear as shearing continues. It is clearly shown in Fig. 7.5d that deformations localize into one distinct narrow shear band, which is inclined at ca. 45° after the peak shear strength. Although a persistent shear band is formed, it can be seen from Fig. 7.5e that it is discontinuous during the increasing shear strength parts of the fluctuations (see Fig. 7.4). The inclination angle becomes slightly less than 45° as the test proceeds (see Fig. 7.5f). One must bear in mind that the simulations are carried out

using a periodic cell. Therefore, the short shear band at the left bottom corner is actually an extension of the shear band running from upper left to lower right.

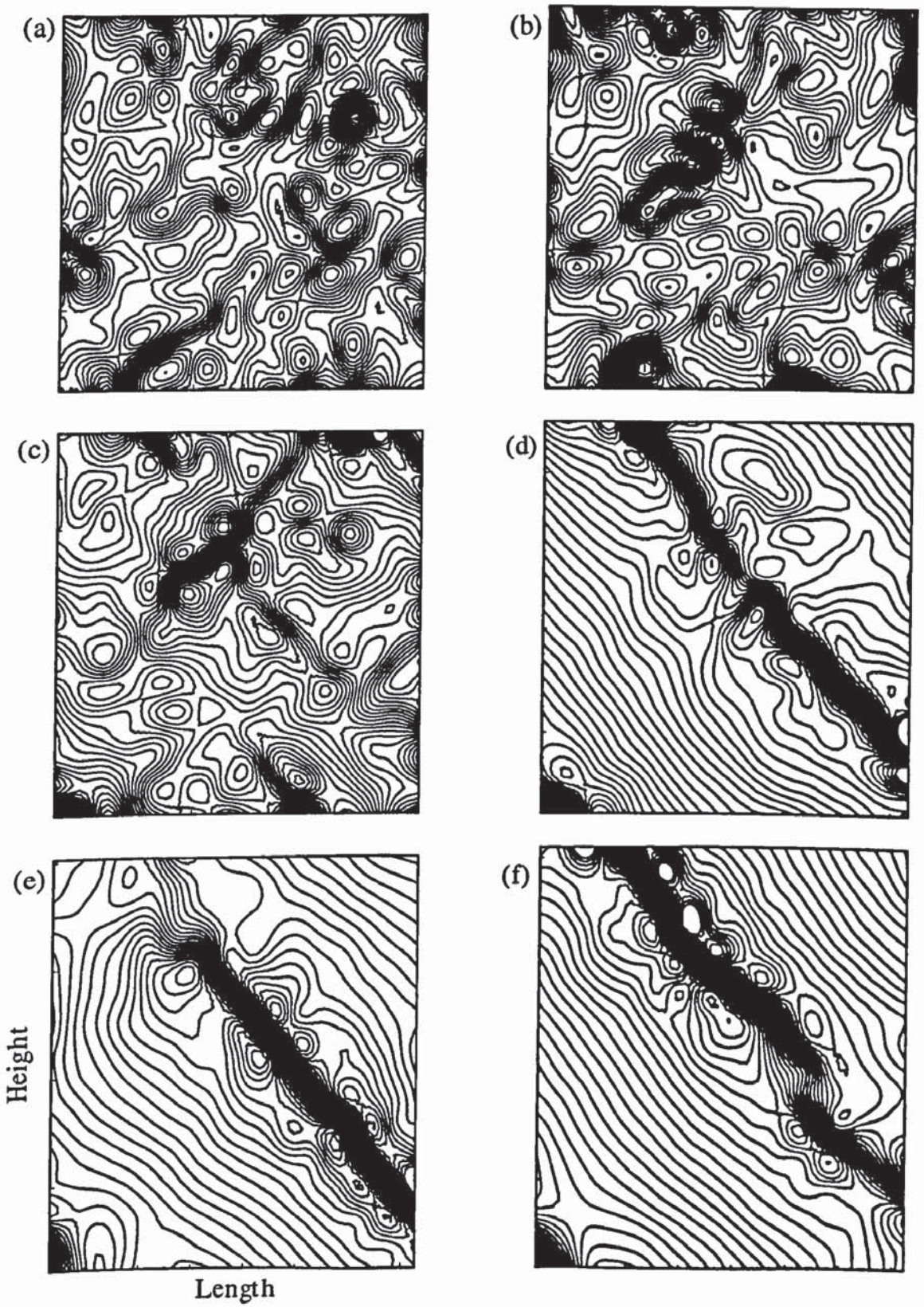

Fig. 7.5 Vertical displacement increment contours in CV test:
(a) 0-1; (b) 1-2; (c) 2-3; (d) 3-4; (e) 4-5; (f) 5-6

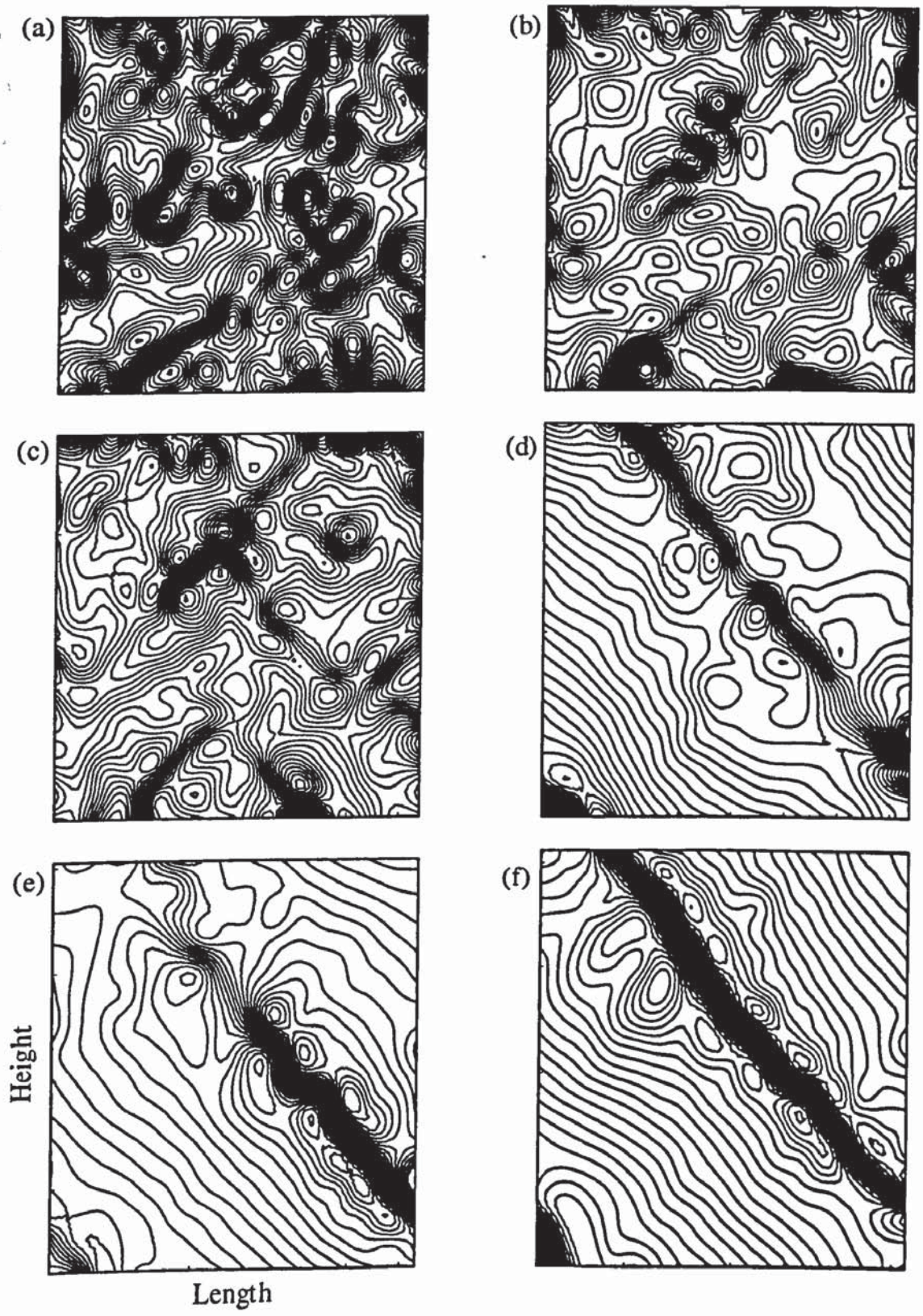

Fig. 7.6 Vertical displacement increment contours in CM test:
(a) 0-1; (b) 1-2; (c) 2-3; (d) 3-4; (e) 4-5; (f) 5-6

The evolution of vertical displacement increment contours for the constant mean stress test is shown in Fig. 7.6. Similar behaviour is observed when compared to that of the constant

volume test as shown in Fig. 7.5. The evolution of $sin\varphi_m$ (in grey) and dilation angle ψ (in black) for the constant mean stress test are presented in Fig. 7.7. It can be seen that ψ increase from 0° to +10° from the beginning of test until the peak strength, then it fluctuates about +5° except for several spikes. According to Roscoe theory, when $\psi \approx +5°$ $\theta_R = \pi/4 + \psi/2 = 47.5°$. Since the dilation angle is so small, the shear band orientation is very similar to that in the constant volume test. However, it is very hard to identify this small difference between these two tests from observation of the displacement increment contours. Han and Drescher (1993) showed that the shear band orientation depended on the confining pressure in biaxial compression tests on dry coarse sands. The experimental results also showed that the shear band orientation was far away from the Coulomb's prediction and at higher confining pressures the results was closer to Roscoe's prediction.

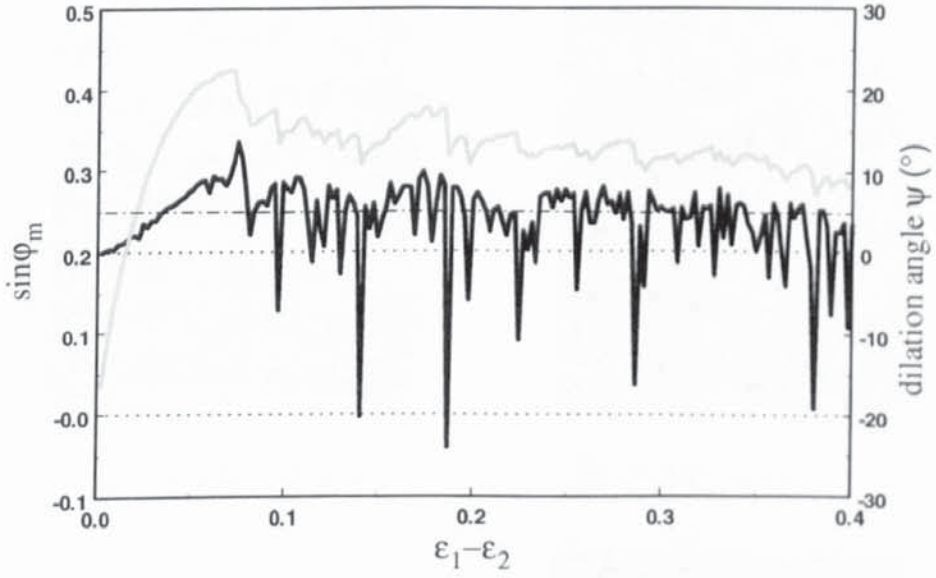

Fig. 7.7 Evolution of $sin\varphi_m$ and ψ in CM test

Figures 7.5 and 7.6 suggest that there are several local shear bands that spontaneously appear within the specimen during the final stage of strain-hardening. However, additional energy is required for the full development. The results suggest that the onset of localization occurs during strain hardening but it is only when strain-softening occurs that a persistent shear band is actually established.

The particle configuration at 26.4% and 41.8% deviator strain for both constant volume and constant mean stress tests are shown in Fig. 7.8. It is clear that deformation patterns in these two tests are essentially identical. As shown in Chapter 6, in constant volume tests,

in order to keep the volume constant the mean stress increases throughout shearing, while in constant mean stress tests the mean stress always remains constant. The results shown in Fig. 7.8 indicate that the mean stress does not have a strong effect on the shear band inclination. Interestingly, in both tests, the angle between the shear band and the minor principle stress direction becomes smaller from 26.4% to 41.8% deviator strain (comparing Figs. 7.8a-b and c-d) and the angles are all less than 45°. This implies that during the shearing process the inclination of the shear band changes due to the changes of the dimensions of the periodic cell. If the shear band orientation is measured at large strain and based on the particle configuration shown in Fig. 7.8 it is not consistent with any of the three classic predictions.

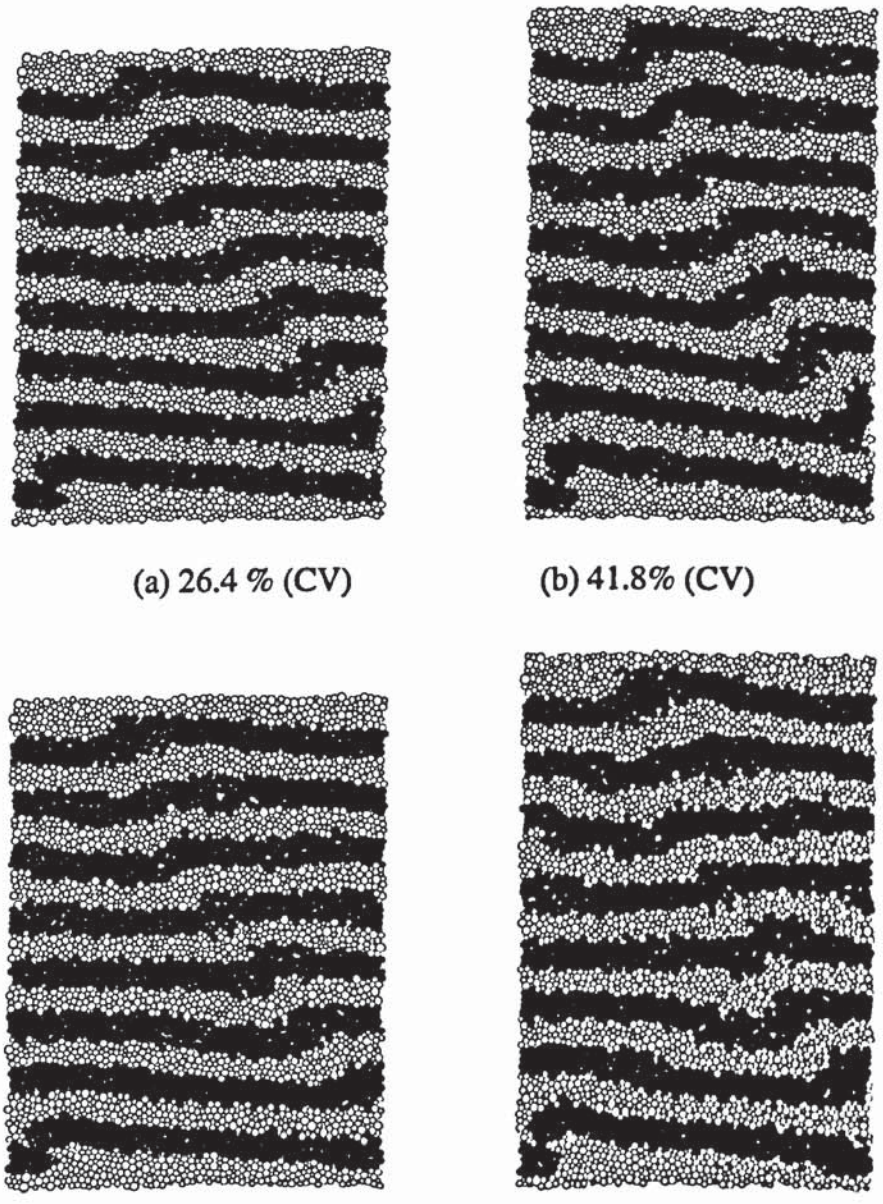

(a) 26.4 % (CV) (b) 41.8% (CV)

(c) 26.4% (CM) (d) 41.8% (CM)

Fig. 7.8 Deformation pattern at large strain

An additional constant volume test was carried out on a rectangular sample with initial aspect ratio of 1.5. This sample has the same mechanical properties and density as the previous square one. The particle configurations of the specimen at three different shear stages are shown in Fig. 7.9. Contrary to the test on the square sample, this sample was compressed in the vertical direction and expanded in the horizontal direction. Consequently, in this test the minor principal stress aligns in the horizontal direction. A shear band can be clearly observed in Fig. 7.9b at 17.6% shear strain. The inclination angle to the minor principal stress direction (horizontal) at this stage is clearly greater than 45°. At 33% shear strain, the sample had deformed to nearly a square shape and the orientation of the shear band is about 45° as shown in Fig. 7.9c. This clearly illustrates that the orientation of the shear band changes with the change in the dimensions of the periodic cell.

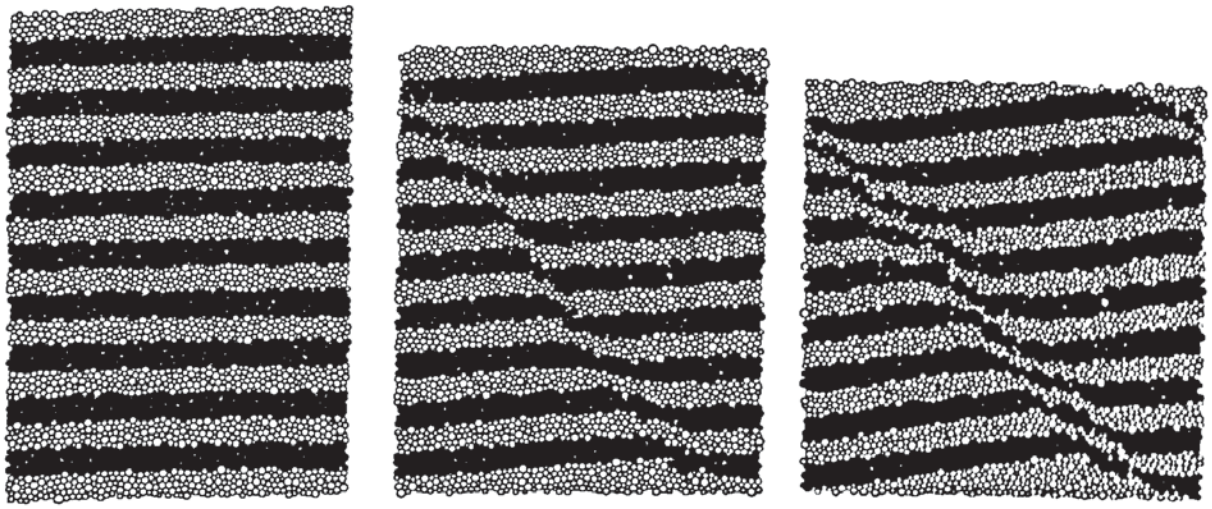

(a) 0% shear strain (b) 17.6% shear strain (c) 33% shear strain

Fig. 7.9 Particle configuration for a sample with initial aspect ratio of 1.5

The corresponding evolution of vertical displacement increment contours is shown in Fig. 7.10. In the figure the results for the stages during which the shear band initiated (Fig. 7.10a-b), become established (Fig.7.10c-d) and at the final stages of the test (Fig. 7.10e-d) are shown. As the specimen changes from a rectangular shape to a square shape gradually the inclination of the shear band also become less inclined to the horizontal direction. Therefore, different values of shear band inclination angle can be obtained as the specimen dimensions change at different stages of the test. In other words, it depends on the initial sample dimensions and when the measurement is taken. This may be, in part, why the orientation of shear bands reported in the literature have various values.

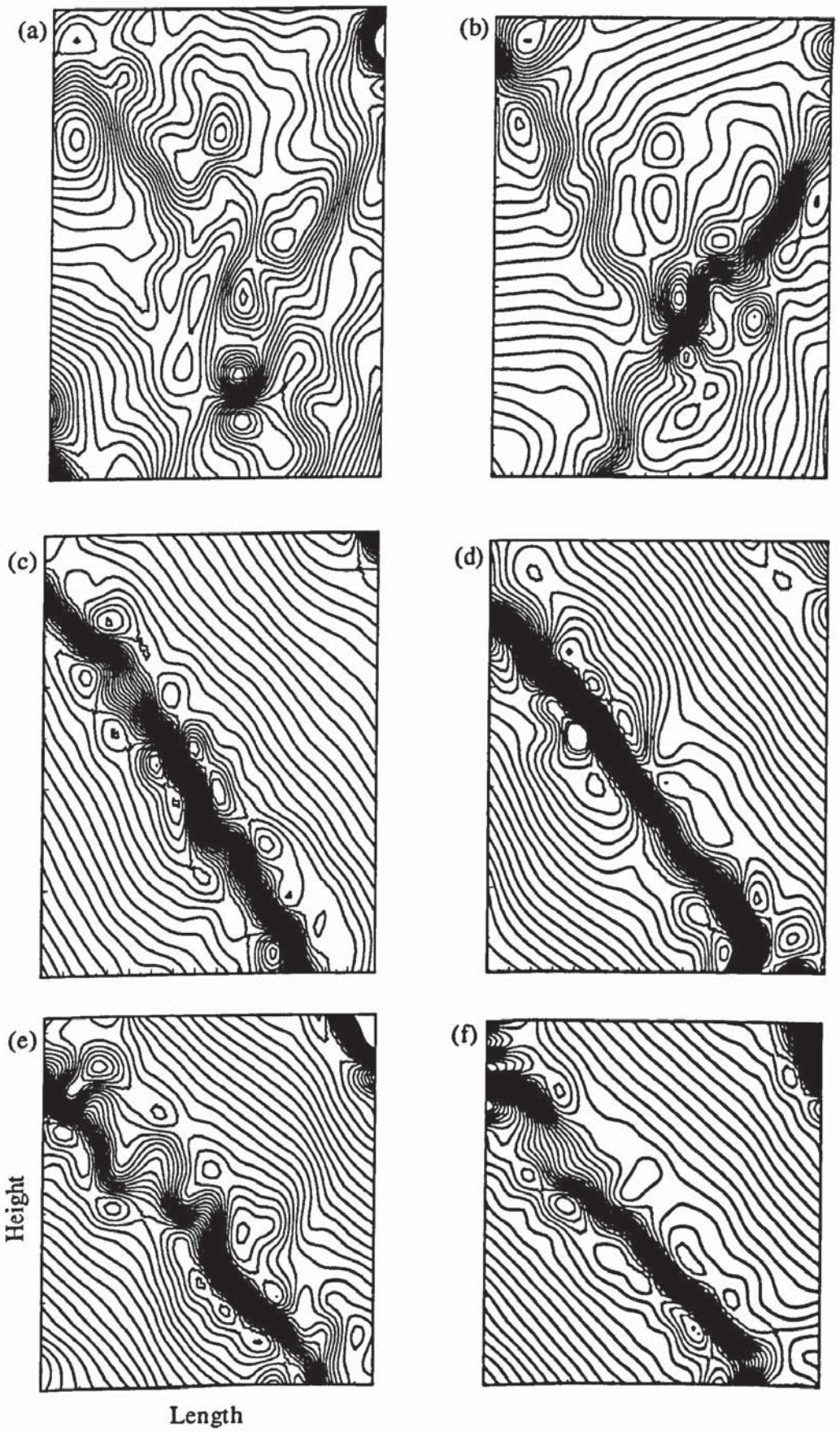

Fig. 7.10 Vertical displacement increment contour for a sample with initial aspect ratio of 1.5: (a) 4.4%-6.6%; (b) 6.6%-8.8%; (c) 8.8%-11%; (d) 11%-13.2%; (e) 28.6%-30.8%; (f) 30.8%-33%

According to the observations from the above two tests with two different sample dimensions it is found that, after the shear band first initiates, its inclination continuously changes with the change in the sample dimensions during the test. In addition, whatever the initial aspect ratio of the sample is, the inclination angle of shear band will decrease during a biaxial compression test. For example, when the square sample with aspect ratio of 1 deforms to a rectangular one of aspect ratio 1.5 the inclination angle decreases from 45° to a value less than 45°. When the rectangular sample with aspect ratio of 1.5 deforms to a square one the inclination angle decreases from a value greater than 45° to 45°. Since all the classic solutions do not take the change in sample dimension into account, they cannot predict this kind of variation in the shear band orientation. Therefore, any agreement with any of these classic predictions is just a coincidence.

The thickness of the shear band can be determined from the width of the intensive band shown in Fig. 7.5. The results show that it is about 10-12 times D_{50} and this is consistent with the previous results from the direct shear tests. It is worth noting that the orientation and thickness of the shear band are measured at the onset of localization. At this early stage the dimensions of the sample is close to the initial state. After large strain, due to the change in the dimension of the sample the orientation of the shear band also changes.

7.4.3 Particle displacement field

The particle locations at any two loading steps can be used to calculate the displacement increments. The measured incremental displacement fields for load steps 2-3 and 5-6 of the constant volume test are given in Fig. 7.11. The amplitudes of the vectors are scaled to the current maximum values as indicated below the diagram. As expected, no clear shear band is observed during the load step 2-3. At this stage, the incremental displacement fields for x, y and resultant components are essentially 'uniform' except for a few hints of localization taking place randomly inside the sample. For step 5-6, the incremental displacement fields for the x and y directions clearly show strong deviations from the linear displacement field with large incremental displacements distributed along an inclined band, which corresponds to the finally developed shear band.

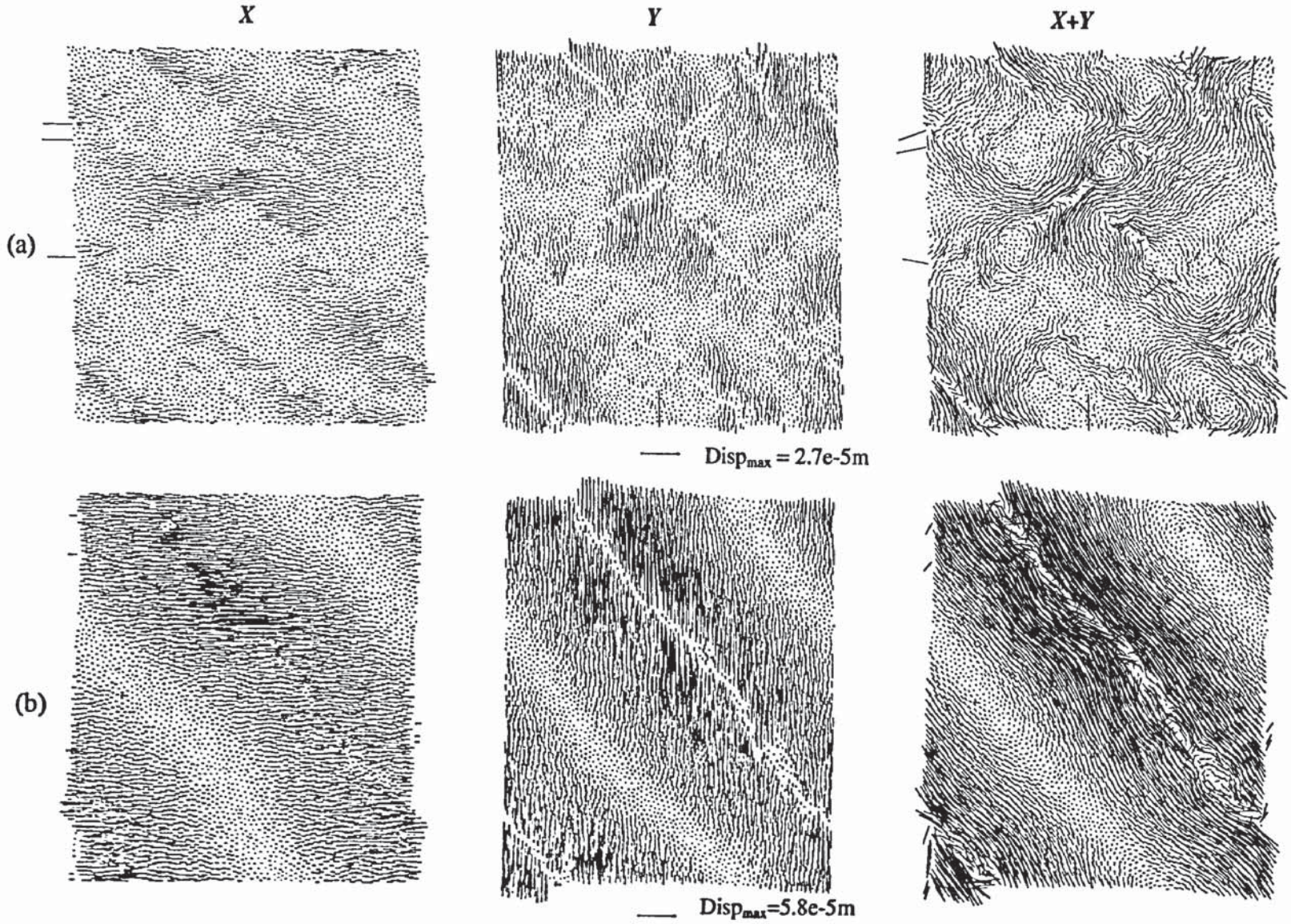

Fig. 7.11 Incremental displacement fields: (a) load step 2-3; (b) load step 5-6

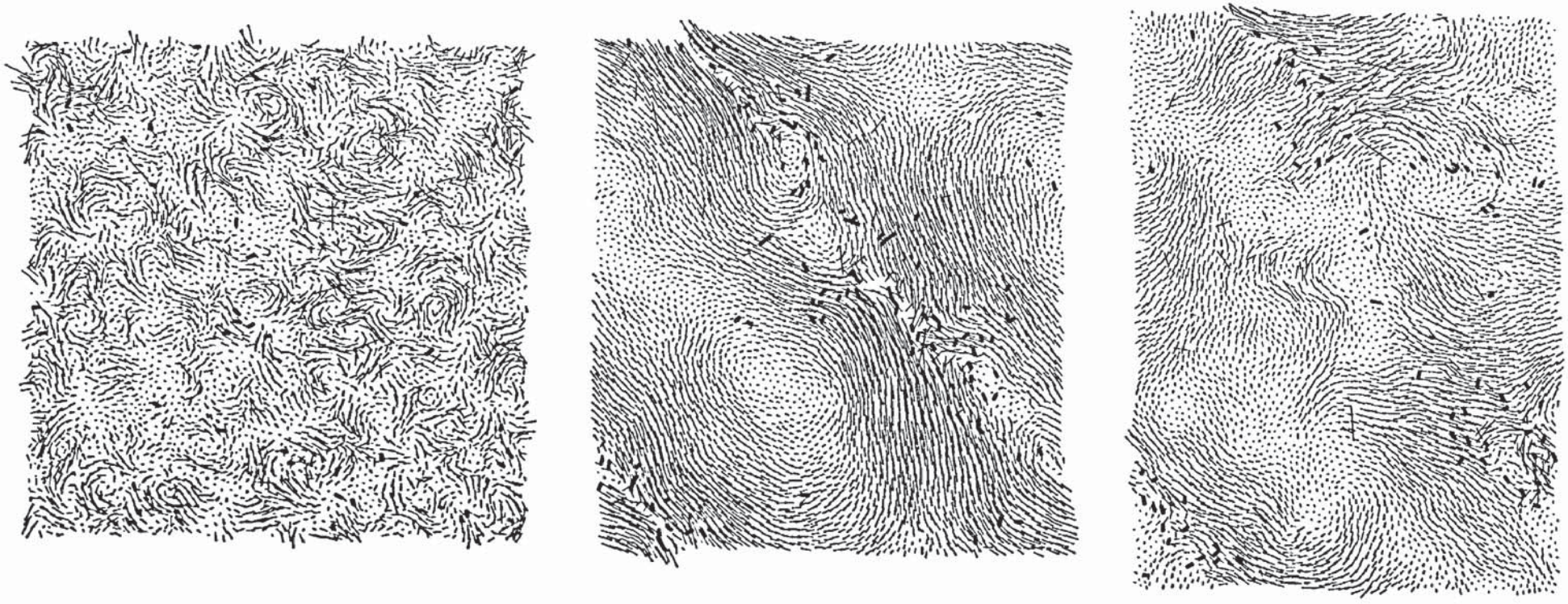

(a) before shearing

(b) at 8% shear strain

(c) end of shearing

Fig. 7.12 Velocity fluctuations and sliding locations

7.4.4 Velocity field and sliding contacts

The fluctuating velocity field and sliding contact locations in the constant volume test are superimposed for several stages of deformation in Fig. 7.12 to explore how these two parameters relate to each other and how they evolve with the shear band deformation. In the fluctuating velocity field the vectors are scaled to the current maximum value, in which the fluctuating velocity is defined as,

$$\tilde{v}_i = v_i - \langle v_i \rangle \tag{7.5}$$

where v_i ($i = 1, 2$) is the particle velocity and $\langle v_i \rangle$ denotes the mean velocity. In periodic cell simulations the mean velocity is given by the strain rates specified.

The sliding contacts are represented by short thick lines, which connect the centres of two contacting particles. Figure 7.12a shows the situation before shearing. It can be seen that the velocity vectors form many local circular cells, which are distributed randomly within the sample. The sliding contacts are also distributed randomly. As shearing continues the velocity vectors rearrange and the large velocities align in opposite directions along a distinct shear zone (Fig. 7.12b), which is very similar to the pattern for the incremental displacement field shown in Fig. 7.11b. In addition, it is clear that most of the sliding contacts take place within the narrow shear zone. The velocity field and sliding contact distribution at the end of shear are presented in Fig. 7.12c. It can be seen that most of the sliding contacts still take place within the shear band. This illustrates that sliding plays an important role in shear band formation.

7.4.5 Particle rotation field

It has been shown that particle rotation plays a dominant role in shear band formation (Bardet and Proubert, 1991, 1992; Oda and Kazama, 1998). The measured particle rotation fields for load increments 2-3 and 5-6 marked in Fig. 7.4 are given in Fig. 7.13, in which open circles denote clockwise (negative) rotation, while solid circles denote anticlockwise (positive) rotation. In Fig. 7.13a and b only rotations larger than 10% of the current maximum particle rotation are shown. It can be seen that in load step 2-3, large rotations occur in a number of inclined narrow bands (Fig. 7.13a). Most of the particles exhibiting large anticlockwise rotations align in one band. On the other hand most of the particle exhibiting large clockwise rotations align in the direction perpendicular to that of the

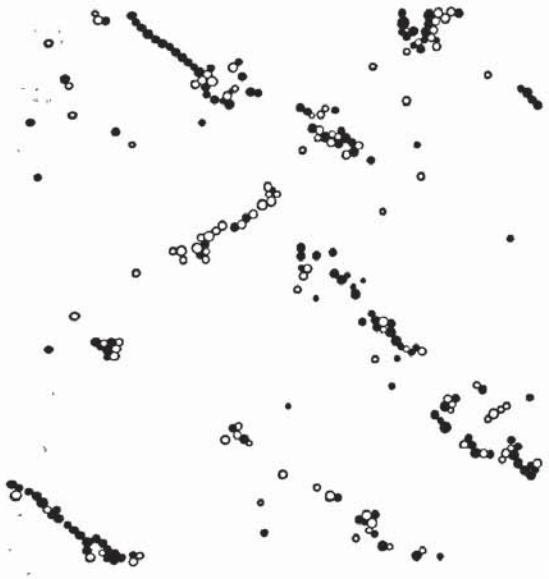

(a) loading step 2-3

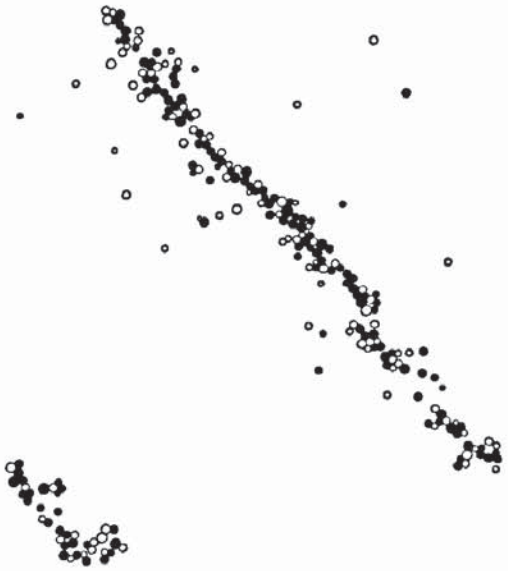

(b) loading step 5-6

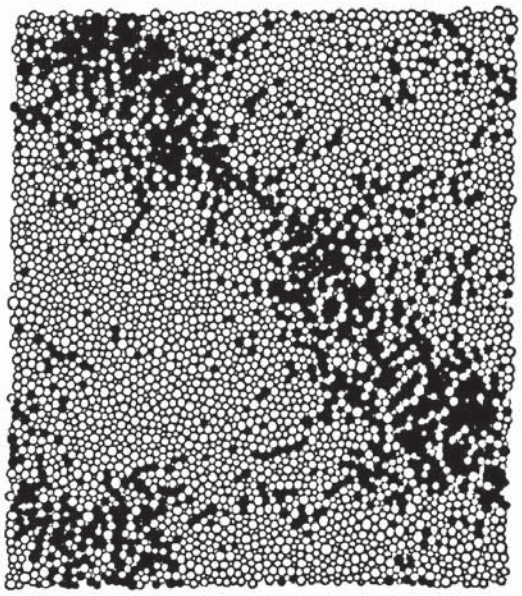

(c) overall rotation field

Fig. 7.13 Particle rotation field

clockwise rotations. During load step 5-6 (see Fig. 13b), it is clear that significant particle rotations are concentrated into one inclined band, at the stage when the shear strain is highly localized (Fig. 7.6f), and most of them are positive rotations. In addition, the overall particle rotation field for this load step is plotted in Fig. 7.13c. It can be seen that positive rotations are almost concentrate in one distinct shear zone. Outside this zone most particles rotate clockwise (negative). It is observed from the rotation fields that, particles within the shear zones rotate in the same direction. Particles outside the shear zone also rotate in the same direction but opposite to the rotation direction of particles within the shear zone. Therefore, there are two types of rotations patterns appear during shear band formation: 1) two particles in contact rotate in opposite direction that occurs at shear band boundaries; 2) rotations dominantly occurs within the shear bands where particles in contact rotate almost in the same direction.

Figure 7.14 shows the average particle rotation across a specified narrow band (one coloured layer width) at the mid-height of the sample for the two load steps 2-3 and 5-6. During load step 2-3 the overall average rotation is $-0.002°$. The average particle rotation across the central band varies around $0°$. For step 5-6, the overall average rotation increases to $-0.185°$ and a sudden jump in the average rotation is observed across the shear band. The rotation reaches a maximum value of $9°$ in the middle of the shear band. The average rotations outside the shear band are negligible and in the opposite direction to the rotation within shear band. Therefore, this figure confirms the observation from the particle rotation field as shown in Fig. 7.13c.

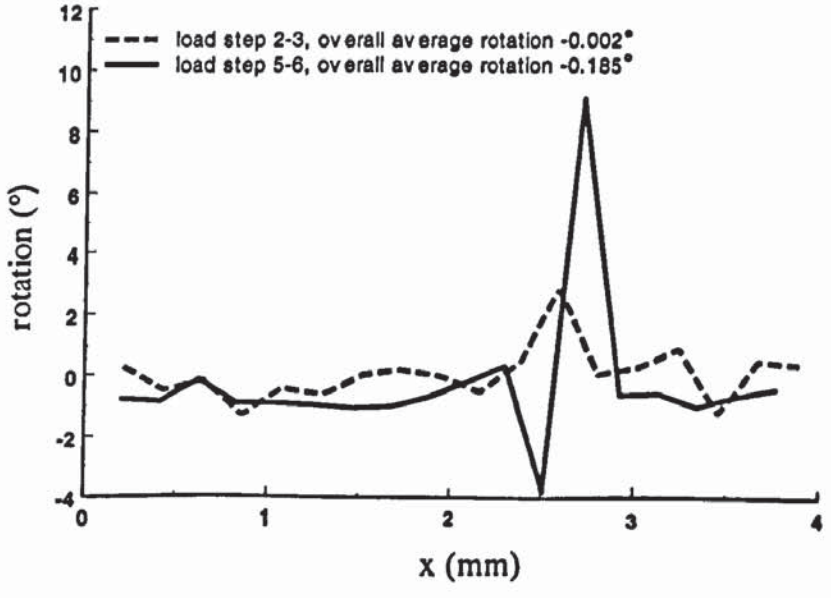

Fig. 7.14 Variation of average particle rotations across the mid-height of the sample

7.4.6 Influence of inter-particle friction

Another constant volume test was carried out in which the inter-particle friction was specified to be 0.2. The final particle configuration of this test is shown in Fig. 7.15. Comparing with Fig. 7.3f, which shows the test with inter-particle friction 0.5, it is clear that the deformation patterns of the two tests are totally different and no shear band can be observed from the test with low inter-particle friction. This implies that the inter-particle friction plays an important role in the formation of shear bands.

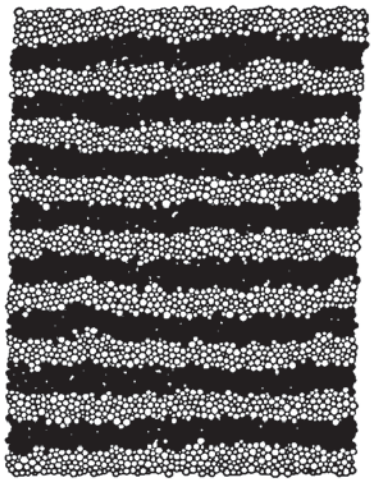

Fig. 7.15 Final particle configuration of sample with inter-particle friction of 0.2

7.4.7 Local void cell evolution

How the local void cells deform during the constant mean stress test are presented in Fig. 7.16, in which areas that expand, during two successive load steps, over one sixtieth of the average single particle area are highlighted by dark shaded blocks. The patterns shown in this figure are similar to the patterns of the particle rotation field in Fig. 7.13. During the load step 2-3 the highly expanding void cells occur in several inclined narrow bands (Fig. 7.16a). During this stage, the total expanding area (ΔA_e) is about twice the total contracting area (ΔA_c) and the number of expanding cells (N_e) is also greater than the number of contracting void cells (N_c). However, the number of highly expanding void cells (N_{el}) is only one quater of N_c and these void cells contribute to more than half of the total expansion area. The high expanding areas are concentrated into one oblique shear band at the post peak stage (Fig. 7.16b). Although N_e becomes less than N_c ΔA_e is still

higher than ΔA_c. It is noted that N_c is about 5.4 times N_{el} at this stage but ΔA_{el} is similar to ΔA_c. This demonstrates that the void ratio inside the shear band expands much more than the remaining area and is also different from the global measurement based on the changes in the sample dimensions.

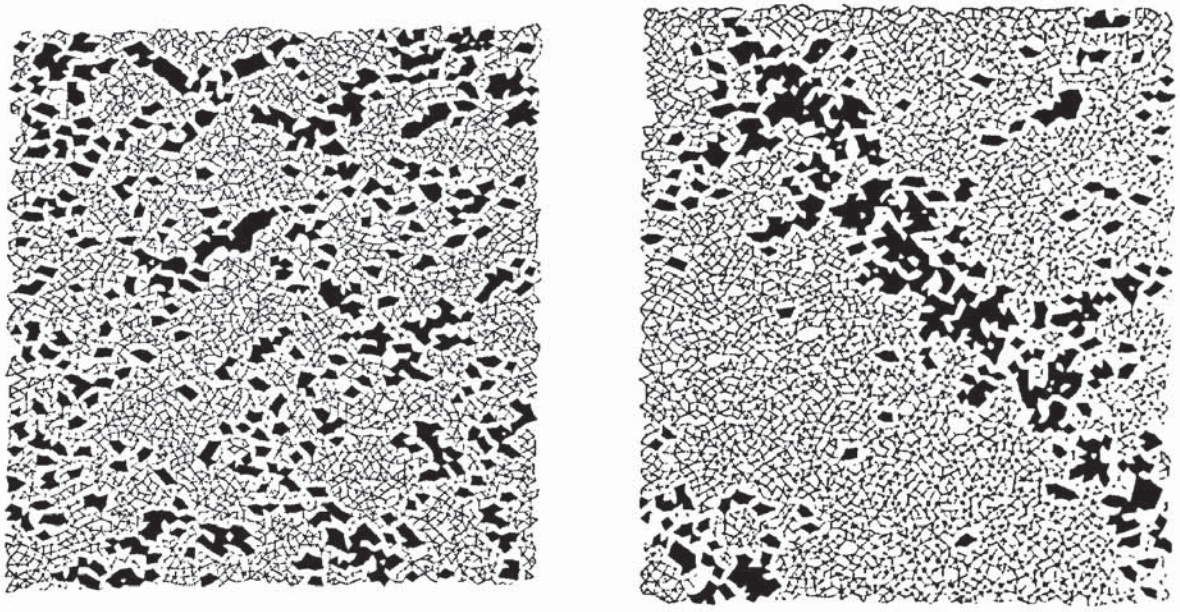

$N_c = 2466$, $\Delta A_c = 0.05074mm^2$
$N_e = 3324$, $\Delta A_e = 0.10211mm^2$
$N_{el} = 605$, $\Delta A_{el} = 0.06792mm^2$

(a) load step 2-3

$N_c = 2868$, $\Delta A_c = 0.10114mm^2$
$N_e = 2448$, $\Delta A_e = 0.12551mm^2$
$N_{el} = 530$, $\Delta A_{el} = 0.10341mm^2$

(b) load step 5-6

Fig. 7.16 Local void cell deformation

7.4.8 Influence of boundaries

It was shown in Chapter 3 that in the biaxial compression tests with the wall boundaries the final particle configurations were different for different wall friction tests (see Fig. 3.21). The corresponding evolution of vertical displacement increment contours for the two constant volume tests are shown in Figs. 7.17-7.18, respectively. It can be seen from Fig. 7.17a that the strain distribution is essentially uniform during the first load step. Heterogeneity appears during load step 1-2 (Fig. 7.17b). The incipient localization that is indicated by two intensive inclined intersecting bands occurs during load step 2-3 (Fig.7.17c). Afterwards, a persistent shear band is gradually established during the subsequent increments (Fig. 7.17d-f). The inclination angle of the shear band is about 58° in this test with zero wall friction. Since this is a constant volume test the overall dilation

angle is zero. The inclination angle of the shear band obviously does not agree with the Roscoe's solution. However, according to Coulomb's prediction $\theta_c = 45° + \varphi_m/2$, and φ_m is about 24° during these load steps so $\theta_c \approx 57°$. Therefore, the measurement of the shear band orientation in this test is consistent with Coulomb's prediction and it is different to the results obtained from periodic cell tests.

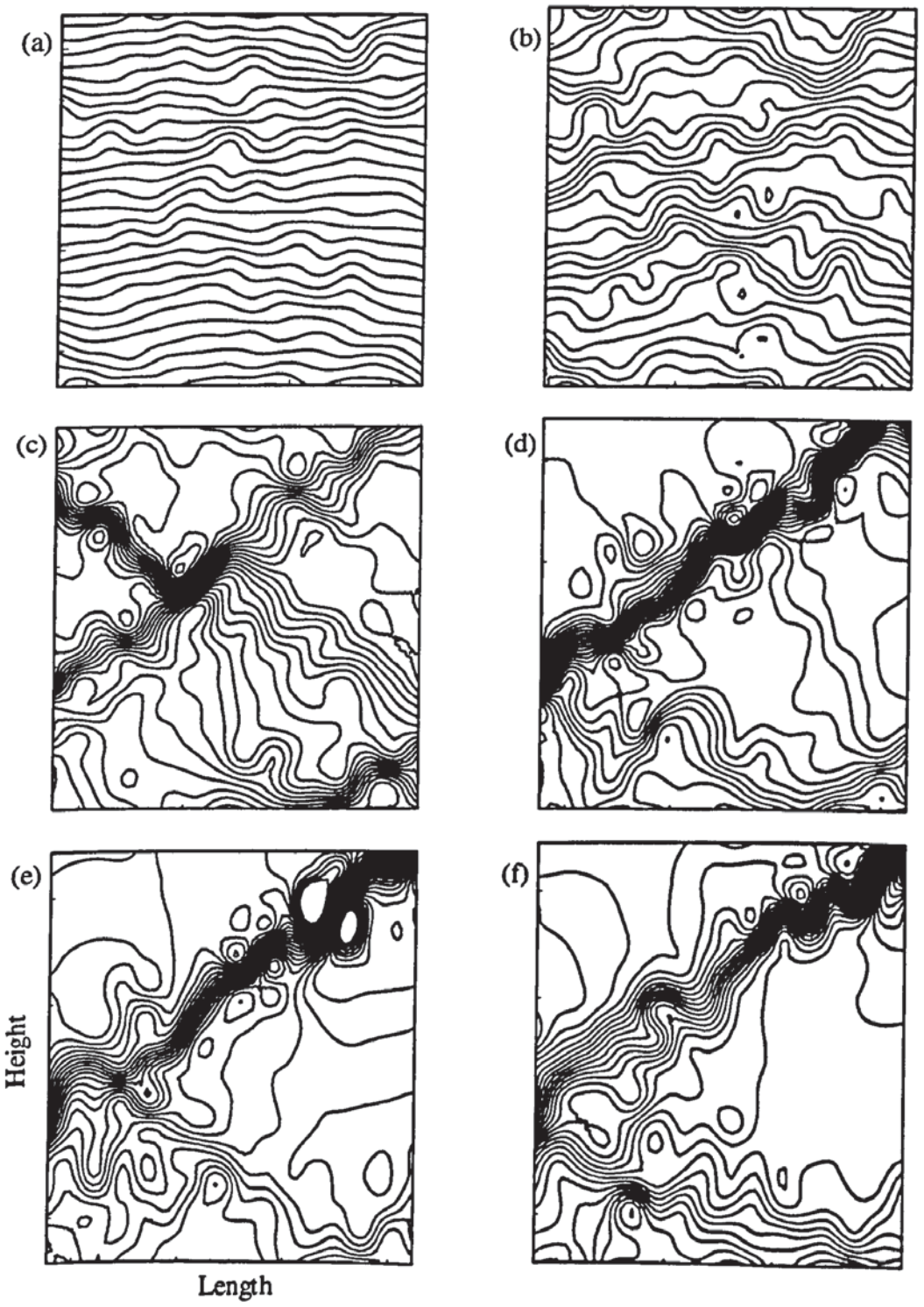

Fig. 7.17 Vertical displacement increment contours for **BCW** test with $\mu_w = 0.0$:

(a) 0-1; (b)1-2; (c) 2-3; (d) 3-4; (e) 4-5; (f) 5-6

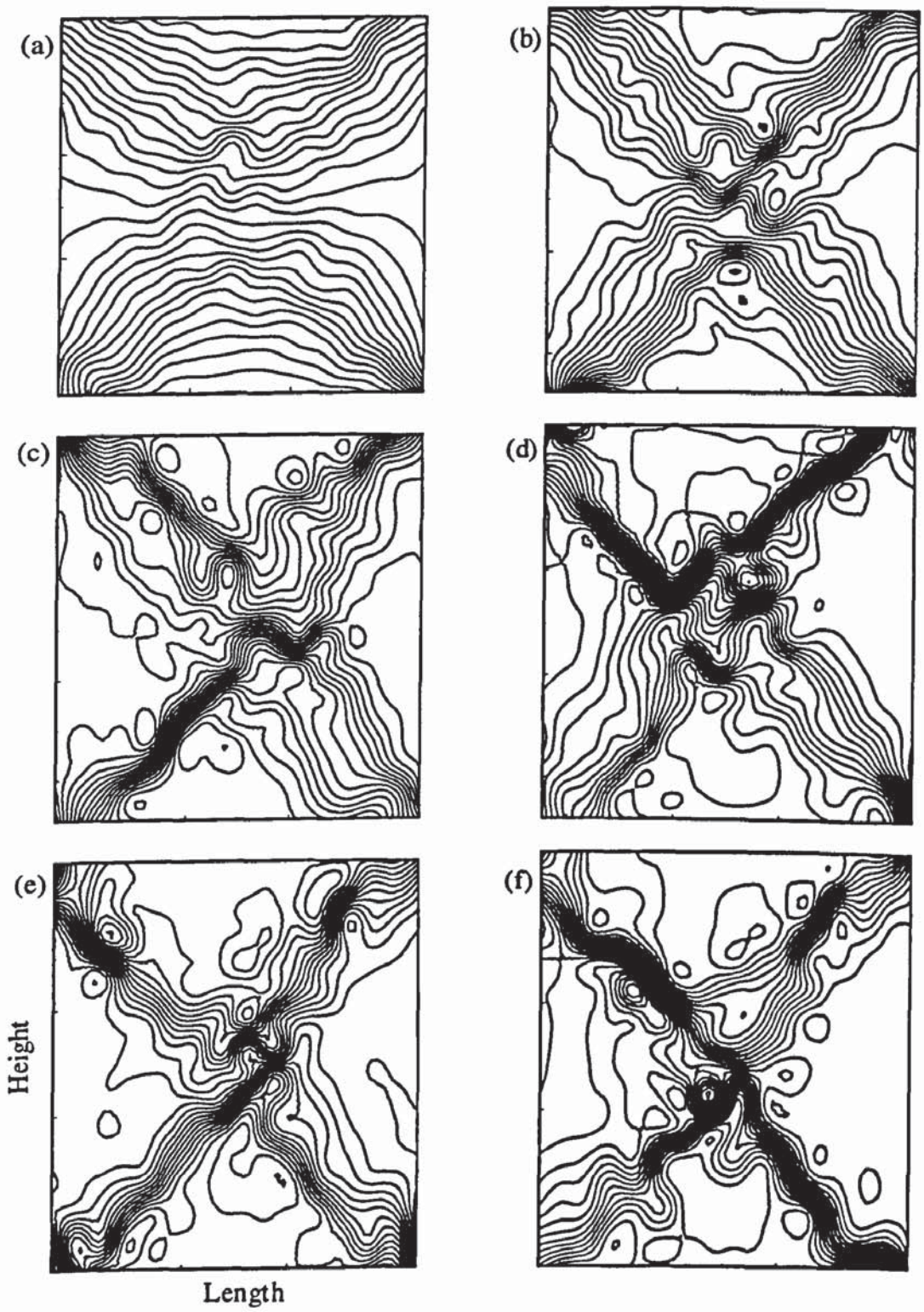

Fig. 7.18 Vertical displacement increment contours for **BCW** test with $\mu_w = 0.5$:
(a) 0-1; (b)1-2; (c) 2-3; (d) 3-4; (e) 4-5; (f) 5-6

The results from the test with the wall friction of 0.5 are presented in Fig. 7.18. It is clear that during the early stage of shearing localization is initiated from the four corners. Two diagonal intersecting bands are then formed (Fig. 7.18b). During the rest of the test the

two bands becomes concentrated in the same direction as they were first initiated. The inclination angles of the two bands are nearly the same and are less than 45°. Figures 7.17 and 7.18 clearly show that the propagation patterns of shear bands are totally different when different wall frictions are specified. Comparing the two figures with Figs. 7.5 and 7.6 suggests that in periodic cell simulations strain localisation occurs randomly within the sample, whereas in the simulations with wall boundaries it originates from the corner of the specimen. Only one persistent shear band is established for samples with periodic boundaries; but this depends on the value of wall friction when real boundaries are considered. In addition the inclination angle of the shear band varies for different boundary conditions.

7.4.9 Force transmission pattern

In general, the average stress tensor of a granular system is defined as,

$$\sigma_{ij} = p\delta_{ij} + \frac{1}{2V}\sum_{1}^{N} m\tilde{v}_i\tilde{v}_j + \frac{2}{V}\sum_{1}^{C} F_j x_i \qquad (7.6)$$

where in the first term p is the fluid pressure, δ_{ij} is Kronecker's delta defined by,

$$\delta_{ij} = \begin{cases} 1, & if \quad i = j \\ 0, & if \quad i \neq j \end{cases}$$

This term is not considered in this simulation since the specimen is assumed to be deformed in a vacuum. The second term is the fluctuating kinetic energy density contribution to the average stress tensor where m and $\tilde{v}_i$ $(i, j = 1, 2)$ are the mass and the fluctuating velocity of every single particle and the summations are over the N number of particles in the volume V of the sample. The third term is the contribution to the total stress tensor due to the contact forces.

The contact force contribution and the fluctuating kinetic energy density contribution to the evolution of deviator stress are shown in Fig. 7.19, in which the contribution from contact forces is shown in black and the contribution from the fluctuating kinetic energy density is shown in grey. It is worth noting that, after peak strength, every sharp drop in the contact force contribution curve is accompanied by a spike in the fluctuating kinetic energy density curve. From a video clip of the force transmission patterns and the

evolution of the deviator stress, it has been demonstrated that every time when a sharp drop in the contact force contribution and a spike of fluctuating kinetic energy density occurs the strong force chains exhibit buckling. After buckling, the strong force chains are rearranged. The details of this video are described in Appendix C and given at http://www.iem.bham.ac.uk/computation/granular/microevo.htm.

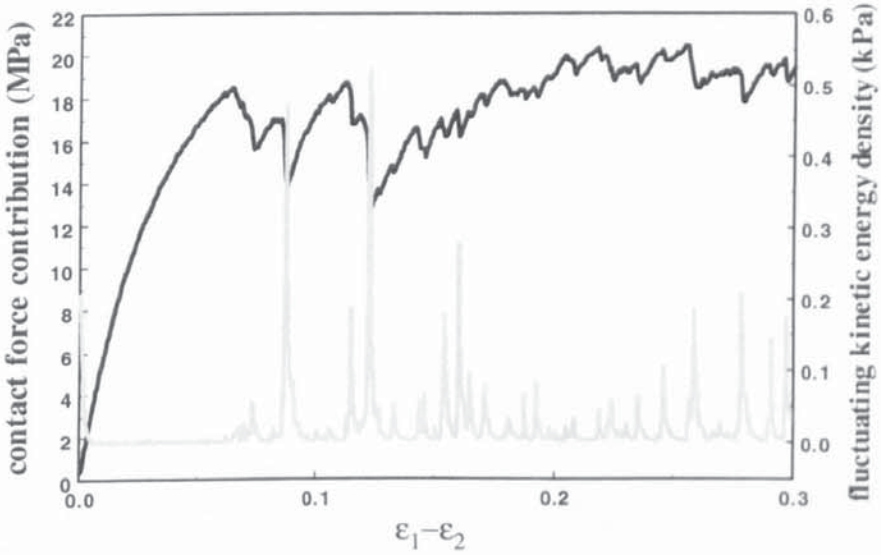

Fig. 7.19 Two types of contribution to the stress tensor

The strong force chains at four different shearing stages in the video clip are shown in Fig. 7.20. Only the forces larger than 1.3 times the average contact force (in order to eliminate those forces that are slightly larger than the average contact force and may change from the weak to the strong sub-network during the test) are shown in the figure. Before the peak strength, as shown in Fig. 7.20a, the strong force chains are orientated in the direction parallel to the major principal stress axis of the sample. Figures 7.20b and c show the strong force chains at 8.8% and 12.2% shear strain when the first and second occurrences of the sharp drop in the contact force contribution and a spike in the fluctuating kinetic energy density occur. Similar force chain patterns can be observed along the shear band direction in both figures. Interestingly, there is a high density of strong forces in the top part of the sample, which are no longer parallel to the horizontal direction, but inclined at ca. 40° to the vertical direction. At the end of shearing, as shown in Fig. 7.20d, this kind of force transmission pattern is still apparent inside the specimen. Although this pattern of force transmission is intermittent and the rearrangement of the force chain is instantaneous, it shows strong correlation with the formation a stable shear band at the end of the test.

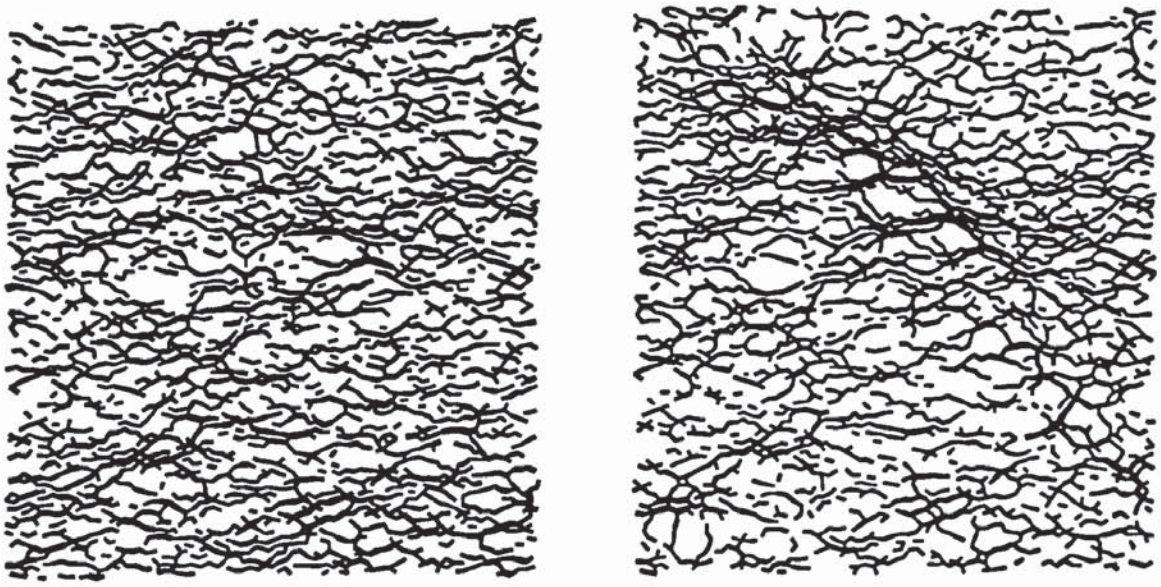

(a) 4.4% shear strain

(b) 8.8% shear strain

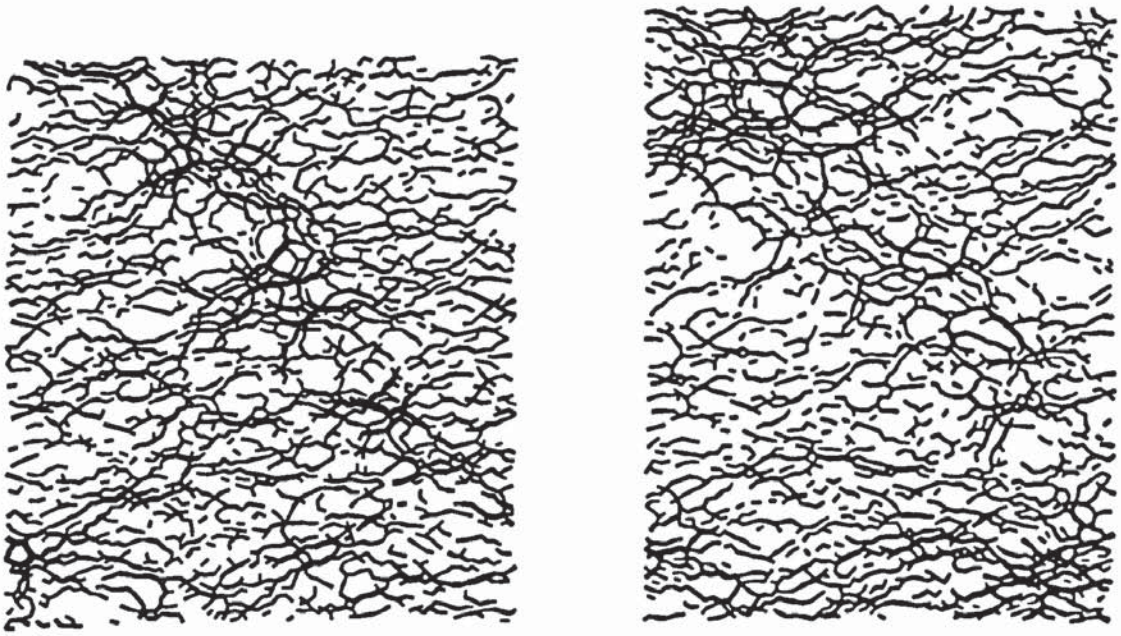

(c) 12.2% shear strain

(d) 28.6% shear strain

Fig. 7.20 Strong force chains at four stages

7.5 Summary

Numerical simulations have been carried out to study the initiation and propagation of shear bands in granular materials. The analyses are mainly based on the results of biaxial compression tests with periodic boundaries so that the effect of boundary conditions can be eliminated. The effect of boundary friction was explored by performing tests with wall

boundaries. The details of incremental displacement and velocity fields as well as the concentration of high particle rotations and high dilatancy along the shear band have been presented. The localisation patterns for the tests with periodic and wall boundaries have also been compared. Based on the results obtained from the numerical experiments, the following conclusions can be drawn:

(1) The observed localisation patterns vary from one test to another due to the different boundary conditions. The results from both constant volume and constant mean stress tests with periodic boundaries indicate that several incipient shear bands in two orthogonal directions are initiated simultaneously in the strain-hardening regime prior to the peak strength, and only one band fully develops during the strain softening stage. However, such patterns were only observed in the test with wall boundaries when the wall friction was zero. Two conjugate shear bands were established in the test with a wall friction of 0.5.

(2) The inclination of the shear band appears to be unpredictable. In the zero wall friction test the shear band orientation is close to Coulomb's prediction. On the other hand, the result obtained with high wall friction test approximates to Roscoe's solution. However, in the periodic cell simulations the angle varies from less than 45° to greater than 45° depending on the initial sample dimensions. Furthermore, it was observed in periodic cell simulations that the orientation of the shear band changed as the dimensions of the cell changed.

(3) The thickness of the shear band is found to be about 10-12 times the average particle diameter in both biaxial compression and direct shear tests and this is consistent with the results reported by other researchers.

(4) It was found that the development of a shear band only occurs if the specimen is above a certain packing density. Otherwise, no strain localisation will appear during the test.

(5) There are significant discontinuities in the displacement and fluctuation velocity field across a shear band. The discontinuities are also manifest in the particle rotation fields, wherein particles within the shear band tend to rotate in one

direction and particles outside the shear band rotate in the opposite direction. It is shown that accompanying the large particle rotations the highly expanding local void cells also occur mainly within the shear band.

(6) Sliding also play a significant role in the shear band deformation. It is found that the sliding contacts predominantly occur within the shear band locations. As described in Chapter 6, most of sliding contacts occur in the weak sub-networks. The contacts within the weak network are not stable and easy to break compared to those in the strong sub-network. The microstructure within the shear band changes during the rearrangement of the particles with broken contacts, which leads to further localisation of shear strain into the narrow zone. In addition, if the inter-particle friction is too low no shear band will be generated.

(7) During shearing, the strong force chains within the shear band become more and more inclined to the major principal stress direction and are unstable due to the loss of contacts inside the shear band. This leads to the collapse of the strong force chains. The force chains also change discontinuously across the shear band. The stress fluctuations correspond with intermittent buckling of the strong force chains that triggers an instantaneous localisation in the fluctuating velocity field followed by the rearrangement of the strong force transmission paths.

CHAPTER 8: CONCLUSIONS AND FUTURE WORK

A systematic study of the quasi-static deformation of granular materials subjected to three different shear mechanisms has been carried out based on DEM simulations. The advantages and disadvantages of the three types of laboratory tests were discussed. The conclusions that can be drawn from this study are summarised in this chapter, followed by recommendations and suggestions for future studies.

8.1 Pure shear deformation of granular materials

The pure shear deformation of granular systems has been examined by carrying out biaxial compression tests using both periodic and wall boundaries. The results indicate that 2D DEM simulations can qualitatively reproduce the mechanical behaviour of real granular materials. It has also been demonstrated that numerical simulations can also provide a useful tool for examining the reliability of physical experiments. It has been shown that essentially identical results are obtained from simulations with two different types of boundaries when the calculations are based on the volume-averaged data. However, calculations based on wall measurements give a higher value of shear strength due to underestimating the principal stresses in the two orthogonal directions.

It has also been revealed that the characteristic behaviour at both the macroscopic and microscopic scales is distinguished by whether or not the system percolates, i.e. enduring connectivity is established in all directions. The transition from non-percolating to percolating systems correlates well with the establishment of a mechanical coordination number of ca. 3.0-3.2.

A unique critical state line was obtained independent of whether the simulation was performed at constant volume or constant mean stress. According to the stress level experienced the critical state behaviour can be divided into three groups: the slope of the CSL is steep if stress levels are less than 1kPa; the CSL is almost horizontal if stress levels are between 1kPa and 1MPa and the slope of the CSL steepens again if the stress levels exceed 1MPa. The percolation threshold divides the CSL into two regimes at a mechanical

coordination number ca. 3.2. The systems that fall into the percolating regime have a mechanical coordination number higher than 3.2 at the critical state. If the system cannot pass the percolation threshold, it will stay in the non-percolating regime.

8.2 Direct shear deformation of granular materials

Simulations of the direct shear test provide useful insights into the material behaviour. It has been shown that the shear strain becomes highly concentrated in the mid-plane of the sample during the test. Large particle rotations also concentrate into the central shear band during shearing and the evolution of the average particle rotation with shear strain is essentially linear. The stress distribution is non-uniform in the sample. Although the stress distribution within the specimen is heterogeneous, it has been shown that the evolution of the stress ratio inside the shear band is similar to that inferred from the boundary force calculations except that the peak value based on the boundary information is a bit higher than that obtained from within the shear band.

It has also been revealed that the porosity developed inside the shear band is much greater than that obtained from boundary observations. This means that true constant volume direct shear tests cannot be performed and, in constant normal stress tests, the dilation determined from the movement of the top boundary of the sample underestimates the real dilatancy inside the shear band.

The simulations have demonstrated that at the critical state the vertical and horizontal normal stresses in the shear band are equal and that the directions of principal stress and strain rate are coaxial. It has been shown that it is the Coulomb friction angle φ_c that is measured in the direct shear test. The conventional interpretation of the location of the Mohr stress circle at the critical state results in an over prediction of the major principal stress.

8.3 Simple shear deformation of granular materials

The simple shear test was designed to mimic the real shear band mode of deformation. The investigations of such a test with different wall friction values have demonstrated that experimental measurements of wall stresses do not reflect the internal state of stress but merely provide information about the average mobilized wall friction. The detailed

examination of stress distribution reveals that the stress distribution inside the sample and on the boundaries are nonuniform from the beginning of the test; so the average stress obtained from the boundary information cannot represent the real state of stress inside the specimen.

The strain distributions are uniform initially and after peak strength hints of non-uniformities appear near the top and bottom boundaries during simple shear deformation. Nevertheless, non-uniformities are less significant than in the direct shear test. Therefore, the simple shear test can impose more uniform distribution of stress and strain to the specimen than direct shear tests.

It has been shown that both the non-coaxiality between the directions of the major principal stress and strain rate and the rate of dilation depend on the ratio of the horizontal to vertical normal stresses at the initial state. Non-coaxiality is not significant for samples with $K_0 = 1.0$. However, if $K_0 \neq 1.0$ the sample shows significant non-coaxiality between the directions of principal stress and strain rate. In such a case, the assumption of coaxiality of the direction of principal stress and strain rate is not valid. It has been demonstrated that the theoretical value of φ_c based on the flow rule (5.14) will be affected by the value of K_0, the dilation angle and the angle of non-coaxiality.

Based on the examination of the deformation of the local void cells it has been found that a large expansion of a void cell encourages particle rotation. When the void cell contracts it restricts the particle rotation.

In terms of the macro- and micro-mechanical behaviour, excellent agreement was obtained, for the sample with $K_0 = 1.0$, between the results of the simple and pure shear test simulations based on the volume-averaged data.

8.4 Localisation of granular materials

It has been shown that a shear band(s) only develops if the specimen has a certain packing density and inter-particle friction. The boundary conditions have a very significant effect on the shear band formation in terms of: the localisation patterns and the shear band inclination. If periodic boundaries are used, several incipient shear bands in two

orthogonal directions are initiated simultaneously in the strain-hardening regime close to the peak strength but only one band fully develops during strain softening. The same final shear band pattern also occurs in the test with zero wall friction. With high wall friction, however, two conjugate shear bands were eventually established by the end of shearing. In the wall boundary tests the localisation starts from the corners of wall boundaries, while in a periodic cell, the localisation initiates inside the specimen. The orientations of the shear bands are also different in simulations with different boundary conditions. In some cases it approximates to the Roscoe solution; in others it approaches the Coulomb prediction. Furthermore, in all the tests simulated the inclination angle decreased during shearing due to the change in specimen dimensions. Since the periodic cell simulations cannot provide precise information in terms of inclination angle of a shear band more work is required to focus on this issue.

In both biaxial compression and direct shear tests the measured thickness of the shear band was about 10-12 times the average particle diameter and this agrees with the results reported by other researchers.

Significant discontinuities were found in both the displacement and fluctuating velocity fields across a shear band. It has been shown that large particle rotations occur in a shear band. In addition, particles within the shear band tend to rotate in one direction and particles outside the shear band rotate in the opposite direction. Irrespective of the overall deformation of the specimen the volume within the shear band is dilated, which is highlighted by the large expansion of local void cells. It has been found that sliding contacts mainly occur within the shear band location. These are five distinct and important characteristics of shear band formation, which have been discovered during this study.

During shearing the strong force chains in the vicinity of the shear band become increasingly inclined to the major principal stress direction and unstable due to the loss of contacts inside the shear band, which leads to the collapse of the strong force chains. It has been shown that the stress fluctuations correspond to intermittent buckling of the strong force chains that triggers an instantaneous localisation in the fluctuating velocity field followed by an order of magnitude jump in the fluctuating kinetic energy density as the strong force transmission paths are re-established. This leads to the establishment of a persistent shear band(s) at the end of the test.

8.5 Limitation and recommendations for future work

Shear deformation of cohesionless particle assemblies have been comprehensively examined in this study. It has been shown that DEM can provide a useful tool to study the behaviour of such materials. It was never meant to model real samples with our simulations. Even a very small sample in the real world would be filled with millions of grains, so the present numerical method and current computer facilities will always be insufficient to model this. Furthermore, all the simulations carried out in this study have been restricted to two-dimensions. Due to the highly kinematic constraints imposed in 2D, it is not clear whether or not the degree of particle rotation observed is exaggerated. In addition, several problems have appeared during this study. For example, the dilation angle curves are not smooth due to the few numbers of particles used. Therefore, three-dimensional simulation with a significant larger number of particles are required and this should be given a high priority in future work.

In order to fully understand the shear deformation of granular materials several topics are worthy of consideration for future work. In this study, it has been assumed that the particles are cohesionless and elastic. Further investigation of shear deformation with cohesive and plastic particles would be useful since such materials are also very common in the real world. The local computer code has facilities to model liquid bridges between particles and this could be adapted to simulate the mechanical behaviour of partially saturated soils. It has been shown that DEM simulations provide a useful tool for understanding and confirming the deformation mechanism inside the shear band. However, the understanding of the localisation phenomena of granular materials is still far from complete and future 3D simulations are necessary if further progress is to be made.

Although wall boundaries have been used in this study to simulate biaxial compression, direct shear and simple shear tests, the specification for the walls was restricted to defining the internal forces on the walls and the interface conditions. Consequently, it was not possible to identify what loads/forces would actually be measured by experimentalists. In order to do this it will become necessary to completely model the containing walls and other parts of the experimental equipment using FEM and CAD techniques that will be combined with the DEM used to model the granular material behaviour.

References

1. Airey, D. W., Budhu, M. and Wood, D. M. (1985). Some aspects of the behaviour of soils in simple shear. Developments in soil mechanics and foundation engineering (Bannerjee & Butterfield Eds.), **2**, London: Elsevier, 185-213.

2. Airey, D. W. (1987). Some observations on the interpretation of shear box test results. Departmental report, CUED/D – SOILS/TR 196, Cambridge University.

3. Alshibli, K. A. and Sture, S. (1999). Sand shear band thickness measurements by digital imagine techniques. Journal of Computing in Civil Engineering, **13**(2), 103-109.

4. Alshibli, K. A. and Sture, S. (2000). Shear band formation in plane strain experiments of sand. Journal of Geotechnical & Geoenvironmental Engineering, **126**(6), 495-403.

5. Arthur, J. R. F., Dunstan, T., Al-Ani, Q. A. J. L. and Assadi, A. (1977). Plastic deformation and failure in granular media. Geotechnique, **27**(1), 53-74.

6. Assadi, A. (1975). Rupture layers in granular materials. PhD Thesis, University of London.

7. Bagi, K. (1996a). Geometrical modelling of granular assemblies. Acta Technica Acad. Sci. Hung., **107**(1-2), 1-16.

8. Bagi, K. (1996b). Stress and strain in granular assemblies. Mechanics of Materials, **22**, 165-177.

9. Bardet, J. P. and Proubet, J. (1991). A numerical investigation of the structure of persistent shear bands in granular media. Geotechnique, **41**(4), 599-613.

10. Bardet, J. P. and Proubet, J. (1992). Shear-band analysis in idealized granular material. Journal of Engineering Mechanics, **118**(2), 397-415.

11. Barnes, D. J. (1985). A study of the micro-mechanics of granular materials. PhD thesis, Aston University, Birmingham.

12. Bassett, R. H. (1967). The behaviour of granular materials in the simple shear apparatus. PhD thesis, University of Cambridge.

13. Bathurst, R. J. and Rothenburg, L. (1988). Micromechnical aspects of isotropic granular assemblies with linear contact interactions. Journal of Applied Mechanics, **55**, 17-23.

14. Been, K., Jefferies, M. G. and Hachey, J. (1991). The critical state of sands. Geotechnique, **41**(3), 365-381.

15. Bishop, A. W., Green, G. E., Garga, V. K. Andresen, A. and Brown, J. D. (1971). A new ring shear apparatus and its application to the measurement of residual strength. Geotechnique, **21**(4), 273-328.

16. Bjerrum, L. and Landva, A. (1966). Direct simple shear tests on a Norwegian quick clay. Geotechnique, **16**(1), 1-20.

17. Blackburn, D. J. (1983). An investigation into the mechanics of regular arrays of discs and spheres. PhD thesis, Aston University, Birmingham.

18. Borin, D. L. (1973). The behaviour of saturated kaolin in the simple shear apparatus. PhD thesis, University of Cambridge.

19. Budhu, M. (1979). Simple shear deformation of sands. PhD thesis, University of Cambridge.

20. Budhu, M. (1984) Non-uniformities imposed by simple shear apparatus, Can. Geotech. J., **21**(1), 125-137.

21. Casagrande, A. (1940). Characteristics of cohesionless soils affecting the stability of slopes and earth fills. Boston Society of Civil Engineering, 1925-1940.

22. Christofferesen, J., Mehrabadi, M. M. & Nemat-Nasser, S. (1981). A micro-mechanical description of granular material behaviour. J. Appl. Mech., ASME, **48**, 339-344.

23. Cole, E.R. (1967). The behaviour of soils in the simple shear apparatus. PhD thesis, University of Cambridge.

24. Collin, A. (1846). Experimental investigation on sliding of clay slopes. Translated by Schriever, W. R., University of Toronto Press, 1956.

25. Coulomb, C. A. (1776). Sur une application des regales de maximis et minimis a quelques problems es statique, relatifs a L'Architecture. Memoirs Academic Royale des Sciences, **7**, p343.

26. Cundall, P. A. (1971). A computer model for simulating progressive large-scale movements in blocky rock systems, Pro. Symp. Soc. Rock Mech., Nancy, **2**, Art 8.

27. Cundall, P. A. (1974). A computer model for rock-mass behaviour using interactive graphics for the input and output of geometrical data. Report for the Missouri River Divison, U.S. Army Crops of Engineers, University of Minnesota.

28. Cundall, P. A. (1978). Ball – A computer program to model granular media using the distinct element method. Technical note TN-LN-13, Advance Technology Group, Dames and Moore, London.

29. Cundall, P. A. and Strack, O. D. L. (1979a). A discrete numerical modal for granular assemblies. Geotechnique, **29**(1), 47-65.

30. Cundall, P. A. and Strack, O. D. L. (1979b). The discrete numerical modal as a tool for research in granular media. Part II. Report to National Science Foundation, Dept. of Civil & Mineral Engrg., University of Minesota, Minneapolis, Minnesota.

31. Cundall, P. A., Drescher, R. A. and Strack, O. D. L. (1982). Numerical experiments on granular assemblies; Meassurements and observations. IUTAM Conference on Deformation and Failure of Granular Materials, Delft, 31 Aug.-3 Sept., 355-370.

32. Cundall, P. A. (1988). Computer simulation of dense sphere assemblies. Micromechanics of Granular Materials, Satake & Jenkins (Eds.), 113-123.

33. Dantu, P. (1957). A contribution to the mechanical and geometrical study of non-cohesion masses. Proc. 4th Int. Conf. on Soil Mechanics & Foundation Engineering, 144-148.

34. Davis, E. H. (1968). Theories of plasticity and failures of soil mass. In Soil Mechanics, Selected Topics (Ed. I. K. Lee), London: Butterworth.

35. de Josselin de Jong, G. (1972). Discussion: Session II. Stress-strain behaviour of soils. Proc. Roscoe Memorial Symp. (Parry, Ed.), 258-261.

36. de Josselin de Jong, G. and Verruijt, A. (1969). Etude Photo-Elastique d'un Empilement de Disques, Cahiers du Group Francais de Rheologie, **2**(1), 73-86.

37. de Josselin de Jong, G. (1988). Elasto-plastic version of the double sliding model in undrained simple shear tests. Geotechnique, **38**(4), 533-555.

38. Desrues, J., Chambon, R., Mokni, M. and Mazerolle, F. (1996). Void ratio evolution inside shear bands in triaxial sand specimens studied by computed tomography. Geotechnique, **46**(3), 529-546.

39. Dounias, G. T. and Potts, D. M. (1993). Numerical analysis of drained direct and simple shear tests. Journal of Geotechnical Engineering, **119**(12), 1870-1891.

40. Drescher, A. and de Josselin de Jong, G. (1972). Photoelastic verification of a mechanical model for the flow of a granular materials. J. Mech. Phys. Solids, **20**, 337-351.

41. Dyer, M. R. and Milligan (1984). A photoelastic investigation of the interaction of a cohesionless soil with reinforcement placed at different orientations. Proc. Int. Conf. Institu. Soil and Rock Reinforcement, Paris: Press Ponts ET Chaussees, 257-262.

42. Dyvik, R., Berre, T. and Raadim, B. (1987). Comparison of truly undrained and constant volume direct simple shear tests. Geotechnique, **37**(1), 3-10.

43. Feda, J. (1982). Mechanics of particulate materials. Elsevier Scientific Publishing Co., Amsterdam, the Netherlands.

44. Finno, R. J., Harris, W. W., Mooney, M. A. and Viggiani, G. (1996). Strain localization and undrained steady state of sand, Journal of Geotechnical Engineering 122, No. 6, 462-473.

45. Finno, R. J., Harris, W. W., Mooney, M. A. and Viggiani, G. (1997). Shear bands in plain strain compression of loose sand. Geotechnique, **47**(1), 149-165.

46. Goodman, M. A. and Cowin, S. C. (1971). Two problems in the gravity flow of granular materials. J. Fluid. Mech., **45**, 321-339.

47. Goodman, M. A. and Cowin, S. C. (1972). A continuum theory for granular materials. Arch. Rational Mech. Anal., **44**, 249-266.

48. Hadamard, J. (1949). Lecons sur propagation des ondes et les equation de L'hydrodynamique. Cholsea, Pub. Co.

49. Hambly, E.C. (1969). Plane strain behaviour of soft clay. PhD thesis, University of Cambridge.

50. Han, C. and Vardoulakis, I. (1991). Plane-strain compression experiments on water-saturated fine-grained sand. Geotechnique, **41**(1), 49-78.

51. Han, C and Drescher, A (1993). Shear bands in biaxial tests on dry coarse sand. Soils and Foundations, **33**(1), 118-132.

52. Han, C and Vardoulakis, I. G. (1991). Plane-strain compression experiments on water-saturated fine-grained sand. Geotechnique, **41**(1), 49-78.

53. Hansen, B. (1961). Shear box tests on sand. Proc. 5th Int. Conf. Soil Mechanics Foundation Engineering, Paris, **1**, 127-131.

54. Harder, J. and Schwedes, J. (1985). The development of a true biaxial shear tester. Part. Charact., **2**, 149-153.

55. Harris, W. W., Viggiani, G., Mooney, M. A. and Finno, R. J. (1995). Use of stereophotogrammetry to analyze the development of shear band in sand. Geotechnical Testing Journal, **18**(4), 405-420.

56. Hill, R. (1962). Acceleration waves in solids. J. Mech. Phys. Solids, **10**, 1-16.

57. Hill, R. (1967). The essential structure of constitutive laws for metal composites and polycrystals. J. Mech. Physics of Solids, **15**(2), 79-95.

58. Ishibashi, K. and Towatha, I. (1983). Sand response to cyclic rotation of principal stress directions as induced by wave loads. Soils and Foundations, **23**(4), 11-26.

59. Iwashita, K. and Oda, M. (1998). Rolling resistance at contacts in simulation of shear band development by DEM. Journal of Engineering Mechanics, **124**(3), 285-292.

60. Janssen, R. J. M. (2001). Structure and shear in a cohesive powder. PhD thesis, Delft University.

61. Jewell, R. A. (1989). Direct shear tests on sand. Geotechnique, **39**(2), 309-322.

62. Joer, H. A., Lanier, J., Desrues, J. and Flavigny, E. (1992). 1γ2ε: Anew shear apparatus to study the behaviour of granular materials. Geotech. Testing J., ASTM **15**(2), 129-137.

63. Johnson, K. L. (1985). Contact Mechanics, CUP.

64. Kanatani, K. (1981). A theory of contact force distribution in granular materials. Powder Technology, **28**(2), 176-172.

65. Kjellman, W. (1951). Testing the shear strength of clay in Sweden. Geotechnique, **2**, 225-235.

66. Ko, H. Y. and Scott, R. F. (1967). A new soil testing apparatus. Geotechnique, **17**(1), 40-57.

67. Konishi, J., Oda, M. and Nemat-Nasser, S. (1983). Inherent anisotropy in assemblies of oval cross-sectional rods in biaxial compression. Mechanics of Granular Materials: New Models and Constitutive Relations, Jenkins and Satake (Eds.), 31-39.

68. Kraan, M. (1996). Techniques for the measurement of the flow properties of cohesive powders. PhD thesis, Technical University Delft.

69. Kruyt N. P. and Rothenburg, L. (1996). Micromechanical definition of the strain tensor of granular materials. Journal of Applied Mechanics, **118**, 706-711.

70. Kuhn, M. R. (1999). Structure deformation in granular materials. Mechanics of Materials, **31**, 407-429.

71. Lade, P. V. (1978). Cubical triaxial apparatus for soil testing. Geotech. Testing J., ASTM **1**(2), 93-101.

72. Lambe, T. W. (1951). Soil Testing for Engineers. John Wiley & Sons, New York, p 80.

73. Lanier, J. and Zitouni, Z. (1987). Development of a data base using the Grenoble true triaxial apparatus. Proceedings of a Workshop on Constitutive Equations for Granular Non-Cohesive Soils, Cleveland, Rotterdam: Balkema, 47-58.

74. Lanier, J. and Jean, M. (2000). Experiments and numerical simulations with 2D disks assembly. Powder Technology, **109**, 206-221.

75. Leygue, M. L. (1885). La poussee de terres. Ann. Des Ponts et Chaussecs, Sixth Ser. **10**(2), 788.

76. Lian, G, Thornton, C. and Kafui, D. (1998). TRUBAL - A 3D computer program for modelling particle assemblies. Departmental Report, Civil Engineering Department, Aston University.

77. Liu, C-H, Nagel, S. R., Schecter, D. A., Coppersmith, S. N., Majumdar, S., Narayan, O. and Witten, T. A. (1995). Force fluctuations in bead packs. Science, **269**, 513-515.

78. Massoudi, M. and Mehrabadi, M. M. (2001). A continuum model for granular materials: considering dilatancy and the Mohr-Coulomb criterion. Acta Mechanica, **152**, 121-138.

79. Matsuoka, H., Iwata, Y. and Sakakibara, K. (1986). A constitutive model of and clays for evaluating the influence of rotation of principal stress axes. Pro. 2nd Intl. Symp. Numer. Models Geomech., Ghent, 67-78.

80. Matsuoka, H., Liu, S., Sun, D. and Nishikata, U. (2001). Development of a new in-situ direct shear test. Geotechnical Testing Journal, **24**(1), 92-102.

81. Mindlin, R. D. and Deresiewicz, H. (1953). Elastic spheres in contact under varying oblique force, Journal of Applied Mechanics, **20**, 327-344.

82. Misra, A. and Jiang, H. (1997). Measured kinematic fields in the biaxial shear of granular materials. Computers and Geotechnics, **20**(3/4), 267-285.

83. Moreau, J.-J. (1994). Some numerical methods in multibody dynamics: applications to granular materials. Euro. J. Mech. **A13**, 93-114.

84. Morgenstern, N. R. and Tchalenko, J. S. (1967). Microscopic structures in Kaolin subjected to direct shear. Geotechnique, **17**, 309-328.

85. Muhlhaus, H. B. and Vardoulakis, I. (1987). The thickness of shear bands in granular materials. Geotechnique, **37**(3), 271-283.

86. Nemat-Nasser, S. and Okada, N. (2001). Radiographic and microscopic observation of shear bands in granular materials. Geotechnique, **51**(9), 753-765.

87. Nguyen, M. L. and Coppersmith, S. N. (2000). Scalar model of inhomogeneous elastic and granular media. Physical Review E, **62**(4), 5248-5262.

88. Ni, Q., Powrie, W, Zhang, X and Harkness R. (2000). Effect of particle properties on soil behaviour: 3-D numerical modelling of shear box tests. Geotechnical Special Publication, n96, 58-70.

89. Oda, M. (1972). Initial fabrics and their relations to mechanical properties of granular material. Soils and Foundations, **12**(1), 17-36.

90. Oda, M. and Konishi, J. (1974). Microscopic deformation mechanism of granular material in simple shear. Soils and Foundations, **14**, 25-38.

91. Oda, M. (1977). Co-ordination number and its relation to shear strength of granular materials. Soils and Foundations, **17**(2), 29-42.

92. Oda, M., Konishi, J. and Nemat-Nasser, S. (1980). Some experimentally based fundamental results on the mechanical behaviour of granular materials. Geotechnique, **30**(4), 479-495.

93. Oda, M., Nemat-Nasser, S. and Mehrabadi, M. M. (1982). A statistical study of fabric in a random assembly of spherical granules. Int. J. Anal. Methods Geomech., **6**, 77-94.

94. Oda, M., Konishi, J. and Nemat-Nasser, S. (1983). Experimental micromechanical evaluation of the strength of granular materials: effects of particle rolling. Mechanics of Granular Materials: New Models and Constitutive Relations, Jenkins and Satake (Eds.), 21-30.

95. Oda, M. and Kazama, H. (1998). Microstructure of shear bands and its relation to the mechanisms of dilatancy and failure of dense granular soils. Geotechnique, **48**(4), 465-481.

96. Oda, M. and Iwashita, K. (2000). Micro-deformation mechanism of shear banding process based on modified distinct element method. Powder Technology, **109**, 192-205.

97. Pearce, J. A. (1971). A new triaxial apparatus. Stress-strain behaviour of soils. Proceedings of the Roscoe Memorial Symposium, Henley-on-Thames: Foulis, 330-339.

98. Peltier, M. R. (1957). Experimental investigations on the intrinsic rupture curve of cohesive soils. Proceedings of Fourth International Conference on Soil Mechanics and Foundation Engineering, London, 1957, **1**, 179-182.

99. Potts, D. M., Dounias, G. T. and Vaughan, P. R. (1987). Finite element analysis of the direct shear box test. Geotechnique, **37**(1), 11-23.

100. Radjai, F., Jean, M., Moreau, J. J. and Roux, S. (1996). Force distributions in dense two-dimensional granular systems. Physical Review Letters, **77**(2), 274-277.

101. Radjai, F., Wolf, D. E., Roux, S., Jean, M. & Moreau, J. J. (1997). Force networks in dense granular media, Powders & Grains 97, Behringer & Jenkins (Eds.), 211-214.

102. Rice, J.R. (1977). The localization of plastic deformation. In K.T. Koiter (ed.), Theoretical and Applied Mechanics: 207-220. Amsterdam: North-Holland.

103. Roscoe, K. H. (1953). An apparatus for the application of simple shear to soil samples, Proc. 3nd Int. Conf. Soil Mech. Found. Eng., **1**, 186-191.

104. Roscoe, K. H. (1970). The influence of strain in soil mechanics. Geotechnique, **20**(2), 129-170.

105. Rothenburg, L. (1980). Micro-mechanics of idealised granular materials. PhD Thesis, Dept. of Civil Engineering, Carleton Univ., Ottawa.

106. Rothenburg, L. and Selvadurai, A. P. S. (1981). A micromechanical definition of the Cauthy stress tensor for particulate media. Proc. Int. Symp. on the Mechanical Behaviour of Structured Media, Ottawa, Part B, 469-486.

107. Rothenburg, L. and Bathurst, R. J. (1989). Analytical study of induced anisotropy in idealized granular materials. Geotechnique, **39**(4), 601-614.

108. Rothenburg, L. and Bathurst, R. J. (1992). Micromechanical features of granular assemblies with planar elliptical particles. Geotechnique, **42**(1), 79-95.

109. Rowe, P.W. (1962). The stress-dilatancy relation for static equilibrium of an assembly of particles in contact, Proc. Roy. Soc. A, **269**, 500-527.

110. Rudnicki, J.W. and Rice, J.R. (1975). Conditions for the localization of deformation in pressure-sensitive dilatant materials. J. Mech. Phys. Solids, **23**, 371-394.

111. Saada, A. S. and Townsend, F. C. (1981). State of the art: Laboratory strength testing of soils, Lab. Shear Strength of Soils, ASTM Special Technical Publication 740, 7-77.

112. Saada, A. S. (1988). Hollow cylinder torsional devices: their advantages and limitations. Advanced triaxial testing of soil and rock, ASTM STP 977, 766-795. Philadelphia: American Society for Testing and Materials.

113. Satake, M. (1978). Constitution of mechanics of granular materials through the graph theory. Proc. U.S.-Jap. Seminar on Continuum-Mechanical and Statistical Approaches in the Mechanics of Granular Materials, Tokyo, 47-62.

114. Satake, M. (1982). Fabric tensor in granular materials. IUTAM Conference on Deformation and Failure of Granular Materials, Delft, 31 Aug - 3 Sept., 63-68.

115. Satake, M. (1985). Graph-theoretical approach to the mechanics of granular materials, 5th International Symposium on the Continuum Models of Discrete Systems, Nottingham, 14-20 July, 163-173.

116. Satake, M., and Jenkins, J. T. (Eds.) (1988). Micromechanics of granular materials, Proc. Of the US/Japan Seminar on the Micromechanics of granular Materials, Elsevier.

117. Satake, M. (1992). A discrete mechanical approach to granular materials. Int. J. Engrg. Sci., **30**, 1525-1533.

118. Satake, M. (1993a). Discrete-mechanical approach to granular media. Powder & Grain 93, Thornton (Eds.), 3-9.

119. Satake, M. (1993b). New formulation of graph-theoretical approach in the mechanics of granular materials. Mech. of Mater., **16**, 65-72.

120. Savage, S. B. (1979). Gravity flow of cohesionless granular materials in chutes and channels. J. Fluid Mech., **92**(1), 53-96.

121. Scarpelli, G. and Wood, D. M. (1982). Experimental observations of shear band patterns in direct shear tests. IUTAM Conference on Deformation and Failure of Granular Materials, Delft, 31 Aug.-3 Sept., 473-484.

122. Schofield A. N. and Wroth C. P. (1968) Critical State Soil Mechanics, (McGraw-Hill, London), p295.

123. Shen, C. K., Sadigh, K and Hermann, L. R. (1978). An analysis of NGI simple shear apparatus for cyclic soil testing: dynamic geotechnical testing. ASTM Spec. Tech. Publ. 654, 148-162.

124. Shibuya, S., Mitachi, T. and Tamate, S. (1997). Interpretation of direct shear testing of sands as quasi-simple shear. Geotechnique, **47**(4), 769-790.

125. Skempton, A. W. and Bishop A. W. (1950). The measurement of the shear strength of soils. Geotechnique, **2**(2), 90-108.

126. Sowers, G. F. (1961). Large scale direct shear tests on broken rock. Proceedings of Fourth International Conference on Soil Mechanics and Foundation Engineering, Paris, **2**, 717-720.

127. Sowers, G. F. (1963). Strength testing of soils. Laboratory Shear Testing of Soils. ASTM STP 740, Young and Townsend (Eds.), 3-21.

128. Standard Shear Testing Technique for Particular Solids Using the Jenike Shear Cell. UK Institution of Chemical Engineers. London 1989.

129. Strack, O. D. L. and Cundall, P. A. (1978). The distinct element method as a tool for research in granular media: Part I. Report to the National Science Foundation, NSF Grant ENG75-20711.

130. Stroud, M.A. (1971). The behaviour of sand at low stress levels in the simple shear apparatus. PhD thesis, University of Cambridge.

131. Tatsuoka, F., Sakamoto, M. Kawamura, T. and Fukushima, S. (1986). Strength and deformation characteristics of sand in plane strain compression at extremely low pressures. Soils and Foundations, **26**(1), 65-84.

132. Tatsuoka, F., Pradham, T. B. S. and Horii, N. (1988). Discussion on direct shear tests on reinforced sand. Geotechnique, **38**(1), 148-153.

133. Taylor, D. W. (1948). Fundamentals of soil mechanics. New York: Wiley.

134. Tejchman, J and Bauer, E. (1996). Numerical simulation of shear band formation with a polar hypoplastic constitute model. Computers and Geotechnics, **19**(3), 221-244.

135. Thomas, T.Y. (1961). Plastic flow and fracture of solids. Academic press.

136. Thornton, C. and Barnes, D. J. (1986). Computer simulated deformation of compact granular assemblies. Acta Mechanica, **64**, 45-61.

137. Thornton, C. and Randall, C. W. (1988). Applications of theoretical contact mechanics to solid particle system simulation. Micromechanics of Granular Materials, Satake and Jenkins (Eds.), 133-142.

138. Thornton, C. and Sun, G. (1993). Axisymmetric compression of 3D polydisperse systems of spheres. Powder & Grain 93, Thornton (Eds.), 129-134.

139. Thornton, C. (1993). On the relationship between the modulus of particulate media and surface energy of the constituent particles. J. Phys. D: Appl. Phys., **26**, 1587-1591.

140. Thornton, C. and Sun, G. (1994). Numerical simulation of general 3D quasi-static shear deformation of granular media. Numerical Methods in Geotechnical Engineering, Smith (Eds.), 143-148.

141. Thornton, C. (1997). Force transmission in granular media. KONA Powder and Particle, **15**, 81-90.

142. Thornton, C. and Antony, S. J. (1998). Quasi-static deformation of particulate media. Phil. Trans. R. Soc. Lond. A, **356**, 2763-2782.

143. Thornton, C. and Zhang, L. (1999). The jamming transition during constant volume shear flow of granular materials. Pro. 13th Int. Cong. on Rheology, **2**, 432-434.

144. Thornton, C. (2000a). Numerical simulations of deviatoric shear deformation of granular media. Geotechnique, **50**(1), 43-53.

145. Thornton, C. (2000b). Microscopic approach contributions to constitutive modelling. Euro-conference on Constitutive Modelling of Granular Materials, Kolymbas (Eds.), 193-208.

146. Thornton, C. (Ed.) (2001). Powder Technology, Special issue on Numerical Simulations of Discrete Particle Systems, **109**(1-3).

147. Ting, J. M., Meachum, L. and Rowell, J. D. (1995) Effect of particle shape on the strength and deformation mechanisms of ellipse-shaped granular assemblages. Engineering Computations, **12**, 99-108.

148. Vardoulakis, I., Goldscheider, M. and Gudehus, G. (1978). Formation of shear bands in sand bodies as a bifurcation problem. Int. J. Numer. and Analytical Methods in Geomech., **2**, 99-128.

149. Vardoulakis, I. (1980). Shear band inclination and shear modulus of sand in biaxial tests. Int. J. Numer. and Analytical Methods in Geomech., **4**, 103-119.

150. Vardoulakis, I. and Graf, B. (1985). Calibration of constitutive models for granular materials using data from biaxial experiments. Geotechnique, **35**(3), 299-317.

151. Vardoulakis, I. and Sulem, J. (1995). Bifurcation Analysis in Geomechanics, London: Blackie Academic & Professional.

152. Vermeer, P. A. (1990). The orientation of shear bands in biaxial tests. Geotechnique, **40**(2), 223-256.

153. Williams, J. R. and Rege, N. (1997a). The development of circulation cell structures in granular materials undergoing compression. Powder Technology, **90**, 187-194.

154. Williams, J. R. and Rege, N. (1997b). Coherent vortex structures in deforming granular materials. Mechanics of Cohesive-Frictional Materials, **2**, 223-236.

155. Wood, D. M. (1990). Soil behaviour and critical state soil mechanics. New York: CUP.

156. Wroth, C. P. and Bassett, R. H. (1965). A stress-strain relationship for the shearing behaviour of a sand. Geotechnique, **15**(1), 32-56.

157. Zhang, L. & Thornton, C. (2001). Numerical simulations of biaxial compression. Proc. Int. Cong. for Particle Technology: PARTEC 2001, Nuremberg, (CD-ROM).

158. Zhang, L. and Thornton, C. (2002). Numerical simulations of the direct shear test. Proc. 4th World Congress of Particle Technology, Sydney (CD-ROM).

159. Zhu, Y., Shukla, A. and Sadd, M. H. (1996). The effect of microstructural fabric on dynamic load transfer in two dimensional assemblies of elliptical particles. J. Mech. Phys. Solids, **44**, 1283-1303.

APPENDIX A: THE DISCRETE ELEMENT METHOD AND THE PROGRAM - TRUBAL

A.1 Introduction

The Discrete Element Method (DEM) was originally developed by Cundall (1971, 1974) for the analysis of movements within rock block systems. It is a time-dependent finite difference technique, which may be used to simulate the progressive movements of particles within an assembly. Later Cundall and Strack (1979a, 1979b) incorporated the methods into the computer program 'BALL', which is capable of simulating the behaviour of an irregular assembly of discs under given boundary conditions. Cundall's 3D version TRUBAL was introduced to Aston University in 1989. Since then, extensive modifications and enhancements have been made to the original TRUBAL code.

The application of the DEM to assemblies of particles requires cyclic calculations. For every calculation cycle, the translational and rotational accelerations of the particles are updated according to Newton's second law of motion by dividing the sum of the contact forces for each particle by its mass. Numerical integration of these accelerations is then performed over a small timestep to give new velocities and displacements for each particle. The velocities of each particle are used to find the relative approach between contacting particles, which is in turn used to calculate the contact force increments (normal and tangential), providing a check is made to ensure that contact still exists. The contact forces are resolved to obtain the out-of-balance forces on each particle, from which new accelerations of each particles are then calculated at the next time-step. The above operations are repeated for each time step so that the motion of the whole particle assembly can be determined.

In the original two-dimensional code BALL, linear springs and dashpots were used to model the interactions between contiguous particles. In order to simulate quasi-static deformation, it was necessary to incorporate global damping terms into the equations of motion to dissipate sufficient energy. In the Aston version of the three-dimensional code TRUBAL, the interaction between contiguous particles are modelled by algorithms based

on theoretical contact mechanics. Details of algorithms and equations used in DEM are presented in the following sections for three dimensional sphere assemblies. The choice of the control parameters required to ensure quasi-equilibrium during deformation is also discussed.

A.2 Newton's second law of motion

A time-dependent finite difference scheme is applied to the cyclic calculation of the incremental contact forces and progressive movements of the particles. For each calculation cycle, the translational and rotational accelerations of each of the constituent particles are given by Newton's second law of motion. According to which, the motion of a particle over a time step Δt are governed by the following equations,

Translation $$F_i - \beta_g v_i = m\frac{\Delta v_i}{\Delta t} \qquad \text{(A.1)}$$

Rotation $$M_i - \beta_g \omega_i = I\frac{\Delta \omega_i}{\Delta t} \qquad \text{(A.2)}$$

where $i = 1, 2, 3$ indicates the three components in x, y, and z directions, F_i is the out-of-balance force component of the particle, M_i is the out-of-balance moment on the particle due to the tangential contact forces; v_i is the translational velocity component, ω_i is the rotational velocity component; m is mass of the particle, I is the rotational inertia of the particle and β_g is the global damping coefficient (if used).

A.3 Force-displacement laws at contacts without adhesion

A.3.1 Normal contact force

For two contacting particles of radii R_i (i = 1, 2), a contact between them exists if their boundaries overlap, i.e. when the relative approach of the centriod of the two particles in contact satisfy the following condition,

$$\alpha < R_1 + R_2 - D \qquad \text{(A.3)}$$

where $D = \sqrt{(x_2 - x_1)^2 + (y_2 - y_1)^2 + (z_2 - z_1)^2}$ is the distance between the centres of the

two particles, and x_i, y_i, z_i ($i = 1, 2$) are the coordinates of the centres.

According to Hertz theory, the normal pressure distribution acting over a small circular contact area with radius a and the normal contact force N is expressed as,

$$N = \frac{4E^*}{3R^*}a^3 \tag{A.4}$$

where E^* and R^* are defined as,

$$\frac{1}{E^*} = \frac{1-\nu_1^2}{E_1} + \frac{1-\nu_2^2}{E_2} \tag{A.5}$$

$$\frac{1}{R^*} = \frac{1}{R_1} + \frac{1}{R_2} \tag{A.6}$$

E_i and ν_i ($i = 1, 2$) denote the Young's modulii and Poisson's ratios of the particles, respectively. Since $\alpha = a^2/R^*$, which may be substituted into (A.4), the normal contact force due to the relative approach α is given by

$$N = \frac{4E^*}{3}\left(R^*\alpha^3\right)^{1/2} \tag{A.7}$$

from which the normal contact stiffness is defined as

$$k_n = \frac{\partial N}{\partial \alpha} = 2E^*\left(R^*\alpha\right)^{1/2} \tag{A.8}$$

Within a time step, if the increment of the relative approach between the two spheres is $\Delta\alpha$, it follows that the corresponding incremental normal force at the contact can be given as,

$$\Delta N = 2E^* a \Delta\alpha \tag{A.9}$$

A.3.2 Tangential contact force

The tangential force at the contact of two spheres is modelled by the theory of Mindlin and Deresiewicz (1953), which predicts that if two contacting surfaces are subjected to an increasing tangential displacement δ, then relative slip is initiated at the perimeter and progresses inward over an annular area of the contact surface. The incremental tangential

force ΔT due to the incremental tangential displacement $\Delta\delta$ depends not only on the loading history but also on the variation of the normal force. The incremental tangential force can be obtained from the following equation (for more details see Thornton and Randall, 1988).

$$\Delta T = 8G^{*}a\theta_k\Delta\delta + (-1)^k\mu\Delta N(1-\theta_k) \tag{A.10}$$

where

$$\theta_k = 1 \tag{A.11}$$

if $|\Delta T| < \mu\Delta N$. Otherwise,

$$\theta_k = \begin{cases} \sqrt[3]{1-\dfrac{T+\mu\Delta N}{\mu N}} & \text{if } k=0 \\ \sqrt[3]{1-\dfrac{(-1)^k(T-T_k)+2\mu\Delta N}{2\mu N}} & \text{if } k=1,2 \end{cases} \tag{A.12}$$

where $k = 0, 1, 2$ denotes the paths of loading, unloading and reloading respectively, $\Delta\delta$ is the increment of the relative tangential displacement of the two contact spheres at the contact, μ is the friction coefficient, T_k represents the historical tangential force from which unloading or reloading commenced and G^{*} is defined as,

$$\frac{1}{G^{*}} = \frac{2-\nu_1}{G_1} + \frac{2-\nu_2}{G_2} \tag{A.13}$$

where G_i ($i = 1, 2$) is the shear modulus of each particle. In (A.12), T_k needs to be updated as $T_k = T_k - (-1)^k\mu\Delta N$ to allow for the effect of the variation of the normal force at each time step.

A.4 Motion update

The contact point is midway between the intersecting points C_A and C_B of the two contacting particles, as shown in Fig. A1. Unit vectors n and t are orthogonal, n being in the normal direction to the contact plane and in the direction of the line joining the centres. The direction cosines n_i are defined as,

$$n_i = \frac{x_{Bi} - x_{Ai}}{D} \tag{A.14}$$

x_{Ai} and x_{Bi} are the centre coordinates of the two spheres. In 2D, n_i may be written as $n_1 = cos\theta$ and $n_2 = sin\theta$ where θ is the inclination of the contact normal vector to the horizontal axis of the global reference frame.

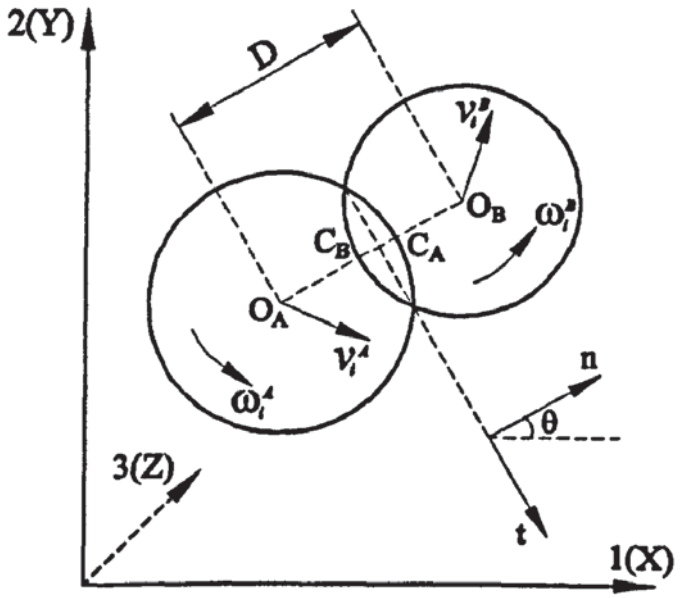

Fig. A1 Kinematics of two contacting spheres

Since n and t are orthogonal,

$$n_i t_i = 0 \tag{A.15}$$

The interaction force between each pair of contacting particles is computed in an incremental way in TRUBAL. The relative movement at the contact has three components: the relative normal approach along the centre line of the two particles, the relative tangential displacement between the two contacted surfaces and the relative rotation of the two particles. Since the area of the contact is very small, the twisting resistant at the contact due to the relative rotation about the line joining the centroids of the two particles is ignored and hence only the normal and tangential contact forces are considered.

For a pair of particles in contact, if the linear and rotational velocities are noted as v_i^A, ω_i^A

and v_i^B, ω_i^B respectively, the relative normal displacement increment at the contact in a time step can be given as,

$$\Delta\alpha = (v_i^B - v_i^A)n_i\Delta t \tag{A.16}$$

where $i = 1, 2, 3$ indicates the three components.

In a time-step, the component of the relative tangential displacement increment at the contact between the two particles is,

$$\Delta\delta_i = (v_i^B - v_i^A)\Delta t - \Delta\alpha n_i - (\omega_{i+1}^A n_{i+2} - \omega_{i+2}^A n_{i+1})R_A\Delta t - (\omega_{i+1}^B n_{i+2} - \omega_{i+2}^B n_{i+1})R_B\Delta t \tag{A.17}$$

where R_A and R_B are the radii of the two sphere and all the subscripts i, $i+1$, $i+2$ should be rotated from 1 to 3.

The computation of the incremental force due to the normal relative displacement increment is straight forward by substituting $\Delta\alpha$ into appropriate (A.9). The updated normal force at the contact is given as,

$$N_C^{new} = N_C^{old} + \Delta N \tag{A.18}$$

where N_C^{new} represents the updated normal contact force, N_C^{old} is the previous normal contact force and ΔN is the normal force increment.

A normal damping force is calculate as,

$$N_D = 2\beta_c\sqrt{mk_n}\Delta\alpha/\Delta t \tag{A.19}$$

where $\beta_c(<1)$ is the coefficient of contact damping, k_n is the normal stiffness. Then, the total normal force contribution to the out-of-balance force of each sphere is calculated as,

$$N^{new} = N_C^{new} + N_D \tag{A.20}$$

The computation of the tangential force increment due to the tangential displacement increment differs according to the interaction law used. If Mindlin's no-slip solution is used, the tangential force-displacement relationship is linear elastic. As a result, the resultant tangential force increment can be calculated from its components by substituting $\Delta\delta_i$ into (A.10). However, adding the tangential force increment to the previous

tangential force is much complicated due to the fact that the contact plane may have rotated. Consequently, the direction of the previous tangential force and displacement should be adjusted.

In three dimensions, the resultant tangential displacement can have any orientation in the contact plane. In order to identify the loading path of the resultant tangential force, the direction of the resultant tangential displacement has to be identified. In the current version of TRUBAL, the direction of the resultant tangential displacement at the first time step of each contact is regarded as positive. For any subsequent time step, suppose the previous resultant tangential displacement is δ and its orientation, after corrected by accounting for the rotation of the contact plane, is defined by the components δ_i ($i = 1, 3$). It follows that the updated tangential displacement components due to the incremental displacement should be given as,

$$\delta_i^{new} = \delta_i + \Delta\delta_i \tag{A.21}$$

The sign and magnitude of the updated resultant tangential displacement are given by the following equation,

$$\delta^{new} = sign(\delta)\,sign(\delta\Delta\delta_i)\sqrt{\delta_i^{new}\delta_i^{new}} \tag{A.22}$$

For more details of how to determine the rotation of the contact plane, how to correct the previous tangential force and displacement and how to determine the sign of the updated resultant tangential displacement, see Lian *et al* (1998). From the updated resultant tangential displacement, the magnitude of the resultant tangential displacement increment is obtained as,

$$\Delta\delta = \delta^{new} - \delta \tag{A.23}$$

which is used to obtain the resultant tangential force increment ΔT by using (A.10-12). Then the resultant tangential force is updated as,

$$T_C^{new} = T_C^{old} + \Delta T \tag{A.24}$$

The updated resultant tangential force is then compared with the sliding criterion. If the sliding criterion is exceeded then the tangential force is reset to the limiting value. The

direction of the resultant tangential force is assumed to be in the same direction of the tangential displacement and its components are given as,

$$T_i^{new} = T^{new} \frac{\delta_i^{new}}{\left|\delta^{new}\right|} \tag{A.25}$$

The tangential damping force at a contact is given by,

$$T_D = 2\beta_c \sqrt{mk_t}\,\Delta\delta/\Delta t \tag{A.26}$$

where k_t is the tangential stiffness and the total tangential force contribution to the out-of-balance force of each sphere is calculated as,

$$T^{new} = T_C^{new} + T_D \tag{A.27}$$

From the updated total normal and tangential contact forces, the contribution to the out-of-balance force of each sphere is obtained as,

Sphere A $$F_i^A = -N^{new} n_i - T_i^{new} \tag{A.28}$$

$$M_i^A = R_A\left(n_{i+1} T_{i+2}^{new} - n_{i+2} T_{i+1}^{new}\right) \tag{A.29}$$

Sphere B $$F_i^B = N^{new} n_i + T_i^{new} \tag{A.30}$$

$$M_i^B = -R_B\left(n_{i+1} T_{i+2}^{new} - n_{i+2} T_{i+1}^{new}\right) \tag{A.31}$$

The new resultant forces and moments acting on each sphere at time t are used to determined the new accelerations $\ddot{x}_i$ and $\ddot{\theta}_i$ according to Newton's second law of motion. With global damping, Newton's second law of motion for each sphere is given as,

$$F_i + mg_i - \beta_g \frac{v_i^{new} + v_i^{old}}{2} = m\frac{v_i^{new} - v_i^{old}}{\Delta t} \tag{A.32}$$

$$M_i - \beta_g \frac{\omega_i^{new} + \omega_i^{old}}{2} = I\frac{\omega_i^{new} - \omega_i^{old}}{\Delta t} \tag{A.33}$$

From which the updated velocity components v_i and ω_i are obtained,

$$v_i^{new} = \frac{m/\Delta t - \beta_g/2}{m/\Delta t + \beta_g/2} v_i^{old} + \frac{F_i + mg_i}{m/\Delta t + \beta_g/2} \tag{A.34}$$

$$\omega_i^{new} = \frac{I/\Delta t - \beta_g/2}{I/\Delta t + \beta_g/2}\omega_i^{old} + \frac{M_i}{I/\Delta t + \beta_g/2} \tag{A.35}$$

The new values for the velocities are used to update the positions and rotations of the spheres by further numerical integration. The relative displacement increments for each sphere are given as following,

Translation $\Delta x_i = v_i \Delta t$ (A.36)

Rotation $\Delta\Phi_i = \omega_i \Delta t$ (A.37)

where Δx_i and $\Delta\Phi_i$ are the translational and rotational displacement increments.

The position and orientation of a particle are updated as:

$$x_i^{new} = x_i^{old} + \Delta x_i \tag{A.38}$$

$$\Phi_i^{new} = \Phi_i^{old} + \Delta\Phi_i \tag{A.39}$$

The new results of displacement are used to calculate the contact force in the next calculation cycle. These equations are applied to each particle in turn. After the motion update is completed, the force sum F, and the moment sum M, of each particle are reset to zero at the end of each cycle.

A.5 Program TRUBAL

The basic structure of TRUBAL is similar to the original program developed by Cundall. However, in order to perform different simulations, modifications have been made and extensions have been provided from time to time since the program was introduced to Aston in 1989. As a time-dependant finite difference schemed numerical analysis program, the main part of TRUBAL is the cyclic simulation module, within which the evolution of contact forces and particle movements is calculated as described in the previous section. The other parts include an assembly generation module which is used to generate particles and to define particles; an external control module which is used to perform a wide range of simulation experiments and an output module which provides a large selection of graphic and print out options to interpret the simulation results.

A.5.1 Data structure

In the original TRUBAL code all data are stored in a single array *A(I)*, The array *A(I)* is partitioned into several sub-arrays containing information about the particles, boxes and the link lists of address for particles and contacts. The data structures of this array are shown in Fig. A2a.

The variables M_1, M_2, M_3 and M_5 are set to fixed values at the start of a new problem, after the user has declared how many particles and boxes are required. M5 indicates the memory limit, which is set in the program. The addresses of M_2, M_3 and M_{3A} indicate the upper limits of the array of ball data, wall data and box data, respectively. Variables M_{1A}, M_{2A} and M_4 can be dynamically located as the user creates more particles and walls or as the requirements for contacts change during the test. The storage scheme for the link lists and contact arrays is shown in Fig. A2b.

A.5.2 Searching scheme

In DEM, particles are allowed complete freedom to interact with each other. An efficient scheme is needed to identify possible candidates for contact with a given particle. It is computationally prohibitive to check all possible pairs of particles. The method devised in TRUBAL confines the search to pairs that are in contact or close enough to be in contact at a later time during the simulation.

The rectangular cell containing the assembly of particles is divided into smaller boxes. The boxes are initially square having dimension *DEL*. *DEL* should be larger than the diameter of the largest sphere. However, in order to search for contacts efficiently, this value should normally be less than twice the largest sphere diameter. The first step in the contact detection scheme is to form link lists for each box by mapping all constituent particles into the appropriate boxes. An "envelope space" with dimension of $2(R+TOL)$ is assigned to each particle and mapped into the box or boxes it occupies (Fig. A3), where R is the radius of the particle and TOL is the tolerance of a specified gap distance, which is a very small value. The second step is the contact searching. Two particles are considered

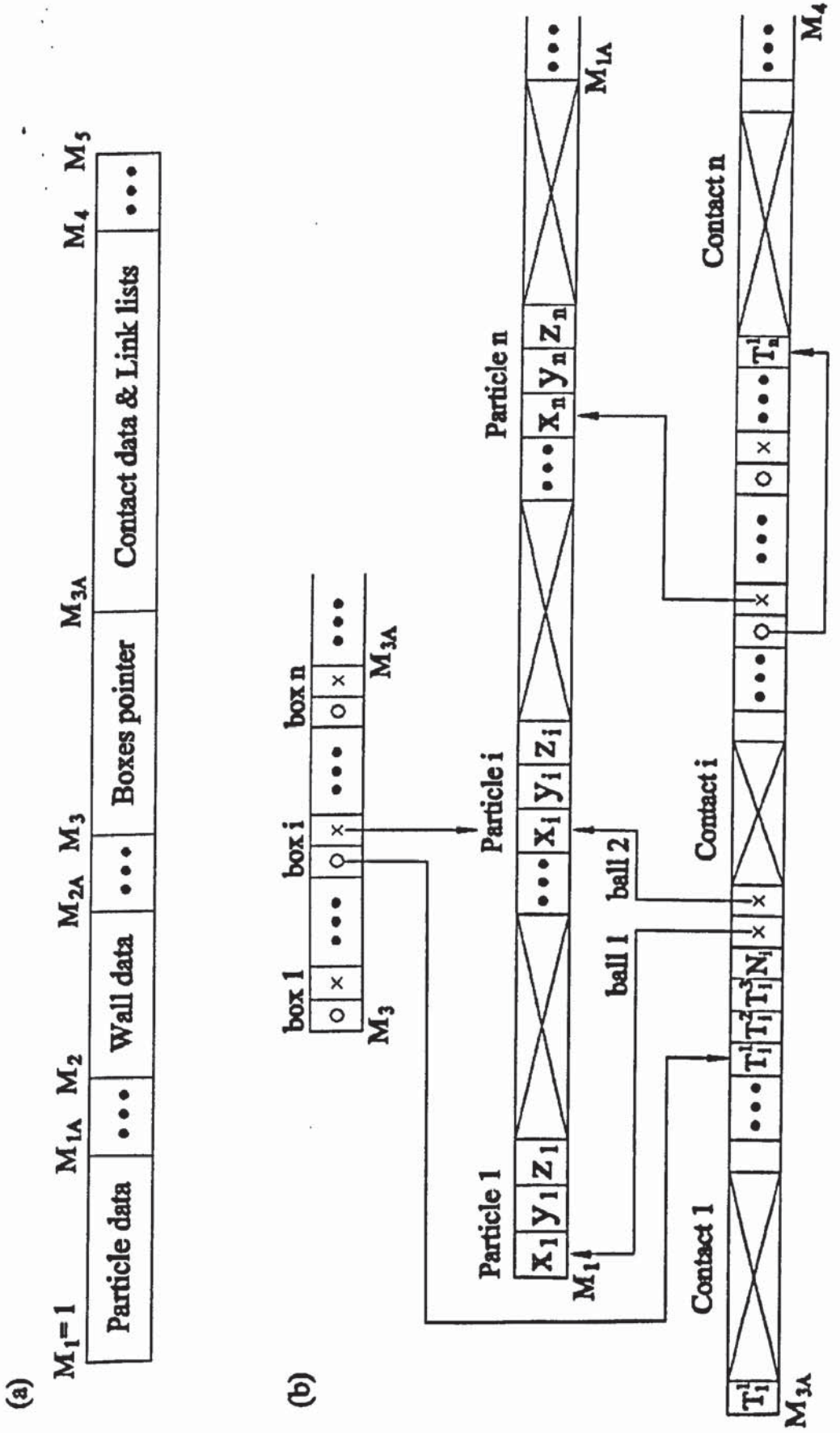

Fig. A2 Data structure of TRUBAL: (a) partition of array *A(I)*;
(b) scheme of contacts and links

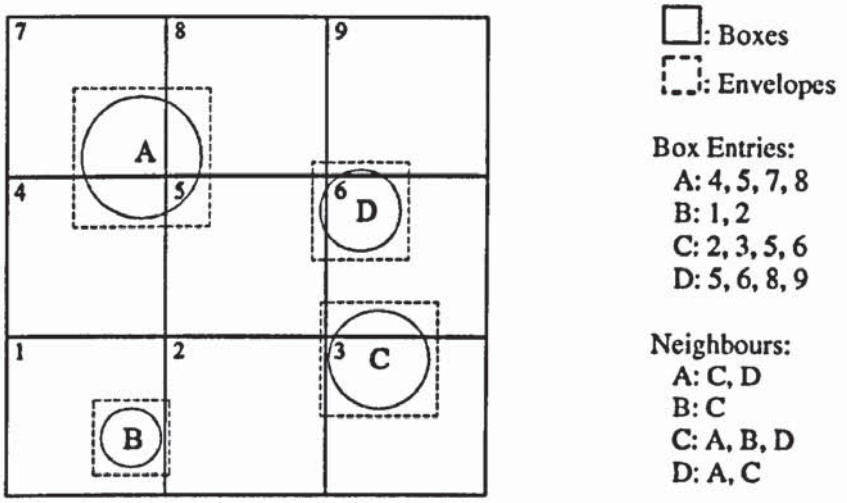

Fig. A3 Searching scheme

to be neighbours and checked for contact if they are both mapped into at least one common box (Fig. A3). In periodic cell simulations the dimensions of each box will change according to the specified strain rate. In other types of simulation the dimensions of the box will remain unchanged.

A.5.3 Control scheme

In order to make it possible to simulate a wide range of problems related to assemblies of particles, TRUBAL provides a number of control schemes to apply different types of external conditions. There are also a selection of commands, which are designed to specify the initial conditions, material properties or interaction laws for the simulations.

A.5.3.1 Stain control mode

When using periodic boundaries the evolution of the system may be achieved by specifying either a stress control mode or strain control mode. In order to control the deformation of the system, a uniform strain-rate tensor $\dot{\varepsilon}_{ij}$ is specified according to which all the spheres in the cell move, as though their centres are points in a continuum, to satisfy the equation,

$$\Delta x_i^s = \dot{\varepsilon}_{ij} x_j \Delta t \qquad \text{(A.40)}$$

where x_i ($i = 1, 2, 3$) are the coordinates of the sphere centre and Δt is the small time step used to advance the evolution of the system. Additional incremental displacements occur as a result of the interactions between contiguous spheres.

Superimposing the incremental displacements due to the strain rate field on the updated incremental displacement due to the out-of-balance force leads to the total incremental displacement of each particle as,

$$\Delta x_i = \Delta x_i^F + \Delta x_i^S \tag{A.41}$$

where Δx_i^F ($i = 1, 2, 3$) represents the updated incremental displacements of each sphere due to the out-of-balance force as described in Section A.4.

The strain control mode only works for assemblies with periodic boundaries. For an assembly with periodic boundaries, any particles that intersect one face of the unit cell have images that intersect the opposite face of the cell. Hence, the particles intersecting the periodic boundaries of the unit cell are self-balancing. For an assembly without periodic boundaries, particles lying on the periphery of the assembly are not self-balanced and are free to move outwards. In this case, an alternative boundary control technique is required such as wall boundaries, see previous chapters concerning the wall boundaries and Appendix B.

A.5.3.2 Servo-control mode

The strain control mode permits any desired strain path to be applied. TRUBAL also provides a servo-controlled option. The function of a servo-control mode is to permit any desired stress path to be followed. With the servo-control mode, the applied strain field is continuously adjusted according to the difference between the desired stress state and the measured stress state. At each time step, the strain rates are set to,

$$\dot{\varepsilon}_{ij}^S = g\left(\sigma_{ij}^d - \sigma_{ij}^m\right) \tag{A.42a}$$

or,

$$\dot{\varepsilon}_{ij}^S = \dot{\varepsilon}_{ij} + g(\sigma_{ij}^d - \sigma_{ij}^m) \tag{A.42b}$$

depending on which servo-control mode is selected. The parameter g is the *GAIN* of the servo mechanism, σ_{ij}^{d} is the desired stress state to be achieved and σ_{ij}^{m} is the measured average stress state of the assembly.

In the application of the servo-control, a limit is set for the maximum strain rate allowed for the simulation. This is necessary when high velocities are developed should the measured stress differ greatly from the desired stress. The limit of the maximum allowed strain rate is given by the servo-control command together with the *GAIN* parameter.

A.5.4 Control parameters for quasi-equilibrium

A.5.4.1 Damping

In order to model a quasi-static process using a dynamic method such as DEM, it is necessary to provide some means to absorb the excess kinetic energy within the system. A viscous damping can be added into the equations of motion to achieve convergence to a steady state equilibrium of the system. Damping in granular materials is a real phenomenon. It is the global response of the combined effect of all mechanisms of energy dissipation present in the system. These mechanisms are complex and difficult to model, especially for discontinuous systems. Therefore, instead of representing the phenomenon in its complexity, simplified methods are used to account for the global damping response. Artificial damping is used for this purpose. The program TRUBAL provides two types of viscous damping and damping is specified in terms of the Rayleigh damping parameters. Rayleigh damping involves stiffness-proportional (contact) damping β_c and mass-proportional (global) damping β_g.

Contact damping considers the energy losses during the force transmission through the solid particles. This type of damping is modelled by a dashpot. The damping force is calculated to be proportional to the normal and tangential force increments. Having calculated the contact forces between spheres, damping forces are calculated and added to the contact forces to give the total contributions to the out-of-balance forces of each sphere. The contact damping is important for a simulated assembly to reach quasi-equilibrium. Without it, the contact force between particles will continue to oscillate indefinitely. The contact damping parameter β_c is given by,

$$\beta_c = \frac{frac}{2\pi\omega} \tag{A.43}$$

where *frac* is the fraction of critical damping at the modal frequency ω.

The global damping is a type of mass proportional damping. It operates in the form of classical Rayleigh damping and is handled in the subroutine, which calculates the motion of each sphere. The mass proportional damping can be envisaged as dashpots that connect all constituent particles to the reference axes of the simulated system. For each sphere, the resistance force of global damping that is exerted on the sphere is opposite to its velocity vector (both translational and rotational) of the sphere. The effect of global damping is like immersing the constituent particles in a viscous fluid. It is useful to dissipate the kinetic energy during the final stage of preparation of a system in order to avoid excessive computer time. However, before the system is subjected to the desired computer simulated experiment, the global damping must be switched off. The global damping parameter β_g is obtained as,

$$\beta_g = 2\pi * frac * \omega \tag{A.44}$$

A.5.4.2 Numerical stability

Numerical instability is a potential problem in the explicit time-finite-difference procedure used in TRUBAL. The source of instability is the integration time-step. If it is greater than a critical time-step, the scheme is unstable and the results of the simulation are unreliable. In the current version of TRUBAL, the time step is based on the consideration of the Rayleigh wave speed of force transmission around the surface of elastic bodies. Upon application of a force on an elastic body, the Rayleigh waves are propagated along the surface with a velocity of,

$$v_R = \alpha\sqrt{\frac{G}{\rho}} \tag{A.45}$$

where ρ is the density of the particle and α is the root of the following equation,

$$(2-\alpha^2)^4 = 16(1-\alpha^2)\left[1-\frac{1-2\nu}{2(1-\nu)}\alpha^2\right] \tag{A.46}$$

from which an approximate solution may be obtained as,

$$\alpha = 0.1631\nu + 0.876605 \tag{A.47}$$

where ν is Poisson's ratio.

For an assembly of many spherical particles, the highest frequency of Rayleigh wave propagation is determined by the smallest sphere, which gives the critical time step as,

$$\Delta t_c = \frac{\pi R_{min}}{v_R} = \frac{\pi R_{min}}{\alpha}\sqrt{\frac{\rho}{G}} \tag{A.48}$$

The above equation assumes that the property type of all constituent particles is the same. However, if there are different material types for the constituent particles, the critical time step for the highest Raleigh wave frequency should be the lowest among those determined by different material types. The actual time step used in TRUBAL is a multiple of the Rayleigh critical time step by a value of FRAC which is normally less than 0.5 depending on the problem considered,

$$\Delta t_c = \Delta t_c * FRAC \tag{A.49}$$

A.5.4.3 Density scaling

As described above, the time step used in the simulations is based on the minimum particle size and Raleigh wave speed. Consequently, for particles of diameter ca. 10mm the time step would be ca. 1μs. In order to simulate quasi-static deformation by using a strain rate of not more than 10e-5 s^{-1}, it would require 10^{10} time steps to apply 10% strain. Therefore, to complete the simulations within a reasonable time scale, the notional particle density is scaled up by a factor of 10^{12} in order to use a time step ca. 1 s. As a consequence, the forces and displacements, and hence the stresses, strains and energy are not affected; the velocities and accelerations are reduced by orders of magnitude but these are not of concern when considering quasi-static behaviour.

APPENDIX B: MODIFICATIONS TO TRUBAL FOR SHEAR TESTS WITH WALL BOUNDARIES

Three types of shear tests involving walls can be simulated by the program TRUBAL now: biaxial compression tests (**BCW**), direct shear tests (**DST**) and simple shear tests (**SST**). Since the simulation is restricted to 2D mode, the code should be modified further to carry out 3D simulations. The input commands that should be specified to run these numerical tests, together with the code implemented into TRUBAL and some examples of input command files are listed in this appendix.

B.1 New parameters

Some important parameters added in TRUBAL to perform three different tests with wall boundaries are listed as follows,

WALTYP : To identify the type of shear test. This parameter is normally set to **–1**.

WMAX(3) : To save current specimen dimensions in three directions (*x*, *y*, *z*).

W_OLD(3) : To save specimen dimensions in three directions at the last time step.

OUTFLG : This flag is set as **TRUE** only when the particle is outside of a specified interior region.

In order to obtain results suitable for analysis, an output file named **wfor.txt** will be generated when the command **'print wall'** is specified. The different parameters used in this file are listed as follows:

FNi, FTi : The total normal force and tangential force on the wall. (*i=1, N*).

wl1, wl2 : The current dimensions of the sample.

gama : To save the shear strain in each time step.

msig1,msig2 : The principal stresses in a specified interior region.

msig11, msig12, msig21, msig22 : The components of the stress tensor in a specified interior region.

wsig1,wsig2 : The principal stresses for the whole sample.

wsig11, wsig12, wsig21, wsig22 : The components of the stress tensor for the whole sample.

volm : To save the volume of a specified interior region.

mfab1,mfab2 :The principal fabrics in a specified interior region.

mfab11, mfab12, mfab21, mfab22 : The components of the fabric tensor in a specified interior region.

deltay :The displacement increment in the vertical direction (**DST** and **SST** only).

B.2 New commands

WTY n

This selects the type of shear test. **WTY 0** selects a **BCW** test, **WTY 1** a **SST** test, and **WTY 2** a **DST** test.

DWALL (AWALL) n [ROT x_o y_o ω]

Rotation of a wall is implemented in the program TRUBAL. This command can create or alter a finite plane wall n to rotate about a fixed point P (x_o, y_o) with an angular velocity ω (see Fig. B.1). The fixed point P can be chosen either inside the wall (Fig. B.1a) or outside the wall (Fig. B.1b). The distances between P and the wall endpoints A and B are l_1 and l_2, respectively.

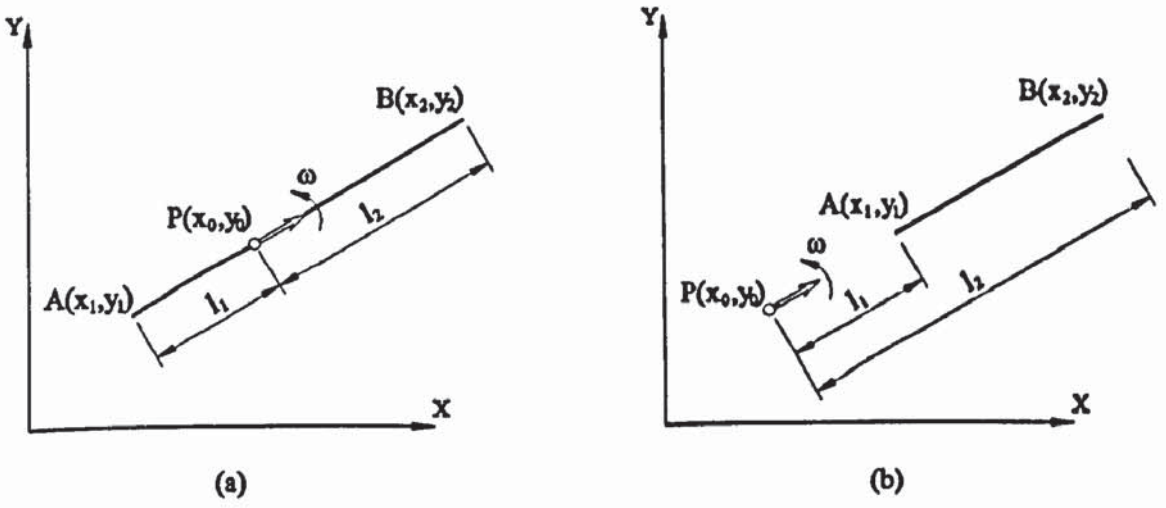

Fig. B.1 Definitions of a rotating wall

In each time step the coordinates of the wall end points A and B are calculated as,

$$x_i^{new} = l_i \cos\theta + x_0 \tag{B.1}$$

$$y_i^{new} = l_i \sin\theta + y_0 \tag{B.2}$$

where θ is the current angle of the wall to the horizontal direction.

Note: Although the **WINDOW** command is an old command in TRUBAL, one should specify this area before carrying out the direct shear tests or simple shear test in order to limit the central part or shear band.

B.3 Changes in wall array contents

Each wall array allocated between M_2 and M_{2A} contains the following:

W(1) - W(4):	Parameters d, a, b, c which define a plane in the form of $d = ax + by + cz$; or R, x_0, y_0, z_0 to define a spherical wall in the form of $R^2 = (x-x_0)^2 + (y-y_0)^2 + (z-z_0)^2$
W(5):	Normal or radial force set by servo control for the wall
W(6):	Maximum normal or radial velocity of the wall set by servo
W(7) - W(9):	Components of wall velocity V_x, V_y, V_z
W(10):	**Radial velocity for a spherical wall and a rotating plane wall, empty for other plane walls**
W(11):	measured normal or radial force on the wall
W(12):	Code indicating wall type, 1 for plane wall , 2 for spherical wall
W(13):	To identify extent of plane wall (1 for finite, 0 for infinite)
W(14):	GAIN or servo control mechanism
W(15) - W(17):	Components of wall displacement increment in x, y, z directions
W(18):	Wall displacement increment for spherical wall, empty for plane wall
W(19) - W(21):	Components of wall force in x, y, z directions
W(22) - W(23):	**Wall displacement increment in x, y directions for the second corner (B) of a rotating wall**
W(24):	To identify the type of plane wall: 1 for inclined wall; otherwise, 0
W(25):	Wall material type
W(26) - W(31):	Lower and upper limits of plane wall in x, y, z directions
W(32) - W(43):	Coordinates of wall corner points (x_i, y_i, z_i) $i = 1, 4$
W(44) - W(45):	**Coordinates of the fixed point (x_0, y_0) in rotation wall**
W(46) - W(47):	**Length of the fixed point to two corner points of a rotating wall (l_1, l_2)**

W(48): **Initial cycle number**

W(49): **Initial inclination of a rotating wall**

W(50) - W(51): **Total displacement in *x*, *y* directions for the top wall in shear tests**

B.3 Main modifications in TRUBAL for shearing tests with walls

The additional facilities incorporated in the program TRUBAL are mainly in subroutines **HFORD, WALMOT** and **WALL.** The actual modified parts are given below.

```
C     ========================
      SUBROUTINE WALL(IAW,ISW)
C     ========================
C ---- DEFINE A WALL OR ALTER WALL PARAMETERS IN GRANULE ----
                                  ... ... ... ... ... ...
  170 if(RVAR(NPAR+3).eq.0.0) then
        A(IAW+9)=0.0
        A(IAW+6)=0.0
        A(IAW+7)=0.0
        A(IAW+8)=0.0
        NPAR=NPAR+3
        goto 50
      endif
      A(IAW+43)=RVAR(NPAR+1)
      A(IAW+44)=RVAR(NPAR+2)
      A(IAW+9)=RVAR(NPAR+3)*degrad
      A(IAW+47)=float(NTOT)
      A(IAW+48)=0.0
      A(IAW+49)=0.0
      A(IAW+50)=0.0
      if(ia(iaw+23).eq.0) then
        ia(iaw+23) = -1
        if(A(IAW+2).eq.0.0.and.A(IAW+1).ne.0.0) A(IAW+48)=PI/2.0
      else
        slope=-a(iaw+1)
        ang=datan(slope)
        A(IAW+48)=ang
      endif
      A(IAW+21)=A(IAW+14)
      A(IAW+22)=A(IAW+15)
      wl1=-sqrt((A(IAW+31)-A(IAW+43))**2+(A(IAW+32)-A(IAW+44))**2)
      wl2=sqrt((A(IAW+37)-A(IAW+43))**2+(A(IAW+38)-A(IAW+44))**2)
      A(IAW+45)=wl1
      A(IAW+46)=wl2
      if(waltyp.eq.1) then
        NW = (IAW-M2)/NVARW + 1
        NW2 = MOD(NW+1,4)
        if(NW2.eq.0) NW2=NW2+4
        IAW2=M2+NVARW*(NW2-1)
        A(IAW2+9)=A(IAW+9)
        A(IAW2+47)=A(IAW+47)
        A(IAW2+48)=0.0
        if(A(IAW2+2).eq.0.0.and.A(IAW2+1).ne.0.0) then
          wl3=A(IAW2+31)-RVAR(NPAR+1)
```

```
          A(IAW2+46)=wl3
        else
          wl3=A(IAW2+32)-RVAR(NPAR+2)
          A(IAW2+45)=wl3
        endif
      endif
      NPAR=NPAR+3
      GOTO 50
                                  ... ... ... ... ... ...
      RETURN
      END


C     ====================================
      SUBROUTINE WALMOT(B,IWCODE,IWS,IWNC)
C     ====================================
C  Calculate wall position according to grid motion
                                  ... ... ... ... ... ...
      goto (1,2) iwcode
    1 if(twod.and.b(10).ne.0.0) then
        angt1=b(49)
        angt2=b(10)*TDEL*(float(NTOT)-b(48))+angt1
        if(abs(iwnc).eq.1) then
          h1=b(46)
          h2=b(47)
          x1=b(44)
          y1=b(45)
          b(15)=h1*(qcos(angt2))+x1-b(32)
          b(16)=h1*(qsin(angt2))+y1-b(33)
          b(22)=h2*(qcos(angt2))+x1-b(38)
          b(23)=h2*(qsin(angt2))+y1-b(39)
        else
          angt1=angt2-b(10)*TDEL
          if(b(46).ne.0.0) then
            dx=-b(46)*(dtan(angt2)-dtan(angt1))
            dv=dx/TDEL
            b(15)=b(15)+dx
            b(7)=dv
            if(FSERVO.ne.0.0) b(16)=b(16)+b(8)*TDEL
          else if(b(47).ne.0.0) then
              dy=b(47)*(dtan(angt2)-dtan(angt1))
              dv=dy/TDEL
              b(16)=b(16)+dy
              b(8)=dv
          endif
        endif
        if(angt1.eq.0.0.or.iwnc.eq.-1) then
          if(iwnc.eq.-1) iwnc=1
          goto 40
        endif
        goto 25
      endif
                                  ... ... ... ... ... ...
      RETURN
      END


C     ========================
      SUBROUTINE HFORD(C,B1,B2)
C     ========================
C  3-D FORCE/DISPLACEMENT LAW
```

```
                                    ... ... ... ... ... ...
      do 2 i = 1,idm
           ddel      = del(i)
           I3        = I+3
           dpb1(i)   = b1(i)
           dpb1(i3)  = b1(i3)
           IF(WFLAG) THEN
             BETAST=BETAW
             IF(IWC.EQ.1) THEN
                                    ... ... ... ... ... ...
c end points of inclined wall (2D) --> (xw1,yw1), (xw2,yw2)
                        dpxw1 = b2(32) + b2(15)
                        dpyw1 = b2(33) + b2(16)
                        if(twod.and.b2(10).ne.0.0) then
                          dpxw2 = b2(38) + b2(22)
                          dpyw2 = b2(39) + b2(23)
                        else
                          dpxw2 = b2(38) + b2(15)
                          dpyw2 = b2(39) + b2(16)
                        endif
c limits of wall extent
                                    ... ... ... ... ... ...
c to calculate linear velocity for incline rotating wall
                       if(twod.and.b2(10).ne.0.0) then
                         dpxint = dpb2(1) - a(iab2+43)
                         dpyint = dpb2(2) - a(iab2+44)
                         b2(7)=-dpyint*b2(10)
                         b2(8)=dpxint*b2(10)
                       endif
                                    ... ... ... ... ... ...
           ELSE
             dpb2(i)=b2(i)
             dpb2(i3)=b2(i3)
           ENDIF
      8    dpz(i)    = dpB2(I) + dpB2(I3) - dpB1(I) - dpB1(I3)
                                    ... ... ... ... ... ...
        RETURN
        END
```

B.4 Examples of command files used for a simple shear test

Stage 1: Sample preparation and consolidation

```
START 0.007 0.007 0.00035 400 5100 4 log
2D box with 5000 particles
2-D
frac .3
dia 0.000030 1
dia 0.000040 2
dia 0.000050 3
dia 0.000060 4
dia 0.000070 5
dia 0.000080 6
dia 0.000090 7
```

```
ymd 8.34e9 1
ymd 8.34e9 2

prat 0.35 1
prat 0.35 2

dens 9.17e3 1
dens 9.17e3 2

fric .05 1
fric .01 2

gra 0.0 -9.81 0.0

dwall fp 0.001405 0.000400 0.000175 0.001405 0.006600 0.000175  m 2
dwall fp 0.001000 0.001405 0.000175 0.006000 0.001405 0.000175  m 2
dwall fp 0.005595 0.000400 0.000175 0.005595 0.006600 0.000175  m 2

agg cub 1 0.0014051 0.0055949 0.001545 0.004535 0.0 0.00035
rgen 15 7 1 1
rgen 151 6 1 1
rgen 605 5 1 1
rgen 958 4 1 1
rgen 605 3 1 1
rgen 151 2 1 1
rgen 15 1 1 1
plo cir wal
cyc 20000
... ...
cyc 20000

agg cub 1 0.0014051 0.0055949 0.004005 0.006995 0.0 0.00035
rgen 15 7 1 1
rgen 151 6 1 1
rgen 605 5 1 1
rgen 958 4 1 1
rgen 605 3 1 1
rgen 151 2 1 1
rgen 15 1 1 1

cyc 20000
... ...
cyc 20000

sav sst.0
stop
```

Stage 2: Introducing the top wall

```
restart sst.0
2D box with 5000 particles
gra 0.0 0.0 0.0
dwall fp 0.001 0.00583 0.000175 0.006 0.00583 0.000175 v 0 -0.02 0 m 2

cyc 20000
... ...
cyc 20000

sav sst.1
stop
```

Stage 3: Compress sample to desired density

```
restart sst.1
2D box with 5000 particles

frac .1
dens 917e14 1
dens 917e14 2
damp .05 .5 1 0 1
damp .07 .5 1 0 0
awall 1  v 0.0000001 0.0 0.0
awall 2  v 0.0 0.0000001 0.0
awall 3  v -0.0000001 0.0 0.0
awall 4  v 0.0 -0.0000001 0.0

cyc 10000
print info stress
... ...
cyc 10000
print info stress

sav sim.88
stop
```

Stage 4: Shearing

```
restart SIM.88
2D box with 5000 particles

fric 0.5 1
fric 0.5 2
*define shear test type
wty 1

*define the fix point on the rotation wall
awall 1 R 1.4661413E-03 0.0035 0.00115
awall 3 R 5.5338587E-03 0.0035 0.00115

*set servo control to the top wall
awall 4 SE 0.001 2.0e7 2.8e-7

*1
cyc 4000
print info deform stress part chi con epart wall
... ...
*10
cyc 4000
print info deform stress part chi con epart wall
save sim.40k
... ...
*1
cyc 4000
print info deform stress part chi con epart wall
... ...
*10
cyc 4000
print info deform stress part chi con epart wall
save sim.560k
stop
```

APPENDIX C: SIMULATION VIDEOS

Four videos have been made during the examination of the biaxial compression test with periodic boundaries. These clips are available at http://www.iem.bham.ac.uk/computation/granular/microevo.htm. Some brief explanations of the videos are provided in this appendix.

C. 1 Video clip 1: v831.gif

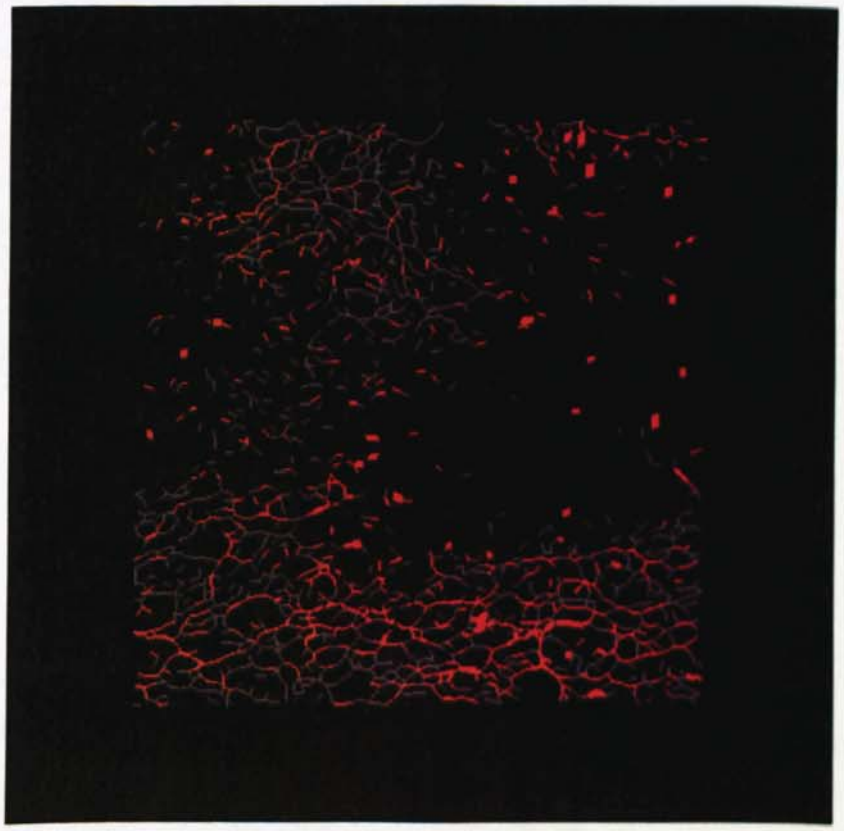

http://www.iem.bham.ac.uk/computation/granular/movies/MicrostructEvolution/v831.gif or see the enclosed CD-ROM

This video shows the force connectivity diagram of an intermediate system with solid fraction 0.584 during the period from the beginning of biaxial compression until enduring connectivity has been established. In this video, the contact forces greater and less than the

average force are shown by red and grey lines, respectively. The system considered here is initially non-percolating. As shearing proceeds, the individual particles begin to cluster. Finally, a percolating system is developed around 9.5% deviator strain. More details concerning this video are provided in Chapter 6.

C.2 Video clip 2: v832.gif

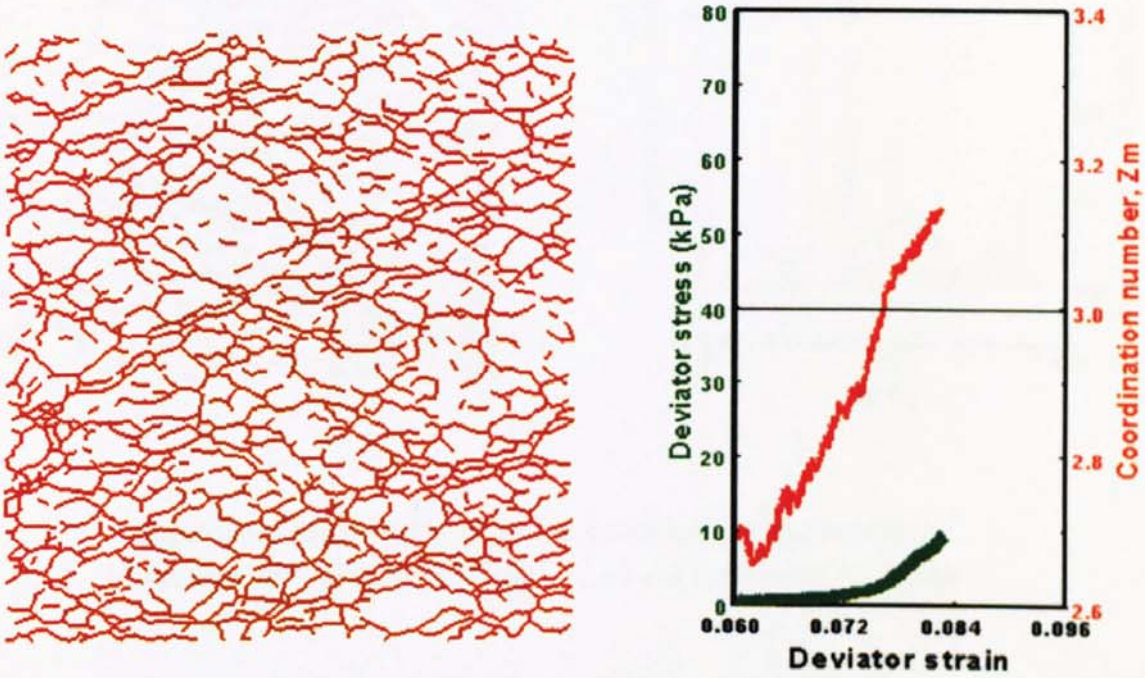

http://www.iem.bham.ac.uk/computation/granular/movies/
MicrostructEvolution/v832.gif or see the enclosed CD-ROM

This video shows the evolution of strong force chains (left hand side) and the simultaneous evolution of both the mechanical coordination number (shown in green) and the deviator stress (shown in red), which are presented on the right hand side of the video, for the system with solid fraction 0.585. Biaxial compression during the transition from 6% to 9.5% deviator strain is illustrated. At 6% deviator strain, the system is still non-percolating, but at 9.5% deviator strain, enduring connectivity (percolation) is established. It can be seen from this video that the transition from a non-percolating to a percolating system correlates well with the establishment of a mechanical coordination number of ca. 3.0.

C.3 Video clip 3: fked90.gif

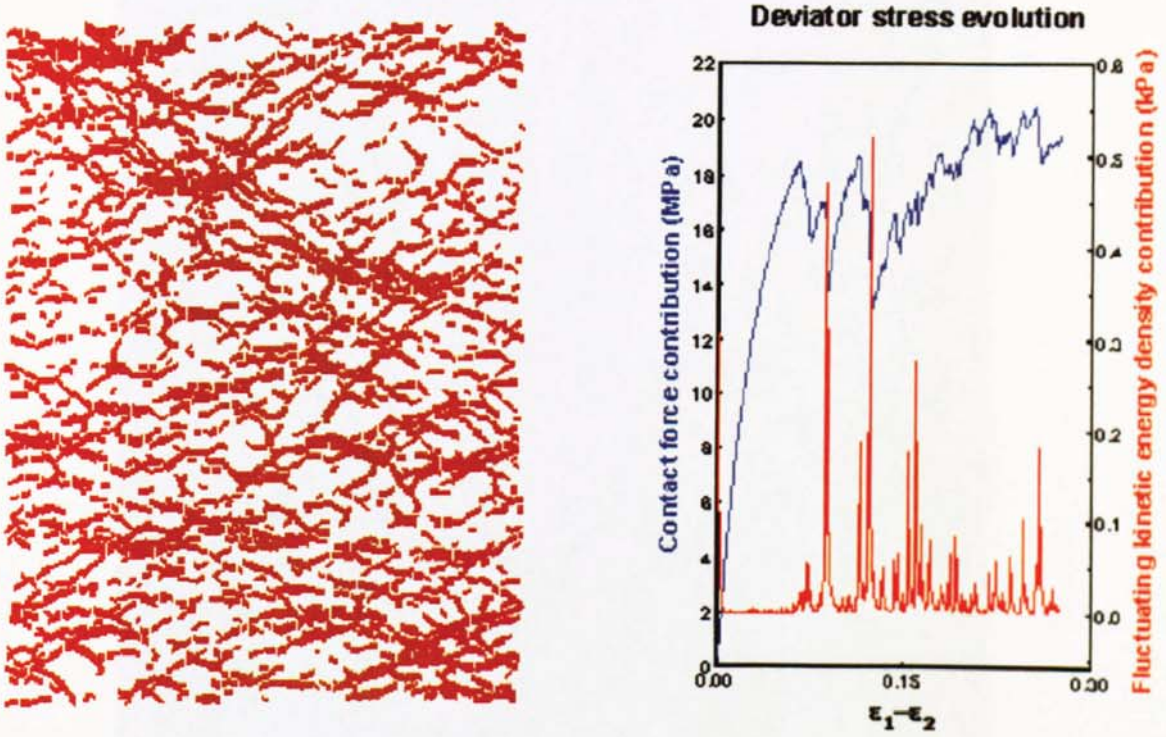

http://www.iem.bham.ac.uk/computation/granular/movies/
MicrostructEvolution/fked90.gif or see the enclosed CD-ROM

The evolution of the strong force chains for the dense system of solid fraction 0.635 is shown in this video, in which only the strong forces larger than 1.3 times the average force are shown on the left. The evolution of deviator stress is presented on the right hand side of this video. The contributions to the deviator stress include two parts: the contact force portion is shown in blue and fluctuating kinetic energy density portion is shown in red. It can be seen that there are several spikes in the fluctuating kinetic energy density curve. In addition, these spikes are always accompanied by drops in the contact force contribution curve. When playing the video at high speed it is clear that the stress fluctuations lead to intermittent buckling of the strong force chains, which triggers an instantaneous localisation in the fluctuating velocity field followed by rearrangement of the strong force transmission paths.

C.4 Video clip 4: vel90.gif

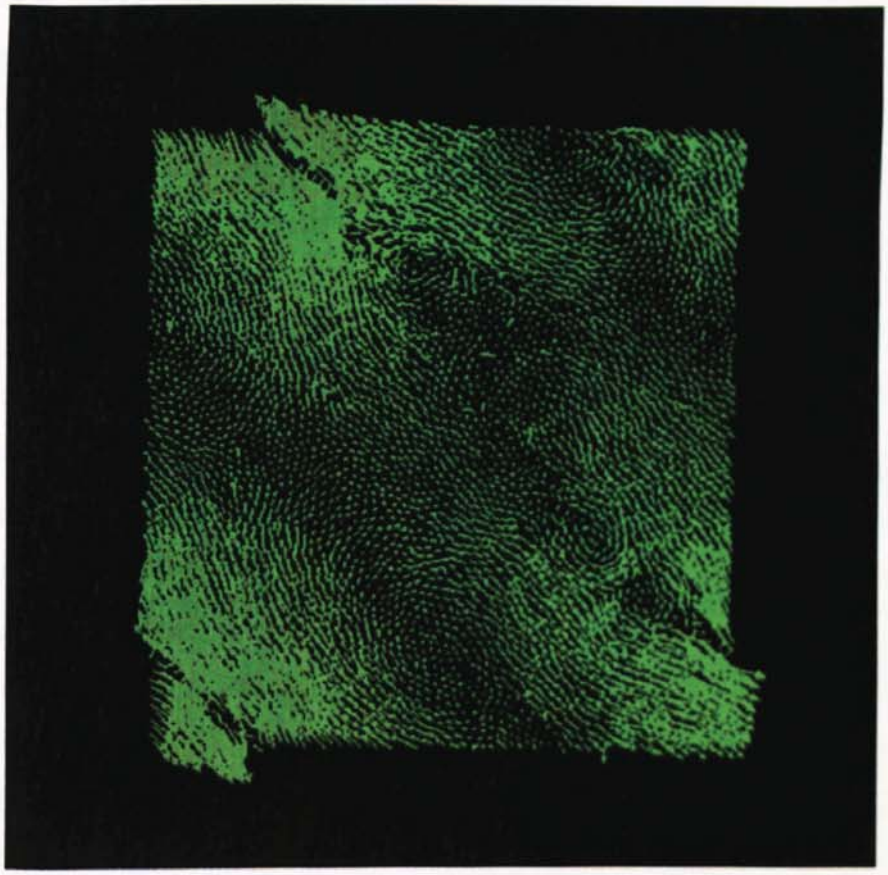

http://www.iem.bham.ac.uk/computation/granular/movies/
MicrostructEvolution/vel901.gif or see the enclosed CD-ROM

This video shows the fluctuating velocity field for the system with a solid fraction of 0.635. The aim of making this video was to investigate localisation phenomena in granular materials. According to Hill (1962), a shear band is considered as a thin material layer that is bounded by two material discontinuity surfaces of the velocity gradient. From this video the appearance of strain localisation starts around the peak shear strength. More analyses concerning the strain localization are provided in Chapter 7.

APPENDIX D: A COMPARISON BETWEEN TWO SHEAR SCHEMES FOR THE SIMPLE SHEAR TEST

D.1 Introduction

There are two shear schemes that can be chosen to simulate the simple shear test. The models of these two schemes are illustrated in Fig. D.1. For the same specimen we can rotate about either the mid-points of the side walls (O, O') or the base points (B, C) to perform the simple shear test. For convenience, the scheme in which the vertical walls rotate about their mid-points O and O' is referred to scheme 1 (Fig. D.1a); and scheme 2 is when the vertical walls rotate about the intersection of the side and bottom walls at nodes B and C (Fig. D.1b). In scheme 1, when the two vertical walls rotate, the top and bottom walls are translated using a compatible horizontal velocity in opposite directions. In scheme 2, the bottom wall BC is fixed. Only the top wall AD is displaced horizontally as the two vertical walls rotated. In both schemes the top wall can move in the vertical direction in the constant normal stress test. The sample II described in Chapter 5, which is with wall friction of 0.5, is chosen to perform the simple shear test using these two different shearing schemes in order to examine whether the shearing scheme will affect the behaviour of the specimen. Detailed analyses of the results with scheme 1 were presented in Chapter 5. In this Appendix, the microscopic and macroscopic results obtained from these two different shearing schemes are compared.

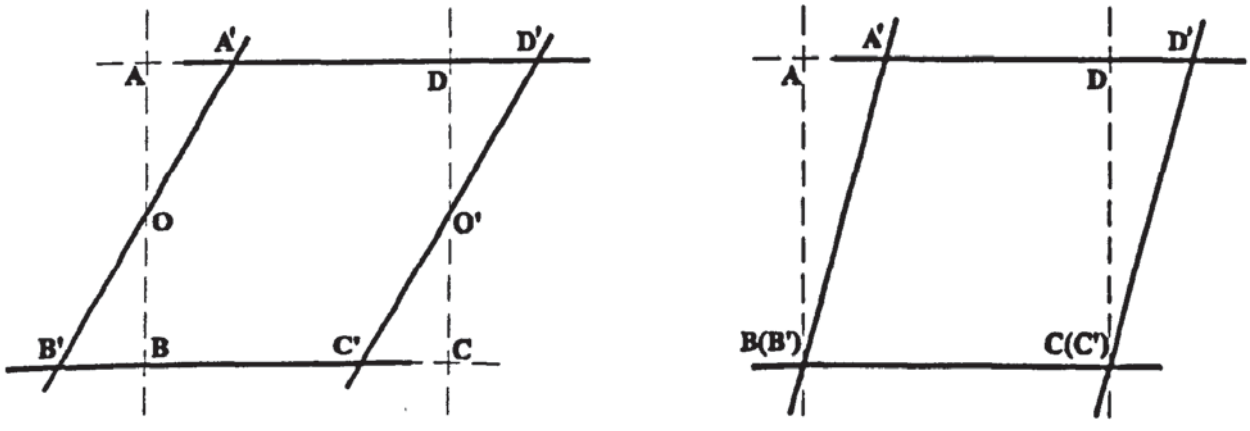

(a) scheme 1 (rotate about O, O') (b) scheme 2 (rotate about B, C)

Fig. D.1 Two shear schemes for the simple shear test

D.2 Force transmission pattern and the velocity field

The force transmission and velocity field diagrams obtained from both schemes at the peak stage are compared in Figs. D.2-3, respectively. It can be seen that large forces align diagonally, indicating the major principal stress direction for both shear schemes (Fig. D.2). The force transmission patterns are essentially the same for both shear schemes.

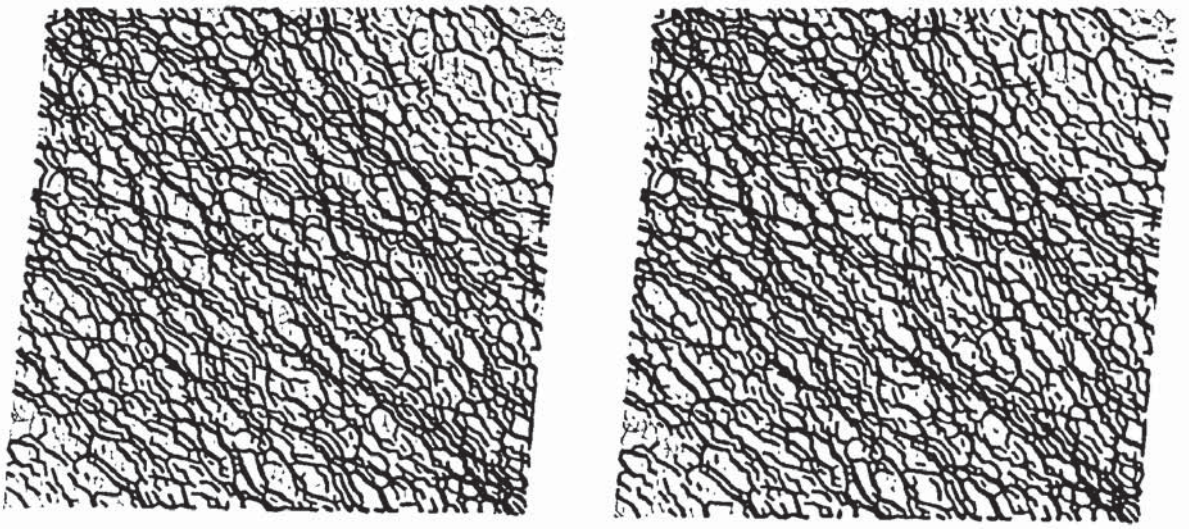

(a) (b)

Fig. D.2 Comparison of force transmission pattern: (a) scheme 1; (b) scheme 2

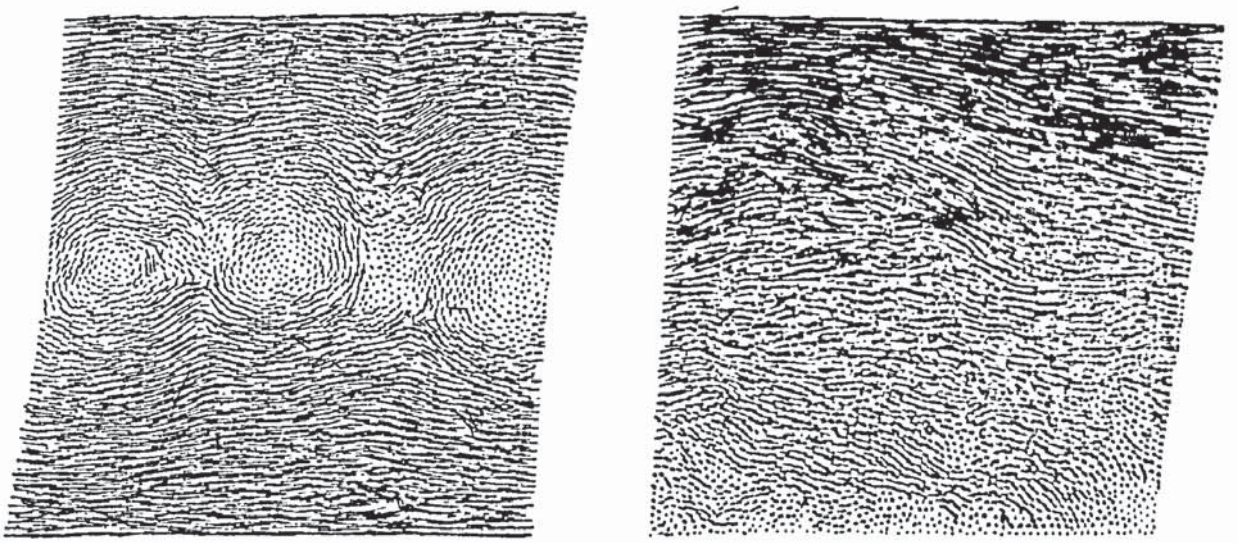

(a) (b)

Fig. D.3 Comparison of velocity field: (a) scheme 1; (b) scheme 2

In the sample sheared using scheme 1, the velocities of the particles near the top and bottom walls are clearly in two opposite horizontal directions. Consequently, there are several circulation cells in the central part of the sample (Fig. D.3a). When scheme 2 is chosen the magnitude of the velocity gradients reduce from top to bottom of the sample. However, no circulation cells are observed (Fig. D.3b). By comparing these two schemes it is clear that the non-uniformity of velocities always appears near the hinges where the wall rotation is applied in simple shear tests.

D.3 Macroscopic behaviour

The measured normal and tangential forces acting on each wall for scheme 2 are presented in Fig. D.4. The notations used in the following figures are the same as those in Chapter 5 (Fig. 5.4). It can be seen that the magnitude and the evolution of these forces measured using scheme 2 are similar to those obtained from scheme 1, as shown in Fig. 5.6b.

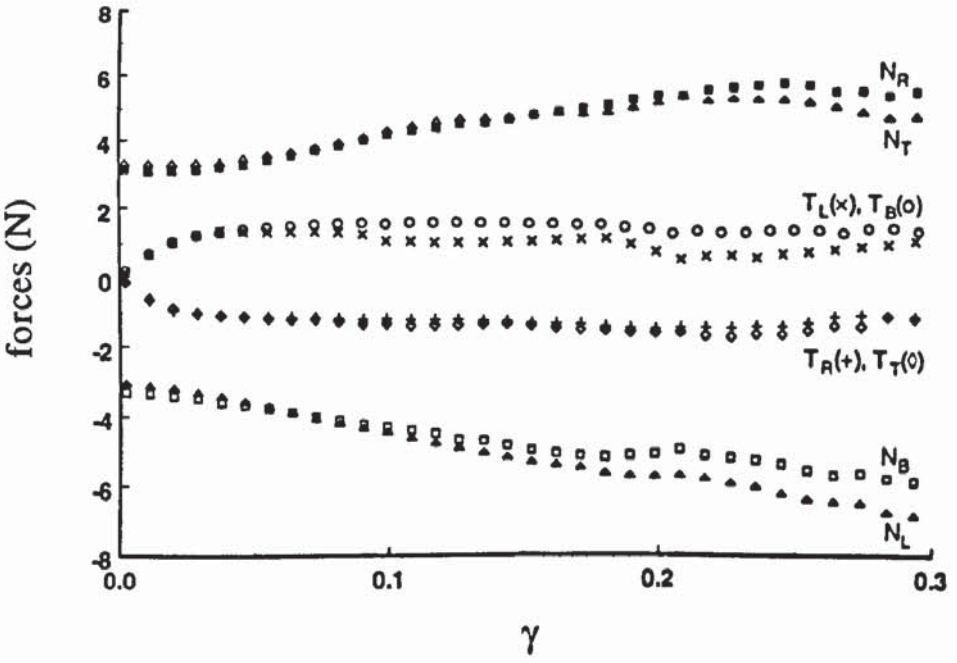

Fig. D.4 Wall forces in scheme 2

The corresponding normal and shear stresses measured from the boundaries and the stress tensor for scheme 2 are shown in Fig. D.5. Again, similar results as those obtained from scheme 1, as shown in Fig. 5.8, can be found. The stress ratios obtained from the stress tensor ($tan\varphi_c$) and from boundary measurements (T/N) for both schemes are presented in

Fig. D.6. It is clear that the results are essentially identical. Therefore, from the point of view of macroscopic behaviour of the specimen, the results are independent of the shear scheme chosen.

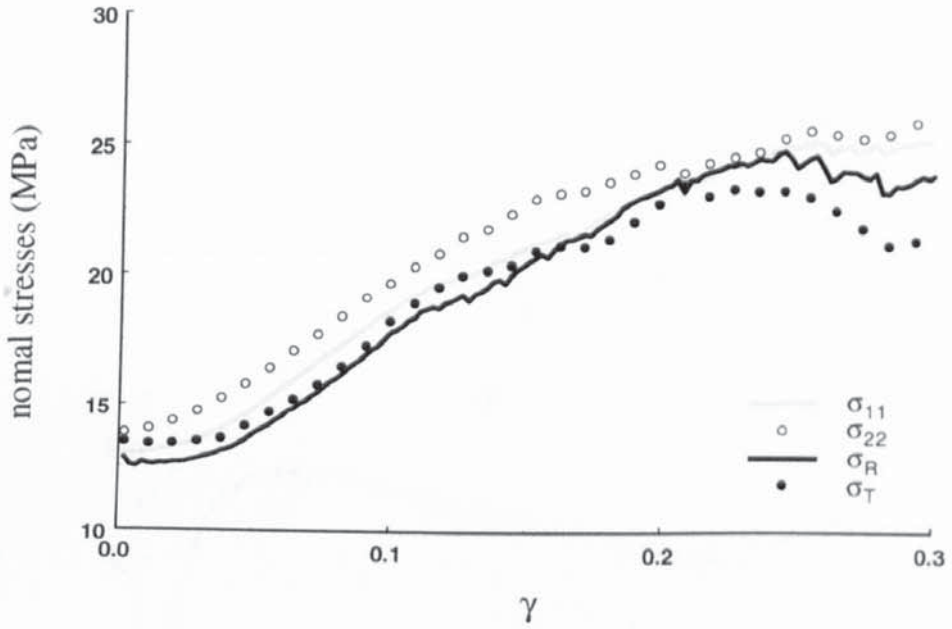

(a) normal stresses

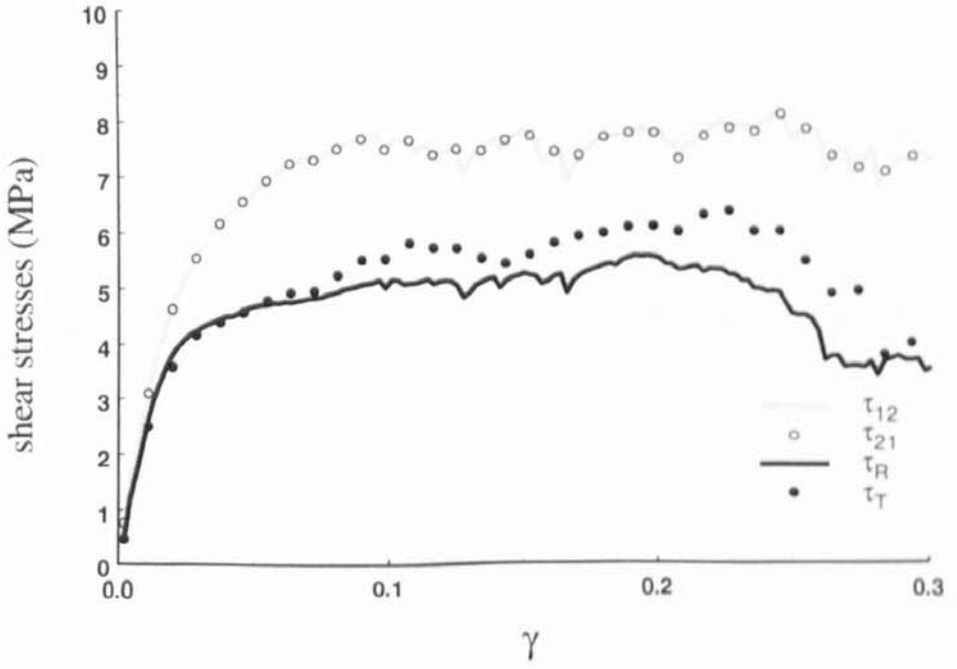

(b) shear stresses

Fig. D.5 Stress-strain curves for scheme 2

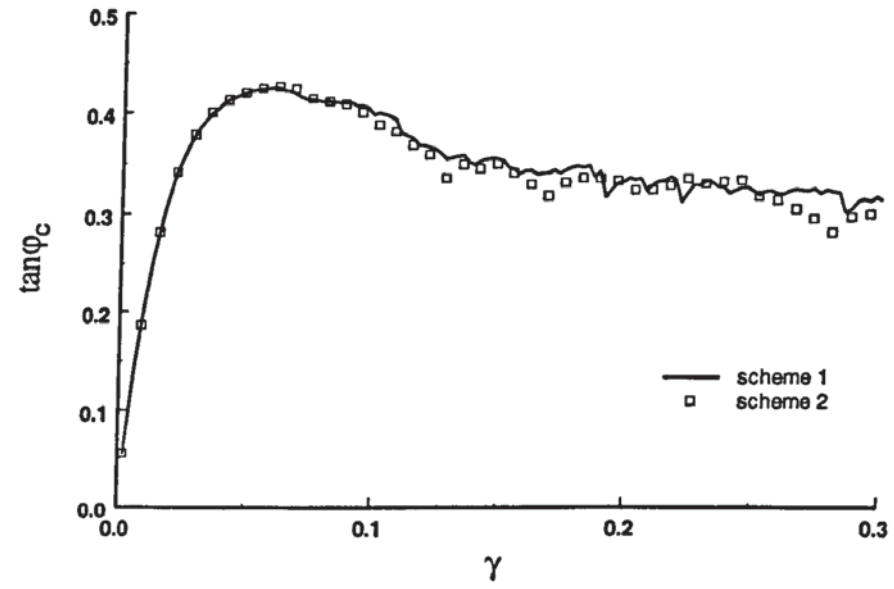

(a)

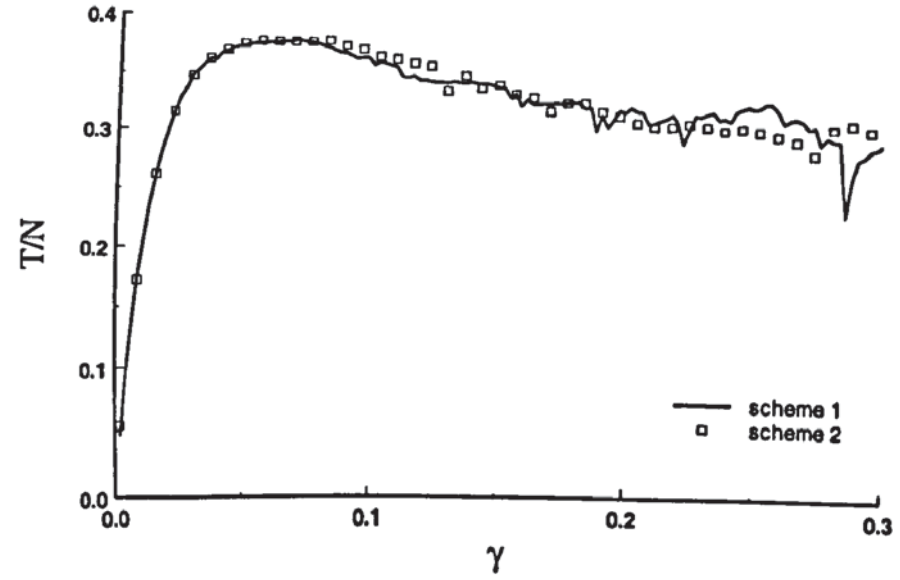

(b)

Fig. D.6 Comparison of evolution of stress ratio: (a) $tan\varphi_c$; (b) T/N

D.4 Microscopic behaviour

The microscopic behaviour, including the evolution of the mechanical coordination number, the structural anisotropy, and the ratio of sliding contacts are compared in Fig. D.7 for both schemes. It can be seen that the microscopic aspects obtained from these two schemes are also essentially identical. Therefore, the same microscopic behaviour of the specimen can be obtained regardless of which shear scheme is used.

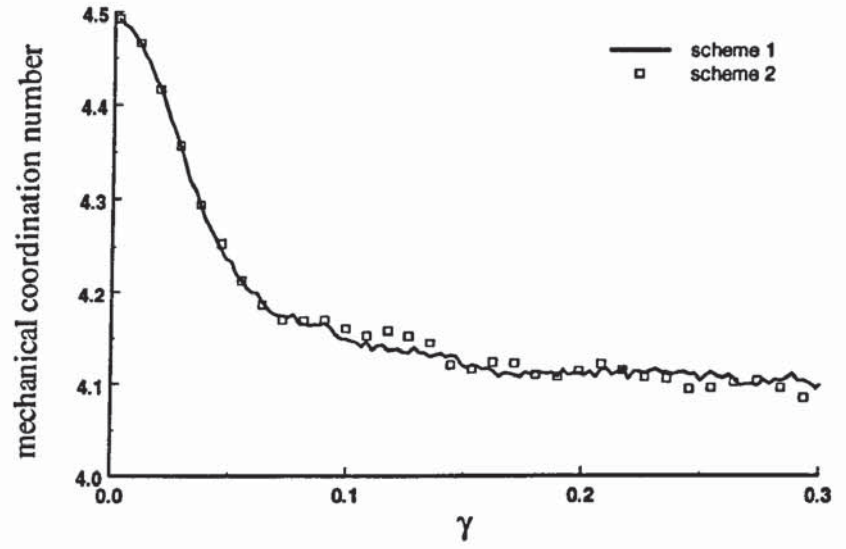

(a) mechanical coordination number, Z_m

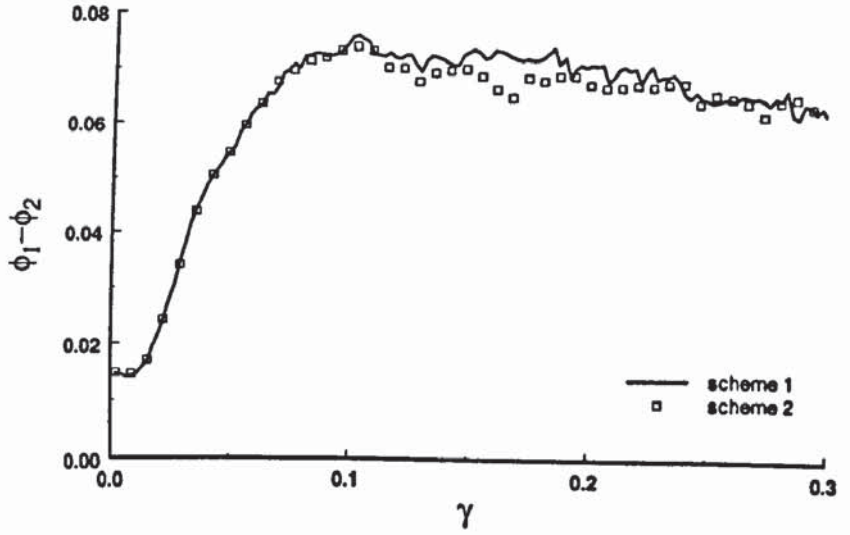

(b) induced anisotropy

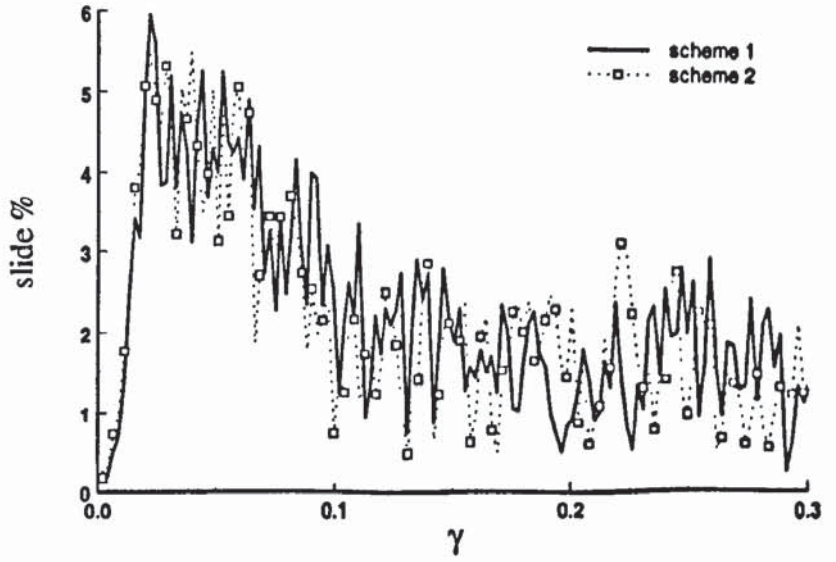

(c) sliding contacts

Fig. D.7 Microscopic behaviour

D.5 Summary

In this appendix, two different shear schemes for the simple shear test have been examined. It has been shown that similar results can be obtained with both schemes. The only difference between these two schemes is reflected by the velocity field. When scheme 1 is employed the non-uniformity is found at the mid-height of the specimen. On the other hand, the non-uniformity appears at the bottom boundary with scheme 2. This difference does not affect the macro- and microscopic behaviour of the specimen. It is therefore suggested that either shear scheme can be chosen to perform simple shear tests.